BAKU STATE UNIVERSITY

7th INTERNATIONAL CONFERENCE MTP-2021: MODERN TRENDS IN PHYSICS

DECEMBER 15 - 17, 2021
BAKU STATE UNIVERSITY
BAKU, AZERBAIJAN

PROCEEDINGS

VOLUME I

BAKU STATE UNIVERSITY
33, Academician Zahid Khalilov Street,
Baku, Azerbaijan
Phone: (+994 12) 430 32 45
Fax: (+9942 12) 598 33 76
E-mail: info@bsu.edu.az

ISBN 978-9952-546-52-1

ISSN: 2522-4352

Co-organizers:

STAR-NET
Regional Network for Education and Training in Nuclear Technology

SAPIENZA
Università di Roma

JINR

BAKU STATE UNIVERSITY

7th INTERNATIONAL CONFERENCE MTP-2021:
MODERN TRENDS IN PHYSICS

DECEMBER 15-17, 2021

BAKU STATE UNIVERSITY, BAKU, AZERBAIJAN

PROCEEDINGS

VOLUME I

BAKU - 2021

Conference organized by
Baku State University

In collaboration with
STAR-NET Regional Network for Education and Training in Nuclear Technology
Joint Instute for Nuclear Research, Dubna
University of Szeged, Hungary
Sapienza University of Rome, Italy

Conference website: http://mtp2021.bsu.edu.az/

Proceedings of the 7th international conference MTP-2021: Modern trends in Physics. Volume I. December 15-17, 2021. Baku State University. Baku, Azerbaijan 2021. – 250 p.

ISSN: 2522-4352

ISBN: 978-9952-546-52-1

Editor in Chief:

Deputy Editors in Chief:

Editorial Board:

Executive Editors:

Editorial Assistants:

CONTENTS

MODELING AND SIMULATION OF STRUCTURE-PROPERTY RELATION IN Fe-BASED NANOALLOYS VIA COMPUTATIONAL MATERIALS SCIENCE

AO MEKHRABOV, EA IRMAK, MV AKDENIZ

Novel Alloys Design and Development Laboratory (NOVALAB), Department of Metallurgical and Materials Engineering, Middle East Technical University, Dumlupinar Blv. No: 1, 06800-Ankara, Turkey
E-mail: amekh@metu.edu.tr

Nanoalloys are present very complex structures and properties, which crucially depend on their size, composition and chemical ordering, and which can therefore be tailored for specific and industrially relevant applications – as in data storage, optical devices, catalysis etc. So, controlling and tailoring the structure and properties of nanoalloys, and determining their phase diagrams, require the concerted effort of experiment and computer modeling and simulation. In this present study the modeling and simulation of structural stability and local structural evolutions in 6 nanometer FeNi3 nanoparticles have been investigated by using classical molecular dynamics (MD) simulation method combined with embedded atom model (EAM) in Large-scale Atomic/Molecular Massively Parallel Simulator (LAMMPS). MD simulations have been performed for both in crystalline and glassy state of FeNi3 alloy system by making use of pairwise interatomic interaction potentials and electron densities calculated via EAM method. The formation and evolution of structures and their stability have been analyzed at a wide temperature range (300-1900K) by calculating radial distribution functions (RDF), interatomic distances (ID), coordination numbers (CN), core-to-surface concentration profiles, as well as Voronoi analysis. It was shown that, although some deviations in the structural properties occurred during the heat treatment, the 6 nm crystalline and amorphous nanoparticle exhibited the same crystal structure and local atomic configuration with its bulk counterpart at room temperature.

Keywords: Computer Modelling and Simulations, Iron-nickel nanoalloys, Molecular dynamics, Embedded atom model
PACS: 02.70.Ns, 07.05.Tp, 61.46.+w, 61.82.Bg, 64.70.Kb, 71.20.Be, 81.30.Hd

Introduction

There is a growing research interest on the modeling and simulation of the magnetic nanoalloys, since the unique and sometimes superior chemical and physical properties of the nanoalloys can be tuned and, consequently, new structural motifs can be created by varying the type of constituent elements, atomic and magnetic ordering, as well as size and shape of the nanoparticles for several promising research and application areas [1]. For new generation magnetic nanoalloys, it is important to predict structure-property relations in advance because of the complexity increased by the various structural and geometrical forms in addition to the size-dependent structure [2]. Among the magnetic nanoalloys, Fe-Ni based magnetic nanoalloys have promising usage area in the diversified engineering applications, such as radar absorbing materials in aerospace and stealth industry, catalyst, and biomedical applications, due to their superior mechanical, electrical, optical and magnetic properties with high surface area [3,4]. However, there is not enough study regarding these usage areas of the Fe-Ni nanoalloys because of the concern of the agglomeration, oxidation, and degradation; therefore, it is essential to predict and determine the thermally stable size and shape of the nanoparticles [5].

To supply this demand and make a contribution to the literature, structural evolution of the crystalline and amorphous structure of $FeNi_3$ nanoalloys with 6 nm diameter have been modeled and simulated at a wide temperature range (300-1900K) by molecular dynamics method.

Methodology

Computer simulation techniques have been widely used to investigate structural properties of the Fe-Ni based bulk and nanostructured alloys for a long time. Atomic and magnetic ordering, order-disorder and ferromagnetic-paramagnetic transformation characteristics and also interrelation between atomic and magnetic ordering phenomena in binary $FeNi_3$ and ternary Ni_3(Fe, Me) (Me= W, Mo, Cr, Mn, Nb, etc.) bulk intermetallics have been widely investigated in terms of classical theory of ordering and electronic theory of binary and multicomponent alloys in ab-initio pseudopotential approximation [6-12]. Although the first principle calculations on the Fe-Ni based alloys have been used to predict the properties from atomistic level [13, 14], the molecular dynamics simulations with many-body potentials are mainly preferred because of its applicability to the large systems having more than hundreds of atoms. However, to acquire accurate and efficient results from the molecular dynamics simulations, interatomic potential energy functions have a crucial effect [15].

Therefore, in this study, structural evolutions of Fe-Ni based nanoalloys have been studied by using molecular dynamics (MD) method in Large-scale Atomic/Molecular Massively Parallel Simulator (LAMMPS) with embedded atom model (EAM). EAM is based on the density functional theory and it considers many-body interaction through the electron density of the systems. Therefore, EAM gives more accurate results than the pairwise interaction models with reasonable computational time for Fe-based systems [16-18]. According to EAM model [16], the energy of the system which consists of N-atoms is expressed as Eq.-s (1) and (2),

$$E = \sum_{i} F_i\,(\rho_i) + \frac{1}{2}\sum_{ij} V_{ij}(r_{ij}) \tag{1}$$

$$\rho_i = \sum_{i \neq j} \psi(r_{ij}) \tag{2}$$

Here, F_i represents the embedding function which depends on the electron density (ρ_i) and many-body interaction of the system. V_{ij} denotes the pair potential as a function of the distance between atoms and ψ is the electronic potential function.

In this study, the EAM parameters that were determined by Bonny et al. [16] were utilized to investigate the structural evolution of the $FeNi_3$ system. For solving the equation of motions of atoms in MD, Verlet algorithm was considered with Nose-Hoover thermostat and barostat. Among the ensembles typically used for molecular dynamics, namely the microcanonical (NVE), canonical (NVT) and isothermal–isobaric (NPT) ensembles, the NPT ensemble was applied in this study because it accurately describes experimental conditions by controlling temperature and pressure at the same time [19, 20]. During the simulation of the crystalline nanosystems, it has been assumed that they have the same crystal structure with their bulk counterparts because of containing more than 100 atoms and MedeA - LAMMPS molecular dynamics simulator program system was used for generating the spherical crystalline nanoparticle with the 6 nm diameter, having cubic structure, the length of one edge was 2.8 nm (10168 atoms in total). The temperature dependence of the structural evolution of the nanocrystalline alloys was investigated by raising the temperature to 1700 K with 200 K temperature intervals under vacuum condition. Before the simulation of nanoparticle, the system was relaxed by the conjugate-gradient energy minimization method.

However, during the simulation of the amorphous nanoalloys, a different method was applied. Firstly, a nanoparticle was subtracted from the simulated amorphous bulk alloy. A non-periodic boundary condition was applied to simulate the amorphous 6 nm $FeNi_3$ nanoparticle (9784 atoms in total). Then, the subtracted nanoparticle was melted and equilibrated at 1900 K in order to remove local atomic configurations from the solid phase. Finally, the temperature of amorphous nanoparticle was decreased gradually to room temperature with the overall cooling rate of 10^{12} K/s and equilibrated at each stage by waiting for 10 nanoseconds. The heat-treated $FeNi_3$ crystalline and amorphous nanoparticles were illustrated by using VMD molecular graphics program. The radial distribution function (RDF) has been utilized to verify the structural evolutions of the crystalline/amorphous $FeNi_3$ bulk and nanoparticles during heating and cooling.

Although radial distribution functions are commonly used 2-D functions to represent the 3-D atomic distribution in the nanoalloys, however sometimes they remain incapable to describe complex structures. Amorphous structures, unlike crystalline ones, do not have periodic and symmetric atomic arrangements. A convenient method revealing the three dimensional (3-D) atomic configurations existing in amorphous alloys is Voronoi analysis. Voronoi analysis gives distribution function of the polyhedral structure of space closer to an atom than any other particle, so it defines the characteristic arrangement of near neighbor's atoms. Thus, Voronoi tessellation analysis was implemented with the OVITO software to investigate the local atomic structures in complex systems [21]. Moreover, the Voronoi tessellation is important to determine the coordination numbers (CN) which is related to the lattice structure. Coordination number is the number of contacted particles and it is hardly measured experimentally, so obtaining CN by computational methods is very important [22].

Results and discussion

Before performing the simulations of the nanoparticles, firstly, bulk structure was modeled. The bulk form of $FeNi_3$ alloy, having 27436 atoms, was generated by repeating the $L1_2$-type ordered structured unit cell along [111] direction in nineteen times. After the relaxation of the system at 0 K under the periodic boundary conditions, the temperature was increased to 2600 K under 1 atm pressure and stabilized for $5x10^5$ MD time steps. This temperature is higher than the melting temperature which is enough to homogenize the liquid structure. Then, the temperature decreased to 300 K with 200 K temperature steps and $2.3x10^{11}$ K/sec cooling rate. At each stage, the system was relaxed until the equilibrium was reached. At 300 K, it was observed that the system had a crystal structure. That's why, to obtain the amorphous bulk structure, the system was cooled from 2600 K to 300 K by fast cooling which was involved $1x10^5$ MD steps and $2.3x10^{13}$ K/sec cooling rate. The volume change during heating and cooling for the bulk $FeNi_3$ alloy with the amorphous structure is shown in Figure 1.

During the heating process, there was a sudden jump in the volume-temperature curve which is the sign of the melting of an alloy. However, we did not observe the sudden change in the volume during the slow-cooling, which indicated that no crystallization occurred and the amorphous structure was preserved at room temperature. Also, presence of amorphous structure was proven by the calculated radial distribution function (RDF) which is illustrated in Figure 2b. The RDF of the bulk crystal structure had a regular structure and there wasn't any possibility of finding a particle between the peaks, Figure 2a. The first peak location on the RDF curve of the crystalline bulk $FeNi_3$ alloy indicates to the nearest neighbor interatomic distance which was estimated as 2.436 Å at 300 K. The location of the second peak corresponds to the alloy lattice parameter which was found to be 3.5 Å, meaning that simulated bulk crystal structure of $FeNi_3$ is $L1_2$-type ordered face-centered cubic. On the other hand, there was a lack of ordered atomic arrangements for fast cooling (2.3×10^{13} K/sec cooling rate) of $FeNi_3$ alloy which is another sign of the preserved amorphous structure at room temperature, Figure 2b.

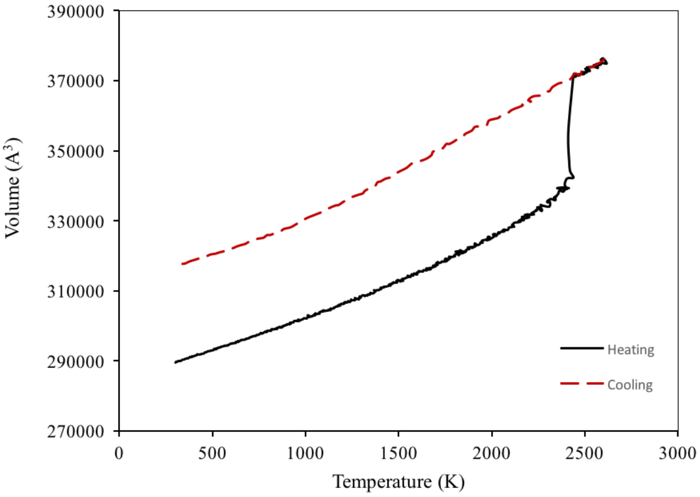

Fig. 1. The volume change of the FeNi3 amorphous alloy during heating and cooling.

RDF's variation with temperature for the crystalline $FeNi_3$ nanoparticles with 6 nm diameter, having 2542 Fe atoms and 7626 Ni atoms (10168 atoms in total) are illustrated in Figure 3a. According to the RDF of the crystalline nanoparticle, there are a peak broadening effect at the surface of nanoparticle probably due to surface melting, however on the inner side of the nanoparticle some ordered atomic arrangement with 3.5 Å lattice parameter was preserved until 1300 K temperature. The RDF's for amorphous nanoparticle with same diameter with 2450 Fe atoms and 7334 Ni atoms (9784 atoms in total) is given in Figure 3b. According to Figure, the peaks started to appear at 300-900 K temperature range having some valley between the peaks which became deeper at 900 K temperature of amorphous nanoparticle. It is evident from Figures 3 that, at 300 K temperature the first and the second peak of the RDF of the initially amorphous 6 nm nanoparticle had almost the same height and width with RDF of crystalline nanoparticle. Also, during the cooling process of the amorphous nanoparticle with 6 nm diameter, the lattice parameter changed from the 3.556 Å at 900 K, where crystallization started, to 3.5 Å at room temperature which is consistent with the lattice parameter of the initially crystalline $FeNi_3$ nanoparticle reported in the literature [23]. This means that the 6 nm amorphous $FeNi_3$ nanoparticle completely transformed to the crystalline structure at room temperature, even though it did not have a compact structure as the initially crystalline nanoparticle.

The coordination numbers (CN) of the initially crystalline and amorphous 6 nm $FeNi_3$ nanoparticle has been determined from their RDF's. CN of crystalline nanoparticle remained almost constant at around 11.5 during heat treatment, which is close to the CN of the bulk $FeNi_3$ alloy (12) with $L1_2$-type ordered crystal structure at room temperature. It was shown that, although the coordination number of the initially amorphous $FeNi_3$ nanoparticle fluctuated during the cooling process, it also approached to 11.5 at room temperature [24].

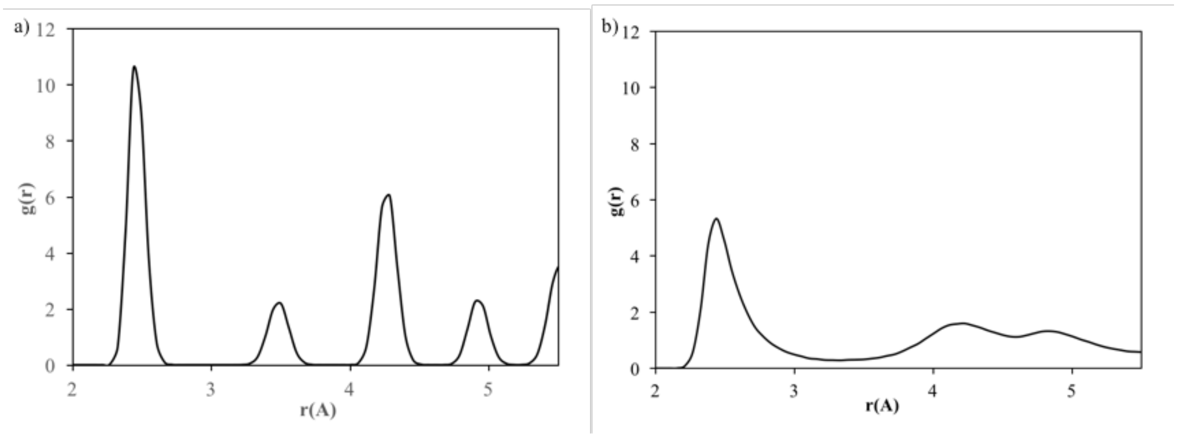

Fig. 2. The RDF of the $FeNi_3$ bulk alloy: a) crystalline and b) amorphous structures.

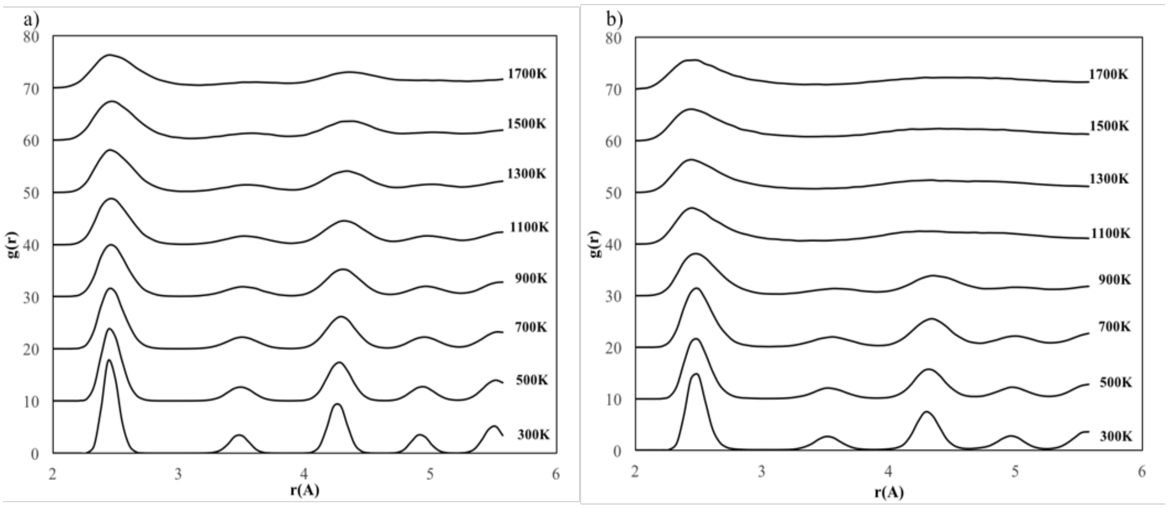

Fig. 3. The RDF variation with temperature for 6 nm $FeNi_3$ nanoparticles having initially: a) crystalline and b) amorphous structures.

The core-to-surface concentration profiles, for the 6 nm crystalline and amorphous nanoparticles at 300 K and 1700 K, are shown in Figure 4. According to Figures 4a and 4b, for crystalline nanoparticles if the initial ordered structure at 300 K have been deformed at 1700 K, but mixing pattern did not change and formation of core-shell structure was not observed.

One of the main factors that lead to formation of the core-shell structure in nanoalloys is the difference between atomic sizes- small atoms are located in the core of the particle but the larger ones form an outer shell that surrounds the core [25]. In Fe-Ni system, Fe and Ni atoms have the similar radius, such as 0.126 nm and 0.125 nm, respectively. Therefore, even though some Ni atoms are located in the core side, an ordered mixing pattern formation is consistent with the findings in literature [25]. Regarding the amorphous nanoparticle, it is evident from Figures 4c and 4d that, although a small amount of Ni atoms is located in the core side and melted Fe atoms stayed at the surface of nanoparticle, a mixed pattern of Fe and Ni atoms was established at the end of the cooling process. From the morphological point of view, 6 nm crystalline nanoparticle mostly preserved its spherical shape even at high temperatures. On the other hand, with the decreasing temperature, the irregular shape of the 6 nm amorphous nanoparticles evaluated to the sharp-sphere shape at 300 K, which means the 6 nm nanoparticle had a capability to undergo transformation from its initial shape to geometrically more stable shape.

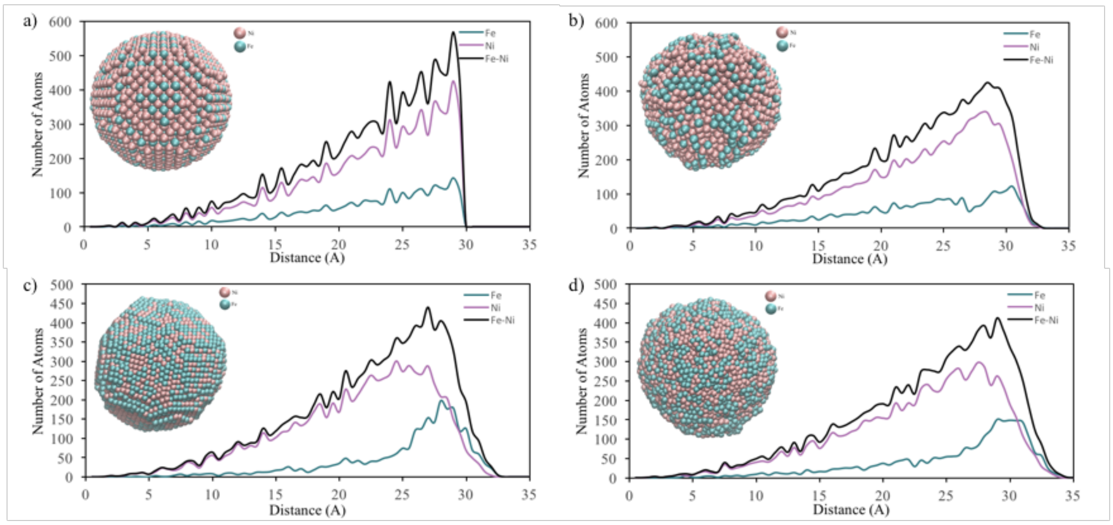

Fig. 4. Core-to-surface concentration profiles of 6 nm $FeNi_3$ nanoparticles: crystalline nanoparticle at a) 300 K and b) 1700 K; amorphous nanoparticle at c) 300 K and d) 1700 K.

According to Voronoi analysis, all of the local atomic configurations in solid phase were completely different from the liquid phase of the 6 nm amorphous nanoparticle, Figure 5. Moreover, the nanoparticles simulated with different ways had common polyhedrons at room temperature, such as <0,6,4,2>, <0,5,6,2>, <0,7,4,1>, <0,7,4,2> and <0,5,6,1>, indicating that the 6 nm $FeNi_3$ amorphous nanoparticle generally transformed to the crystalline structure at 300 K. Besides, the total coordination numbers of the 6 nm nanoparticles determined from the Voronoi tessellation, were found to be in between 12 and 13 atoms which are also consistent with the coordination number of the FCC crystalline structure.

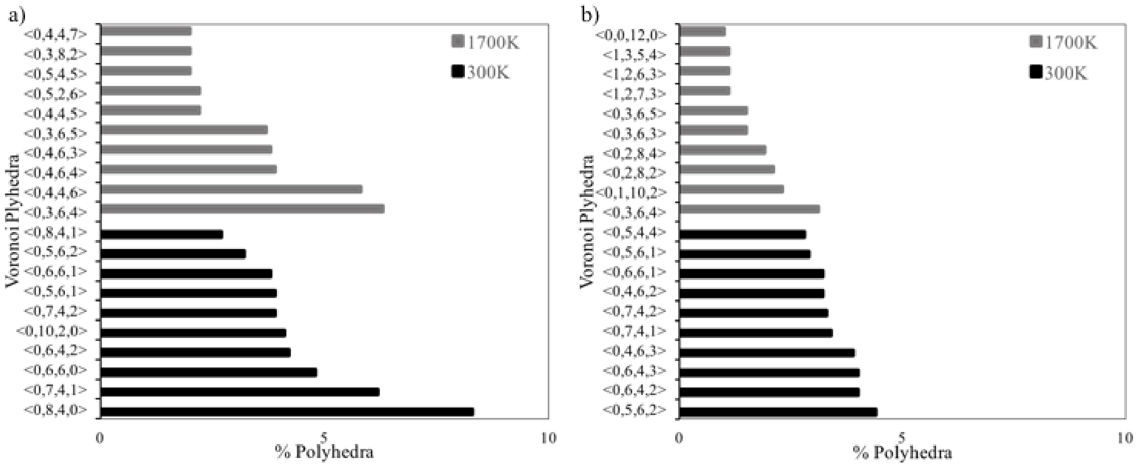

Fig. 5. The Voronoi tessellation results for initially a) crystalline and b) amorphous structures.

Conclusion

Temperature effect on the formation and evolution of structures and their stability for the crystalline and amorphous $FeNi_3$ nanoalloys with 6 nm diameter have been investigated at wide temperature range (300-1900K) by means of molecular dynamics simulations combined with embedded atom model. Firstly, the $FeNi_3$ nano system was modeled by assuming that, systems with more than 100 atoms have the same crystal structure as their bulk counterpart; then the temperature augmentation process applied. Afterward, the spherical nanoparticles with 6 nm diameter were also obtained by subtracting them from the simulated amorphous bulk counterpart at 1900 K, and the obtained amorphous nanoparticle incrementally cooled down to room temperature. Then, the structural evolution of these nanoparticles was analyzed by means of radial distribution functions, coordination numbers, core-to-surface concentration profiles, and Voronoi analysis. It has been shown that, while the nanoparticles deformed slightly at high temperatures, however, they owned same FCC crystalline lattice structure having ordered mixing pattern with 3.5 Å lattice parameter and 12-13 coordination number at room temperature, even though they were modeled in different ways.

Acknowledgements

This work was supported by the Scientific Research Projects (BAP) Coordination of METU with project number of GAP-308-2018-2725 and also, computing resources used in this work were provided by the National Center for High Performance Computing of Turkey (UHeM) under grant number of 4004752017, which authors gratefully acknowledge.

References

1. Moussa Sh., Abdelsayed V., El Shall M.S., Chemical synthesis of metal nanoparticles and nanoalloys, In Nanoalloys, Elsevier Inc., 2013, 416 p.
2. Ferrando R., Jellinek J., Johnston R.L., Chem. Rev. 2008, v. 108, p. 845.
3. Bazin D., Fechete I., Garin F.C., Barcaro G., Negreiros F.R., Sementa L., Fortunelli A., Reactivity and catalysis by nanoalloys, In Nanoalloys, Elsevier Inc., 2013, p. 283.
4. Zhou P. H., Deng L. J., Xie J. L., Liang D. F., Chen L., and Zhao X. Q., Journal of Magnetism and Magnetic Materials 2005, v. 292, p. 325.

5. McNamara K., Tofail Syed A.M., Biomedical applications of nanoalloys, In Nanoalloys, Elsevier Inc., 2013, p. 345.
6. Matysina Z.A., Mekhrabov A.O., Babaev Z.M., and et al. Phys. Stat. Sol.(b) 1986, v. 138, p. 399.
7. Mekhrabov A.O. Fiz. Metal. Metalloved. 1986, v. 62 (5), p. 1023.
8. Mekhrabov A.O., Babaev Z.M., and et al. Fiz. Metal. Metalloved. 1986, v. 61 (6), p. 1089.
9. Matysina Z.A., Mekhrabov A.O., and et al. J. Phys. Chem. Sol. 1987, v. 48, p. 419.
10. Matysina Z.A., Mekhrabov A.O., and Babaev Z.M. Fiz. Metal. Metalloved. 1987, v. 64, p. 202.
11. Babaev Z.M., Menshikov A.Z., Mekhrabov A.O., Valiev E.S. Fiz. Metal. Metalloved. 1987, v. 64, p. 762.
12. Mekhrabov A.O. Hyperfine Interactions 1990, v. 59, p. 337.
13. Cheng H. P. and. Ellis D. E. Physical Review B 1989, v. 39 (17), p. 12469.
14. Mishin Y., Mehl M. J., and Papaconstantopoulos D. A. Acta Materialia 2005, v. 53 (15), p. 4029.
15. Halicioglu and Bauschlicher Jr. C. W. Reports on Progress in Physics 1988, v. 51 (6), p. 883.
16. Bonny G., Pasianot R. C. and Malerba L. Modelling and Simulation in Materials Science and Engineering, 2009, v. 17, p. 025010.
17. Akdeniz M.V. and Mekhrabov A.O. J. of Alloys and Compounds 2019, v. 788, p. 787.
18. Yalcin M., Mekhrabov A. O. and Akdeniz M. V. Acta Physica Polonica A 2014, v. 125 (2), p. 600.
19. Furio Ercolessi, A molecular dynamics primer, Technical report, International School for Advanced Studies (SISSA-ISAS), Trieste, Italy, 1997.
20. Tuckerman M.E., Alejandre J., López-Rendón R., Jochim A.L.and Martyna G.J. Journal of Physics A: Mathematical and General 2006, v. 39 (19), p. 5629.
21. Shimono M. and Onodera H. Metals 2015, v. 5, p. 1163.
22. Wang C. C., Dong K. J and Yu A. B. AIP Conference Proceedings 2013, 1542, p. 353.
23. Chicinas I., Pop V., Isnard O., Le Breton J. M., and Juraszek J. Journal of Alloys and Compounds 2003, v. 352 (1-2), p. 34.
24. Nirouei M., Jafari A. and Boustani K. Journal of Superconductivity and Novel Magnetism 2014, v. 27(12), p. 2803.
25. Aguado Andrés A., Modeling the electronic and geometric structure of nanoalloys, In Nanoalloys, Elsevier Inc., 2013, p. 75.

DIELECTRIC FUNCTION AND CRYSTALLINITY OF POLYCRYSTALLINE FILMS

YN ALIYEVA, EA BAGIEV, EH ALIZADE, JN JALILI, AH BAYRAMOV and NT MAMEDOV

Institute of Physics, ANAS, 131 H. Javid str., Baku, Az 1143, Azerbaijan
E-mail: yegana.aliyeva@science.az

In addition to the conventional degree of crystallinity, based on the photon energy independent material constants such as mass density, thermodynamic functions, and crystalline structure the spectral and optical crystallinities are introduced in the same manner for after-growth optical characterization of the polycrystalline films. The introduced parameters are based on the imaginary part of dielectric function and the integrated absorption derived from this part, respectively and need knowledge of the complex dielectric function for single crystal or amorphous phase as reference and for the studied polycrystalline film in a broad spectral range. Polycrystalline ZnO thin films obtained by magnetron sputtering on glass substrates under different oxygen/argon gas mixture (O/Ar ratio 0-6 %) at substrate temperatures 200, 300 and 400°C are examined by room temperature spectroscopic ellipsometry in the photon energy range from 0.74 to 6.5eV to check how the introduced parameters work. It is shown that spectral crystallinity provides the degree of the deviation of the measured dielectric function from the perfect crystal case. The optical crystallinity is likely to be an optical counterpart of the conventional degree of crystallinity based on the commonly used material constants.

Keywords: computer modelling and simulations, iron-nickel nanoalloys, molecular dynamics, embedded atom model
PACS: 02.70.Ns, 07.05.Tp, 61.46.+w

Introduction

Optical constants of thin films of crystalline, polycrystalline and amorphous materials are of key importance for the design and performance of optical and optoelectronic devices. In this sense, one of the main issues to address is precise "optical" condition of the film that is necessary to provide the desirable optical or optoelectronic performance. This condition is ultimately predetermined by the degree of structural order (disorder) in the film and the parameter that directly addresses this issue is the degree of crystallinity that shows the fractions of crystalline and amorphous phases in total volume of a material. This fundamental parameter, determined using mass density, X-ray diffraction (XRD), Raman spectroscopy, and differential scanning calorimetry (DSC) techniques is especially widely used in polymer science [1-4] since crystallinity has a big impact on density, hardness, and transparency of polymer coatings.

Along with fundamental importance, crystallinity is a very useful parameter helping to select the optimal thin film preparation technology. The point is that high perfection of the film is not always good for device performance as delivered by the case of CIGS thin film solar cells whose performance directly depends on defects and does not imply the highest film crystallinity. [5,6] This fact even more underlines the practical importance of the knowledge of the degree of crystallinity.

Generally, optical constants and dielectric function are quite widely used for thin film characterization as entities sensitive to the perfection of the film. [7-13] However, they depend on photon energy and. therefore, seem irrelevant as entities suitable for defining such a constant like degree of crystallinity. On the other hand, optical functionality of the optical or optoelectronic materials is directly depended on their dielectric function - a fundamental material constant that can be referred to as the fingerprint of a material. Therefore, it is reasonable to assess them using some parameter based on this function and allowing to evaluate the compatibility of their optical condition with the required optical functionality.

The purpose of this work is to introduce such parameter and to check how it works in application to a number of polycrystalline ZnO and ZnO:Al thin films which received XRD and AFM (atomic force microscopy) characterization and were at our disposal.

Samples and experimental results

The examined ZnO and ZnO:Al thin films with the nominal thickness of 100 nm were deposited onto 1.0 mm thick, 2x2 cm size soda lime glass substrates. The deposition was carried out with a RF magnetron sputtering technique (EVOVAC deposition system, Angstrom Engineering Inc., Canada) in a pure argon ambient and oxygen/argon gas mixture with different O/Ar ratio (2-6 %O_2) at 200-400°C substrate temperatures. ZnO and ZnO:2%Al targets of 99.99% purity were used for the sputtering. Deposition rate was 1 Å/sec. Prior to the deposition all of the substrates were chemically cleaned by acid. After chemical cleaning, the substrates were rinsed in de-ionized water in ultrasonic bath and then dried under pure nitrogen flow. All of the measurements were carried out on the "as-prepared" films, which were not subjected to thermal annealing, etching and other treatment.

X-Ray diffraction (XRD) measurements were carried out using a Bruker D2 Phaser diffractometer (Germany) in θ-2θ scan mode with Ni-filtered CuKα radiation (λ=1.54060 Å) source. All samples exhibited only (0 0 2) reflection in XRD patterns indicating their belonging to the hexagonal wurtzite structure.

The surface morphology of the films was investigated using a Smart SPM 1000 AIST NT (Tokyo Instruments, Japan) high-resolution atomic force microscope (AFM).

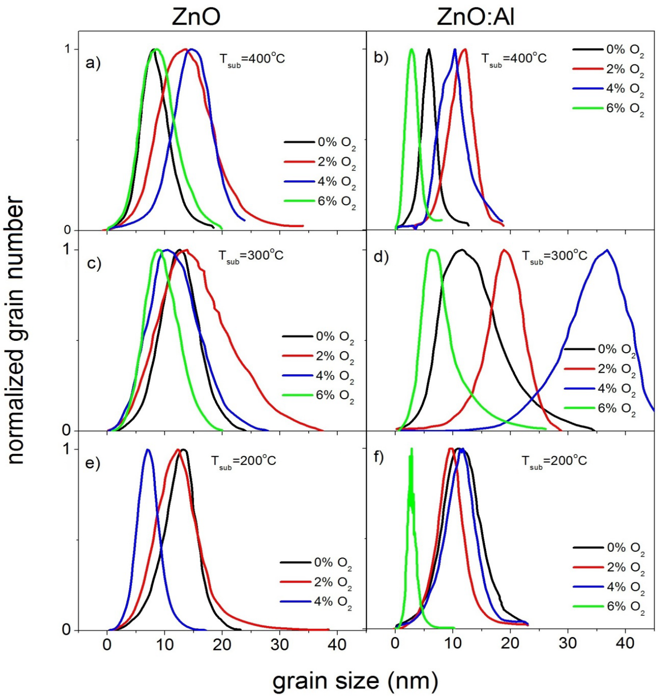

Fig. 1. The size distribution of the normalized number of grains as obtained from AFM measurements.

Fig. 1 shows the size distribution of the number of microcrystallites (grains) for totally 23 samples of ZnO and ZnO:Al thin films obtained at 400 (a,b), 300 (c,d) and 200oC (e,f) at 0 (black curves), 2 (red curves), 4 (blue cueves) and 6% O2 (green curves) in Ar/O2 gas mixture.

According to Fig. 1, most samples show quite narrow distribution of grain sizes with well defined peaks corresponding to the maximum number of grains. It is essential for further optical considerations that grain dimensions are mainly below 20 nm. In one case (Fig. 1, f, green curve) the grains even are of 2.5 nm that is already nanoscale. Interesting, the thin film with just-mentioned nanograins has exhibited "more crystalline" dielectric function than the one with 10 nm grains (Fig. 1, f, red curve) later selected as a prototype of amorphous phase.

All 23 samples were tested by spectroscopic ellipsometry (SE) at incident angles Φ equal to 50, 55, 60, 65 and 70o with particular details described earlier in one of the works [13].

Fig. 2 shows ellipsometric data for eight samples as an example to illustrate the sufficiently good quality of the fits to three-phase optical model that was consisted of roughened surface layer, ZnO or ZnO:Al layer and substrate and was universally applied to all samples in this work Real and imaginary parts of the complex dielectric function retrieved from ellipsometric data in Fig. 2 are given in Fig. 3.

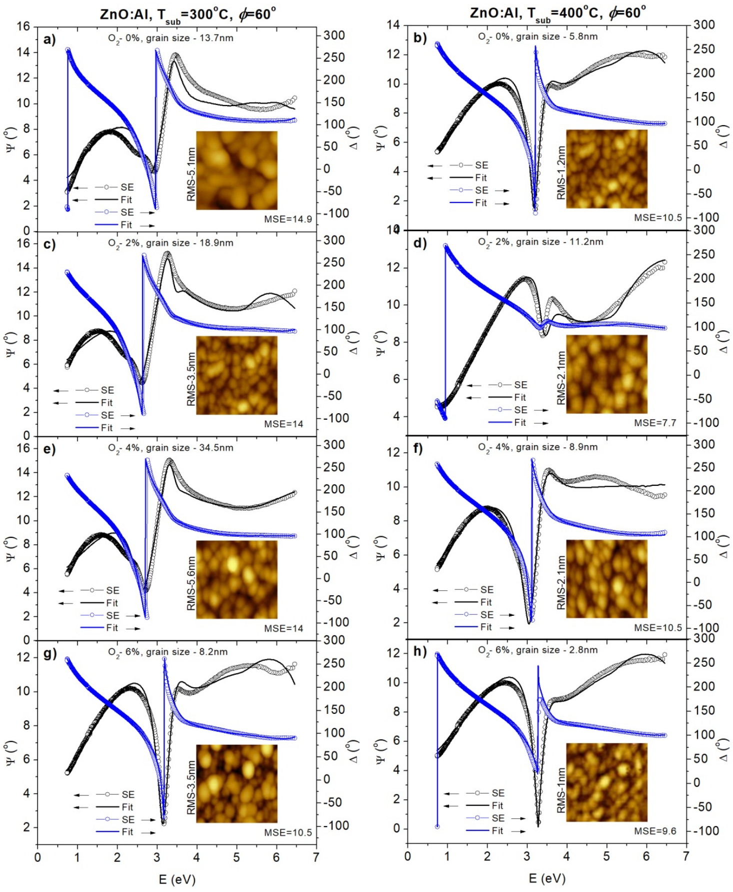

Fig. 2. Ellipsometric parameters Ψ (open dark circles) and Δ (open dark circles) at incident angle of 60^{o} and their fits (dark and blue solid curves, respectively) to optical model for polycrystalline ZnO: Al thin films deposited at 300 and 400^{o}C at 0 (a,b), 2 (c,d), 4 (e,f) and 6% O₂ in Ar/O₂ gas mixture. Inserts: AFM images of the surfaces of the studied samples.

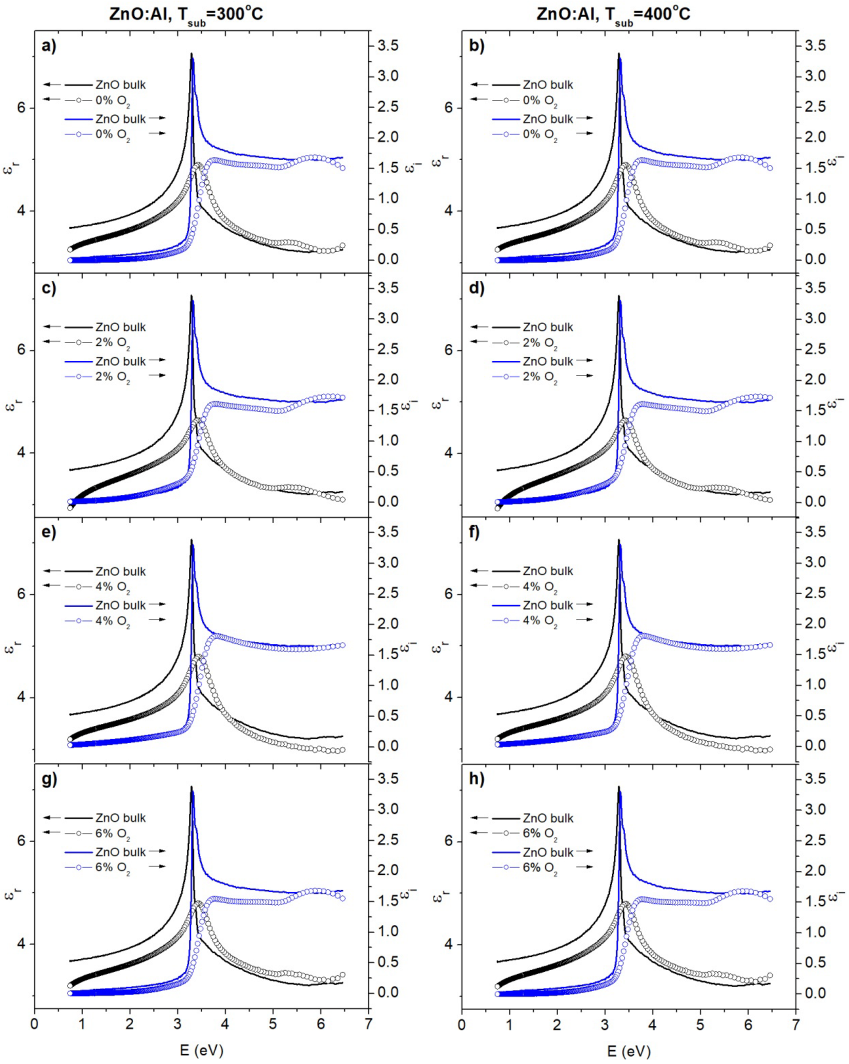

Fig. 3. The photon energy dependence of real (left vertical scales) and imaginary (right vertical scales b, d, f, h) parts of dielectric function of single crystalline ZnO (black solid curves) and polycrystalline ZnO:Al thin films (open dark and blue circles) obtained at 300 (a, c, e, g) and 400°C (b, d, f, h) in Ar/O_2 atmosphere with oxygen concentration 0 (a,b), 2 (c,d), 4 (e,f) and 6% (g,h).

The retrieved dielectric functions look very similar in spite of the sizable difference in grain size between the films obtained under different technological conditions. Let us now see whether they actually differ from each other and what is this difference (if any) by using the parameters introduced in next section.

Formulation and discussion

Unlike the real part (ε_r)of dielectric function, the imaginary part (εi) and integrated absorption ($\int E\varepsilon_i dE$) derived from this part are additive functions and, same as any other material constant (P), can formally be used for determination of the degree of crystallinity (χ_c), defined generally as

$$\chi_c = \frac{P - P^a}{P^c - P^a} \qquad (1)$$

where P is the measured value of the material constant, Pc and Pa are its values for single crystalline and amorphous phases, respectively. Once P, Pc and Pa are known, the degree of crystallinity is found immediately from Equation (1).

Taking the photon energy independent material constant, particularly, mass density gives the interval from 0 (amorphous case) to 1 (crystalline case) for variation of χc from Equation (1) since density of amorphous material is always smaller than that of crystalline one.

In application to imaginary part of dielectric function, Equation (1) can be re-written as

$$\chi_c = \frac{\varepsilon_i^{\mu c} - \varepsilon_i^{a}}{\varepsilon_i^{c} - \varepsilon_i^{a}} \tag{2}$$

where $\varepsilon_i^{\mu c}$ is the imaginary part of dielectric function of a microcrystallite (isolated crystallite), ε_i^{c} and ε_i^{a} are the imaginary parts of dielectric functions of single crystalline and amorphous phases, respectively.

The imaginary part of dielectric function depends on mass density since amount of the matter per unit volume and, hence, density of states for each quasi-particle in solid will increase (decrease) for bigger (smaller) mass density. However, it is hardly possible to expect from imaginary part to strictly follow the mass density since the number of states (per unit volume in init energy interval) contributing to dielectric response is expected to grow in amorphous phase at least in some spectral ranges, because of cancelation of selection rules for transitions inherent in crystalline solids. Therefore, the variation limits for χ_c from Equation (2) are rather uncertain and depend on the selected photon energy. A good illustration of χ_c behavior with photon energy is provided by inserts in Fig. 4 with χ_c plotted as a function of photon energy according to Equation (2). In this equation the imaginary part of dielectric function of amorphous phase was taken equal to that (Fig. 5, a, insert, red curve) of the already mentioned sample ZnO:Al obtained at 200oC and 2% O_2 in Ar/O_2 gas mixture. The obtained SE-based dielectric function was used for microcrystallite and the E⊥C (here E is electrical vector of the incident light, C-optic axis) component (Fig. 5, a, insert, black curve) of the well-known dielectric function for single crystal [15, 16]. Let us conditionally call χ_c in Equation (2) spectral crystallinity.

It is clearly seen in all inserts that spectral χc not only depends on photon energy but also sometimes exceeds 1 and even adopts negative values in some ranges of photon energy. Therefore, it is better to introduce spectral crystallinity in the form that is free from the last two deficiencies and reads as follows:

$$\chi_c^m = 1 - \frac{\left|\varepsilon_i^{\mu c} - \varepsilon_i^{c}\right|}{\varepsilon_i^{\mu c} + \varepsilon_i^{c}} \tag{3}$$

where superscript m means the modified spectral crystallinity. The second term in Equation (3) shows the degree of declination of the imaginary part ($\varepsilon_i^{\mu c}$) from its value for single crystal. The behavior of the spectral crystallinity χ_c^m is shown in Fig. 4.

Now the degree of crystallinity shows only spectral dependence and varies within 0 to1 limits. Note that the value of spectral crystallinity in Equation (3) written for amorphous phase may not be 0 and equals

$$\chi_c^m(amorphous) = 1 - \frac{|\varepsilon_i^a - \varepsilon_i^c|}{\varepsilon_i^a + \varepsilon_i^c} \tag{4}$$

This value has to be considered as amorphous zero. and remembered when making conclusions.

Another approach is based on integrated absorption. Being taken in a broad spectral range, the integrated absorption is practically temperature independent unless the material undergoes some structural changes. [17] The other name of this entity is spectral weight (SW) [18] and studies based on SW are currently performed quite intensively especially in application to narrow band gap materials such as topological insulators. [18]

Let us now use the standard definition of the degree of crystallinity and re-write Equation (2) and Equation (4) as

$$\chi_c = \frac{\int_{E_1}^{E_2} E(\varepsilon_i^{\mu c} - \varepsilon_i^a)dE}{\int_{E_1}^{E_2} E(\varepsilon_i^c - \varepsilon_i^a)dE} \tag{5}$$

And

$$\chi_c^m = 1 - \frac{\left|\int_{E_1}^{E_2} E(\varepsilon_i^{\mu c} - \varepsilon_i^c)dE\right|}{\int_{E_1}^{E_2} E(\varepsilon_i^{\mu c} + \varepsilon_i^c)dE} \tag{6}$$

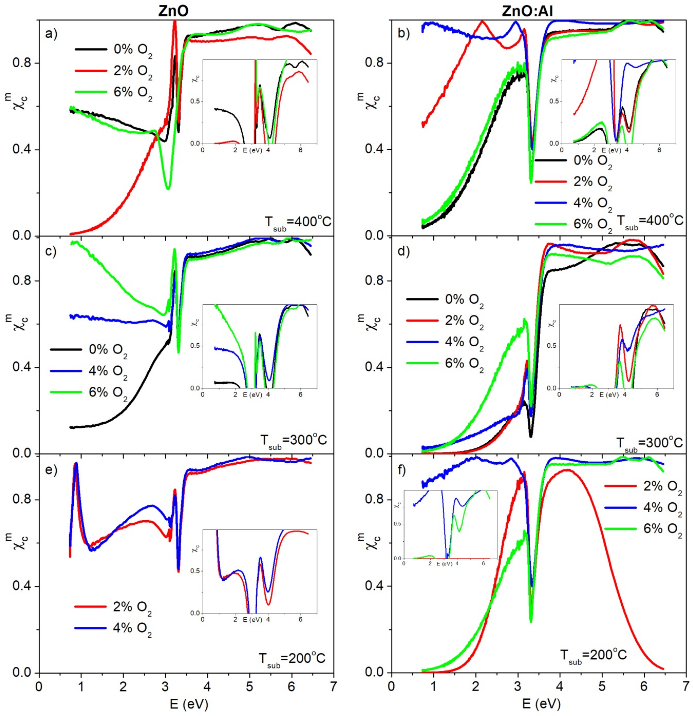

Fig. 4. Introduced by Equation (3), the spectral crystallinity χ_c^m as a function of photon energy for ZnO (a, c, e) and ZnO: Al (b, d, f) thin films obtained at 400 (a, b), 300 (c, d) and 200°C (e, f) and 0 (black curves), 2 (red curves), 4 (blue curves) and 6% O$_2$ (green curves) in Ar/O$_2$ gas mixture. Inserts show spectral crystallinity introduced by Equation (2).

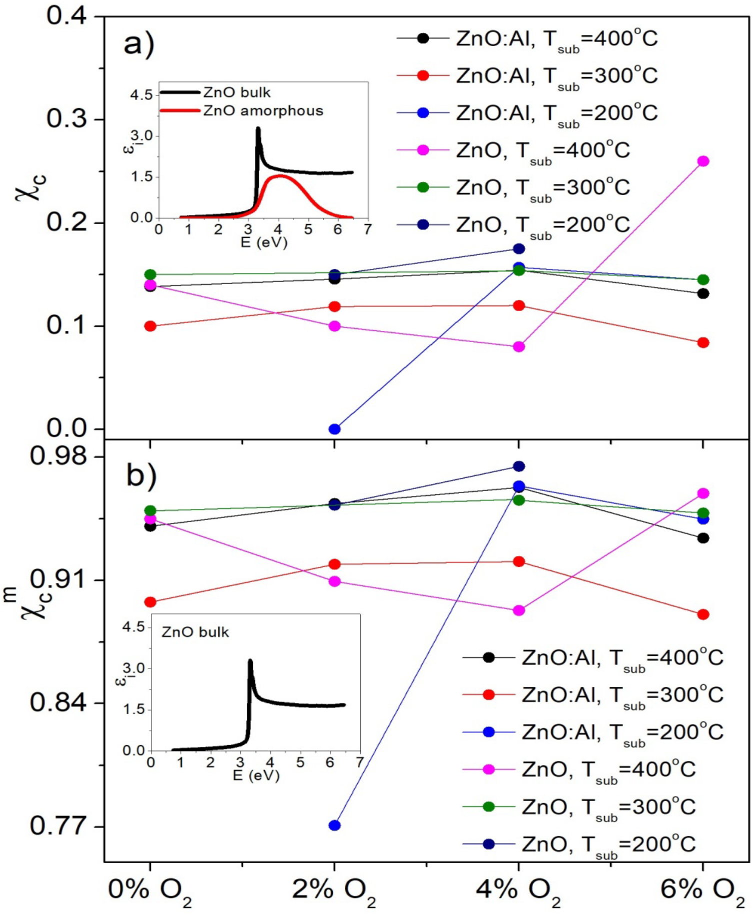

Fig. 5. Optical crystallinities introduced according to Equation (4) -a and Equation (5)- b as a function oxygen concentration in Ar/O_2 mixture for ZnO:Al and ZnO films obtained at different substrate temperatures. Inserts show dielectric functions of the reference crystalline and amorphous thin films.

It is often convenient to consider only non-crystalline and crystalline parts of the polycrystalline films without referring to the frequently unknown dielectric function of the amorphous phase. Note that Equation (6) does not contain dielectric function of this phase and is more convenient for application. Nevertheless, at least a hypothetic dielectric function of amorphous phase can always be found using Bruggeman effective medium approximation (BEMA) [21] as recently shown by Sela and Haspel [22].

Conclusions

New parameters based on imaginary part of dielectric function are introduced for after-growth characterization of polycrystalline films of the optical and optoelectronic materials. The parameter called spectral crystallinity is considered to be helpful for indirect monitoring of the structural changes which occur in polycrystalline film in comparison with reference crystalline material.

The parameter based called optical crystallinity is expected to be able to more adequately estimate the real structure of polycrystalline film than, say, XRD since XRD data are not sensitive to micropores which are always present in polycrystalline films. In this sense, optical crystallinity is close to the degree of crystallinity determined by mass density measurements.

Both parameters need further approbation on polycrystalline films of different commercial materials.

Acknowledgments

This work was completed within the research program "Development of preparation technology of multifunctional convertors based on nanosized structures" supported by Azerbaijan National Academy of Sciences.

References

1. Rian A.J., Brass W., Mant G.R., Derbyshire G.E. Polymer 1994, v. 35 (21), p. 4537.
2. Kumar R., Husain, Khan Z.H. Digest Journal of Nanomaterials M.and Biostructures 2011, v. 6 (3), p. 1317.
3. Shen X., Hu W., Russell T.P. Macromolecules 2016, v. 49 (12), p. 4501.
4. Doumeng M., Makhlouf L., Berthet F., Marsan O., Delb´e K., Denape J., Chabert F. Polymer Testing 2021, v. 93, p. 106878-1.
5. Ramanathan K., Contreras M.A., Perkins C.L., Asher S., Hasoon F.S., Keane J., Young D, Romero M., Metzger W., Noufi R., Ward J., Duda A. Prog. Photovolt. Res. 2003, v. 11, p. 225.
6. Ramanathan K., Teeter G., Keane J.C., Noufi R. Thin Solid Films 2005, v. 480-481, p. 499.
7. Nguyen H.V., Collins R.W. Physical Review B, 1993, v. 47 (4), p. 1911.
8. Joo H.Y., Kim H.J., Kim S.J., Kim S.Y. Thin Solid Films 2000, v. 368, p. 67.
9. Li X.D., Chen T.P., Liu P., Liu Y., Liu Z., Leong K.C. Journal of Applied Physics, 2014, v. 115, p. 103512-1.
10. Li X.D., Chen T.P., Liu Y., Leong K.C. Optics Express 2014, v. 22 (19), p. 23086.
11. Bouzour M.B., Battie Y., Dalmasso S., Zaïbi, Oueslati M., En Naciri A. Superlattices and Microstructures 2017, v. 104, p. 24.
12. Darma Y., Chichvarina O., Purbayanto M.A.K., Nurfani E., Setiawan F.G., Ding J., Rusydi A. Physica Status Solidi A 2018, p. 1800458-1.
13. Guilbert A. A.Y., Schmidt M., Bruno A., Yao J., King S., Tuladhar S.M., Kirchartz T., Alonso M.I., Goñi A.R., Stingelin N., Haque S.A., Campoy-Quiles M., Nelson J. Advanced Functional Materials 2014, v. 24 (44), p. 6972-1.
14. Mammadov E., Naghavi N., Jehl Z., Renou G., Tiwald T., Mamedov N., Lincot D.,. Guillemoles J. F. Thin Solid Films 2014, v. 571 (3), p. 593.
15. Jellison G.E., Boatner L.A. Physical Review B 1998, v. 58 (7), p. 3586.
16. Shokhovets S., Spieß L., Gobsch G. Journal of Applied Physics 2010, v. 107, p. 023509-1.
17. Mamedov N., Shim Y.G., Okada W., Tashiro R., Wakita K. Physica Status Solidi B 2015, v. 252 (6), p. 1248.
18. Xu B., Zhang Y., Alizade E.H., Jahangirli Z.A., Lyzwa F., Sheveleva E., Marsik P., Li Y.K., Yao Y.G., Wang W., Shen B., Dai Y.M., Kataev V., Otrokov M., Chulkov E.V., Mamedov N.T., Bernhard Ch. Physical Review B 2021, v. 103 (12), p. L121103-1.
19. Neumann M.D., Cobet C., Kaser H., Kolbe M., Gottwald A., Richter M., Esser N. Review of Scientific Instruments 2014, v. 85, p. 055117-1.
20. Rakel M., Cobet C., Esser N., Gori P., Pulci O., Seitsonen A., Cricenti A., Nickel N.H., Richter W. The Science and Culture Series — Physics/EPIOPTICS-9, 2008, p. 115.
21. Bruggeman D.A.G. Ann. Phys. (Leipzig) 1935, v. 24, p. 636.
22. Sela M., Haspel C. Applied Optics 2020, v. 59 (28), p. 8822.

SPECTROSCOPIC ELLIPSOMETRY AND FREE CARRIER PLASMA EDGE: TOOLOGICAL INSULATORS CASE

NT MAMEDOV[1], EH ALIZADE[1], ZS ALIEV[1,2], YN ALIYEVA[1], KhN AKHMEDOVA[1,2],
SM BAGIROVA[1], TG MAMMADOV[1], NA ABDULLAYEV[1,3], IR AMIRASLANOV[1,3],
SS RAGIMOV [1,3], and ZA JAHANGIRLI[1,3]

[1]Institute of Physics, Azerbaijan National Academy of Sciences, Baku, Azerbaijan
[2]Azerbaijan State University of Oil and Industry, Baku, Azerbaijan
[3]Baku State University, Baku, Azerbaijan
E-mail: n.mamedov@physics.ab.az, mamedov@pe.osakafu-u.ac.jp

By exploiting the high sensitivity of Fourier transform infrared (FTIR) variable angle spectroscopic ellipsometry (SE) in the mid-infrared spectral range and using simple Drude free carrier absorption model, room temperature free carrier plasma edge (FCPE) of the samples of the classic topological insulators (TIs) Bi_2Se_3, Bi_2Te_3 and Sb_2Te_3 was determined along with concentration and mobility of free carriers. The last two parameters coincide with those retrieved with an accuracy of 10% from Hall measurements. A tendency to purely circular polarization of the reflected light and remarkable behavior of S_3 Stocks parameter with increasing incident angle were disclosed for studied samples in a photon energy region below (FCPE) where the real part $\varepsilon_1(\omega)$ of the dielectric function shows a metal-like behavior; i.e. $\varepsilon_1(\omega)<1$. The retrieved SE-based effective mass of electrons in n-type Bi_2Se_3 sample is in excellent agreement with that obtained recently from quantum oscillations of Hall resistance in bulk n-Bi_2Se_3. SE-based hole effective masses of p-Bi_2Te_3 and Sb_2Te_3 are also given. The obtained SE-based high frequency dielectric constants of the studied TIs are well reproduced by ab-initio calculations of dielectric function.

Keywords: spectroscopic ellipsometry, free carrier plasma edge, dielectric constants, band structure
PACS: 51.70.+f, 07.60.Fs, 71.20.-b

Introduction

Spectroscopic ellipsometry (SE) is commonly recognized as one of the most powerful tools for optical studies of the various excitations in solids and liquids. Being a self-referencing optical technique, it is superior over optical reflection and allows more accurate determination of such a fundamental material constant as dielectric function in a broad photon energy range [1].

Quantum phases of matter continue to be among the hottest spots of condensed matter physics. Especially strong interest is attracted to topological insulators [2], rapidly growing worldwide after the recent discovery of the first magnetic topological insulator [3].

Topological insulators are promising materials for application in low-energy consumption electronics and spintronics [4], as well as for realization of such fundamental physical effects as quantum anomalous Hall effect [5] and topological magneto-electric effect [6] at elevated temperatures.

Topological insulator (TI) or quantum spin Hall phase [2], which is a spin analogue of the quantum Hall effect is an insulator in the bulk and a metal on the surface. Correspondingly, TI exhibits the gapped bulky electronic states and the gapless surface electronic states. The last, therefore, behave like metallic states.

The existence of a thin metallic layer on the surface of TI is a consequence of the strong spin-orbital interaction that leads to the inverted bulk bandgap as compared to the bandgap that appears without spin-orbit interaction. Bandgap inversion changes the trivial topology inherent in ordinary insulator (or semiconductor) to the robust non-trivial topology inherent in TI. The robustness of TI against external deformations is similar to the robustness of Mobius strip (an analogue of TI) whose topology cannot be reverted back to the one of ordinary strip (an analogue of ordinary insulator or semiconductor) by any deformation.

Surface states of TI are characterized by linear dispersion in the form of so-called Dirac cone with helical spin structure and fixed direction of electron spin relative to the wave vector for all Fermi surface. Such peculiarity rules out any possibility of backscattering of the electrons without changing the direction of their spins. In other words, scattering on phonons and non-magnetic impurities is forbidden. Owing to time reversal symmetry, metallic properties of the surface states of TI are protected and the states on the top of Dirac cone are at least two-fold degenerated [7].

However, if time reversal symmetry is broken, a gap appears in Dirac point and material can transform into the state of quantum anomalous Hall effect [8]. Another condition for realization of the quantum anomalous Hall effect requires from Fermi level to be inside the magneto-induced gap [9].

The classic 3D TIs, Bi_2Se_3, Bi_2Te_3 and Sb_2Te_3 exhibiting band inversion near the centre of the Brillouin zone (BZ) are characterized by small bulk energy gaps, high group velocities, and small effective masses, which are prerequisites of high-efficiency thermoelectric materials [10]. However, high concentration of free carriers in the bulk make it difficult to get use of topologically-induced dissipation-free surface conductivity. Therefore, monitoring the free carrier density and Fermi level position in TIs is very important. Along with well known resistivity and Hall effect measurements, such monitoring can be done by contactless optical methods.

Free carrier density predetermines the photon energy position of the free carrier plasma edge (FCPE) in dielectric function [11,12]. FCPE of classic TIs has been thoroughly studied using reflection spectroscopy (RS) [13-15]. On the other hand, SE has been applied to bulk crystals of classic TIs only for studies of fundamental interband transitions [16]. Photon energy range of free carrier absorption has not been accessed by SE, except for a recent work [17] that found some inconsistency between the real position of FCPE and the one retrieved from RS data.

The present work is purposed to iluminate the possible reason of this inconsistency and considers FCPE and its determination by means of SE and RS in the light of the resources and accuracy provided by both methods.

SE vs RS in determination of dielectric function

Ellipsometric measurements are designed for determination of the state of polarization of the reflected light. This state is described by two parameters, Ψ (Psi) and Δ (Delta), indicated in Fig. 1 by red arrows. These parameters enter the principle equation of ellipsometry , which is written for isotropic case as [18]

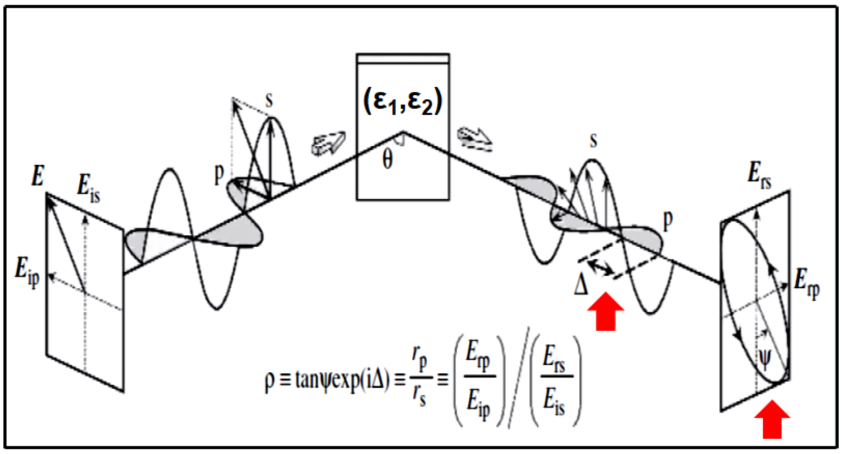

Fig.1. Schematics of ellipsometric measurements. Ellipsometric parameters, Ψ and Δ are indicated by red arrows. The incident light has both s- and p-components, exactly as in J.A.Woollam M2000 DI and IR-VASE ellipsometers used in this work.

$$\rho = \tan\Psi \exp(i\Delta) \tag{1}$$

where ρ is the ratio of the amplitude reflection coefficients, r_p and r_s for p- and s-polarized components of the reflected light, respectively. On the other hand, r_p and r_s are defined as the ratios E_{rp}/E_{ip} and E_{rs}/E_{is} of the electrical vectors of p- (E_{rp} and E_{ip}) and s- (E_{rs} and E_{is}) polarized components of the reflected and incident light, respectively. In other words, ρ reflects the change in state of polarization of the light due to reflection from a material with complex dielectric function $\varepsilon=\varepsilon_1+i\varepsilon_2$ from which Fresnel amplitude reflection coefficients, r_p and r_s are unambiguously determined. The real (ε_1) and imaginary (ε_2) parts of dielectric function of the material are then found after substitution of r_p and r_s expressed via ε_1 and ε_2. and solution of Eq. (1). In the overwhelming number of cases Eq. (1) is solved using regression analysis.

Along with getting a self-consistent or Kramers-Kronig compatible solution of Eq. (1) for real and imaginary parts of dielectric function in any arbitrary chosen photon energy range, the measured ellipsometric parameters, Ψ and Δ also allow determination of all four Stokes prameters, S_0, S_1 , S_2 , and S_3 which completely describe the state of light polarization. The Stokes prameters are known to obey the following relation [18];

$$S_0 = \sqrt{S_1^2 + S_2^2 + S_3^2} \tag{2}$$

and are grouped in a vector quantity called the Stocks vector defined as:

$$S = \begin{bmatrix} S_0 \\ S_1 \\ S_2 \\ S_3 \end{bmatrix} = \begin{bmatrix} I_0 \\ I_x - I_y \\ I_{+45} - I_{-45} \\ I_L - I_R \end{bmatrix} \tag{3}$$

where I_0 represents the total intensity of the light, I_x, I_y, I_{+45} and I_{-45} the intensities of light linearly polarized along the axes and at 45° apart, I_L and I_R the intensities of components polarized circularly left and right.

Particularly important for the case considered in the present paper is parameter S_3 that represents difference between the normalized right-handed or clockwise and left-handed or anti-clockwise circular components of the considered light. Note that for linearly polarized light S_3 equals 0. For purely circular light S_3 adopts either +1 or -1 value.

Determination of dielectric function from RS measurements requires, in contrast with SE, obligatory application of Kramers -Kronig relations in the photon energy range from 0 to ∞, which is practically impossible since RS measurements are always performed in a limited photon energy range. In spite of this fact, current RS measurements backed up by elaborated program packages allow determination of dielectric function with reasonable accuracy, which, however, is below accuracy provided by SE. This factor is particularly decisive in selection between SE and RS for free carrier plasma edge studies

Besides, RS measurements generally provide information only about S_o Stocks parameter, making it impossible to observe interesting polarization peculiarities of light reflection below free carrier plasma edge.

Dielectric function, plasmons and free carrier plasma edge

The propagation of light through a bulk plasma-like isotropic non-magnetic medium is described by Maxwell's equation $\nabla \cdot \mathbf{D} = 0$ (where $\mathbf{D}=\varepsilon\ \mathbf{E}$) or

$$\varepsilon(\omega)\ \nabla\ \mathbf{E} = 0. \tag{3}$$

The trivial solution $\nabla\ \mathbf{E}=4\pi\rho=0$ corresponds to the null charge density ρ within a homogeneous system and a transverse electric field. The second solution corresponds to ε(ω)=0. In this case the zero value of ρ is no longer required. In other words, the electric field may have a longitudinal contribution and charge fluctuations may appear leading to a purely longitudinal mode called the bulk plasmon. Plasmons are given by the poles of the loss function $\varepsilon(\omega)^{-1}$ and produce peaks at some energy (ω^p) in the imaginary part of the loss function taken with sign minus; i.e. $-\mathrm{Im}\ \varepsilon(\omega)^{-1}$. Plasmons play a fundamental role in the screening of electromagnetic fields within matter, and may be detected through inelastic scattering of electrons by using electron energy loss spectroscopy (EELS) or through resonant scattering of light by using resonance Raman spectroscopy.

The frequency ω at which ε(ω)=0 condition for electron gas is fulfilled is called plasma frequency ω_p. The well known Drude dielectric function is

$$\varepsilon^D(\omega) = 1 - \frac{\omega_p^2}{\omega^2} \tag{4}$$

and leads to plasma oscillations at its zero. The plasma frequency ω_p is equal to

$$\omega_p = \left(\frac{4\pi N e^2}{m^*}\right)^{\frac{1}{2}} \tag{5}$$

where N is the free electron density, e is the electron charge and m* is the electron effective mass. However, the zero crossing point of the real part (ε_1) of dielectric function of a material is defined by screened plasma frequency known also as free carrier plasma edge (FCPE):

$$\omega_p^{scr} = \left(\frac{4\pi N e^2}{\varepsilon_\infty m^*}\right)^{\frac{1}{2}} \tag{6}$$

where ε_∞ is the high frequency dielectric constant in a transparent region just below the onset of interband optical transitions.

In this work, J.A.Woollam M2000 DI and IR-VASE ellipsometers were employed to obtain dielectric function of monocrystalline n-Bi_2Se_3, p-Bi_2Te_3 and p-Sb_2Te_3 over the photon energy range 0.05 - 6.5 eV at room temperature. The fee carrier density, obtained from Hall measurements beforehand was 2.5x 10^{19} cm^{-3} for n-Bi_2Se_3, 1.2x 10^{19} cm^{-3} for p-Bi_2Te_3 and 8.1x 10^{19} cm^{-3} for p-Sb_2Te_3.

The measured ellipsometric parameters Ψ and Δ, which contain all information about the real and imaginary parts of dielectric function were fitted using the same Drude and Lorentz oscillators at incidence within 60 to 72^o angular range to account for intra- and inter-band optical transitions, respectively. The dependence of Drude-based dielectric function upon photon energy (E) was taken in the well-approbated form [19]

$$\varepsilon^D(E) = \frac{-\hbar^2 e^2 N\mu}{\varepsilon_0(\mu m^* E^2 + ie\hbar E)} \tag{7}$$

where μ is the carrier mobility and m* is the carrier effective mass.

As a result, both real part (ε_1) and imaginary part (ε_2} of dielectric function, as well as the zero-crossing point of $\varepsilon_1(\omega)$ or ω_p^{scr} and plasmons in $-\mathrm{Im}[\varepsilon_1(\omega) + i\varepsilon_2(\omega)]^{-1}$ were determined with high accuracy. Besides, remarkable behavior of polarization state of the light reflected from the surface of the studied TIs was disclosed, as shown in Fig.2 for the wavenumber (or energy) dependence of S_3 Stocks parameter.

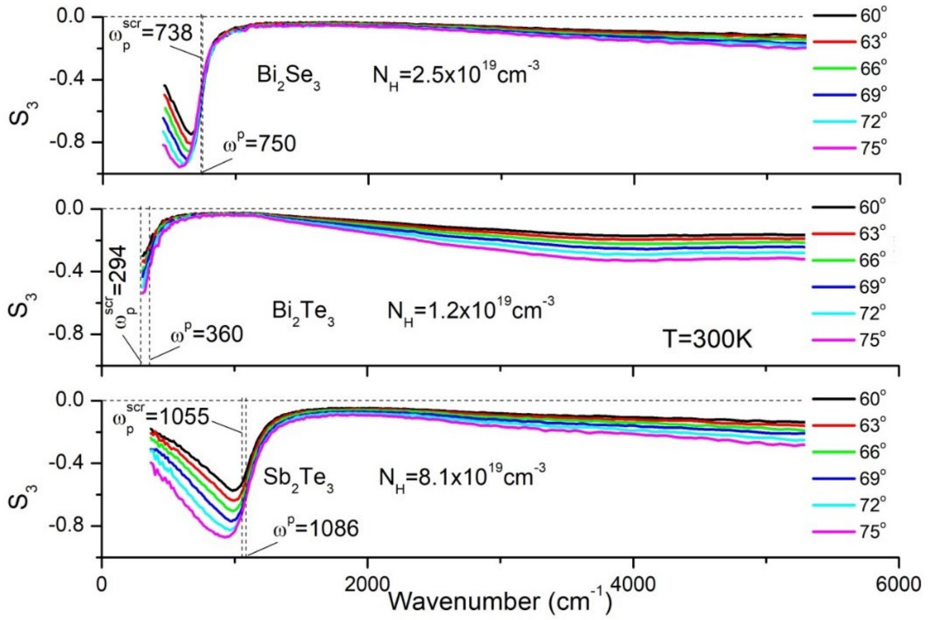

Fig. 2. S_3 Stokes parameter of the light reflected from the studied topological insulators. FCPE (ω_p^{scr}) and plasmon position (ω^p) are also given for convenience.

For all three studied TIs S3 shows a minimum below ω_p^{scr}, and moves towards smaller wavenumbers, simaltaneously becoming more and more circularly polarized.

Linearly polarized light can become circularly or, in general, elliptically polarized after reflection from a metal surface if the incident light has both s- and p-polarized components shown in Fig. 1. In the case of purely circular polarization the phase difference Δ between s- and p-polarized components (Fig.1) is π/2. According to Fig.2, the Δ for the maximum ellipticity (the minim on S3 in Fig. 2) tends to π/2 with increasing incident angle. Note that such conversion of the linearly polarized light is possible only below FCPE where intraband optical transitions dominate the absorption. and ε1(ω) shows a metal-like behavior; i.e. ε1(ω)<1. Above FCPE the interband optical transitions take over and ε1(ω) shows a semiconductor-like behavior; i.e. ε1(ω)>1. Indeed, no polarization peculiarities are detected on S3 of all thee TIs above FCPE (Fig.2).

Along with Hall concentration (NH) and mobility (μH), obtained from Hall measurements, Table I shows the parameters retrieved from the obtained SE-based dielectric function for each TI. Hall and SE based concentration (NH and NDrude), as well as mobility (μH and μDrude) for each TI agree with each other within the accuracy (10%) of Hall measurements, providing solid grounds for contactless optical determination of these parameters.

Table 1. Room temperature Hall concentration (N_H), Drude concentration (N_{Drude}), Hall mobility (μ_H), Drude mobility (μ_{Drude}), screened plasma frequency (ω_p^{scr}), plasmon frequency (ω^p), plasma frequency (ω_p), carrier effective mass (m*) in free electron mass unit (m_e), and high frequency dielectric constant (ε_∞), determined (a) from Eqs. (5) and (6) and (b) by using Kramers-Kronig relations.

TI	N_H	N_{Drude}	μ_H	μ_{Drude}	ω_p^{scr}	ω^p	ω_p	m*	$\varepsilon_\infty{}^a$	$\varepsilon_\infty{}^b$
	10^{19}cm^{-3}		cm^2(Vs)$^{-1}$		cm^{-1}			m_e		
n-Bi_2Se_3	2.5	2.50	575	513	738	750	3764	0.160	26.0	30.8
p-Bi_2Te_3	1.2	1.27	316	316	294	360	2666	0.162	82.2	74.8
p-Sb_2Te_3	8.1	8.89	347	271	1055	1086	7282	0.152	47.6	51.9

[a] $\varepsilon_\infty = \left(\frac{\omega_p}{\omega_p^{scr}}\right)^2$

[b] $\varepsilon_\infty = 1 + \frac{2}{\pi}\int_{E_g}^{\infty}\frac{\varepsilon_2\ (E)}{E}dE$, where E_g is band gap energy.

For n-Bi_2Se_3, which has a simple structure of the conduction band, the effective electron mass determined from SE-based measurements is 0.160 m_e (Table 1) and exactly coincides with that determined recently from quantum oscillations of the Hall resistance in bulk Bi_2Se_3 [20]. For p-Bi_2Te_3 and Sb_2Te_3, the SE-based effective hole mass is 0.162 and 0.152 m_e (Table 1), respectively. However, the last two TIs have a complicated structure of the valence band and comparison of the SE-based hole effective mass with literature data, which are quite ambiguous. is rather difficult.

Let us now turn to SE-based high frequency dielectric constant ε_∞. The imaginary (a) and real (b) parts of dielectric function calculated within band structure we obtained earlier [17] is shown in Fig.3 for all three TIs. The value of ε_∞ is then easily found from Fig. 3b to be as large as 28 for Bi_2Se_3, and around 60 and 48 for Bi_2Te_3 and Sb_2Te_3, respectively.

Being compared with dielectric constants in Table I, the calculated values excellently reproduce the SE-based ε_∞ for Bi_2Se_3 and Sb_2Te_3. For Bi_2Te_3 the calculated value is quite consistent with the SE-based one, being somewhat smaller.

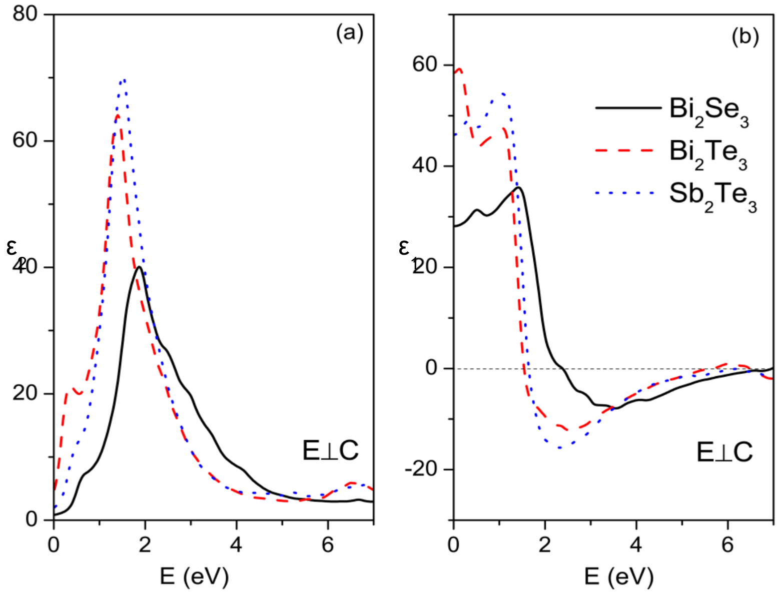

Fig. 3. Imaginary (a) and real (b) parts of dielectric function obtained from ab-initio calculations of band structure of Bi_2Se_3, Bi_2Te_3 and Sb_2Te_3 [17].

Conclusion

Spectroscopic ellipsometry and reflection spectroscopy have been compared to show the superiority of the former in the studies of free carrier plasma edge. Fourier transform infrared variable angle spectroscopic ellipsometry has then been successfully applied to the samples of classic 3D TIs and the basic bulk parameters of these TIs, retrieved from SE measurement have been found to be in a very good agreement with those obtained using non-optical techniques. Infrared SE can, therefore, be considered as the indispensible tool for accurate characterization of free plasma edge and plasmons in solids, particularly, in TIs, in which bulk band gaps are rather small since they are of the order of magnitude of spin-orbital interaction that is the only driving force of band inversion and topology change.

Acknowledgements

The authors acknowledges the support of the Science Development Foundation under the President of the Republic of Azerbaijan (grant number EİF-BGM-4-RFTF-1/2017-21/04/1-M-02).

References

1. Mamedov N., et al. Phys. Stat. Sol. A 2006, v. 203 (11), p. 2873.
2. Hasan M.Z. and Kane C.L. Review Modern Physics 2010, v. 82(4), p. 3045.
3. Otrokov M.M., et al. Nature 2019, v. 576, p. 416.
4. Chen Y. P. Procedings SPIE 2012, v. 8373, p. 83730B-1.
5. Zhang R. Yu, W., et al. Science 2010, v. 329 (5987), p. 61.
6. Zhang D., et al., Phys. Rev. Lett. 2019, v. 122 (20), p. 206401-1.
7. Chang C. Z., Wei P., and Moodera J. S. MRS Bulletin 2014, v. 39 (10), p. 867.
8. Chang C. Z. and Li M. J. Physics: Condensed. Matter 2016, v. 28 (12), p. 123002-1.
9. Tokura Y., Yasuda K., and Tsukazaki A. Nature Reviews Physics. 2019, v. 1, p. 126.
10. Heremans J., Cava R. Phys. Rev. 1952, v. 85, p. 338.

11. Pines D. Rev. Mod. Phys. 1956, v. 28, p. 184.
12. Pietro P. Di, et al. Phys. Rev. B 2012, v. 86, p.045439-1.
13. Butch N. P., et al. Phys. Rev. B 2010, v. 81, p. 241301(R)-1.
14. Xu B., et al. Phys. Rev. B 2021, v. 103 (12), p. L121103-1.
15. Dubroka A., et al. Phys. Rev. B 2017, v. 96, p. 235202-1.
16. Mamedov N., et al. JVST B 2019, v. 37 (6), p. 062602-1.
17. Fujiwara H., Spectroscopic ellipsometry: principles and applications, John Wiley & Sons, Ltd, 2007, 361 pages.
18. Tiwald T. E., Thompson D. W., Woollam J. A., Paulson W., and Hance R. Thin Solid Films 1998, v. 313-314, p. 661.
19. Busch M., et al. Scientific Reports 2018, v. 8, p. 485-1.

EXPERIMENTAL STUDY OF INFLUENCE OF DIFFERENT LEVELS OF HELIO-GEOPHYSICAL ACTIVITY FLUCTUATIONS ON THE FUNCTIONAL STATE OF THE ADULT FEMALE BRAIN

AA ALLAHVERDIYEVA[1,2], AR ALLAHVERDIYEV[1], ES BABAYEV[2]

[1]Institute of Physiology named after A.I.Garayev of the ANAS, Baku, Azerbaijan
[2]Baku State University, Baku, Azerbaijan
E-mail: elchin.babayev@gmail.com

In this paper we present the results of a personalized study of the bioelectrical activity of the human brain of females aged between 30-35 in a state of relaxed wakefulness on geomagnetically quiet (calm) days (when planetary geomagnetic index Kp = 1-2) and on days with weak geomagnetic disturbances (Kp = 4). Registration of bioelectric activity of the human brain was carried out on a computerized encephalograph "Neuron-Spectrum-5". Using "Neuron-Spectrum.NET" software for EEG recording and analysis, we have studied artifact-free 10 second EEG segments of both hemispheres with the temporal areas. Geomagnetic Kp index is used in analysis which is a more reliable index for study of changes in EEG characteristics. The conducted electrophysiological studies indicated increase in the index, frequency and amplitude of the delta-rhythm on the days of geomagnetic disturbances against the background of a decrease in the index, frequency and amplitude of the beta-1 rhythm. An increase in the index, amplitude and frequency of the fast-frequency beta-2 rhythm, mainly in the right hemisphere was observed in the geomagnetically disturbed days. The right hemisphere accent of the beta-2 rhythm intensification in response to an increase in geomagnetic activity is probably associated with a greater activation of the right hemisphere, which is responsible for emotional reactions. Considering that the theta-rhythm is generated by the structures of the hippocampal formation, a diffuse increase in the severity of the theta-rhythm on days of geomagnetic disturbance indicates the activation of the septo-hippocampal system and an increase in its contribution to the formation of the bioelectric activity of the cortical regions. It is known that the subcortical structures and the hippocampal formation are a sensitive screen that reacts to fluctuations of the external physical environment.

Keywords: bioelectrical activity, fluctuations, human brain, encephalograph, geomagnetic index
PACS: 87.64.-t, 87.65.+y, 96.60.Ly

Introduction

Space weather (heliogeophysical activity) changes not only affects the functioning and reliability of technical systems in space and on the ground, but may also endanger the biosphere, particularly, human beings. A number of works dedicated to investigation of these kinds of influences reveals that not only central, but also the vegetative nervous system of human beings is very sensitive to geomagnetic disturbances [1, 2, 3].

Geomagnetic storms are one of the most important constituents of space weather, which in turn affect living organisms, including the human beings and their functional health state. Studies reveal that during geomagnetic disturbances the number of hospitalized patients remarkably increases, cases of epileptic seizures and various paroxysmal conditions, nervous breakdowns and suicidal attempts become comparatively more frequent [4,5,6,7,8,9]. There are signs on the aggravation of existing diseases and an increase in the mortality rate of patients in days with space weather disturbances [10]. Among practically healthy people, there are also various responses to changes of heliogeophysical conditions [11, 12, 13]. A number of researchers have established a relationship between the functional state of the human brain and geomagnetic activity [14, 15, 16.] A nonspecific response of neurons to electromagnetic oscillations has been revealed [17]. A synchronizing effect of electromagnetic oscillations on brain activity has been shown, causing a decrease in the seizure threshold and, under certain conditions, provoking paroxysmal states and seizures [18].

The existing experimental data and results of recent studies testify to the individual reaction of the organism to geomagnetic disturbances which depends on the constitutional characteristics and functional state. The bioelectrical activity of the human brain (EEG), reflecting the functional state of the cerebral cortex, formed under the regulatory influence of activating and deactivating mechanisms of nonspecific systems, has age-sex characteristics [19, 20, 21]. Data available in the scientific literature on the age-sex aspects of the problem (the influence of space weather fluctuations on the functional activity of the human brain) are rather insufficient and do not fully reveal the neurophysiological mechanisms of brain activity [22, 23, 24].

We continued our studies on the influence of geomagnetic field disturbances on the functional state and adaptive capabilities of the human brain of healthy individuals. In this paper we present results of a personalized study of the bioelectric activity of the human brain of women aged 30-35 years in a state of relaxed wakefulness on geomagnetically quiet days (geomagnetic index Kp = 1) and on days with weak geomagnetic disturbances (Kp = 4).

Methods and experiments

Experiments involved practically healthy women aged 30-35 years (25 females). Taking into account the fact that individual values of EEG characteristics are variable and have a wide range of fluctuations, personalized studies with further comparative graphical presentation of the data obtained are preferable to analyze their dynamics. The registration of the bioelectric activity of the brain was carried out on a computer encephalograph – “Neuron-Spectrum-5” (“Neurosoft”), from the areas (leads) of the right and left hemispheres, respectively: frontal poles - Fp2 and Fp1, frontal - F4 and F3, central - C4 and C3, parietal - P4 and P3, occipital - O2 and O1, anterotemporal - F8 and F7, central temporal - T4 and T3, posterior - temporal - T6 and T5 - parts of the cerebral cortex according to the international scheme 10-20%, in days with a calm and disturbed geomagnetic situation. Using “Neuron-Spectrum.NET” software (“Neurosoft”) for EEG recording and analysis, 10 seconds segments of artifact-free EEGs were analyzed in a state of calm wakefulness with closed eyes. The indices, amplitudes and frequency characteristics were calculated for the delta, theta, alpha, low-frequency beta-1 and fast-frequency beta-2 spectra of bioelectric activity. For clarity of the age dynamics of indicators, at the next stage of the analysis using the Microsoft Excel, a comparative analysis of the corresponding characteristics of the EEG recorded on days of geomagnetic disturbances with calm days was carried out.

The information about geomagnetic situation in the considered region (Baku) was provided by the Astrophysics Department of Baku State University. In this study we used Kp geomagnetic index.

Results and discussion

Routine EEG analysis on quiet days indicated the absence of organic changes, local and diffuse pathological and paroxysmal signs in the structure of activity. Visually, the EEG of most women reflected the normative EEG or mild dysfunction of the meso-diencephalic structures (Fig.1).

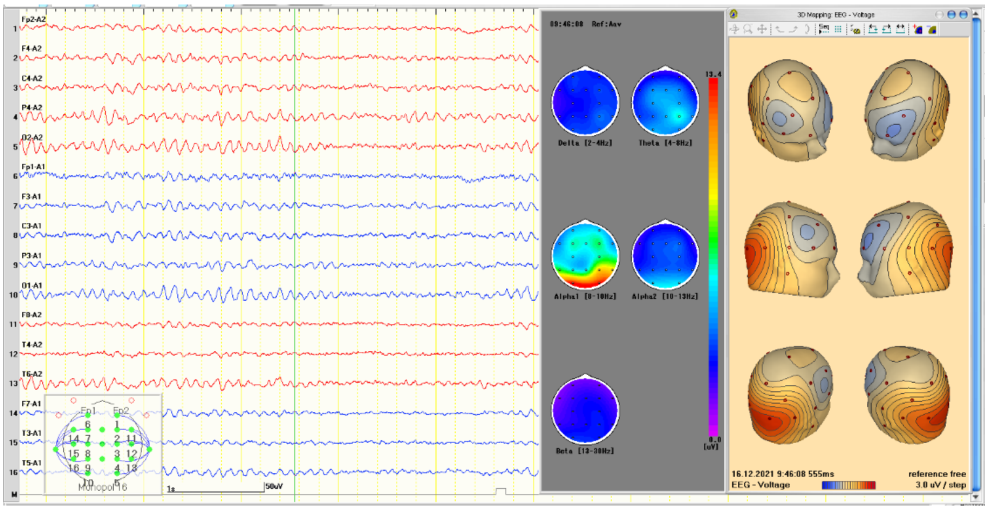

Fig. 1. EEG of a 30-year-old woman in a state of calm wakefulness on geomagnetically calm days; the areas of the right hemisphere are shown in red, the left hemisphere is in blue, and the areas of the cerebral cortex under study are from top to bottom left. 2D - representation of frequency characteristics is shown by regions, 3D - severity of amplitude indicators of rhythms by regions.

On the geomagnetically disturbed days on the EEG of most females, differences were revealed by computer analysis on cartograms of the severity of frequency ranges of rhythms (Fig. 2) and on a deeper analysis of the EEG presented below.

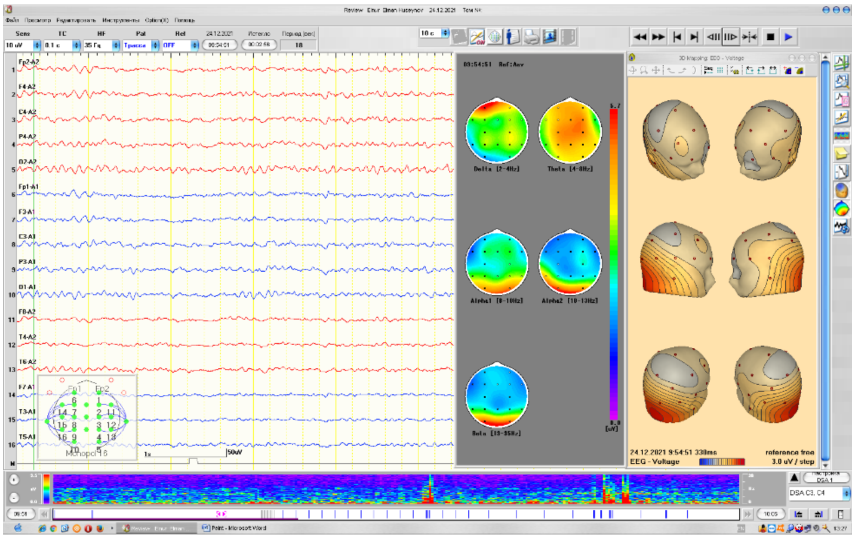

Fig. 2. EEG of most females, differences were revealed by computer analysis on cartograms of the severity of frequency ranges of rhythms.

At the same time, in four women in the frontal-parietal regions of both hemispheres, mainly bilaterally-synchronously pointed and sharp waves were recorded, exceeding the background in amplitude (Fig.3). The recording area of the flashes, their frequency range and bilateral synchrony indicate the diencephalic genesis of paroxysmal activity, which was apparently provoked by the reaction of these brain regions to the disturbances of the geomagnetic situation.

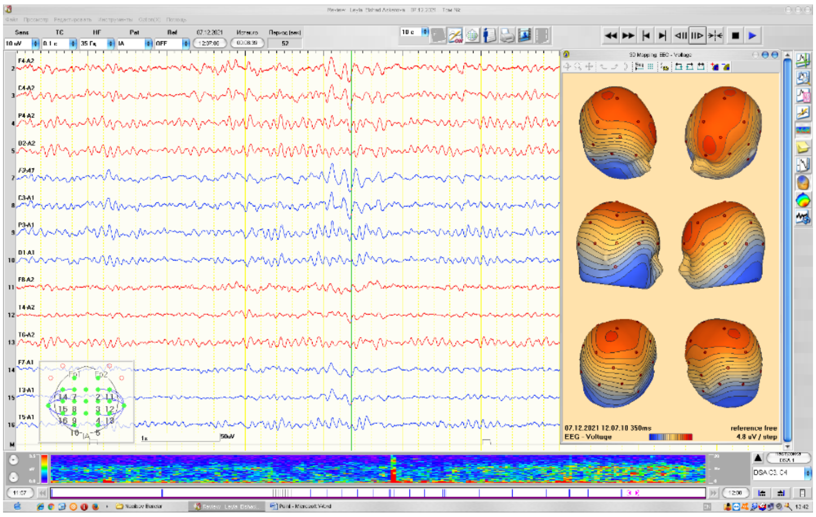

Fig. 3. EEG of a 35-year-old woman in a state of calm wakefulness on geomagnetically disturbed days; the areas of the right hemisphere are shown in red, the left hemisphere is in blue, and the areas of the cerebral cortex under study are from top to bottom left. 2D - representation of frequency characteristics are shown by regions, 3D - severity of amplitude indicators of rhythms by regions.

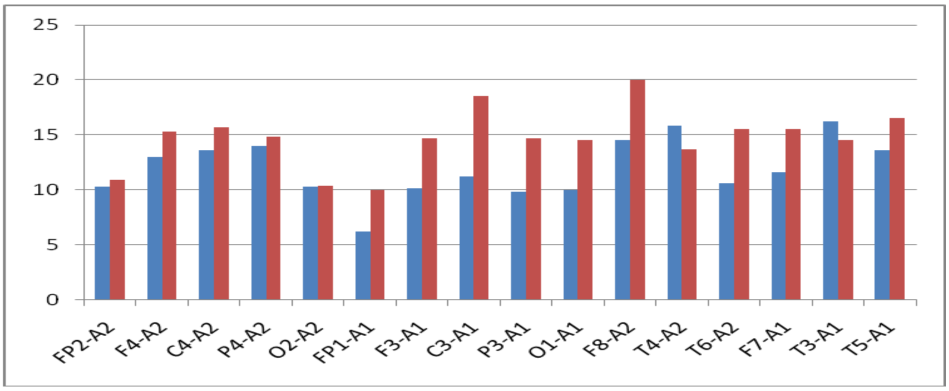

Fig. 4. Diagram of the dynamics of the theta-rhythm index in a 35-year-old woman on calm days (blue) and on days with weak geomagnetic disturbances (red). The abscissa shows the cortical areas of both hemispheres, the ordinate shows the percentage values of the indices.

In the available literature there are reports on the suppression of the activity of endogenous melatonin during periods of increased solar activity which entails a decrease in the threshold of convulsive readiness of neurons characterized by paroxysmal mood [25]. A certain role in the occurrence of paroxysmal states and seizures is attributed to the effect on the bioelectrical activity of the human brain of the synchronizing components of electromagnetic waves [18]. Identified by us pointed and acute flashes in the EEG structure, provoked by an increase in the geomagnetic activity, are in the context of these data. The detected changes in the bioelectrical activity of the human brain make it possible to refer these females to the “risk” group on paroxysmal conditions.

Fig. 4 shows a diagram of the dynamics of the theta-rhythm index on days with geomagnetically disturbed conditions in comparison with calm days.

One can see that on days with Kp = 4, the theta-rhythm index increases in all areas of the human brain, being most pronounced in the central caudal areas of the left hemisphere.

Below there are diagrams of the dynamics of the amplitude (Fig. 5A) and frequency (Fig. 5B) of theta-rhythm on days with a geomagnetically disturbed situation in comparison with calm days.

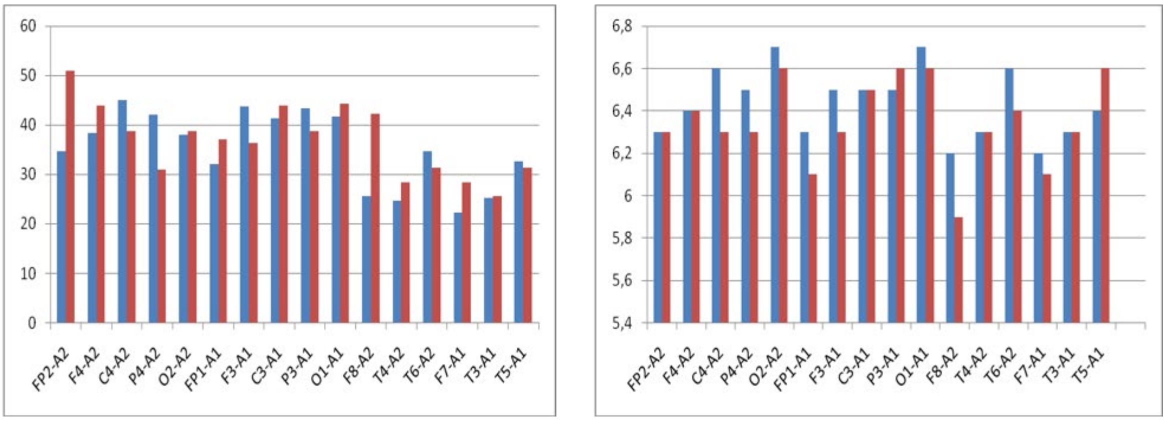

A B

Fig. 5 Diagram of the distribution of the amplitude (A) and frequency (B) of theta-rhythm in a 35-year-old woman on days with weak geomagnetic disturbances (red) in comparison with calm days (blue). On the abscissa axis - cortical areas (leads), on the ordinate - the value expressed as the difference between the values of the amplitudes and the difference between the values of the theta-rhythm frequency on days of geomagnetic disturbances and on days of calm geomagnetic conditions.

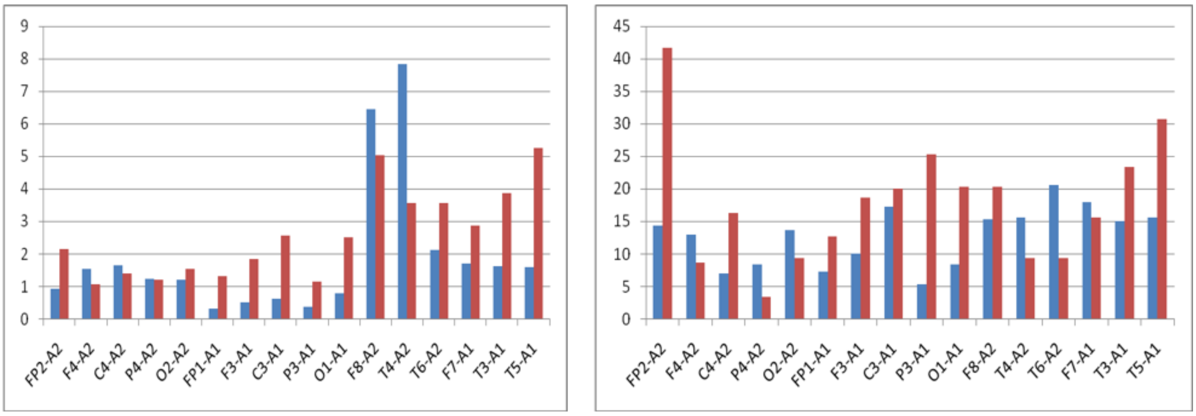

A B

Fig. 6. Diagrams of the dynamics of the index (A) and amplitude (B) of the delta-rhythm in a 35-year-old woman on calm days (blue) and on days with weak geomagnetic disturbances (red). The abscissa shows the cortical regions of both hemispheres, the ordinate shows the percentage values of the indices and the value expressed as the difference between the amplitude values on days of geomagnetic disturbance and on days of calm geomagnetic conditions.

The amplitude of the theta-rhythm on days of disturbance in the geomagnetic situation increased, mainly in the temporal regions, with a right hemispheric accent, against the background of a decrease in its frequency. On weakly geomagnetically disturbed days, in comparison with calm days, there was a diffuse increase in the index (Fig. 6A), amplitude (Fig. 6B), and frequency of the delta-rhythm.

The reverse dynamics in the EEG structure was traced by low-frequency beta activity, while on the days of geomagnetic disturbance, a decrease in the index (Fig. 7), amplitude (Fig. 8A) and frequency (Fig. 8B) of the beta-1 rhythm was observed.

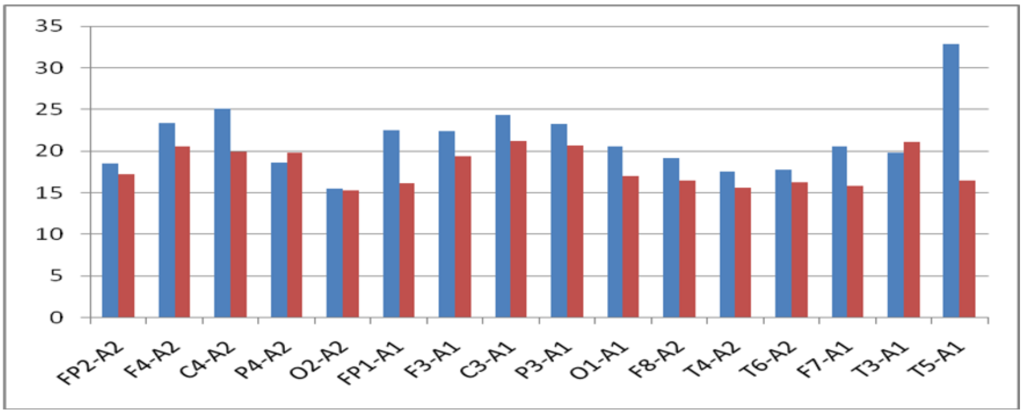

Fig. 7 Diagram of the dynamics of the low-frequency beta-rhythm index in a 35-year-old woman on calm days (blue) and on days with weak geomagnetic disturbances (red). The abscissa shows the cortical areas of both hemispheres, the ordinate shows the percentage values of the indices.

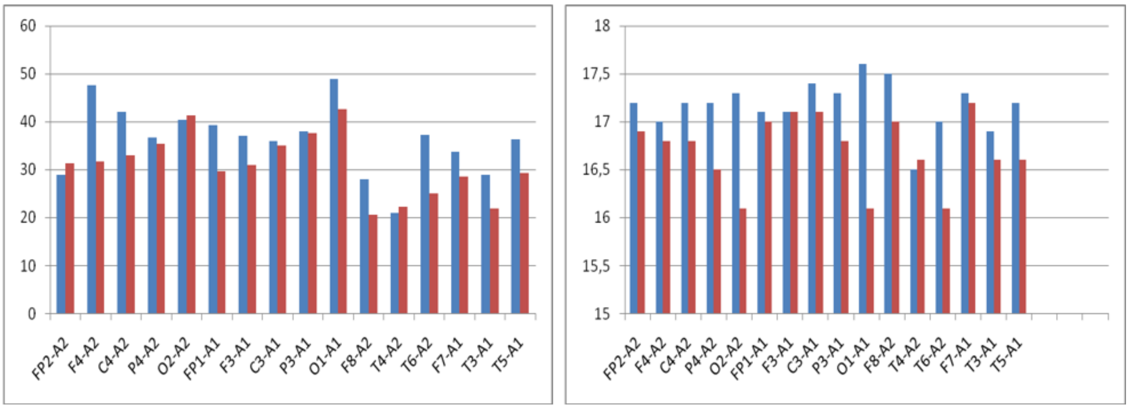

A B

FIg.8. Diagram of the distribution of the amplitude (A) and frequency (B) of the low-frequency beta-rhythm in a 35-year-old woman on days with weak geomagnetic disturbances (red) in comparison with calm days (blue); the ordinate axis is the value expressed as the difference between the values of the amplitudes and the difference between the values of the beta 1-rhythm frequency on days of geomagnetic disturbances and on days of calm geomagnetic conditions.

On the days of geomagnetic disturbances, an increase in the index (Fig. 9), frequency and amplitude of waves in the beta-2 frequency range was observed. At the same time, the changes affected mainly the right hemisphere.

The above personified results of studies of the bioelectric activity of the human brain of practically healthy women of 30-35 years old on calm (Kp = 1) and geomagnetically disturbed days (Kp = 4) and their comparative analysis indicate the peculiarities of the EEG structure, depending on the geomagnetic activity. It is important to note that on days with a weak geomagnetic disturbances, in comparison with quiet days, there is a diffuse increase in the index and in the right temporal region of the amplitude of the theta rhythm, against the background of a decrease in its frequency, a diffuse increase in the index, frequency and amplitude of the delta rhythm, against the background of decrease in the decrease in the index, frequency and amplitude of beta-1-rhythm.

At the same time, the indicators of the fast-frequency beta-2-rhythm traced the increase in the index, frequency and amplitude, mainly in the right hemisphere. Considering that the theta-rhythm is generated by the structures of the hippocampal formation, a diffuse increase in the theta-rhythm index on days of geomagnetic disturbance indicates the activation of the septo-hippocampal system and an increase in their contribution to the formation of the bioelectric activity of the cortical regions. The assumption is confirmed by the opinion that the subcortical structures, including the hippocampal formation, are a sensitive screen that responds to fluctuations of the external environment.

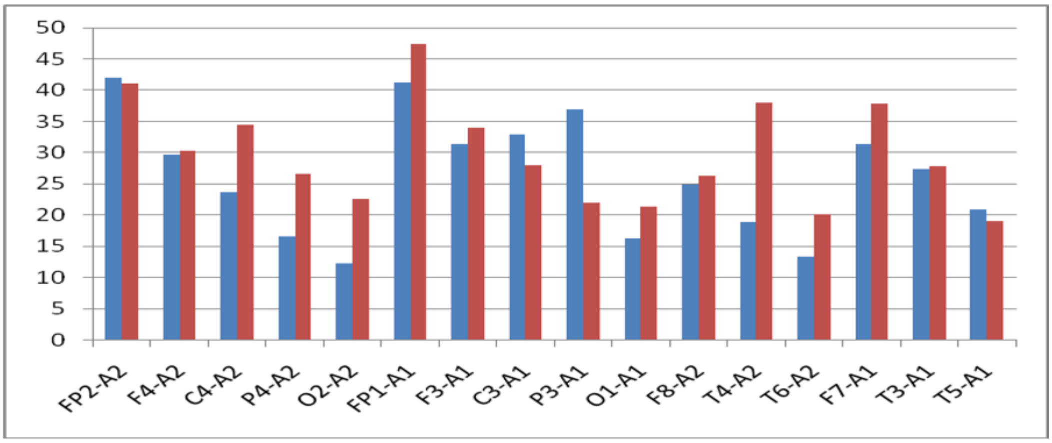

Fig. 9 Diagram of the dynamics of the high-frequency beta-rhythm index in a 35-year-old woman on calm days (blue) and on days with weak geomagnetic disturbances (red). The abscissa shows the cortical areas of both hemispheres, the ordinate shows the percentage values of the indices.

The data on the relationship between changes in the coherence of the theta-rhythm and space weather fluctuations are in accordance with our results [15]. We mention available information on the participation of the hippocampus in emotional reactions [26], data on the close correlation of the severity of theta and delta rhythms with autonomic activity and the level of emotional excitability [27,28]. The increase in the percentage representation of the theta rhythm, which reflects an increase in the activity of the hippocampus, revealed by us, with an increase in the level of geomagnetic disturbance, indicates an increase in emotional tension in the functional activity of the brain.

Of interest is the increase in the index, frequency and amplitude of the delta rhythm on the days of geomagnetic disturbances against the background of a decrease in the index, frequency and amplitude of the beta-1 rhythm. Obtained in the structural organization of the EEG, on days of geomagnetic disturbances, the ratio of slow-fast rhythms, indicate an imbalance in the activity of the activating and deactivating links of nonspecific systems. At the same time, there is an increase in the ascending synchronizing influences and a weakening of activation messages. An increase in the index, amplitude and frequency of the fast-frequency beta-2 rhythm, mainly in the right hemisphere, is of interest on the days when the geomagnetic activity increases.

The increase in the severity of the beta-2 rhythm observed on the days of geomagnetic disturbances, against the background of a decrease in the representation of the beta-1 rhythm and an increase in the values of the characteristics of the delta rhythm, on the one hand, may be associated with a compensatory reaction of cerebral regulatory formations in response to the imbalance in the nonspecific systems and the predominance of slow activity in the EEG structure. On the other hand, the right hemisphere accent of the beta-2 rhythm intensification in response to an increase in geomagnetic activity is probably associated with a greater activation of the right hemisphere, which is responsible for emotional reactions. At the same time, paroxysmality on the EEG in a part of practically healthy women, provoked by an increase in the geomagnetic activity, suggests the need to develop a complex of preventive and therapeutic measures in the “risk” group and take into account the possibility of developing paroxysmal states in matters of vocational guidance and aptitude.

Conclusions

Obtained in the structural organization of the electroencephalogram, on days of geomagnetic disturbance, the ratio of slow-fast rhythms, indicate an imbalance in the activity of the activating and deactivating links of nonspecific systems. There is an increase in ascending synchronizing influences and a weakening of activation messages.

The increase in the severity of the beta-2 rhythm with a right hemispheric accent observed on the days of geomagnetic disturbance on the background of a decrease in the representation of the beta-1 rhythm and an increase in the values of the delta rhythm characteristics is associated with a compensatory reaction of the brain regulatory formations in response to the imbalance in the links of nonspecific systems and the prevalence of in the structure of the EEG of slow activity.

The right hemisphere emphasis of increase of beta-2 rhythm, in response to increased geomagnetic activity, is probably associated with greater activation of the right hemisphere, which is responsible for emotional responses. On days of geomagnetic disturbances, in EEG in some women in the frontal-parietal regions of both hemispheres, bilaterally-synchronously there were registered the pointed and sharp waves exceeding the background by amplitude.

The area of registration of flashes, their frequency range and bilateral synchronization indicate the diencephalic genesis of paroxysmal activity provoked by the reaction of these cerebral regions to the geomagnetic disturbances.

Paroxysmality on the EEG, provoked by an increase in the geomagnetic situation, suggests the need to develop a number of preventive and therapeutic measures in the so called “risk” group.

References

1. Khorseva, N.I. Izv. Atmos. Ocean. Phys. 2013, v. 49, p. 839. https://doi.org/10.1134/S0001433813080033
2. Tsandekov P. A. Chelovek-priroda-obshestvo: teoriya i praktika bezopasnosti jiznedeyatelnosti, ekologii i valeologii 2015, v. 1 (8), p. 14 (in Russian).
3. Rozhkov, V.P., Trifonov, M.I., Bekshaev, S.S. et al. Neurosci Behav Physi 2018, v. 48, p. 317. https://doi.org/10.1007/s11055-018-0564-x
4. Parshina S.S., Tokaeva L.K., Dolgova E.M., Afanas'eva T.N., Samsonov S.N., Petrova V.D., Kaplanova T.I., Potapova M.V., Vodolagina E.S. Pathophysiological and adaptive-compensatory mechanisms of hemorheological disorders in patients with unstable angina pectoris in different periods of the 11-year solar cycle. In: New information technologies in medicine, biology, pharmacology and ecology: International Conference IT + M&Ec'2016 (Gurzuf, 02.06–12.06.2016) / ed. prof. Gloriozova E.L., M. INIT, 2016. p. 294-299 (in Russian).
5. Samsonov S.N., Strekalovskaya A.A., Malysheva L.A., Petrova P.G., Zakharova F.A. Yacut Medical Journal 2016, v. 2 (54), p. 52 (in Russian).
6. Samsonov S.N., Manykina V.I., Kleymenova N.G., Parshina S.S., Petrova P.G., Strekalovskaya A.A., Geomagnetic pulsations and life on Earth, New information technologies in medicine, biology, pharmacology and ecology: International Conference IT + M&Ec'2016 (Gurzuf, 02.06–12.06.2016), ed. prof. Gloriozova E.L., M. INIT, 2016. p. 299-307.
7. Azcárate T., Mendoza B., Levi J.R.bAdvances in Space Research 2016, v. 58 (10), p. 2116. https://doi.org/10.1016/j.asr.2016.05.048
8. Ragul’skaya, M.V., Rudenchik, E.A., Chibisov, S.M. et al. Bull Exp Biol Med. 2015, v. 159, p. 269. https://doi.org/10.1007/s10517-015-2939-0
9. Papathanasopoulos P., Preka-Papadema P., Gkotsinas A., Dimisianos N., Hillaris A., Katsavrias C., Antonakopoulos G., Moussas X., Andreadou E., Georgiou V., Papachristou P., Kargiotis O. Clinical Neurology and Neurosurgery 2016, v. 146, p. 82. https://doi.org/10.1016/j.clineuro.2016.04.023
10. Achkasova Iu N, Bryzgunova N.I, Klimenko L.I., Novgorodov N. P. Problemy Kosmicheskoĭ Biologii 1982, v. 43, p. 109 (in Russian).
11. Belisheva N.K., Chernous S.A., Vinogradov A.N., Izuchenie zavisimosti funktsionalnoqo sostoyaniya organizma cheloveka ot qlobalnikh I lokalnikh variatsiy geokosmicheskikh agentov v usloviyakh Zapolyarya, Nauchnoe obespechenie razvitiya tekhnobiospheri Zapolyarya: baza znaniy I paket innovatsionnikh predlojeniy (multimediyniy informatsionniy resurs), Razdel RFFI-Murmanskaya oblast, Sever-2006, otv. Red. Vinogradov A. N., p. 23-54, Alatiti: Izd. KNS RAN, 2006 – Elecktro. Opt. disk (514 Mb)
12. Verko N.P., Grigoryev P.E., Kokareva M.A., Dobreva I.I. Uchenie zapiski Tavricheskogo natsionalnogo universiteta im. V.I. Vernadskogo 2006, v. 19 (58), p. 41.
13. Gorgo Y.P., Ilin V.N., Milinevskiy G.P., Shevchenko V.E., Osobennosti funktsionirovaniya organizma zimovshikov pri adaptasii k usloviyam Antarktidi, Materiali mejdunarodnoqo simpoziuma Geliogeofizicheskie faktori I zdorovye cheloveka, Novosibirsk: OOO RITS, 2005, p. 54-55
14. Belov D.R., Getmanenko J.V., Kiselyov B.V. Russian Journal of Physiology 2001, v. 87, p. 296.
15. Novik O.B., Smirnov F.A. Biophysics 2013, v. 58 (3), p. 554.
16. Khorseva N.I., Zenchenko T.A., Grigal P.P., Preliminary results of sensitivity estimation of psychophysiological parameters from the geomagnetic activity, Sudak, Crimea, Ukraine, 1-6 October 2007, Proceedings of VII International Crimean Conference “Cosmos and Biosphere”, p. 80 (in Russian)
17. Kholodov I.A. Radiation biology. Radioecology 1998, v. 38 (1), p. 121.
18. Luk'yanova S.N. Radiation biology. Radioecology 2002, v. 42 (3), p.308.
19. Sokolova L.S., Machinskaya R.I. Human Physiology 2006, v. 32 (5), p. 499.

20. Bakhtin O.M. Proceedings of the XVI International Conference on Neurocybernetics 2012, v.2, p.26 (in Russian).
21. Gribanov A.V., Dzhos Y.S. Annals of the Russian academy of medical sciences 2016, v. 71(1), p. 52.
22. Varentsova I. A., Chesnokova V. N., Sokolova L. V. Human Ecology 2011, Issue 2, p. 47.
23. Pavlov K.I., Mukhin V.N., Klimenko V.M., Kamenskaya V.G. Izvestiya. Atmospheric and Oceanic Physics 2016, v. 52, p. 737.
24. Filatov M.A., Popov Yu.M., Polukhin V.V., Prasolova A.A. Journal of New Medical Technologies 2015, Issue 4, p. 5.
25. Persinger M. A., St-Pierre L. S., Koren S. A. Perceptual and Motor Skills 2001, v. 92, p. 183. https://doi.org/10.2466/pms.2001.92.1.183
26. Churilova T.M. Physiology of the Central Nervous System: Textbook. Stavropol: SKSI, 2005, p. 264 (in Russian)
27. Butova O. A., Grischko E. A. Vestnik SGU 2009, v. 63 (4), p. 235.
28. Tsandekov P.A. Scientific records of the Kramskoy Engineering and Pedagogical University. Series Pedagogy. Psychology 2017, v. 1(7), p. 169 (in Russian).

SPATIAL STRUCTURE OF EXORPHIN-C MOLECULE

LN AGAYEVA[1], AA ABDINOVA[2], SR AKHMEDOVA[3] and N. AKHMEDOV[1]

[1]Baku State University, Baku, Azerbaijan
[2]Azerbaijan State Pedagogical University, Baku, Azerbaijan
[3]Azerbaijan Technical University, Baku, Azerbaijan
E-mail: afiyat.abdinova@gmail.com; asimnara@mail.ru; Nicatahmadov@bsu.edu.az

Endorphins - opioid peptides synthesized by the brain, have been known for a long time. However, in addition to them, there is a whole class of opioids that are part of dietary proteins. Since they enter the body from the outside, they are called exorphins. This group includes peptides released from wheat gluten protein (exorphins A, B, and C) and milk caseins (casomorphins), cytochromes (cytochrophins), and a number of others. The conformational capabilities of the exorphin C molecule (Tyr1-Pro2-Ile3-Ser4-Leu5-OH) have been studied by the method of theoretical conformational analysis. The potential function of the system is chosen as the sum of non-bonded, electrostatic, torsion interactions and the energy of hydrogen bonds. Low-energy conformations of the exorphin molecule and the dihedral angles of the main and side chains of amino acid residues included in the molecule were found, the energy of intra- and intersubstance interactions was estimated. It has been shown that the spatial structure of the exorphin molecule is represented by eight structural types. It can be assumed that the molecule performs its physiological functions in these structures. These three-dimensional structures make it possible to propose synthetic analogs for a given molecule. The results obtained can be used to elucidate the structural and structure-functional organization of exorphin molecule.

Keywords: exorphin, endorphin, opioid, structure, conformation.
PACS: 87.15 Aa, 36.20.Ey, 06.30.Bp

Introduction

Endorphins – o pioid peptides synthesized by the brain, have been known for a long time. However, in addition to them, there is a whole class of opioids that are part of dietary proteins. Since they enter the body from the outside, they are called exorphins. This group includes peptides released from wheat gluten protein (exorphins A, B, and C) and milk caseins (casomorphins), cytochromes (cytochrophins), and a number of others.The discovery of the opioid activity of peptide components of food gave grounds to suggest that some types of food can act on the central nervous system like opiate drugs. It has been shown that hemorphin-6 and exorphin C cause hyperalgesia and increased anxiety in animals. Beta-casomorphin-7, on the other hand, lowers anxiety and pain sensitivity. All peptides partially reduce motor activity and orientation-exploratory response. In general, exorphin C and hemorphin-6 in the studied doses, in contrast to beta-casomorphin-7, do not exhibit the neurotropic properties usually characteristic of opioids. They can be characterized rather as functional antagonists of endogenous opioid peptides. Their presence in dietary proteins, apparently, is a consequence of "random" rearrangements of amino acids and does not carry any biological meaning. In contrast to this, beta-casomorphins, acting as exohormones, are capable of exerting significant adaptogenic and other effects on the mammalian central nervous system [1].

We have investigated the structural and functional organizations of the opioid peptides enkephalins, endorphins, endomorphins, dynorphins, neoendorphins and adrenorphins, and we are currently investigating the spatial structure of molecules of rubiscolins, soymorphins, exorphins and casomorphins. This work is a continuation of our previous research [2-4].

Section

The molecule was calculated using the method of theoretical conformational analysis. The potential function of the system is chosen as the sum of non-bonded, electrostatic and torsion interactions and the energy of hydrogen bonds. Nonvalent interactions were assessed by Lennard-Jones potential. Electrostatic interactions were calculated in a monopole approximation according to the Coulomb's law using partial charges on atoms. The conformational possibilities of the exorphin molecule were studied under the conditions of the water environment. The energy of hydrogen bonds was estimated using the Morse potential.

In presenting the calculation results, we used the classification of peptide structures by conformations, forms of the main chain, and shapes of the peptide backbone. Conformational states are completely determined by the values ϕ, ψ of the dihedral angles of the main and side chains of all amino acid residues included in a given molecule. Forms of the main chain of a fragment are formed by combinations of forms of R, B, L residues in a given sequence. Forms of the main chain of a dipeptide can be divided into two classes - folded (f) and unfolded (e) forms, which are called shapes. All conformations are grouped by backbone shape, and shapes are grouped by shape. To designate the conformational states of the residues, identifiers of the X_{ij} type are used, where X defines the low-energy regions of the conformational map φ–ψ: R(φ, ψ=–180°–0°), B(φ=–180°–0°; ψ=0⍰–180°), L(φ,ψ=0°–180°) and P(φ=0°–180°; ψ=–180°–0°) ij... = 11..., 12..., 13..., 21... define the position of the side chain (χ_1, χ_2, ...) with the index 1 corresponding to the angle value in the range from 0 to 120°, 2 - from 120° to -120°, and 3 - from -120° to 0°. The designations and readings of the angles of rotation correspond to the IUPAC-IUB nomenclature [5].

Discussion and Conclusions

The three-dimensional structure of the exorphin-C molecule (Tyr1-Pro2-Ile3-Ser4-Leu5-OH) was investigated based on the low-energy conformations of the corresponding amino acid residues. The pentapeptide molecule exorphin C contains the amino acid residue proline. It is known that the form of the backbone is high-energy in front of the R proline. Therefore, for this molecule exorphin C, the conformations of eight shapes were calculated. The energy distribution of the calculated conformations of the exorphin C molecule is shown in Table 1. The calculation results show that the conformations of four shapes eeef, efee, efef, and efff fall into the energy range 0–2 kcal/mol, and they are represented by twenty-one conformations. The relative energies of the conformations of the shapes eeff, effe, eeee, and eefe are greater than 2 kcal/mol. Thus, the conformations of all eight shapes fall into the energy range 0-3 kcal/mol (Table 1). The most stable conformations of the exorphin C molecule were selected from each shape, which are presented in Table 2. Here, the energy contributions of nonvalent ($U_{nv.}$), electrostatic ($U_{el.}$), torsion ($U_{tors.}$) interactions and the relative ($U_{rel.}$) energy of the optimal conformations of the exorphin molecule are indicated. C. Energy of intra- and intersubstance interactions, geometric parameters of four conformations, the relative energy of which is less than 2.0 kcal/mol, are presented in Tables 3, 4. Figure 1 shows the spatial arrangement of amino acid residues in these low-energy conformations of the molecule.

Table 1. The energy distribution of the conformations of the exorphin C molecule

№	Shapes	Conformation	Energy range, kcal/mol					
			0-1	1-2	2-3	3-4	4-5	5>
1	e e e f	B B B R R	3	3	3	2	1	1
2	e f e e	B R B B B	4	2	-	1	3	13
3	e f e f	B R B R R	3	4	2	2	1	1
4	e f f f	B R R R R	-	2	8	2	3	8
5	e e f f	B B R R R	-	-	3	1	6	4
6	e f f e	B R R B B	-	-	2	2	2	17
7	e e e e	B B B B B	-	-	2	2	3	20
8	e e f e	B B R B B	-	-	1	5	3	5

In the conformations presented in Table 2, the energy of non-bonded interactions in low-energy conformations changes in the energy range (-18.2) - (-15.7) kcal/mol, electrostatic interactions (-0.4) - (1.7) kcal/mol, torsion interactions (3.1) - (4.5) kcal/mol (Table2). The energy range 0-5.0 kcal/mol contains 12 conformations of the eeef shape, 10 conformations of the efee shape, 12 conformations of the efef shape, and 15 conformations of the efff shape. The global conformation of the exorphin-C molecule is the B_2 B B_{22} R_{21} R_{32} conformation of the eeef shape. The conformation is beneficial in terms of non-bonded and torsional interactions. Effective di- and tripeptide interactions arise in this conformation, Tyr1 effectively interacts with the dipeptide fragment Pro2-Ile3, the contribution of which is (-9.5) kcal/mol, also Ile3 with Ser4 and Leu5, which contributions are (-4.7) kcal/mol and Ser4 - Leu5 (-2.8) kcal/mol. The B_3 R B_{32} B_{32} B_{31} conformation of the efee shape has a relative energy of 0.1 kcal/mol. In this conformation, Tyr1 effectively interacts simultaneously with all subsequent amino acid residues, which contribution is (-12.7) kcal/mol, also Pro2 - Ile3, Ile3 with Ser4 - Leu5, Ser4 - Leu5, which contribution is (-7.4) kcal/mol. The B_3 R B_{32} R_{32} R_{31} conformation of the efef shape also has a relative energy of 0.1 kcal/mol; it differs from the previous conformation in the shape of the Ser4 and Leu5 backbones. Therefore, the energy contribution of amino acid residues to the total energy is almost the same as the previous conformation. Conformation B_3 R R_{12} R_{32} R_{31} of shape efff has a relative energy of 1.8 kcal/mol, is favorable for non-valence interactions and not favorable for electrostatic interactions. This conformation gives rise to strong interactions of the Tyr1 residue with the Pro2-Ile3-Ser4-Leu5 residues, the contribution of which is (-15.6) kcal/mol, the Pro2 residue with the Ile3-Ser4-Leu5 residues, the contribution of which is (-3.3) kcal/mol (Table 3).

The energy range of 2-5 kcal/mol contains 32 conformations of the shapes eeff, effe, eeee, and eefe (Table 1). Among these conformations, it should be noted the conformation $B_3RR_{31}B_{32}B_{33}$ with a relative energy of 2.2 kcal/mol. It is beneficial for electrostatic interactions and not beneficial for non-bonded interactions. In other conformations of these shapes, the contribution of non-bonded interactions is less than in the global conformation (Table 2).

Thus, the spatial structure of the exorphin-C molecule can be represented by four structural types and it can be assumed that the molecule performs its physiological functions in these structures. Based on the obtained three-dimensional structures, it is possible to assume its synthetic analogs for this molecule. The theoretical conformational analysis of the tetrapeptide molecule exorphin-C has led to such a structural organization of the molecule that does not exclude the implementation by the molecule of a number of functions that require strictly specific interactions with various receptors.

Table 2. Energy contributions of non-valent (U_{nv}), electrostatic (U_{el}), torsional (U_{tors}) interactions and the relative energy (U_{rel}) of the optimal conformations of the molecule exorphin C

№	Shapes	Conformation	U_{nv}	U_{el}	U_{tors}	U_{tot}	U_{rel}
1	e e e f	B_2 B B_{22} R_{21} R_{32}	-18.2	1.6	3.1	-13.7	0
2	e f e e	B_3 R B_{32} B_{32} B_{31}	-18.4	0.7	4.1	-13.6	0.1
3	e f e f	B_3 R B_{32} R_{32} R_{31}	-18.1	1.1	3.4	-13.6	0.1
4	e f f f	B_3 R R_{12} R_{32} R_{32}	-18.5	3.2	3.3	-11.9	1.8
5	e e f f	B_2 B R_{32} R_{12} R_{12}	-16.2	0.8	3.8	-11.6	2.1
6	e f f e	B_3 R R_{31} B_{32} B_{33}	-15.7	-0.4	4.5	-11.5	2.2
7	e e e e	B_2 B B_{22} B_{12} B_{12}	-17.1	1.7	4.4	-11.1	2.5
8	e e f e	B_2 B R_{32} B_{12} B_{12}	-16.8	1.6	4.3	-10.9	2.8

Table 3. Energy inside and between residual interactions in the conformations of the molecule exorphin C: B_2 B B_{22} R_{21} R_{32} (U_{rel}=0 kcal/mol, first line), B_3 R B_{32} B_{32} B_{31} (U_{rel}= 0.1 kcal/mol, second line), B_3 R B_{32} R_{32} R_{31} (U_{rel}= 0.1 kcal/mol, third line), B_3 R R_{12} R_{32} R_{32} (U_{rel}=1.8 kcal/mol, fourth line)

Tyr1	Pro2	Ile3	Ser4	Leu5	
2.0 2.4 2.4 3.0	-5.6 -4.4 -4.3 -3.8	-3.9 -2.8 -2.6 -2.5	-0.1 -3.8 -3.6 -3.2	-1.8 -2.9 -2.3 -6.1	Tyr1
	0.2 0.3 0.3 0.2	-0.6 -2.0 -2.1 -1.8	-0.2 -0.5 -0.7 -1.0	0 0 0 -0.5	Pro2
		0.3 0.6 0.3 1.4	-2.0 -1.5 -1.3 -0.7	-2.7 -2.0 -1.3 -0.6	Ile3
			0.7 1.1 1.1 1.2	-2.8 -1.9 -2.7 -2.2	Ser4
				-0.2 -0.3 -0.3 1.2	Leu5

Table 4. Geometric parameters (in degrees) of low energy conformations of the molecule exorphin C

	B_2 B B_{22} R_{21} R_{32}	**B_3 R B_{32} B_{32} B_{31}**	**B_3 R B_{32} R_{32} R_{31}**	**B_3 R R_{12} R_{32} R_{32}**
Tyr1	-65 117 174 171 72 0	-70 156 167 -67 110 0	-70 157 170 -69 108 0	-81 150 -179 -69 102 0
Pro2	-60 123 -176	-60 -47 165	-60 -53 168	-60 -38 -179
Ile3	-142 140 174 -178 -175 170 -172	-121 109 -178 -57 -174 177 -175	-107 102 179 -56 -173 173 -171	-71 -45 -173 68 -172 176 -172
Ser4	-92 -59 180 57 179	-96 133 -179 -60 180	-93 -54 179 -63 179	-71 -62 -178 -62 180
Leu5	-115 -60 - -56 172 -175 180	-108 103 - -65 65 180 -179	-105 -60 - -65 63 179 -178	-68 -37 - -56 178 -176 180
ΔU	0	0.1	0.1	1.8

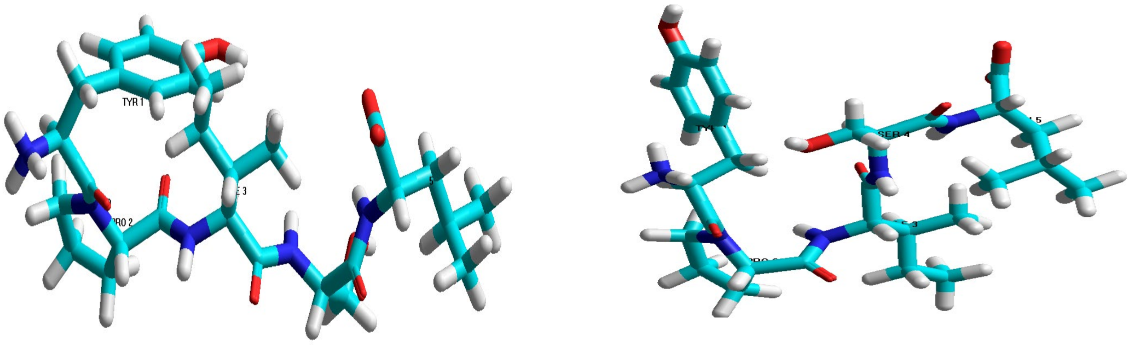

a) B_2 B B_{22} R_{21} R_{32} b) B_3 R B_{32} B_{32} B_{31}

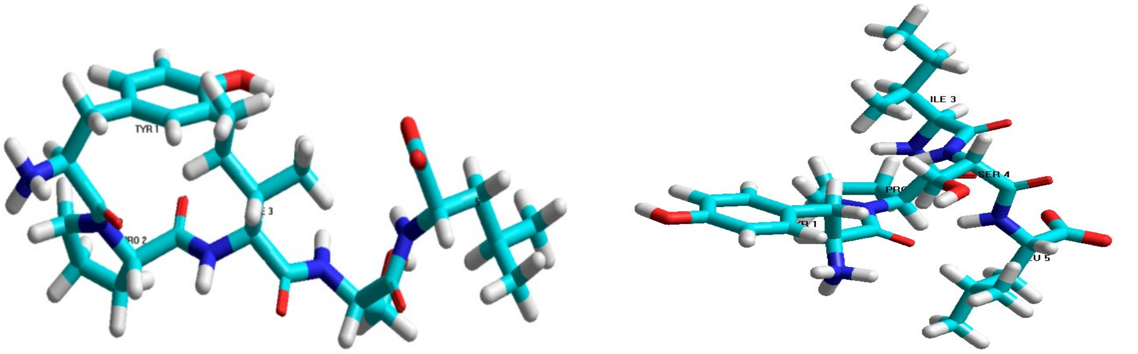

c) B_3 R B_{32} R_{32} R_{31} d) B_3 R R_{12} R_{32} R_{32}

Fig. 1. Atomic model of spatial structure of the exorphine C molecule a), b), c) and d) corresponded to the structures with the relative energies 0 kcal/mol, 0.1 kcal/mol, 0.1 kcal/mol and 0.8 kcal/mol, respectively.

References

1. Chesnokova E.A., Sarycheva N.Y., Dubynin V.A., Kamensky A.A. Physiological Sciences. 2015, v. 46, p. 22.
2. Akhmedov N.A., Agayeva L.N., Akverdieva G.A., Abbasli R.M., Ismailova L.I. J.Chem.Soc.Pak. 2021, v. 43 (05), p. 500. https://jcsp.org.pk/
3. Akhmedov N.A., Agayeva L.N., Akhmedova S.R., Abbasli R.M., Ismailova L.I. IOSR Journal of Applied Physics 2021, v. 13 (5), p. 62. DOİ:10.9790/4861-1305026267 www.iosrjournals.org
4. Agayeva L.N., Abdinova A.A., Akhmedova S.R., Akhmedov N.A. Biophysics 2021, v. 66, (4), p. 531. DOI https://doi.org/10.1134/S0006350921040023
5. IUPAC IUB. Quantities, Units and Symbols in Physical Chemistry, Blackwell Scientific, Oxford, 1993, https://old.iupac.org/publications/books/gbook/greenbook2ed.pdf DOI:10.1134,S0006350921040023.

INFLUENCE OF INTERLAYER INTERACTION CHANGES ON Bi_2Te_3 LAYERED CRYSTALS INTERLAYER BONDS

SSh GAHRAMANOV[1], KSh GAHRAMANOV[1] and NA ABDULLAYEV[1,2]

[1]Institute of Physics of ANAS, Baku, Azerbaijan
[2]Baku State University, Baku, Azerbaijan
E-mail: samir.gahramanov@gmail.com

It is shown that the anomalies observed in the temperature dependence of the crystal lattice parameters and kinetic parameters of bismuth telluride doped with copper and indium Bi_2Te_3<In,Cu> are explained by changes in the chemical bond and the effect of defect centers. The redistribution of the electron density between the metal and the central chalcogen layer in the quintet-layer of the crystal framework, in a certain temperature range, leads to a negative thermal coefficient of linear expansion (TCLE). The polarity of the covalent bond and the decrease in the Bi-$Te^{(2)}$ interatomic distances are directly affected by the magnitude of the interlayer interaction. The energy of thermal motion, when approaching the value of the energy of interlayer interaction, leads to deviation of bonds and to fluctuations in the distribution of electron density in the volume of the crystal.

Keywords: layered crystal, lattice parameters, thermal expansion, covalent bond, chemical bond, resonance bond, electron density
PACS: 61.05.C–, 63.20.Ry, 34.70.+e

Introduction

Bismuth tellurides are complex layered structures, the crystal matrix of which consists of layers separated by weak interactions. Structural fragments of a layered crystal - packets of quintets are much weaker related to each other, than bonds in isotropic crystalline solids, therefore the matrix contains large cavities. The conjugation between the quintet layers is weaker than in the quintets themselves and is carried out, in the opinion accepted today, by Van der Waals forces; however, there is also an opinion about the fraction of the covalent type in the interlayer bonds, which can be enhanced by the introduction of impurities. These impurities can also play the role of an interlayer gap expander. Interatomic interactions within quintet layers can vary depending on factors influencing the interlayer interaction. Impurities that penetrate into the interlayer space affect the characteristics no less than the intralayer impurities and level the properties of the material, although the bond of interlayer impurities with the crystal matrix is much weaker than the bonds in the matrix itself. If we consider the layers of quintets as large molecular associations, and the crystal in the form of a polymolecular system held together by weak interactions, then changes in the material matrix can be determined by the possibility of conformational transitions - intra-layer rotations of atoms. Compound Bi_2Te_3 has a layered rhombohedral lattice of the tetradymite type (Fig. 1) and belongs to crystals of the space group D^5_{3d} (R3m).

In the structure of a five-layer quintet packet …-$Te^{(1)}$-Bi-$Te^{(2)}$-Bi-$Te^{(1)}$-… the bond within the quintet is covalent-ionic, the bond between quintet is a dispersive Van der Waals. There are several opinions regarding the type of bonds between layers within packages. According to some assumptions, covalent-ionic bonds arise between the Bi and $Te^{(1)}$ layers, and purely covalent bonds between Bi and $Te^{(2)}$, proceeding from the fact that the Bi- $Te^{(1)}$ bond is stronger. According to others, the bond in the Bi- $Te^{(1)}$ section is mainly covalent, and between

Bi and $Te^{(2)}$ is mainly ionic, since the distance between the *Bi* and $Te^{(1)}$ layers is approximately equal to the a sum of the covalent octahedral radii, and the *Bi*- $Te^{(2)}$ is greater than the sum of covalent radii and is approximately equal to the sum of ionic radii [1]. In these structural elements, three hybrid orbitals of bismuth, sharing with the $Te^{(1)}$ orbitals, provide a valence bond, the fourth is a lone pair of electrons. The valence bonding orbitals are mainly *p*-character, the fourth orbital is mainly *s*-character.

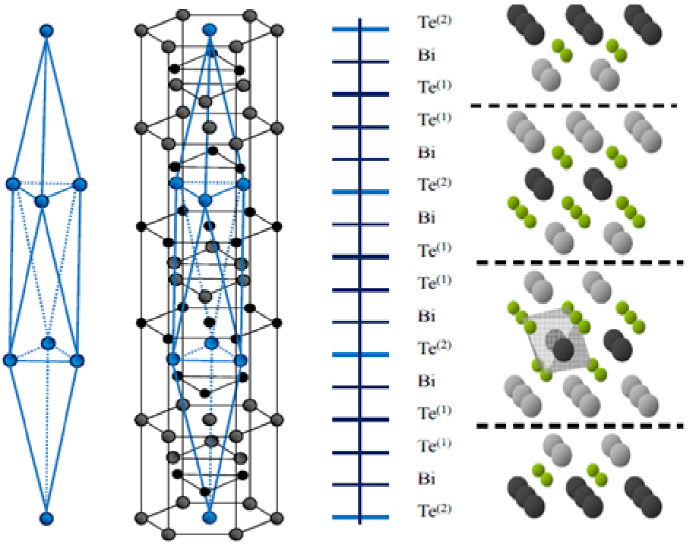

Fig. 1. Rhombohedral and hexagonal unit cells of Bi_2Te_3 (dashed lines separate Van der Waals gaps between quintets; octahedral $Te^{(2)}$ coordination is highlighted).

To form a hybrid *Bi*-$Te^{(2)}$ bond, one electron from the outer pair is transferred to the $Te^{(2)}$ atom located between the double layers. According to Drabble and Goodman [2], the bonding orbits between these atoms are sp^3d^2-hybrids, and the *s*- and *p*-electrons of *Bi* and $Te^{(2)}$ atoms take part in the formation of chemical bonds between atoms. Mooser and Pearson [3,4] suggested a resonance of bonds between $Te^{(2)}$ and bismuth atoms in the presence of p^3d^2 hybridization in Bi_2Te_3. L.Polling [5] also noted the appropriateness of the resonant bonds model. In [6], a theoretical model for bismuth telluride, with and without a covalent bond between layers, and a paramagnetic model for a compound with partial indium substitution are considered. In [7], a model of weak *sp*-hybridization is proposed, where the *s*-band is much lower than the *p*-band, where it is shown that the presence of long-range resonant bonds leads to three-phonon scattering, which reduces the thermal conductivity of the material, also in Bi_2Te_3. Recently, the authors of [8], who were previously inclined towards the model of resonant bonding, including for these materials, proposed a model of metavalent bonding, where there is competition between two types of bonding: covalent pairing of electrons and complete delocalization, characteristic of metals, in which atoms are more degrees are close to each other than conventional covalent bond partners, but to a lesser extent than the dense crystal packing of metals suggests. This metastable bond can be understood as hybridization between different electronic configurations: three valence p-electrons alternate their presence in the six available covalent bonds that exist between a given atom and its octahedral neighbors. A feature of this relationship is the manifestation of strong delocalization in the distribution of electron density in these materials, they have high values of dielectric constants and electronic polarizability. These factors contribute to a large anharmonicity of the lattice and strong phonon-phonon scattering, which leads to low thermal conductivity, as well as to structural instability, anomalous interatomic interaction at large distances.

Analysis of information on the magnitude of the effective charges of ions, their electronic polarizability and the parameters of interionic repulsion caused by the overlapping of electron shells helps to simulate the physical properties of crystals. Studies of Bi_2Te_3 crystals revealed areas with a negative thermal coefficient of linear expansion (TCLE) in the region of 100–200K, which was explained [9] by the influence of changes in the interlayer interaction (between five-layer quintet packets) on the interatomic distances within the layers. The binding energy of molecules is of the order of hundreds of kJ/mol, molecular associates with hydrogen bonds are 12-30 kJ/mol, and in Van der Waals clusters it is 0.4-4 kJ/mol. Since the energy of thermal motion at room temperature ~ 2.5 kJ/mol correlates with the energy of the Van der Waals bond, the rest of the bonds near room temperature can be stable. Although it is difficult to isolate the effect of any type of bond on thermal expansion, it is assumed that these are Van der Waals and other weak bonds.

The temperature dependences of the elastic constants in layered crystals revealed a tendency for a more rapid change in the interlayer elastic constants in comparison with the intralayer ones [10]. It is noted that the change in the values of the elastic constants with temperature is an anharmonic phenomenon and occurs due to two processes: phonon-phonon interaction and lattice deformation due to thermal expansion. The anharmonicity of the bond forces between the layers is substantially greater than the anharmonicity of the intralayer forces. In this case, the fraction of the contribution of thermal expansion to this change is much higher for the “interlayer” elastic constant than for the “intralayer” one [10]. Interlayer (inside a five-layer quintet package) bonds in bismuth and antimony chalcogenides are sensitive to changes in the value of interlayer interaction. The enhancement of the polarity of the bond and the redistribution of the electron density, depending on the broadening of the interlayer distance, can be traced by the shift up the energy scale of the negative TCLE values of the doped crystals. The negative TCLE, accompanied by the overlap of the electronic wave functions of neighboring layers within the quintet, is a consequence of the redistribution of the electron density when the parameters of bonds between the metal and the central chalcogen layer are affected. The $\ldots\text{-}Bi\text{-}Te^{(2)}\text{-}Bi\text{-}\ldots$ connection diagram can explain the mechanism of changes in interatomic distances depending on temperature, as well as the applied uniaxial pressure [11]. At temperatures comparable to the energy of interlayer interaction, this interaction is weakened and the electron density is redistributed into the quintets. The structure of the ion pair can change depending on the temperature, which leads to changes in the perturbing effect of the cation on the electronic system. The shift of the charge to the center of the quintet can lead to an increase in the degree of orbital overlap and an increase in the ionic component of the $Bi\text{-}Te^{(2)}$ bond, since this is energetically favorable, the spin-orbit interaction can also be enhanced: in an ionic pair, an unpaired electron is partially delocalized on the cation and this leads to an increase spin-orbit interaction. As a result, the elastic properties change due to a decrease in the interatomic distances in the $Te^{(1)}\text{-}Bi\text{-}Te^{(2)}\text{-}Bi\text{-}Te^{(1)}$ quintet. A change bonds in the between several different positions can explain the anomaly in thermal expansion of crystals of the Bi_2Te_3 type and a reduction in interatomic distances.

The transformation of the structure during thermally activated processes can lead to the destruction of some bonds and the formation of other bonds, and the presence of metastable and defective centers can enhance this effect. For example, studies of the switching effect in chalcogenide glasses have revealed the competition between the resonance bonds of the crystalline phase and the disorder of the amorphous one [12-14]. A decrease in the interatomic distances in bismuth and antimony chalcogenides [15–17] at negative TCLE values can be associated with fluctuations in the magnitude of the interlayer interaction, which affects the parameters of atomic bonds within the quintet. When activated, defect centers create perturbations and an additional potential that distorts bonds; an increase in disorder leads to disorderly forming of bonds and displacement of atomic positions, thereby affecting the magnitude of the spin-orbit interaction. These centers affect the parameters of the hybrid bond, where the chalcogen ions of the inner layer and bismuth play a decisive role; accordingly, the interaction can be accompanied by the formation or strengthening of chemical bonds. Crystal doping affects the dynamics of the above processes through the interaction of impurity centers with the lattice, modifying the potential and levels of the impurity atom, depending on the type of defect and impurity, and also forming a disordered network of defect centers in the crystal lattice and in the interlayer space. The main elements of the network of defect centers in Bi_2Te_3 are intralayer defects and interlayer islands: intralayer defects are sources of disorder, interlayer defects are covalent bridges.

Of practical interest is the type of defects at which the maximum charge transfer density is achieved with maximum phonon scattering, which makes it possible to increase the thermoelectric figure of merit of the material due to a decrease in thermal conductivity. The features of the structural alignment also strongly affect the mechanical parameters of crystals, which is important for obtaining hardened materials used at high mechanical loads.

Results and discussion

Bi_2Te_3 crystals doped with Cu-0.05 wt% and In-0.1 wt% were obtained by vertical directional crystallization. X-ray diffractometric studies carried out on a diffractometer by Panalytical B.V. X'Pert Pro X-Ray Diffractometer XRD, found the presence of elements on the surface of the cleavage (Fig. 2), which are shown in decreasing order: $CuInTe_2$; In_3Te_4; $BiIn$; $InTe$.

Images of a freshly cleaved crystal surface were obtained on a NT-MDT (SOLVER NEXT) scanning probe microscope at room temperature. On the surface, there are nanoislands up to 1.5 nm in height (Fig. 3), their distribution density is rather low (Fig. 4), the distances between nanoislands, in general, exceed 100 nm, and the probability of charge tunneling between these inhomogeneous defects is smal. X-ray phase analysis was performed on a Bruker AXS GmbH D8 ADVANCE X-ray diffractometer (radiation at 40 kV and 40 mA in $CuK\alpha$, 10° θ<2). The nonlinear behavior of the temperature dependence of the crystal lattice parameters was accompanied by a negative TCLE in the range of 270-280K.

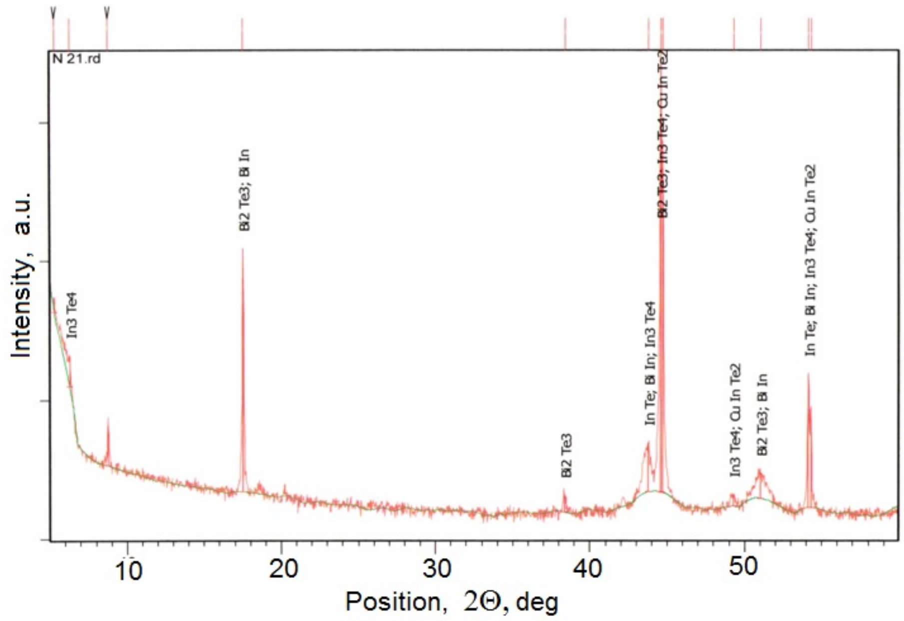

Fig. 2. X-ray diffractogram Bi_2Te_3<In,Cu>.

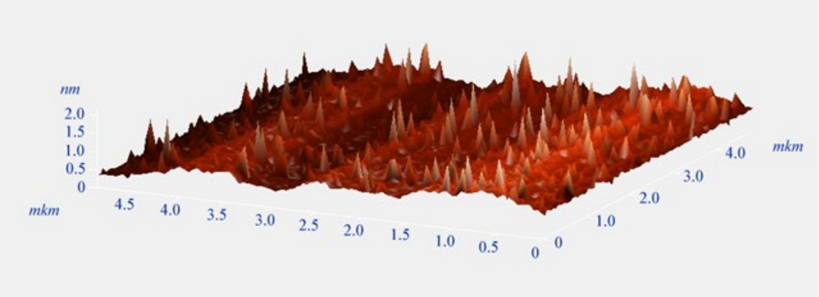

Fig. 3. 3D AFM image of Bi_2Te_3<In,Cu> (0001) surface.

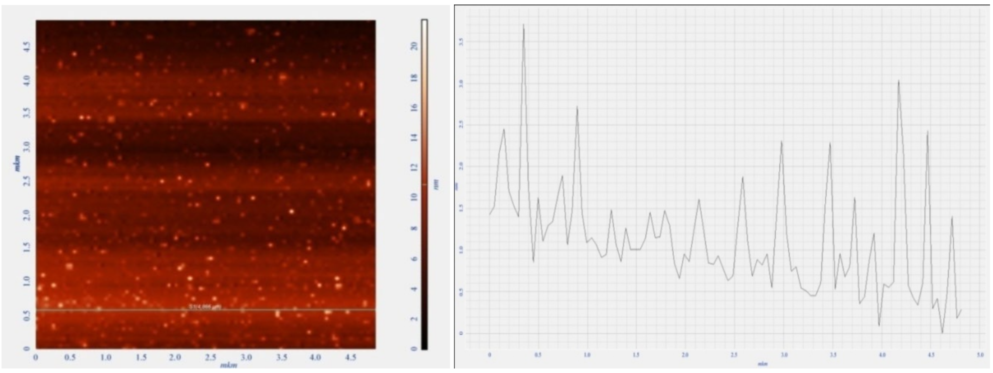

Fig. 4. 2D AFM image of Bi_2Te_3<In,Cu> and a profilogram along the section indicated in the AFM image.

The deviation from the exact structure in the five-layer package is small, the lengths of strong bonds are comparable to $Te^{(1)}$-*Bi*, 3.03Å, and *Bi*-$Te^{(2)}$ - 3.22Å. The $Te^{(1)}$- *Bi*-$Te^{(2)}$ and *Bi*-$Te^{(2)}$ -*Bi* angles are 174.6° and 180°, respectively, due to this slight structural distortion, long-range interactions are weakened, which leads to a weakening hybrid communication. The *Bi*-*Bi* and $Te^{(1)}$-$Te^{(2)}$ interactions, located at a distance of about 6 Å from each other, are equivalent to the interaction with the fourth neighbor. The *Bi*-$Te^{(1)}$ interactions, located at a distance of 9Å, separated by $Te^{(2)}$ -*Bi*, have positive force constants.

This is due to the fact that the hybrid connection around the $Te^{(2)}$ atom is well maintained: the lengths of the Bi-$Te^{(2)}$ and $Te^{(2)}$-Bi bonds are the same, and they make an angle of 180°, as shown above [7]. In [18, 19], in ab initio calculations, taking into account the spin–orbit interaction increases the interlayer forces in Bi_2Te_3 and Bi_2Se_3, which is reflected in a decrease in the interlayer distance. Disregarding the spin-orbit interaction, the distance between the $Se^{(1)}$-$Se^{(1)}$ atoms is 3.35Å, and with allowance for, 3.27Å.

The change in the lattice parameters while maintaining symmetry as a function of temperature is most likely associated with the redistribution of the electron density in the Bi-$Te^{(2)}$ and $Te^{(1)}$-Bi bonds. The latter leads to charge polarization and switching of bonds in the quintet layer, that is, the tellurium sublayer ionically bonded to the bismuth layers, playing a "loosening" role, makes the main contribution to the alignment or switching of valence bonds in the Bi-$Te^{(2)}$ sublattices. As can be seen, the redistribution of the charge and the change in the interatomic distance can also affect the magnitude of the spin-orbit interaction and leveling the corresponding properties of the crystal.

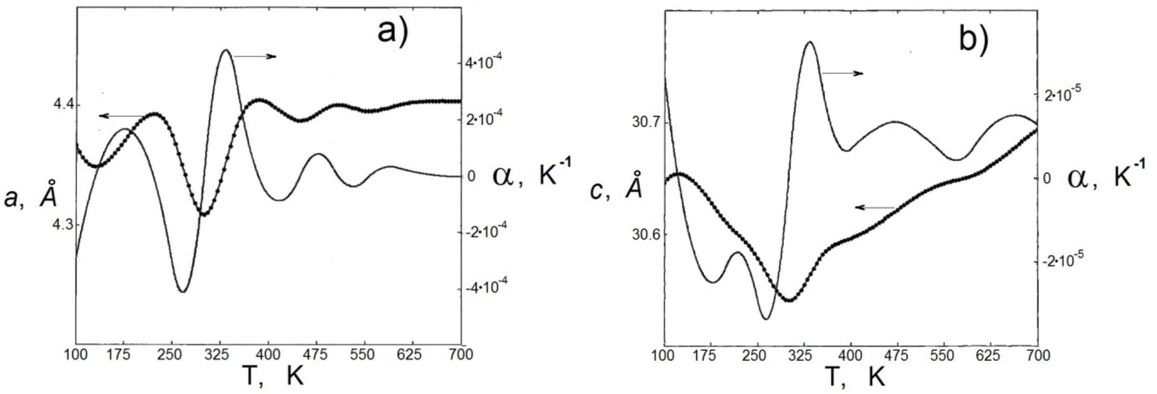

Fig. 5. Temperature dependence of the parameters of the crystal lattice of Bi_2Te_3<In,Cu> in the directions *a* (a) and *c* (b) (the dots indicate the experimental data of the lattice parameters, the continuous line shows the calculated curve of the thermal expansion coefficient).

The bonds within the layers are sensitive to fluctuations in the magnitude of the interlayer interaction. The energy of interlayer interaction, in turn, changes with a change in the value of the interlayer barrier, which is determined by interlayer inclusions that broaden the Van der Waals space and are sources of covalent bridges. Thus, a change in the interlayer interaction at the corresponding ambient temperature affects the Bi-$Te^{(2)}$ bonds and the general form of the electronic structure of the material, while the spin-orbit interaction and interlayer forces are enhanced, which is reflected in a decrease in the interatomic distance within the quintets. Hybrid bonds undergo extremum transitions, changing bond angles and interatomic distances, and a conformational transition occurs. The most pronounced transition is observed at a negative TCLE at 270 K, leading to the above processes by shifting the electron density into the quintet. The periodic change in the structure of interatomic distances through the next temperature cycle of the corresponding energy does not look so pronounced because of the smearing of this effect by the enhancement of vibrational processes of the lattice at higher temperatures.

Impurities and defect centers

A relatively small amount of an impurity can significantly change the properties of these crystals; the mechanisms of this effect are of a different nature. For example, the addition of a small amount of Cu to Bi_2Te_3 sharply decreases the hole conductivity and significantly increases the electronic conductivity. It was noted in [20] that copper atoms entering the Van der Waals gaps lead to general strengthening of the samples due to the formation of $Te^{(1)}$-Cu-$Te^{(1)}$ covalent-ionic bonds, while the copper impurity exerts donor action ($Cu \rightarrow Cu^{1+} + e^{1-}$). Inside the quintet, tellurium can reduce Cu^{2+} ions to Cu^{+}, since the overlap of tellurium *5p* orbitals with copper *3d* orbitals is energetically favorable. In this impurity combination, interlayer copper can lead to the appearance of an insignificant amount of defects of the Cu_{Bi} type, which, having an unstable character due to the variable valence bond with the chalcogen, can affect the temperature changes in the chemical bond and, accordingly, the values of the anion-cation internuclear distances. At certain values of the lattice parameters of the crystal framework, copper atoms can appropriately group and exhibit superionic properties; they are able to switch between several available bonds, these allows copper ions to flow within the entire crystal structure. In this case, low thermal conductivity is provided by the suppression of most of the phonons as a result of anharmonicity and disorder.

The indium impurity acts as an acceptor, antisite defects In_{Te} create in the valence band a larger number of vacancies than antisite defects of Bi_{Te}, since In atoms have 3 *p*-electrons less than *Te* atoms, the formation of such defects requires the transition of two *s*-electrons of *In* to *p*-levels [21]. However, some defects, for example, in the centers of substitution of bismuth with indium InBi, contribute to additional deformation of the crystal environment. Local disordering centers can be a consequence of a phase change in the environment of defect centers in the crystal structure, which leads to the formation of disordered regions of strong charge localization [22]. In such cases, it is necessary to take into account both the incorporation of a defect into the crystal lattice and the relaxation of the adjacent region. Indium, which replaces bismuth in the crystal lattice of Bi_2Te_3, can create a dipole moment due to the vibrations of a higher frequency of In atoms, smaller than bismuth atoms. The crystal lattice near the indium atom is deformed during vibrational motion, but the magnitude of the deformation should rapidly decrease with increasing distance from In. These defects affect the electronic and phonon systems of the material. Due to strong mechanical stresses, these centers dissipate vibrational energy and increase the anharmonicity of vibrations in the layers of the quintet, which affects the decrease in the overall thermal conductivity. The influence of these defects on the electronic structure can occur both directly by changing the concentration of charge carriers, and by affecting the redistribution of the electron density, since their activation can lead to a change in the bond. At In_{Bi} defect centers, the localization of the charge density has a weak type of bond; at certain energies, they can contribute to the creation of bonding states. When exposed to a weak magnetic field, it is also possible to stimulate these extended bonding states.

Under certain conditions, *In* atoms are sources of disorder; they begin to form new stronger bonds, and relatively weak bonds are reformatted into more rigid ones. Intralayer bonds, passing through their extrema, compressing and expanding the lattice in the direction of the *C* axis, are exposed to the *In* centers, which increase the rigidity of the bond in their environment. This process also affects the delocalization of charge carriers when passing through a certain energy range at a temperature course and the effect of a weak magnetic field on the spin ordering and shunting of the current of free charge carriers. When activated, defects create additional disturbances that increase disorder, which leads to the appearance of additional potential that distorts communications. The competition between the resonant bond and the additional potential can form new covalent bonds through the long-range orbitals of large atoms, creating bonding states, this is accompanied by fluctuations in the concentration and mobility of charge carriers. Changes in the interatomic distances in a crystal, coupled with centers of disorder, enhance the delocalization effect. A periodic change in the interatomic distances of the crystal lattice affects the anharmonicity of vibrations of the atoms of the layers and controls the "membrane" effect [23]. *In* enhances anharmonicity, creating disordered centers of deformation of the crystal lattice. These centers create conditions for additional strengthening of the chemical bond in the direction perpendicular to the layers.

Conductive extended states

The state of the quintet layers of the crystal lattice is also affected by the processes occurring in the interlayer space, which directly affect the redistribution of the electron density and changes in the phonon subsystem. It is known that, in layered crystals, part of the superstoichiometric excess and impurities is formed in the interlayer space. A shift of the charge density into the depth of the layer upon broadening of the Van der Waals gap [24], as well as an increase in the number of electrons from donor impurities, can lead to mutual repulsion of lone electron pairs at the $Bi\text{-}Te^{(2)}$ bond and a change in the bond angle. As a result of such a charge shift [25], a greater splitting of molecular orbitals of various types occurs, in this case, non-bonding orbitals are involved in the formation of covalent orbitals. The *Bi* orbitals combine with the *Te* orbitals, with the formation of new bonding orbitals instead of the original nonbonding orbitals, i.e. the bond takes on a metastable ionic-covalent form. When the bonds between the $Te^{(2)}$ and bismuth atoms are hybridized, the initial system overlaps with the $Te^{(2)}$ *p*-orbital and the lone electron pair of bismuth is transformed into a conjugated system, accompanied by a redistribution of the electron density.

The inhomogeneous distribution of the electron density at the lattice centers on both sides of Bi, caused by a change in the valence state and leading to the polarization of the electronic system, can lead to the appearance of static and dynamic waves of charge density. For charge density waves, mixing of the bonding orbital with its antibonding orbital is inherent, while energetically bonding and antibonding levels are arranged symmetrically with respect to the Fermi level. A cycle consisting of 75K, at which fluctuations of the lattice parameter occur, is ~ 0.0065 eV. Approximately the same energy value is observed with fluctuations of the kinetic parameters. The temperature dependence of these parameters, apparently, also shows a partial contribution from the change in the bonding and antibonding bonds, depending on the vibrations of the states corresponding to them near the Fermi level. This is accompanied by a change in the types of charge ordering, as well as changes in the alignment of bonds and changes in the parameters of the crystal lattice. As you can see, the temperature changes the energy state of the bonds, which, by changing the orientation, lead to compression and expansion of the crystal in the direction of the *"C"* axis. A change in valence bonds leads to a change in the charge ordering and, possibly, to its polarization, as in the case of superconductivity in Bi_2Se_3<Cu> [26-28]. The redistribution of electron density can be accompanied by the formation of extended states conducting along long-range hybrid orbitals of heavy elements. Conducting extended states are akin to a long molecule, i.e. at a certain energy, the tunnel bond through the atoms of heavy elements forms a chemical bond of a weak type, since the energy of interaction of the outermost electrons with the nucleus is weak, and the potentially formed new bond is also weak, similar to the correlation interaction of electrons. The hybridization of bonds leads to the appearance of extended states, and an increase or decrease in energy relative to the level of a given state leads to the destruction of extended states and the absence of tunneling. According to the results of studying the kinetic parameters of the material, shunting through extended states had activation peaks at 100K and 150K. The stimulation of these states by a weak magnetic field and their destruction under strong fields were observed: negative magnetoresistance up to 10 kOe. An increase in temperature under magnetic field action led to an increase in negative magnetoresistance from 100K to 170K, then it abruptly dropped to nothing, i.e. the effect of shunting on an extended conducting state was blocked. The destruction of the hybrid bond leads to a return to the previous model of the distribution of bonds in the molecule and, accordingly, the electron density in the quintet. With the exception of the main, largest feature, extrema on the temperature dependences of the Hall coefficient (Fig. 6) and electrical conductivity (Fig. 7), as well as the concentration (Fig. 8) and mobility of charge carriers (Fig. 9) in the region of 77-170K are possible due to an increase in the electronic component during the transition of localized electrons from occupied to unfilled levels with increasing temperature.

The overflow of electron density along the $Bi\text{-}Te^{(2)}$ bond, which enhances the ionicity of the bond, reduces the interatomic distance, and an increase in the concentration of free carriers manifests itself in the value of the conductivity. An indirect confirmation of this is the negative magnetoresistance at 100-170K (Fig. 10, Fig. 11).

The anharmonicity of the bonds, which was pointed out by other authors as the cause of the negative TCLE in the region of 100-200K and the deviation of the bond at T100K-150K, is a consequence of the electron density overflow along the bond. A weak magnetic field, as can be seen, leads to the delocalization of precisely electrons in the metastable configuration of orbitals near the defect centers of disorder. The burst of kinetic parameters is possibly associated with delocalization during the formation of extended bonds, the anharmonicity of bonds and the membrane effect contribute to the overlap of orbitals between layers elements. The overlapping of the electronic functions of the layers leads to the formation of extended states, which in turn leads to an increase in the concentration of charge carriers, conductivity, etc. A weak magnetic field also leads to the formation of extended states through charge delocalization during the spin orientation of bonds.

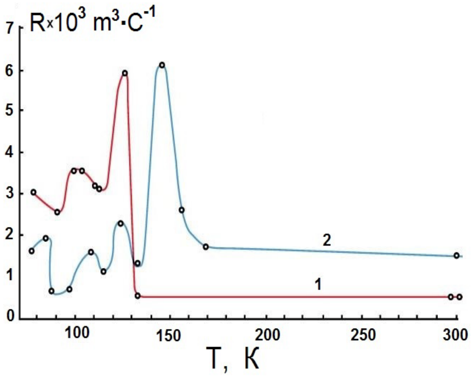

Fig. 6. Temperature dependences of the Hall coefficient R of Bi_2Te_3<In,Cu> sample with the directions of the experiment: 1 - H II c ⊥ J; 2 - H ⊥ c ⊥ J.

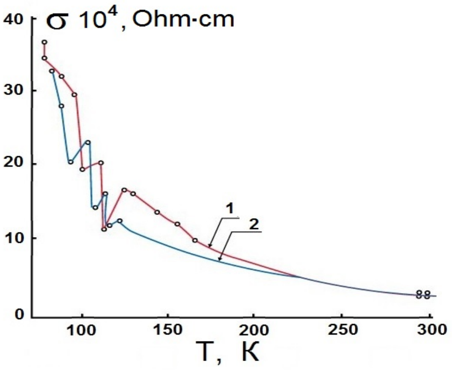

Fig. 7. Temperature dependences of the electrical conductivity of Bi_2Te_3<In,Cu> for the directions of the experiment: 1 - H II c ⊥ J; 2 - H ⊥ c ⊥ J.

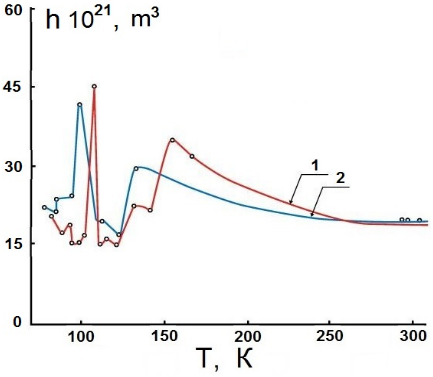

Fig. 8. Temperature dependences of the Hall concentration of charge carriers n Bi_2Te_3<In,Cu> experiment directions: 1 - H II c ⊥ J; 2 - H ⊥ c ⊥ J.

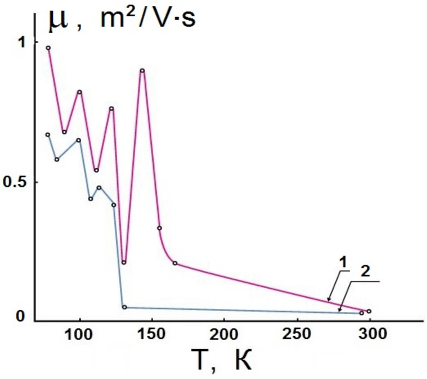

Fig. 9. Temperature dependences of the mobility μ Bi_2Te_3<In,Cu> for the directions of the experiment: 1 - H II c ⊥ J; 2 - H ⊥ c ⊥ J.

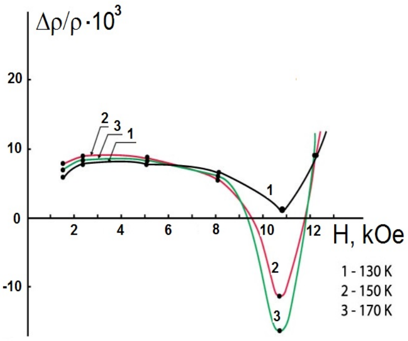

Fig. 10. Dependences of the transverse magnetoresistance Δρ/ρ on the magnetic field H for the Bi_2Te_3<In,Cu> sample at different temperatures: 1 - 130K, 2 - 150K, and 3 - 170K.

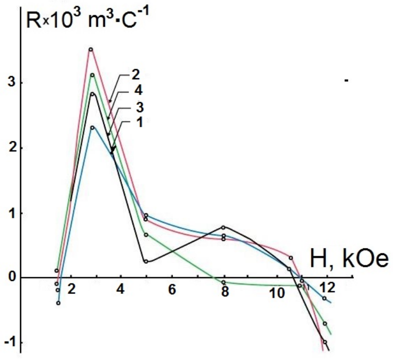

Fig. 11. Hall coefficient R as a function of the magnetic field of Bi_2Te_3<In,Cu> sample at a temperature: 1 - 110K; 2 -120K; 3 - 150K; 4 - 170K.

Conclusion

The polarity of the covalent bond changes, leading to a conformational transition, which is expressed in a decrease in the *Bi-Te*$^{(2)}$ interatomic distances; experimental confirmation of this process was observed in negative TCLE values at temperatures energetically correlating with the value of the interlayer interaction. The resonance of hybrid bonds undergoes transitions along the extrema, changing bond angles and interatomic distances, a conformational transition occurs, the most pronounced was observed at a negative TCLE of about 270K. The change in interatomic distances through the next cycle of the corresponding energy is not so pronounced due to temperature smearing.

The transition temperature depends on the magnitude of the interlayer interaction: covalent bridges formed by interlayer inclusions enhance the interaction between opposite layers of quintet packets, therefore the temperatures at which negative TCLE are observed for pure and doped materials have different values. The energy of thermal motion corresponding to the ambient temperature, when approaching the value of the energy of interlayer interaction, leads to a deviation of the bond and to fluctuations in the distribution of the electron density. The stronger the interlayer interaction, the higher the temperature, i.e. the more energy is required to "soften" it.

Interlayer bonds are more sensitive to changes in the parameters of the external environment, therefore, it can be concluded that the above processes are influenced by fluctuations in interlayer bonds, which affect the hybridization of the orbitals of atoms inside the quintet and lead to a change in the covalent radius. A change in the interlayer interaction, leading to a redistribution of the electron density from the edges of the quintet to the inside of the layer, to a bond with the central chalcogen, changes the bond from a long-range resonant to a covalent form with a fraction of ionicity, and then to an ionic-covalent one, bringing the interatomic distances closer together as the nature of the bond changes.

References

1. Regel AR, Glazov VM. Physical properties of electronic melts, Moscow: Nauka, 1980, 296 p.
2. Drabble J.R., Goodman C.H.L.. J. Phys. and Chem. Solids 1958, v. 5, p. 142. https://doi.org/10.1016/0022-3697(58)90139-2.
3. Mooser E., Pearson W.B.. J. Electronics 1956, v. 1, p. 629. https://doi.org/10.1080/00207215608961467
4. Sluchinskaya IA, Fundamentals of materials science and technology of semiconductors, Moscow, 2002, p. 376.
5. Pauling L. American Mineralogist 1975, v. 60, p. 994.
6. Kagarakis C.A. Journal of Materials Science 1978, v. 13, p. 1594.
7. Lee S., Esfarjani K., Luo T., Zhou J., Tian Z., Chen G.. Nature Communications 2014, v. 5, p. 3525. https://doi.org/10.1038/ncomms4525.
8. Cheng Y., Wahl S., Wuttig M. Phys. Status Solidi RRL 2020, v. 10, p. 2000482. https://doi.org/10.1002/pssr.202000482.
9. Pavlova LM, Shtern Yu.I., Mironov R.E. Thermophysics of high temperatures 2011, v. 49, p. 379. http://mi.mathnet.ru/rus/tvt/v49/i3/p379
10. Abdullaev N.A. Physics of the Solid State 2006, v. 48, p. 623.
11. Luo X., Sullivan M., Quek S.Y. Physical Review B 2012, v. 86, p. 184111. https://doi.org/10.1103/PhysRevB.86.184111.
12. Shportko K., Kremers S., Woda M., Lencer D., Robertson J., Wuttig M. Nature Materials 2008, v. 7, p. 653. https://doi.org/10.1038/nmat2226
13. Wuttig M. Phys. Status Solidi B 2012, v. 249, p. 1843. https://doi.org/10.1002/pssb.201200582
14. Simpson R.E., Fons P., Kolobov A.V., Fukaya T., Krbal M., Yagi T., Tominaga J., Nature Nanotechnology 2011, v. 6, p. 501. https://doi.org/10.1038/nnano.2011.96.

15. Chen X., Zhou H.D., Kiswandhi A., Miotkowski I., Chen Y.P., Sharma P.A., Sharma A.L.L., Hek Hekmaty M.A., Smirnov D., Jiang Z. Applied Physics Letters 2011, v. 99, p. 261912. https://doi.org/10.1063/1.3672198.
16. Kim Y., Chen X., Wang Z., Shi J., Miotkowski I., Chen Y.P., Sharma P.A., Lima Sharma A.L., Hekmaty M.A., Jiang Z., Smirnov D. Applied Physics Letters 2012, v. 100, p. 071907. https://doi.org/10.1063/1.3685465
17. Dutta P., Bhoi D., Midya A., Khan N., Mandal P., Shanmukharao S., Samatham V. Ganesan. Applied Physics Letters 2012, v. 100, p. 251912. https://doi.org/10.1063/1.4730390.
18. Cheng W., Ren S. Phys. Rev. B 2011, v. 83, p. 094301. https://doi.org/10.1103/PhysRevB.83.094301.
19. Wang B.T., Zhang P. Appl. Phys. Lett. 2012, v. 100, p. 082109. https://doi.org/10.1063/1.3689759.
20. Korzhuev M.A., Ivanova L.D. Collection of reports of the International Scientific Conference. Minsk. 2007, October 23-26, p. 108.
21. Kakhramanov K.Sh., Roshal R.M., Alieva L.N., Kasimov M.I. Inorganic Materials 1988, v. 24, p. 1954.
22. Siegrist T., Jost P., Volker H., Woda M., Merkelbach P.,.Schlockermann C., Wuttig M. Nature Materials 2011, v. 10, p. 202. https://doi.org/10.1038/nmat2934.
23. Abdullaev N.A., Suleimanov R.A., Aldzhanov M.A., Alieva L.N. Physics of the Solid State 2002, v. 44, p. 1775.
24. Menshchikova T.V., S.V. Eremeev, E.V. Chulkov. JETP Letters 2011, v, 94, p. 106. http://mi.mathnet.ru/rus/jetpl/v94/i2/p110.
25. Vergniory M.G., Menshikova T.V., Eremeev S.V., Chulkov E.V. JETP Letters 2012, v. 95, p. 230.
26. Hor Y.S., Williams A.J., Checkelsky J.G., Roushan P., Seo J., Xu Q.,.Zandbergen H.W, Yazdani A., Ong N.P., Cava R.J. Phys. Rev. Lett. 2010, v. 104, p. 057001. https://doi.org/10.1103/PhysRevLett.104.057001.
27. Ando Y., Segawa K., Sasaki S., Kriener M. Journal of Physics: Conference Series 2013, v. 449, p. 012033. doi:10.1088/1742-6596/449/1/012033.
28. Kondo T., Nakashima Y., Ota Y., Ishida Y., Malaeb W., Okazaki K., Shin S., Kriener M., Sasaki S., Segawa K., Ando Y. Phys. Rev. Lett. 2013, v. 110, p. 217601. https://doi.org/10.1103/PhysRevLett.110.217601.

MOLECULAR MECHANICS SIMULATION OF CONFORMATIONAL BEHAVIOR OF ANTICANCER AAP-H PEPTIDE

GA AGAEVA, UT AGAEVA and NM GODJAEV

Baku State University, Baku, Azerbaijan
E-mail: gulshen@mail.ru

The anticancer peptide AAP-H is a pentapeptide from the sea anemone Anthopleura anjunae with an amino acid sequence Tyr-Val-Pro-Gly-Pro. The results of numerous studies indicated that AAP-H peptide was nontoxic and exhibited antitumor activities in prostate cancer DU-145 cells in vitro and in vivo. For determination a mechanism of action of this pentapeptide and to investigate its structure-function relations is required the knowledge of the conformational specificity and flexibility of backbone and side chains of molecule allowing a rational design of functional groups acting selectively at their receptor level. The conformational behavior of AAP-H peptide and dynamics of its side chains have been investigated by molecular mechanics method, which allow to determine a whole sets of energetically preferred conformers of peptide molecule. The detailed analysis of the conformational flexibility of AAP-H peptide was founded the limited quantity of stable conformers. The obtained results have shown that the stable conformers of pentapeptide have tendency adopt a beta-turn structure.

Keywords: anticancer peptide, antitumor activities, conformation, molecular mechanics method
PACS: 87.15.He, 87.15.-v, 87.15.Aa, 87.19.xj

Introduction

It is known that some marine organizms possess antithrombotic, antitumor, and antibacterial activities [1]. The bioactive substances of these marine organisms have played important roles in the development of innovative medicines. Prostate cancer (PCa) is one of the most common malignancies of the male urinary system and is also the leading cause of cancer-related death in men [2]. Cancer is a disease characterized by over proliferation, including that due to transformation, apoptosis disorders, proliferation, invasion, angiogenesis and metastasis, and is one of the deadliest diseases [1]. Currently, conservative chemotherapy is used for cancer treatment due to a lack of effective drugs. In 2018, Wu et al. [2] found that AAP-H exhibits certain cytotoxicity against human prostate cancer DU-145 cells, and its mechanism of action might be related to the mitochondria regulated apoptotic pathway. Furthermore, Li et al. [3] found that this molecule induces cell S phase arrest in DU-145 cells. Additionally, in the nude mouse model, this molecule shows a good curative effect on prostate cancer with an obvious decrease in the weight of prostate solid tumors and a slight increase in the weight of nude mice during AAP-H treatment [3,4]. Thus, while the anticancer mechanism of APP-H on prostatic neoplasms might be involved in the mediation of the PI3K/Akt/mTOR pathway, which ultimately induces cell apoptosis through apoptosis pathways mediated by mitochondrial and death receptors [3], AAP-H has great potential in the future for the therapy of prostate cancer. The antitumor mechanism of *Anthopleura anjunae* oligopeptide (AAP-H,YVPGP) in prostate cancer DU-145 cells have been investigated in vitro and in vivo. Results indicated that AAP-H was nontoxic and exhibited antitumor activities. Cell cycle analysis indicated that AAP-H may arrest DU-145 cells in the S phase. The role of the phosphatidylinositol 3-kinase/protein kinase B/mammalian rapamycin target protein (PI3K/AKT/mTOR) signaling pathway in the antitumor mechanism of APP-H was investigated. Therefore, the antitumor mechanism of APP-H on DU-145 cells may involve regulation of the PI3K/AKT/mTOR signaling pathway, which eventually promotes apoptosis via mitochondrial and death receptor pathways. Thus, the hydrophobic oligopeptide (YVPGP) can be developed as an adjuvant for the prevention or treatment of prostate cancer in the future. For determination a mechanism of action of this pentapeptide and to investigate its structure-function relations is required the knowledge of the conformational specificity and flexibility of backbone and side chains of molecule allowing a rational design of functional groups acting selectively at their receptor level. The conformational behavior of AAP-H peptide have been investigated by molecular mechanics method, which allow to determine a whole sets of energetically preferred conformers of peptide molecule. The major aim of the present work is the investigation of conformational dynamics of backbone and side chains for AAP-H peptide by molecular mechanics in vacuum and in polar medium. The structural data are very useful as a guideline in designing analogues with more potent and/or long-lasting biological activity For the determination structure–activity relationship of AAP-H peptide, besides the investigation of it spatial structure, it is necessary to elucidate the roles of the functionally active residues in stabilization of the preferable conformations.

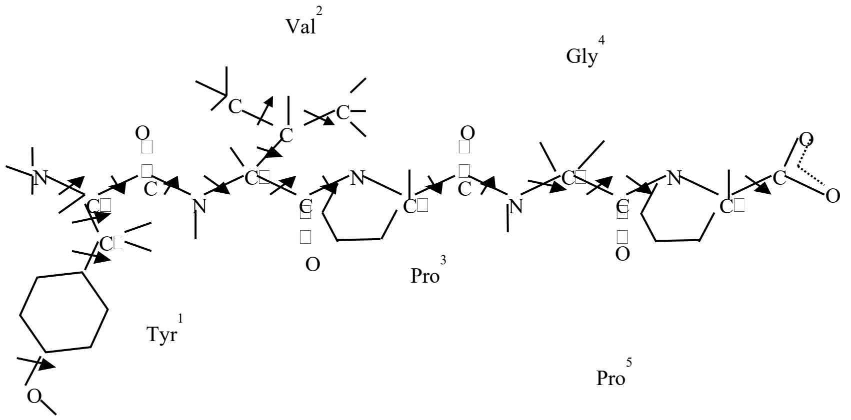

Fig. 1. Amino acid sequence and dihedral angles of anticancer peptide AAP-H.

Method

Molecular mechanics (MM) study of AAP-H peptide conformational properties involves extensive computations of even-increasing fragments, with a set stable forms of each preceding step used as a starting set in the next step. Only those conformations are retained whose energies are smaller than some cut-off values. This cut-off value is usually taken as 5 kcal/mol above the lowest energy. The sequential method was used, combining all low-energy conformations of constitutive residues. The conformational potential energy of a molecule is given as the sum of the independent contributions of nonbonded, electrostatic, torsional interactions and hydrogen bonds energies. The first term was described by the Lennard-Jones 6-12 potential with the parameters proposed by Scott and Scheraga [5]. The electrostatic energy was calculated in a monopole approximation corresponding to Coulomb's law with partial charges of atoms as suggested by Scott and Scheraga [5]. An effective dielectric constant value ε= 1 for vaccum, ε=4 for membrane environment and ε=80 for water surrounding is typically used for calculations with peptides and proteins, which create the effects of various solutions on the conformations of peptides by MM method. The torsional energy was calculated using the value of internal rotation barriers given by Momany et al [5]. The hydrogen bond energy is calculated based on Morse potential Bonding lengths and angles are those given by Corey and Pauling and are kept invariable [6]. The sequence of the residue forms, determined on the conformation map by the dihedral angles φ and ψ of the backbone by the following low-energy areas: R (φ = –180°–0°, ψ = –180°–0°), Ç (φ = –180°–0°, ψ =0°–180°), L (φ = 0°–180°, ψ = 0°–180°), and P (φ = 0°– 180°, ψ = –180°–0°), was considered to be the form of the backbone. The ω angle of the peptide bond was fixed at 180° [6,7]. The conformational energy was minimized using program, written by Maksumov et al [8]. The dihedral rotation angles were counted according to the IUPAC-IUB [9].

Result and discussion

The sequential method was used, combining all low-energy conformations of constitutive residues. The calculated atomic models and variable dihedral angles of AAP-H peptide are given in Fig. 1. The presence of a proline residue in the peptide sequence significantly reduces its conformational possibilities. Unlike other residues, Pro, because of the rigidly fixed N-Ca bond, cannot realize the L state. Furthermore, only the B form of the main chain is sterically admissible for the residue preceding proline [10]. The starting structural approximations for this pentapeptide were chosen with regard to the limitations associated with the Pro residue. The starting structural variants were proposed for the calculation of the optimum conformations of the pentapeptide on the basis of the low-energy conformations of the corresponding amino acid residues with regard to various orientations of their side chains. All available conformations were classified into 4 backbone forms. About 108 initial conformations were used for the global energy minimization. The energy distribution of the calculated conformations of the pentapeptide was presented in Table 1. The lowest-energy conformation of the pentapeptide was shown to be realized for BBRBB backbone form.

Table 1. The optimal conformations of pentapeptide AAP-H in relative energy interval 0-4 kcal/mole)

№	Backbone form	The relative energy interval (kcal/mole)				
		0-1	1-2	2-3	3-4	>4
1	BBBBB					36
2	BBRBB	3	4	3	4	22
3	RBRBB				2	34
4	RBBBB					36

Only 16 of them consist of low-energy conformers the relative energy of which is within 0-4 kcal/mol. The second low energy conformers have RBRBB form of the peptide skeleton. The lowest energy conformation was mainly stabilized by effective interresidual interactions formed between the Tyr^1, Val^2, Pro^3 and *C*-terminal Pro^5 residues. It is found that the strong inter-residue interactions between Val^2 and the following amino acids Tyr^1, Pro^3, Pro^5 make an important contributions toward only dispersion interactions (-4.1,-3.5 and -4.9 kcal/mol, correspondingly). These interactions are characteristic for all low-energy structures of the AAP-H peptide. The distance between two C^a-atoms of Val^2 and Pro^5 is 5.9 Å. There was beta-turn on the segment Val^2-Pro^5.Because the ring structure of the side chain of proline forces the backbone into a conformation that is good for the β-turn. The calculation of stable conformations of the pentapeptide demonstrated a dramatic energy differentiation between the structural types and showed that a stable beta-turn structure is formed in C-terminal tetrapeptide of the molecules. The values of dihedral angles of the two energetically preferential conformations of AAP-H peptide are given in Table 2. The final structure, received by means of MM simulations, after computer-optimization of the lowest-energy conformation of AAP-H peptide is shown in Fig. 2.

Table 2. The values of dihedral angles of low-energy conformations of AAP-H peptide.

Residue	Conformation	Backbone angles			Side chain angles		
		φ	ψ	ω	χ1	χ2	χ3
Tyr	BBRBB RBRBB	-57 -55	139 -57	168 174	175 180	91 90	180 179
Val	BBRBB RBRBB	-135 -128	125 127	177 176	58 61	180 179	183 185
Pro	BBRBB RBRBB	-60 -60	-54 -55	178 180			
Gly	BBRBB RBRBB	-122 -123	88 89	179 179			
Pro	BBRBB RBRBB	-60 -60	138 138	180 180			

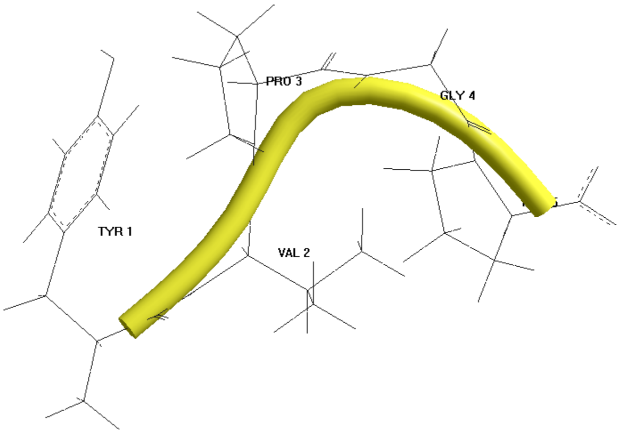

Fig. 2. The final structure, received by means of MM simulations, after computer-optimization of the lowest-energy conformation of AAP-H peptide.

The conformational flexibilities of the few separate residues Tyr and Val in the lowest energy conformations of pentapeptide as the energy dependency of the χ1side corner of the rotation are presented in Fig. 3. As seen from Fig. 3 the side chain of first residue Tyr may realized two eqivalent minimum states in the lowest conformation, but second residue Val has one preferable minimum and relatively energy higher level minimum also.

Thus detailed analysis of the conformational flexibility of AAP-H peptide was founded the limited quantity of stable similar conformers. The obtained results have shown that the stable conformers of pentapeptide have tendency adopt a beta-turn structure.

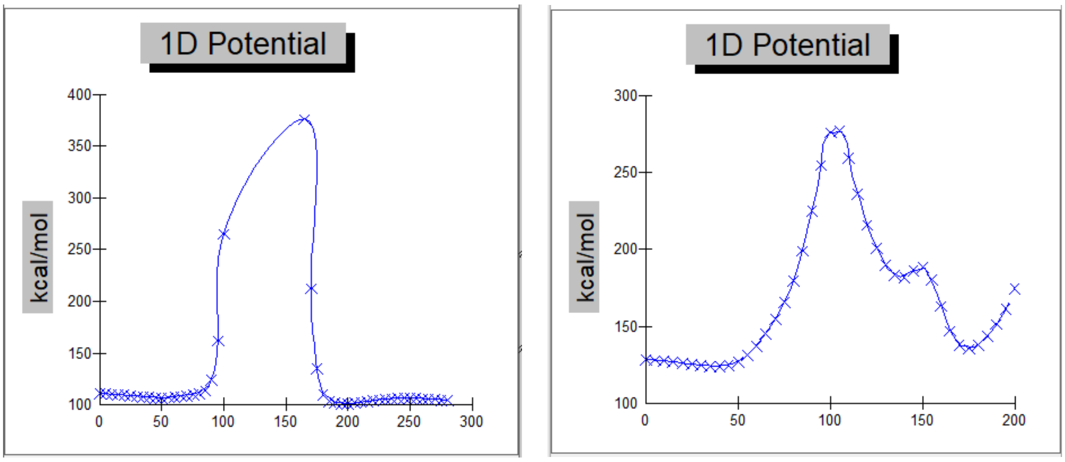

a) b)

Fig. 3. Conformational properties of the first and second residues in the lowest energy conformations of AAP-H peptide: (a) the 1D potential (energy) surface for Tyr residue; (b) the 1D potential (energy) surface for Val.

Conclusion

The obtained results and discussion lead to the following conclusions:

(I) molecular mechanics simulation in polar condition to confirm the small flexibility of the sequence of AAP-H peptide;

(II) the β-turn conformation on C-terminal tetrapeptide segment of peptide was more stabilized by dispersion interactions between residues;

(III) this conformational analysis helped reveal a number of special features of spatial arrangement of this drug-based pentapeptide. The determined stable structures of AAP-H peptide may be used as the basis for the design of further selective agonists.

References

1. Simmons T.L., Andrianasolo E., Mcphail K., Flatt P., Gerwick W.H., Mol. Cancer Ther. 2005, v. 4, p. 333.
2. Wu Z.-Z., Ding G-F., Huang F-F., Yang Z.-S., Yu F.-M., Tang Y.-P., Jia Y.-L., Zheng Y.-Y. and Chen R. Mar. Drugs 2018, v. 16, p.125.
3. Li X., Tang Y., Yu F., Sun Y., Huang F., Chen Y., Yang Z., Ding G. Mar. Drugs 2018, v. 16 (9), p. 325.
4. Arumugam V., Venkatesan M., Ramachandran S., Sundaresan U. Int. J. Pept. Res. Ther. 2017, v. 24, p.13.
5. Momany F., McGuire R., Burgess A., Scheraga H. J. Phys. Chem. 1975, v. 79, p. 2361.
6. Popov E.M. Int. J. Quant. Chem. 1979, v. 16, p. 707.
7. Agaeva G.A., Agaeva U.T., Godjaev N.M. Biophysics (Russian), 2015, v. 60, p.365.
8. Maksumov I.S., Ismailova L.I., Godjaev N.M. J. Struct. Khim.(Russian) 1983, v. 24, p.147.
9. IUPAC-IUB, Quantity, Units and Symbols in Physical Chemistry, Blackwell Scientific Publications, Oxford, 1988, 39 p.
10. Schimmel P.R.,Flory P.J. J. Mol. Biol. 1968, v. 34, p. 105.

PROPERTIES OF THE PP+METAL OXIDE NANOCOMPOSITE BEFORE AND AFTER INFLUENCE ELECTROTHERMAL POLARIZATION

HS IBRAHIMOVA[1], HA SHIRINOVA[2], AA HADIYEVA[1] and FF YAHYAYEV[1]

[1]Institute of Physics of the ANAS, Baku, Azerbaijan
[2]Baku State University, Baku, Azerbaijan
E-mail: hijran90@rambler.ru

It is shown that the thermal properties of polymer nanocomposites change depending on the crystallization mode and intermolecular interaction. Thermophysical parameters of pure isotactic PP and the nanocomposite obtained by three different modes of crystallization are calculated before and after exposure to electrothermopolarization. It was found that after exposure to the ETP in the thermogram of all the nanocomposites a new endomax is observed in the temperature range of 120-130 º.

Keywords: nanocomposites, electrothermal treatment, supramolecular structure, rapid cooling, nitrogen quenching, slow cooling.
PACS: :61.46.w, 82.35.Np, 71.38.k

Introduction

The development of modern technology requires the advancement and study of the properties of new composite materials. One of the most interesting and promising materials is polymer based materials. Since the problem of the interaction of fillers and matrix is quite multifaceted, the development of the technology of polymer-based composite materials is currently determined by scientific research in the field of polymer materials science. Due to the synergetic effect of the properties, composite materials based on metal-containing nanoparticles in a polymer matrix are promising for use in various branches of science and technology. The functional (thermophysical, electrical, magnetic, and electromagnetic) properties of composite nanomaterials can be easily controlled by changing the composition, structure, size, and concentration of nanoparticles in the polymer matrix, as well as changes in the supramolecular structure.

The term "supramolecular structure" is usually used to describe the physical structure of polymer bodies related to various types of macromolecules order. Besides molecular structure, almost all the properties of polymer composites are determined also by the arrangement of segments of macromolecules, aggregation of macromolecules, i.e., ultimately, by the peculiarities of the supramolecular structure. It is known that various morphological forms of supramolecular structure are formed in polymer composites depends on the kinetics of the crystallization process that determined by external conditions. The supramolecular structure of polymer composites is conclusively formed during their processing and obtaining constructional products. Each method of processing - extrusion or casting under pressure, pressing, pneumo-vacuum forming makes its corrections on the supramalecular structure of composites, which in turn determines their basic operational characteristics [1, 2].

Experimental part

The issue of changing the thermal properties of electro-technical materials during operation and manufacture under the influence of electric fields is insufficiently studied. The presented work presents the results of studying the change in the thermophysical parameters of the polymer metal-oxide nanocomposite PP + ZrO2 before and after exposing to electrothermal polarization.

The article aimed to study the influence of electro-thermopolarization on the thermophysical properties of nanocomposites obtained by different crystallization modes. Polymer nanocomposites were produced by introducing ZrO_2 nanoparticles into the polymer solution [3]. The size of the nanoparticles was about 20-30 nm. The hot pressing method was used for the production of the nanocomposite samples at melting temperature of the polymer and under the 15 MPa pressure for 3min. The thickness of polymer nanocomposite films was about 70-100 µm. Three modes of crystallization were chosen for the regulation supramolecular structure of the polymer nanocomposites. In fast cooling mode, polymer melt was cooled by the speed of 20-35deg/sec. During nitrogen quenching, the melted nanocomposite was immersed into the liquid nitrogen and cooled at a rate of about 150-250deg/sec. During slow cooling mode, the melted nanocomposite cools under the pressure until room temperature. In this case, the cooling rate is 0.03 deg/sec.

The samples were exposed to electro-thermal polarization at different values of the electric field strength. For polarization, the films are heated up to the polarization temperature, and during 1 hour stay at this temperature under the electric field. Then polarized samples are cooled to room temperature without removing the field. A high-voltage rectifier is used as a voltage source.

DSC data were obtained on a NETZSCH DSK 204 F1 Phoenix heat flux calorimeter by analyzing melting and crystallization thermograms. DSC records the heat flux, which characterizes the changes occurring in the nanocomposite as a result of heating or cooling. The nanocomposite sample is placed in an aluminum crucible. The mass of the empty aluminum crucible is approximately 0.0001 g, after the placement of the sample into the crucible and it pressed. Weighing the crucible with the sample it is possible to find the mass of the sample. The crucible with the sample is placed in the DSC cell. The studies were carried out at a temperature range of 300-500K with a heating rate of 20 deg/min. Heating occurs in a nitrogen atmosphere at a predetermined rate according to a controlled program, and during the measurement process, the heat flux of the reference and the test material is compared.

Results and discussion

Figures 1 (a) and (b) show thermograms of pure PP film and PP+3%ZrO2 nanocomposites obtained by different crystallization modes. By comparison of the thermos-physical parameters, it is clear that these parameters change for all three modes of crystallization (table1). All thermos-physical properties of polymer nanocomposite differ from pure polymer. Furthermore, with the addition of metal-oxide nanoparticles into the nanocomposite melting enthalpy and consequently the degree of crystallinity decrease. This indicates a partial amorphization of the polymer. Fillers playing the role of active centers exert an orienting effect on macromolecules and lead to the formation of adsorption layers from ordered supramolecular structures. The presence of nanoparticles in the polymer matrix leads to a change in the shape and size of the supramolecular structures. At low concentrations of the nanoparticles, they play the role of crystallization centers. However, further increase in nanoparticles concentration leads to a slowdown in crystallization and a decrease in the degree of crystallinity. It can be assumed that, with an increase in the cooling rate of the polymer nanocomposite, the size of the spherulites decreases. At an artificially created very high rate of cooling of the samples (Quenching into liquid nitrogen), spherulite formation does not have time to occur at all, and aggregates of lamellas form. Another limit condition is a slow cooling mode of samples. During slow cooling of the samples crystallization occurs at a relatively high temperature; spherulites with a size of several microns are formed. The inclusion of metal-oxide nanoparticles into the polymer matrix changes the thermophysical characteristics of polymer-based materials. Figure 1 demonstrates the change of thermo-physical properties of pure polypropylene obtained by fast cooling, before and after the influence of electro-thermal polarization.

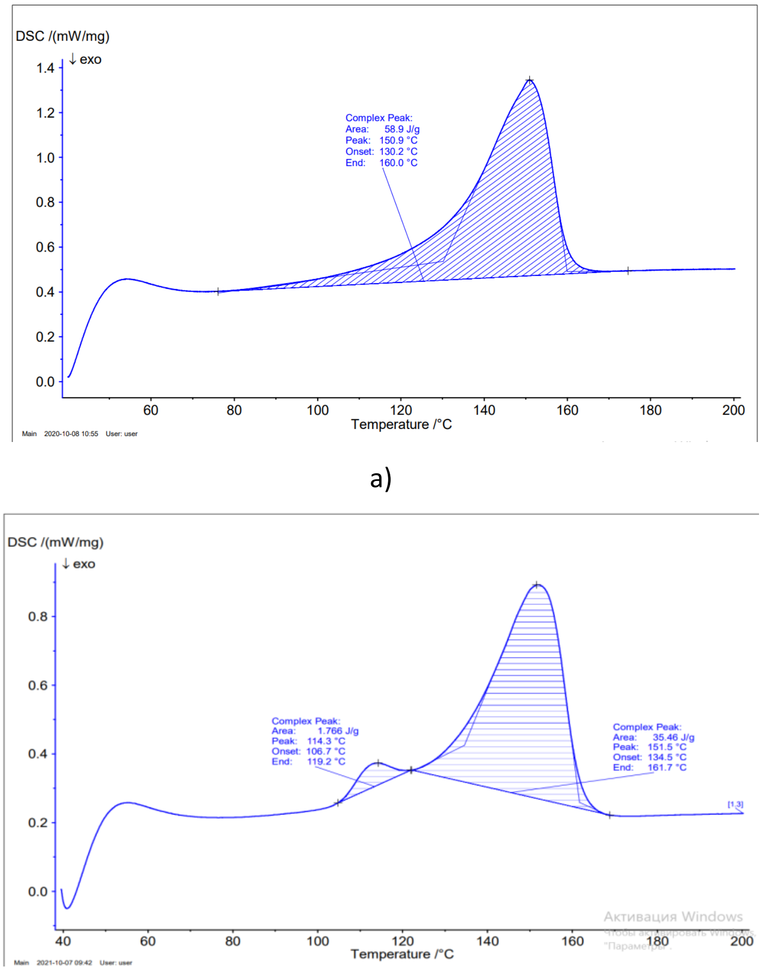

a)

b)

Fig. 1. The change of thermo-physical properties of pure polypropylene obtained by fast cooling:
a) before and b) after influence of electro-thermal polarization.

Figure 2 shows DSC curves for nanocomposites obtained in various modes of crystallization before exposure to ETP.

1- PP+ ZrO2 nanocomposite obtained by slow cooling mode (SC);

2- PP+ ZrO2 nanocomposite obtained by nitrogen cooling (NC);

3- PP+ ZrO2 nanocomposite obtained by fast cooling (FC).

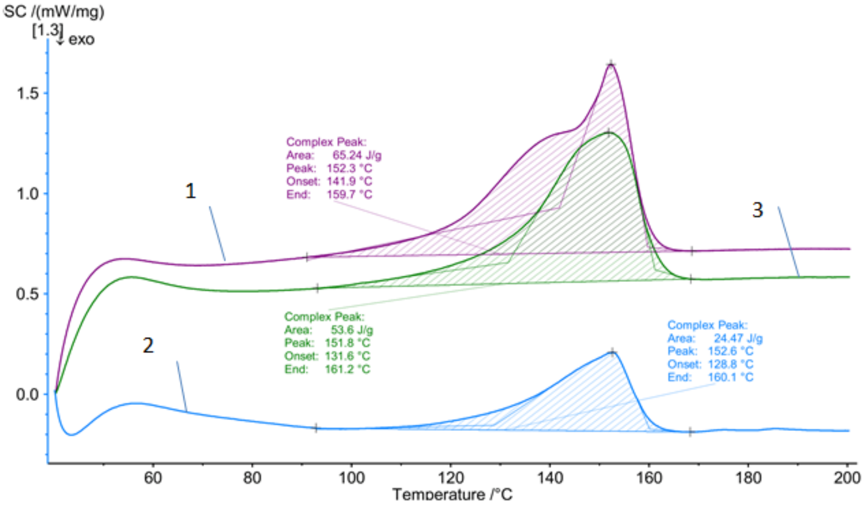

Fig. 2. DSC curves for nanocomposites obtained in various modes of crystallization before exposure to ETP.

PP+ ZrO_2 nanocomposite obtained by nitrogen cooling mode is in a non-equilibrium state and rapidly crystallizes when heated [4]. These samples contain a small region with an ordered structure and possibly defective crystallites. Considering that the thermo-physical properties of nanocomposites depend on their supramolecular structure, the samples obtained by slow cooling mode are least thermo-stable. Supramolecular structure of samples obtained through slow cooling mode consists of coarse-spherulites. In contrast nanocomposites obtained by fast cooling mode consist of small spherulites. This is due to the local destruction of interspherolite areas after ETP. Specimens with a fine-spherulite structure have increased thermos-stability.

Figure 3 shows DSC curves for nanocomposites obtained in various modes of crystallization after exposure to ETP. The curves show one more endomaximum in the temperature range 100-130°C for all modes of crystallization. It is shown that the electric field and temperature have a more significant effect on the thermophysical parameters of both pure polymer and nanocomposite. This fact demonstrates good agreement with Table 1. The influence of ETP is accompanied by a significant change in the thermal effect. A change in the temperature of the endothermic effect and the appearance of a new endothermic peak in the DSC curves of composites indicates the formation of a new crystalline structure. It can be assumed that such a structure occurs at the matrix-filler interface due to the interaction of polymer chains with the surface of the nanoparticles. During heat treatment, micro pores and stressed areas appear in the amorphous phase of the composite.

1- PP+ ZrO_2 nanocomposite obtained by slow cooling mode (SC)

2- PP+ ZrO_2 nanocomposite obtained by nitrogen cooling (NC)

3- PP+ ZrO_2 nanocomposite obtained by fast cooling (FC)

The presence of two melting peaks indicates phase separation of the components. When samples are heated, curing reactions and the formation of a spatial polymer network occur. A polymer web that preserves the microstructure of composite spherulites forms. This change can be due to the stresses that arise in the amorphous disordered regions between adjacent lamellas depending on the crystallization conditions. Crystallization is accompanied by an increase in the density of the nanocomposite. In addition, the already formed crystallites reinforce the composite and prevent its shrinkage. As a result, forces arise that stretch the amorphous, disordered regions of the composite, which leads to the formation of micropores, cracks, and other structural defects. During slow cooling of the samples, the contact between adjacent lamellas is weakened, the most strained molecules have time to relax due to the mobility inside the lamellae. The result indicates the existence of structural elements with different melting points. The samples obtained in the SC mode have a higher degree of strength than the samples obtained in other modes of crystallization. Therefore, their thermal destruction requires comparatively more energy.

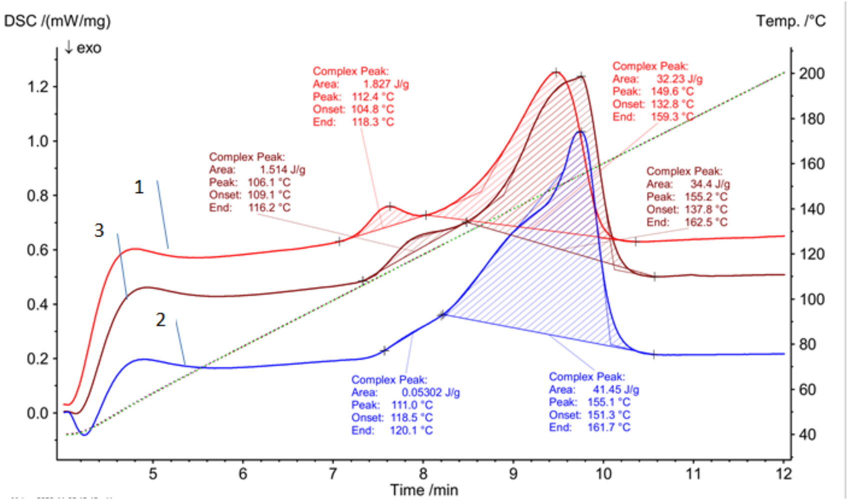

Fig. 3. DSC curves for nanocomposites obtained in various modes of crystallization after exposure to ETP.

Table 1. Thermophysical parameters of PP+ZrO_2 nanocomposites obtained in different mode of crystallization before ETP

Crystallization mode	**Effect start temperature,ºC**		**Peak temperature,ºC**		**Effect end temperature, ºC**		**Entropy, J /K**		**Melting enthalpy, ΔH, J/g**	
	PP	**PP+ZrO_2**	**PP**	**PP+ZrO_2**	**PP**	**PP+ZrO_2**	**PP**	**PP+ZrO_2**	**PP**	**PP+ZrO_2**
Fast cooling mode	129.7	128.8	150.9	152.6	159.5	160.1	0.13	0.05	57.4	24.47
Slow cooling mode	140.1	141.9	151.5	152.3	160	159.7	0.11	0.16	55.95	45.24
Nitrogen cooling mode	130.2	131.6	154.6	151.8	163.6	161.2	0.10	0.12	53.49	4 3.6

Since crystallization is a spontaneous process and is accompanied by a decrease in entropy, the enthalpy of crystallization is always negative. The decrease in enthalpy is a consequence of the denser packing of macromolecules, for which the energy of intermolecular interaction is higher than that before crystallization.

Conclusion

To conclude, the thermophysical properties of pure polypropylene obtained by various modes of crystallization are different from nanocomposites based on this polymer and after ETP. This fact is explained by changes in phase transitions and modification of the supramolecular structure of nanocomposite. The effect of a nanofiller on thermal destruction of nanocomposite is determined by its ability to generate high-modulus interfacial regions. The use of polymers and their nanocomposites for the creation of heat-insulating materials is of great importance in many branches of technology. Considering before mentioned processes, polymer and metal oxide-based nanocomposites can be utilized in the manufacture of electrical insulation systems.

Table 2. Thermophysical parameters of PP+ZrO_2 nanocomposites obtained in different mode of crystallization after ETP

Crystallization mode	**Effect start temperature,ºC**				**Peak temperature, ºC**				**Effect end temperature, ºC**			
	PP		**PP+ ZrO_2**		**PP**		**PP+ ZrO_2**		**PP**		**PP+ ZrO_2**	
	Endomaximums				**Endomaximums**				**Endomaximums**			
	I	**II**	**I**	**II**	**I**	**II**	**I**	**II**	**I**	**II**	**I**	**II**
Fast cooling mode	110	126	105	133	102	136	112	150	105	137	118	159
Slow cooling mode	113	138	118	151	102	137	111	155	125	147	120	161
Nitrogen cooling mode	107	126	109	137	98	123	106	155	111	155	116	162

Crystallization mode	**Entropy, J / K**				**Melting enthalpy, ΔH, J/g**			
	PP		**PP+ ZrO_2**		**PP**		**PP+ ZrO_2**	
	Endomaximums				**Endomaximums**			
	I	**II**	**I**	**II**	**I**	**II**	**I**	**II**
Fast cooling mode	0.02	0.06	0.04	0.07	1.2	24	1.8	32
Slow cooling mode	0.01	0.04	0.02	0.09	0.2	36	0.5	41
Nitrogen cooling mode	0.03	0.06	0.01	0.07	1.1	25	1.5	34

Acknowledgements

This work was supported by the Science Development Foundation under the President of the Republic of Azerbaijan_grants: EİF/MQM/Elm-Təhsil-1-2016-1(26)-71/13/1-M- 38

References

1. Ramazanov M.A., Ibrahimova H.S. Integrated Ferroelectrics 2020, v. 211 (1), p. 102.
2. Gorbunova I. Yu. Plastic mass. 2000, v.), p. 7.
3. Ramazanov M.A., Ibrahimova H.S., Shirinova H.A. J Ferroelectrics 2021, v. 577 (1), p.153.
4. Kurbanova N.I., Guliyev T.M., Ishchenko N. Ya. J. Plastics, 2020, v. 5-6, p. 12.

STUDY OF CHARMED Λ_c^+ BARYON PRODUCTION IN *pp* and *p–Pb* COLLISIONS AT LHC ENERGIES

Z HIFZA and A YASIR

Department of Physics, COMSATS University Islamabad, Park Road, Islamabad 44000, Pakistan
E-mail: yasir_ali@comsats.edu.pk

In this contribution, the production of Λ_c^+ baryon as a function of p_T in proton-proton (pp) collisions at $\sqrt{s} =$ 7 TeV and in proton-lead (p-Pb) collisions at $\sqrt{s_{NN}} =$ 5.02 TeV is studied by using different tunes of Monte-Carlo simulation model PYTHIA 8.303, including Monash tune and color reconnection tunes which implements color reconnection beyond leading color approximations. The simulated data is compared with latest ALICE results on charm baryon production. Color reconnection and multiparton interactions can produce QGP-like effects, such as radial flow-like patterns in these small systems. Therefore, we investigate their effects on different observables like transverse momentum (p_T) distributions, baryon-to-meson ratios (Λ_c^+/D^0) and nuclear modification factor (R_{pPb}).

Keywords: QGP, pp and p-Pb collisions, heavy-ion collisions, PYTHIA 8, Monash, color reconnection, multi-parton interactions.
PACS: 11.30.Fs, 13.20.Fc, 25.75.-q

Introduction

The main goal of high-energy heavy-ion collisions was to understand Quantum Chromo-Dynamics (QCD) under extreme temperature and baryon densities. At ordinary temperatures, the quarks and gluons are confined within hadrons, but at very high temperatures and densities, we have a deconfined phase of quarks and gluons, the Quark Gluon Plasma (QGP). The study of charm production is a powerful tool to investigate the QGP, created under extreme energy densities in heavy-ion collisions [1,2]. Heavy quarks such as charm quarks serve as an excellent probe of QGP since they are produced in pairs at the initial stages of the heavy-ion collisions by partonic hard scattering processes [3]. So they witness the whole evolution of formation of fireball because they are created before the QGP formation, and traverse through the QGP-medium, they interact with its constituents and lose energy. Moreover, the charmed baryon-to-meson ratio (Λ_c^+/D^0) in heavy-ion collisions is sensitive to the charm hadronization mechanisms after the QGP phase. It is proposed that a large number of low and intermediate-momentum charmed hadrons can be produced through recombination (coalescence) of charm quark with other partons from the QGP-medium [4,5]. This leads to the enhancement of the Λ_c^+/D^0 ratio with respect to pp collisions. In addition, the enhancement can be more pronounced by the existence of diquark states in QGP medium and the two-body collision between c quark and [ud] diquark state lead to the formation of Λ_c^+ baryon [6]. The interpretation of the results obtained in heavy-ion collisions requires detailed studies also in smaller systems: pp collisions provide the necessary reference for measurements and allow to test perturbative QCD predictions. Measurements in p-Pb collisions allow us to analyze the cold nuclear matter (CNM) effects due to presence of nucleus in the initial state, which could affect the p_T-distributions at low p_T [3].

Methodology

For simulations, we have used Monte Carlo (MC) event generator PYTHIA 8.303, hereafter referred as PYTHIA 8. PYTHIA 8 program [7], a standalone MC event generator, is a computer simulation program that serves as a standard tool for generating all kinds of collision events and, in particularly the events at RHIC and LHC energies. It contains a variety of physics process including hard and soft interactions, initial- and final-state parton showers, beam remnants, parton distribution, multiparton interactions (MPI), string fragmentation and particle decays. The MultiParton Interactions (MPIs) and Color Reconnection (CR) phenomena play a key role in hadronization. To study their effects, we have used PYTHIA 8 Monash tune [8] and QCD based Color reconnection tunes [9] with three modes (Mode 0,2 and 3) that apply different constraints on the allowed reconnections. Moreover, several measurements in high-multiplicity pp and p-Pb collisions exhibit a similar behavior as that observed in Pb-Pb collisions such as the observation of collective effects in these small systems at LHC [10]. Such a development has important consequences for the analysis of heavy-ion collision data because one should take into account the contribution of the QGP-like effects in pp when comparing with heavy-ion collisions. PYTHIA 8 seem to produce collective-like effects with MPIs and CR mechanism through boosted color strings formed between final partons from independent hard scattering processes [11]. For PYTHIA 8 simulations, both soft and Hard QCD processes have been switched on and comparative analysis has been done. For hard QCD processes, the threshold minimum transverse momentum (pTHaTMin) of 5,10 and 20 GeV/c have been used. The simulated data is compared with ALICE experimental data [12,13].

Results

Figure 1 shows the p_T-differential production cross section of Λ_c^+ baryons in pp collisions at $\sqrt{s} = 7$ TeV at mid-rapidity, obtained using PYTHIA 8 Monash tune and QCD based CR tunes by switching on soft QCD processes on the left panel and hard QCD processes on the right. On the left panel, it is observed that Monash tune under-predicts the data significantly while all three CR modes gives best description of both magnitude and shape of experimental data. On the right panel, it can be seen that the Monash tune under-predicts the data significantly for all three values of pTHatMin. However, the predictions of CR Mode 2 are closer to data for pTHatMin=5 GeV/c. Similar results have been observed in pp collisions at $\sqrt{s} = 5.02$ TeV.

Figure 2 shows the p_T-differential production cross section of Λ_c^+ baryons in p-Pb collisions at $\sqrt{s_{NN}} = 5.02$ TeV in mid-rapidity interval, obtained with PYTHIA 8 Monash tune and CR tunes by switching on Soft QCD processes on the left, and Hard QCD processes on the right. On the left panel, the Monash tune underestimates the data for $p_T < 8$ GeV/c and the predictions becomes consistent with the data for $p_T > 8$ GeV/c. While PYTHIA 8 CR modes describes both the magnitude and shape of the data very well over the entire p_T range. On the right panel, PYTHIA 8 CR Mode 2 with hard QCD processes gives best description of data for pTHatMin=5 GeV/c as compared to other values of pTHatMin, similar to what observed in pp collisions, however the less deviation is observed as compared to pp collisions. All other tunes with pTHatMin=10 & 20 GeV/c under-predicts the data significantly and give harder distributions as compared to pTHatMin=5 GeV/c. This means that the shape of p_T spectra for charmed baryon strongly depends on minimum invariant p_T for hard processes.

The left panel of figure 3 shows the comparison of Λ_c^+/D^0 ratio in pp and p−Pb collisions at $\sqrt{s_{NN}} = 5.02$ TeV as a function of p_T obtained with PYTHIA 8 simulations and measured by ALICE. The ratios measured in both collision systems are consistent with each other, however a larger Λ_c^+/D^0 ratio has been observed in intermediate p_T range of 5 – 8 GeV ⁄ c and a lower value in $1 < p_T < 2$ GeV ⁄ c in p−Pb collisions than in pp collisions. PYTHIA 8 Monash tune fails to explain both the magnitude and p_T trend of Λ_c^+/D^0 ratio, and gives mild p_T dependence.

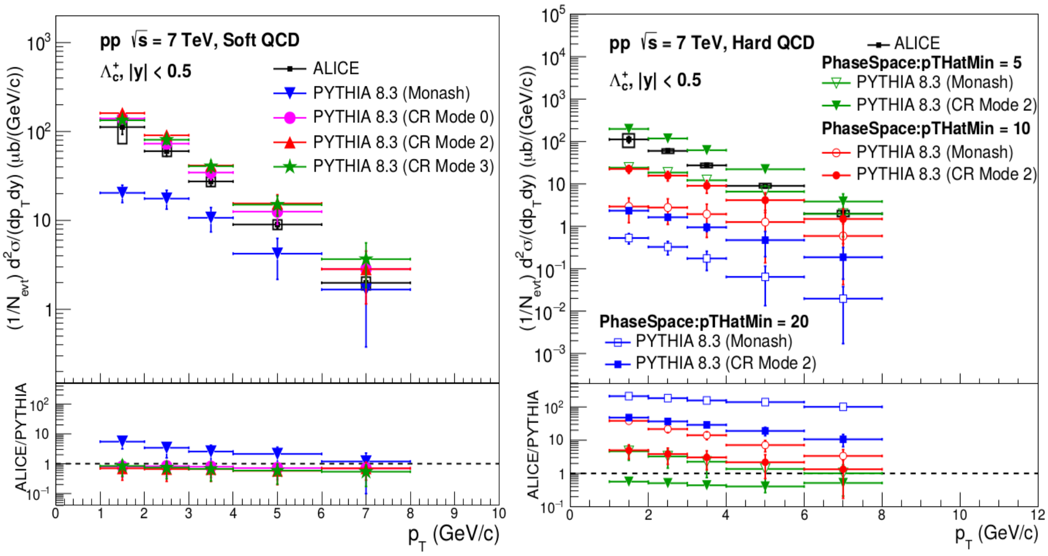

Fig. 1. Transverse momentum distributions of Λ_c^+ baryons in pp collisions at $\sqrt{s} = 7$ TeV, as obtained with PYTHIA 8 Monash tune and CR tunes using SoftQCD processes on the left, and HardQCD processes, on the right.

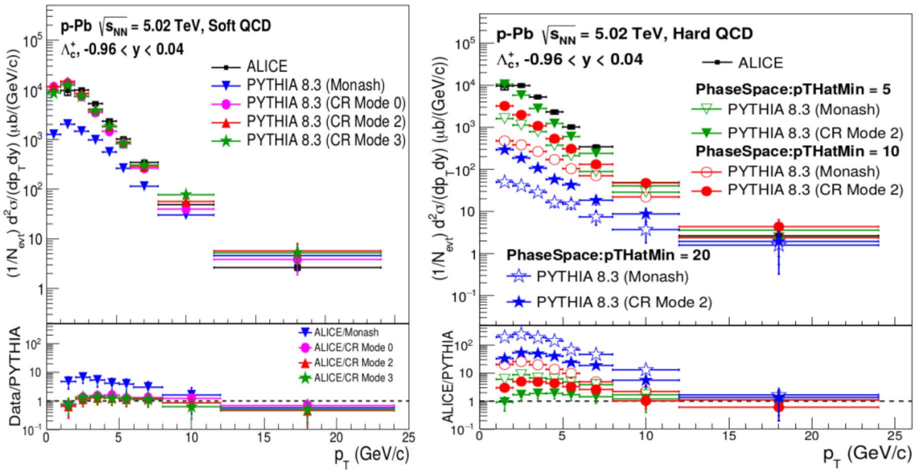

Fig. 2. Transverse momentum distributions of Λ_c^+ baryons in p-Pb collisions at $\sqrt{s_{NN}} = 5.02$ as obtained with PYTHIA 8 Monash tune and CR tunes using Soft QCD processes on the left, and Hard QCD processes, on the right.

However, CR modes which mimics flow like effects, gives enhanced production of Λ_c^+ baryons over D mesons at low p_T, also reproduces the decreasing trend of ratio with increasing p_T. While PYTHIA 8 fails to reproduce the observed peak in p-Pb collisions at intermediate p_T.

The right panel shows the comparison of Λ_c^+/D^0 ratio in pp collisions at $\sqrt{s} = 5.02$ and 7 TeV as obtained with PYTHIA 8 Monash and CR Mode 2 by switching on soft QCD processes. It can be seen that the Λ_c^+/D^0 ratio between two collision energies at mid-rapidity is compatible with each other within uncertainties. However because of wider p_T range in pp collisions at $\sqrt{s} = 5.02$ TeV, a clear decreasing trend with increasing p_T is observed. The Monash tune show energy dependence, giving larger values of Λ_c^+/D^0 ratio in pp collisions at higher energy, while fails to reproduce the observed decreasing trend. PYTHIA 8 CR mode 2 show a slight energy dependence at low p_T ($p_T < 6$ GeV/c), where the predictions are larger at $\sqrt{s} = 7$ TeV with respect to $\sqrt{s} = 5.02$ TeV. Moreover, the Λ_c^+/D^0 ratio is higher at mid-rapidity than at forward rapidity interval at $\sqrt{s} = 7$ TeV. This shows that charm baryons production is enhanced in central rapidity region.

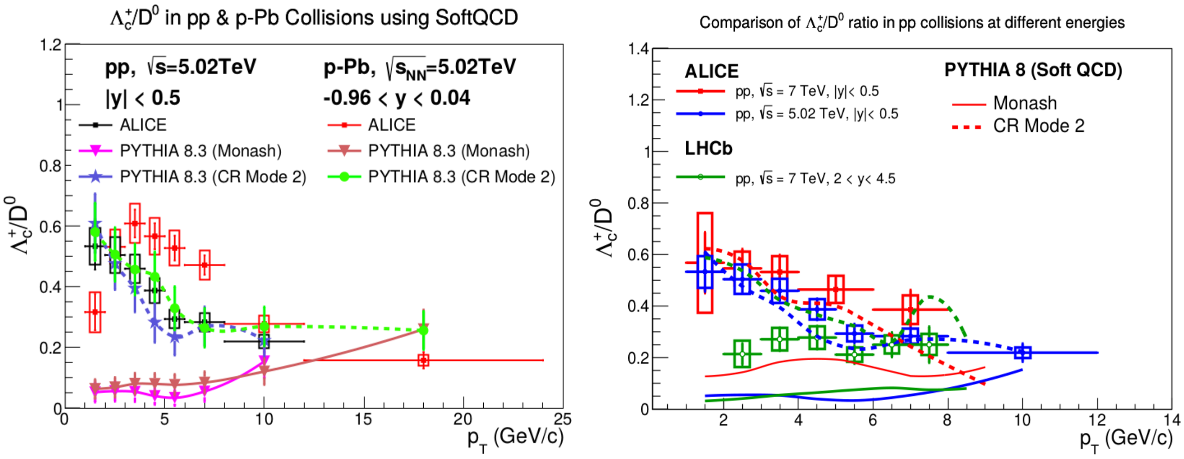

Fig. 3. Λ_c^+/D^0 ratio as a function of p_T in pp and in p–Pb collisions at $\sqrt{s_{NN}} = 5.02$ TeV obtained from PYTHIA 8 simulations using soft QCD processes. On the right, comparison of Λ_c^+/D^0 ratio as a function of p_T in pp collisions at $\sqrt{s} = 7$ TeV and $\sqrt{s} = 5.02$ TeV.

Figure 4 shows the Λ_c^+/D^0 ratio as a function of p_T in pp collisions on the left and in p–Pb collisions on the right at $\sqrt{s_{NN}} = 5.02$ TeV obtained from PYTHIA 8 simulations using hard QCD processes with pTHatMin of 5 and 10 GeV/c. On the left panel, it is observed that Monash tune fails to explain the data, similar to what observed with soft QCD processes. However, the CR Mode 2 for both pTHatMin values gives best description of data and able to reproduce the observed decreasing trend. On the right panel, Monash tune again gives poor description of data while CR Mode 2 gives higher predictions closer to data. However, CR Mode 2 with both pTHatMin of 5 and 10 GeV/c fails to reproduce the peak structure at intermediate p_T, thereby underestimating the data significantly for $2 < p_T < 8$ GeV/c.

We note that the PYTHIA 8 Monash tune is not able to give good description of Λ_c^+/D^0 ratio as a function of p_T for $p_T < 7$ GeV ⁄ c and deviation from the measured data is quite larger. It may be due to the fact that Monash tune implements fragmentation fractions for charm quark from e^-e^+ collisions data. However, the fragmentation parameters for charm quark are not universal among different collision systems. That is why, the predictions of Monash tune deviates significantly from the data. However, the predictions from PYTHIA 8 CR modes (Mode 0,2 and 3) which includes junctions as an additional baryon source, show greater compatibility with measured p_T trend.

Figure 5 shows the nuclear modification factor (R_{pPb}) as a function of p_T in p–Pb collisions at $\sqrt{s_{NN}} = 5.02$ TeV at mid-rapidity in the p_T interval of $1 < p_T < 12$ GeV/c, obtained from PYTHIA 8 Monash tune and CR tunes (Mode 0, 2 and 3) by switching on soft QCD processes. All tunes of PYTHIA 8 give approximately the same predictions for the behavior of R_{pPb} and gives the value about ~0.4–0.6 over entire p_T range. Both the Monash and CR tunes fail to reproduce the peak at intermediate p_T ($4 < p_T < 8$ GeV/c) observed in the ALICE data, that may arise due to cronin effect. So we can conclude that neither of tunes can quantitatively reproduce the magnitude and shape of Λ_c^+ baryon R_{pPb}.

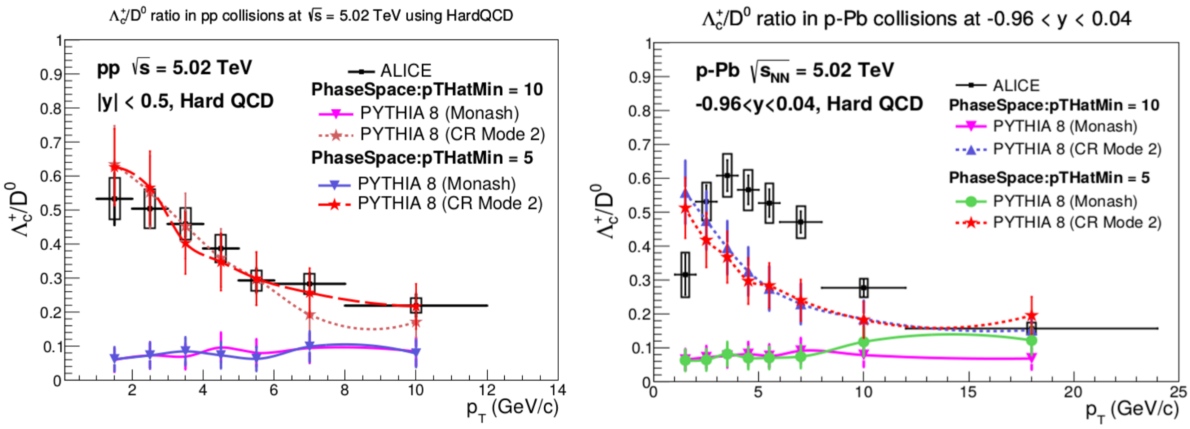

Fig. 4. Λ_c^+/D^0 ratio as a function of p_T in pp collisions on the left and in p–Pb collisions on the right at $\sqrt{s_{NN}} = 5.02$ TeV obtained from PYTHIA 8 simulations using hard QCD processes.

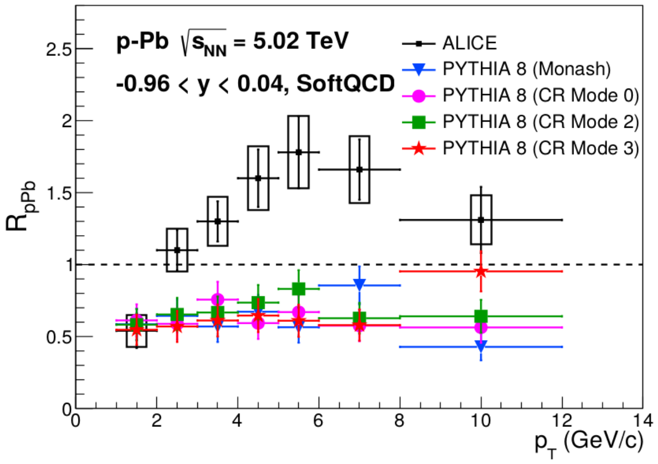

Fig. 5. Nuclear modification factor R_{pPb} of Λ_c^+ baryon in p–Pb collisions at $\sqrt{s_{NN}} = 5.02$ TeV as a function of transverse momentum compared to different tunes of PYTHIA 8 predictions.

Conclusion

Overall, we observed that the PYTHIA 8 Monash tune underestimates the Λ_c^+ production cross section significantly in both collision systems for both soft and hard QCD processes. While PYTHIA 8 CR modes, which mimics flow-like effects, give good explanation of both the Λ_c^+ production cross section and the behavior Λ_c^+/D^0 ratio as a function of p_T in most of the p_T intervals. PYTHIA 8 SoftQCD machinery is more reliable to handle charm production at low

p_T scales (up to 15 GeV/c), although not perfect. Because SoftQCD does a smooth dampening at the otherwise singular $p_T = 0$ limit, and therefore is better suited to handle charm production at low p_T scales while the hard QCD is ill-defined in the p_T →0 limit.

References

1. Bhalerao R.S. et al., Physics at the Large Hadron Collider 2009, p. 105.
2. Braun-Munzinger P. et al., Phys. Rept 2016, v. 621, p.76, arXiv:1510.00442.
3. Zhao J. et al., Progress in Particle and Nuclear Physics 2020, v. 114, p. 103801.
4. Oh Y. et al., Phys. Rev. C 2009, v. 79, p. 044905, arXiv:0901.1382.
5. Greco V.et al., Phys. Lett. B 2004, v. 595 (1-4), p. 202.
6. Lee S.H.et al., Phys. Rev. Lett. 2008, v. 100, p. 222301, arXiv:0709.3637.
7. Sjöstrand T. et al., Comp. Phys. Comm. 2015, v. 191, p. 159.
8. Skands P. et al., Eur. Phys. J. 2014, v. 74 (8), p. 1.
9. Christiansen J.R., Skands P.Z., J. High Energ. Phys. 2015, v. 8, p. 1.
10. Adam J., et al., (ALICE collaboration.), 2016, arXiv:1601.03658.
11. Ortiz Velasquez A et al., Phys. Rev. Lett. 2013, v. 111 (4), p. 042001.
12. Chang B. et al. (ALICE Collaboration), J. High Energ. Phys., 2018, v. 4.
13. Acharya S. et al. (ALICE Collaboration), Phys. Rev. Lett. 2021, v. 127 (20), p. 202301.

INTERACTION NANOPARTICLES WITH PLANTS TOWARDS TO THE INCREASE THE TOLERANCE TO SALINITY AND DROUGHT

IS AHMADOV, FV HASANOVA and ST BABANLI

Baku State University, Baku, Azerbaijan
E-mail: ismetahmadov@mail.ru, faride.hasanli90@gmail,com, babanli-analitik@gmail.com

The application of nanotechnology for an intensive and sustainable agricultural strategy is already underway, which makes the use of nanoparticles important in this strategy. The use of nanoparticles requires clarification of the nature of their interaction with plants. In recent years, the accumulation of nanoparticles in plants, migration from the soil to its organs, the effect on important morphophysiological parameters, photosynthetic activity, biochemical and mineral nutrition processes have been well studied. Significant progress has also been made in the study of salinity and drought, the main abiotic stressors that seriously affect plant growth and productivity. The main task is to increase the plant's tolerance to these factors. The use of nanoparticles holds important promise in increasing plant resistance to salt and drought. Thus, from nanoparticles based on metals, CuO increases the amount of antisan, proline in plants [1], which leads to an increase in drought resistance. ZnO nanoparticles affect the root system of plants, reducing their need for water [2]. Quenching of reactive oxygen species (ROS) is a universal mechanism for increasing plant resistance to abiotic stressors. It is known that stressors cause an increase in ROS in plants, while the activity of catalase and other enzymes rapidly increases. The role of nanoparticles in the regulation of this process is widely studied in the presented article. It was found that nanoparticles of Al, Fe, Zn, Cu, along with morphophysiological changes in plants, increase resistance to salt and drought by changing the activity of enzymes.

Keywords: nanoparticles, plants, stress, plant tolerant
PACS: 87.15.Kg, 87.16.Gj, 87.50.yg

Introduction

At present, there is a great deal of research and extensive scientific information on the interaction of nanoparticles with plants, their movement in plant organs, their entry into cells, the physiological and biochemical effects they create, and the mechanisms that regulate these processes. However, there are still many unresolved issues and questions that require new, more in-depth and molecular research. At the initial stage of application of nanotechnology in plant physiology and agriculture, the main purpose of research was the outline the toxic effects of nanoparticles (NPs) and nanomaterials (NMs) on plants. The key issue in clarifying the effects of NPs on plants is how they enter plant cells, organs, and tissues. Until the answer to this question is found, we will not be able to clarify the exact mechanism of interaction of NPs with plants. The initial interaction of NPs with plants, apparently, occurs through their adsorption on the tissue surface and, consequently, on the cell surface, the appearance of attraction and complementation between charged groups of corona proteins and peripheral and integral proteins that protrude from the electric double layer (EDL) as a dynamic structure on the surface of a charged cell wall or membrane of a living cell.

When nanoparticles (NPs) get into plant systems, for example, into a leaves, their interaction with cuticle, cell wall and cell membrane occurs. Before interaction nanoparticles settle on the surface of epidermal cells, forming individual particles or aggregates [3,4,5]. The first contact or interaction of nanoparticles with plants can occur through their electrostatic adsorption, mechanical adhesion, or hydrophobicity [6]. Nanoparticles that settle on the surface of the plant cell initially accumulate in the space of the apoplast between the cell wall and the plasma membrane and can even move. Their movement occurs under the action of capillary forces or under osmotic pressure [7]. Through the apoplast, nanoparticles can bypass the epidermal and cortical cells at the root and reach the endoderm layer. However, they accumulate in the endoderm layer and cannot pass through the caspar belt [8]. Depending on the size, shape, and surface loads of nanoparticles that move in the apoplast and accumulate in the endoderm layer, they can be exposed to different influences or interact with the plasma membrane of the cell, causing various structural and functional changes in the membrane.

The interaction of nanoparticles with the cell wall and the plasma membrane on the cell surface occurs through van der Waals and electrostatic forces, hydrogen bonds and chemical reactions. Interaction mechanism of NPs with plants could be chemical or physical nature. During chemical interactions are form the reactive oxygen species, disturbance of membrane ion transport intensity [9], oxidative damage [10], and lipid peroxidation [11]. After uptake entry into the plant cells, NPs occurs mixing metal ions and react with sulfhydryl, carboxyl groups and ultimately alter the protein activity. In the progress of understanding the interaction of NP with plants, there are still some aspects that require extensive experimentation. These include the role of the cell wall, the apoplastic and symplastic pathways in the movement of NP through plant organs, and the role of plasmodesmata in the putative pathway of NP passage through the symplastic pathway. There are questions that require experimentation at the cellular level. It is necessary to clarify the following questions: a) what is the mechanism of movement and propagation of NPs through the cell walls? b) what is the mechanism of interaction of NPs with the chemical composition of the cell wall? (c) what is the mechanism of NP movement through the apoplastic space? Do plasmodesmata participate in NP translocation in the plant organism, and if so, what is the mechanism of this process?

Experiment

Interaction of nanoparticles with plant seeds. The interactions of nanoparticles with plant seeds have not been studied well yet. There are evidences that nanoparticles are adsorbed on the surface of seeds and can diffuse into them [13]. The study of Khodakovskaya et al. shown, that multi wall carbon nanotubes can penetrate tomato seed and increase the germination rate by rising water uptake [14]. İmpact of nanoparticles on the seed germination it is a critical stage the uptake of them into the seed. The seed germination is a important stage of plant development and growing. The question of whether nanoparticles diffuse into plant seeds is interesting because of their effect on germination. Experiments show that nanoparticles may enter into the seed. İn our experiments by ESR method we obtained that iron nanoparticles - SPIONs (gamma-Fe_2O_3) may enter through the coat into endosperm of been. For nanoparticles, a stock solution of 1 µg/ml particle in culture medium without any additive was prepared, vortex at maximum speed for 1 minute and bath-sonicated for 10 minutes. In experiments we tried to find out the uptake and internalization of nanoparticles into the seeds. For this purpose we used ESR method. Iron nanoparticles SPIONs (gamma-Fe_2O_3) have a strong ESR signal. In figure 1 was given the ESR signal of the diluted original SPİONs 10 times in distilled water.

The characteristics of ESR signal of diluted ferrofluid SPIONs remained as was original ferrofluid. This case allow us to conduct out of experiments with diluted solutions.

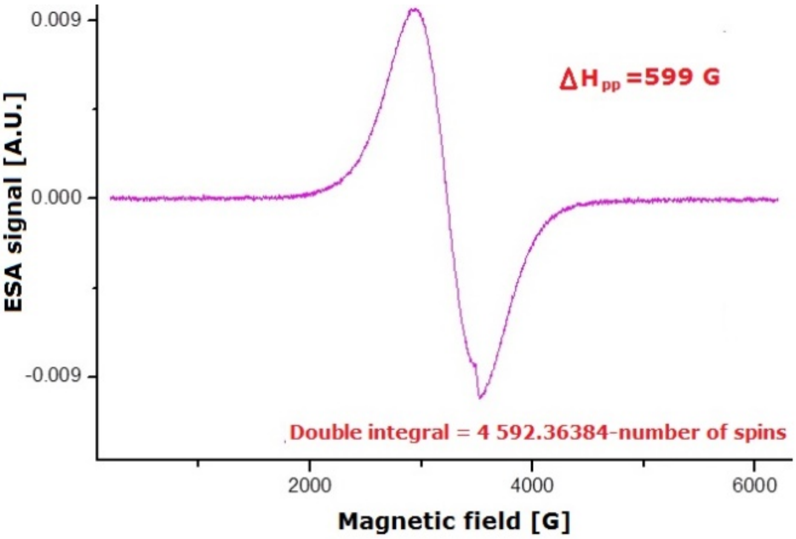

Fig. 1. The ESR signal of diluted solutions of ferro fluid SPIONs.

The seeds of bean were exposed in the solutions of SPIONs for the 24 hours. After exposure in SPİONs seeds have been washed carefully and the coat of seeds was peeled then was separated endosperm. ESR signal checked up in different part of endosperm of seeds. The bean seed has just one outer coat. We have tested ESR signal for endosperm of been, for thin coat. In figure 2 have been shown these ESR signals. As we can see the ESR signal for the outer endosperm of bean seed is 2.4 times larger than for the inner endosperm.

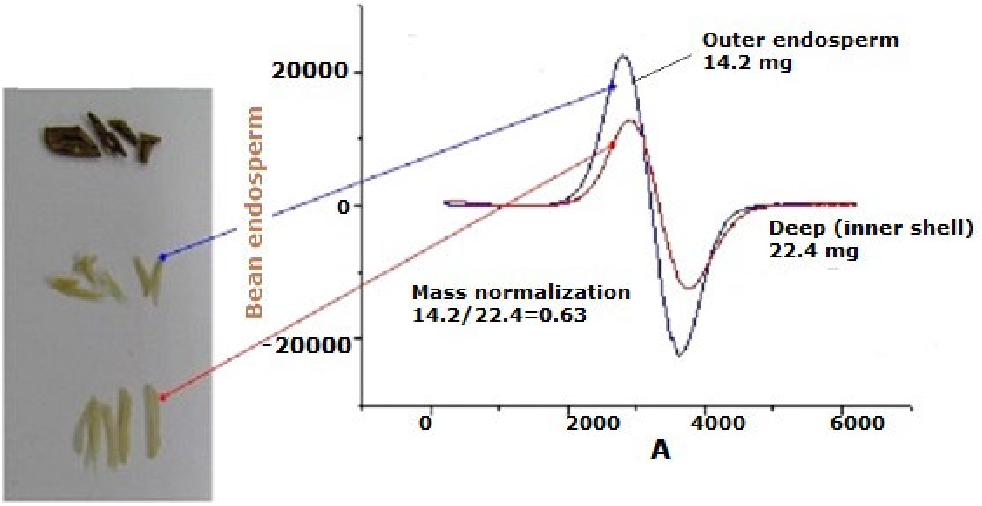

Fig. 2. The ESR signal of SPIONs for been endosperm

Figure 3 shows TEM images of pea seeds impregnated with Ag nanoparticles. For this purpose, incisions were made in the shell, endosperm and embryo of the pea seed and imaged under a TEM microscope. As can be seen in the figure 3, mitochondria, vacuoles and other organelles are clearly visible in pea seeds. The distribution of silver nanoparticles in plant cells, first in the cell wall and the formation of clusters, is clear from their TEM images. The size of these clusters is in the range of 50–400 nm. After a while, nanoparticles are observed to accumulate on the surface of the plasma membrane. Ag nanoparticles accumulated on the surface of the plasma membrane are absorbed into the cytoplasm of the cell over time. It is likely that very small nanoparticles cross the membrane directly, while larger ones enter the cytoplasm through endocytosis. In the cytoplasm, nanoparticles re-form clusters.

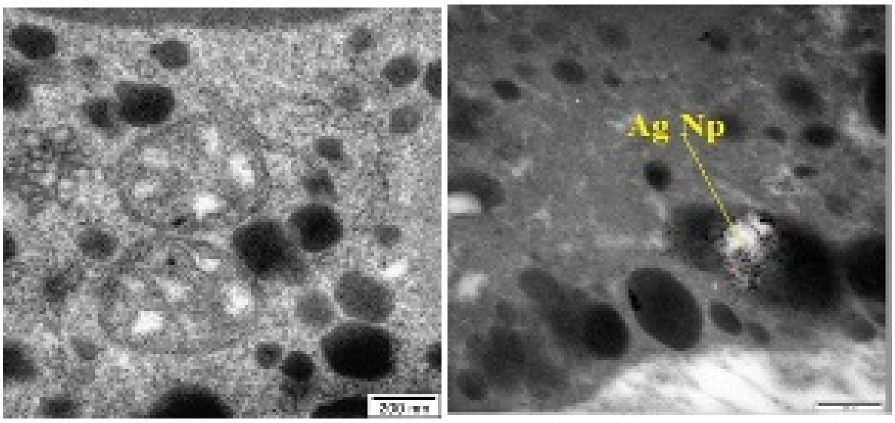

Fig. 3. TEM images of pea seeds impregnated with Ag nanoparticles.

Interaction of nanoparticles with plant roots. NPs are adsorbed from the soil on the surface of plant roots and can be absorbed into cells over time. There are two main ways for NPs uptake by plant roots, the apoplastic and the symplastic route. In plant cell walls are pores between 5 and 20 nm. Nanoparticles that cross porous cell walls can diffuse between cell walls and plasma membrane and be subjected to osmotic pressure and capillary forces Nanoparticles diffusing through the apoplast can reach endodermis.

The symplastic pathway of nanoparticle entrance is through the inner side of the plasma membrane, which is more important than the apoplastic route. Nanoparticles can enter cells by binding to carrier proteins, through aquaporins which are membrane proteins that operate as water channels, ion channels, and endocytosis, or by piercing the cell membrane and creating new pores Endocytic uptake is a pathway of nanoparticle uptake by cells if specific receptor–ligand interactions are taking place. Depending on their morphology, some nanoparticles like carbon nanotubes may pierce their way into the cells and enter cytoplasm.

The mechanism of interaction of CuO, TiO_3, Fe_2O_3 and ZnO nanoparticles with root cells of aquatic plant Trianea bogotensis was studied in this study. For this purpose, the roots of the Trianea plant were stored in a suspension solution of nanoparticles taken and their accumulation on the surface of the roots, physiological changes in the stem cells were observed. The effect of nanoparticles was studied depending on their concentration and exposure time. Observations by light microscopy showed that nanoparticles accumulate on the surface of root cells to form agglomerate structures. In this case, depending on the duration of exposure, the movement of protoplasm in the cells stops, turgor is lost, during prolonged exposure, the roots are separated from the trunk and lose their function. After washing the nanoparticles, the movement of protoplasm in the cells is not restored. This indicates the possibility of nanoparticles entering the cell.

When nanoparticles interact with plant roots, we found that some nanoparticles are adsorbed to the tips of root hairs. As you know, root hairs grow intensively through the tips and in this area protein synthesis is very intensive. The proteins are negatively charged and it can be expected that the positively charged nanoparticles will adsorb to the tip of the root hairs. So we found that nanoparticles that are charged are positively adsorbed at the tip of the root hairs. On the other hand, Zhu et al. (2012) found that roots of radish and ryegrass accumulate more gold nanoparticles than rice and pumpkin, and that positively charged gold nanoparticles are absorbed by the roots faster than negatively charged ones, while the latter moved more efficiently to aerial parts. This phenomenon was explained by the presence of a negative charge in the walls of plant cells, which promotes the accumulation of positively charged nanoparticles in tissues and prevents them from moving through the plant. This suggests that the surface charge of the nanoparticle plays an important role in the interaction of the nanoparticle with the plant cell.

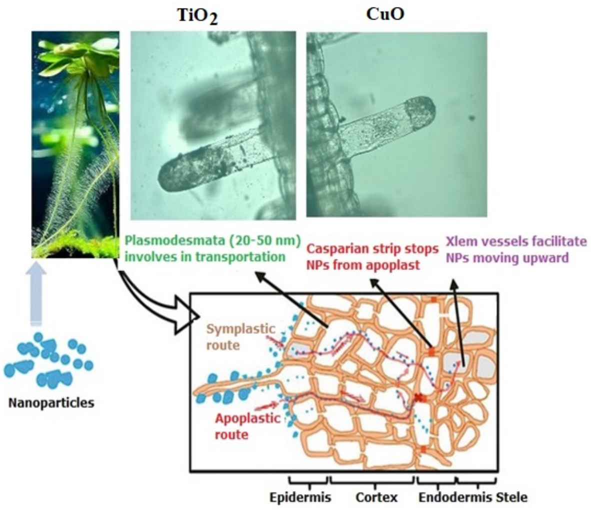

Fig. 4. The adsorption and translocation route nanoparticles root of plants

Interaction of nanoparticles with plant leaves. Nanoparticles are able to penetrate leaf surfaces through stomatal pores and during adsorption on the surface through the cuticula, cell wal. For example, Cucumber (*Cucumis sativus*) can uptake CeO2 nanoparticles through the leaves. Plants that were found to uptake nanoparticles through leaves are *Vicia faba, Zea mays, Arabidopsis thaliana*, wheat, *Lactuca, Cucumis sativus*, and rapeseed. Among the studied nanoparticles that penetrate the leaf pores are polystyrene, CeO2, TiO2, Fe2O3, MgO, ZnO, Zn, Mn, and Ag [15]. Their size ranged from a few nanometers to several hundred nanometers. In summary, evidence indicates that several types of nanoparticles penetrate plant leaves and are internalized. The concentration of nanoparticle accumulated in leaf is larger than that in stems. So nanoparticles can translocate to various plant tissues, including stems, leaves, petioles, flowers, and fruits. It is important to note that nanoparticle bioaccumulation in plants is species specific. For example, Au nanoparticles bioaccumulate in tobacco but not in wheat [16]. Nanoparticle physical properties that are important in plant uptake are size, composition, crystalline state, surface charge, surface functionalization, magnetic properties, hydrophobicity, and/or hydrophilicity. The translocation time of nanoparticles within plants can be very short. For example, carbon-coated magnetic nanoparticle translocates from roots to shoots in less than 24 h after exposure of sunflower, tomato, pea, and wheat [17].

Nanoparticles against stressors. It should be noted that the nature of the response of plants to various stressors at the cellular level is not fully understood. Based on the results of scientific experiments, it can be said that cell membranes play an important role in the response to stressors. For example, plants that are resistant to stressors have a higher stability of cell membranes than those that are not. One of the main responses that occurs in plants during abiotic stress is the formation of active forms of oxygen (ROS) and their intensive accumulation. This leads to a decrease in many physiological processes in plants, such as photosynthesis. Therefore, it is proposed to use nanoparticles to prevent the formation of active forms of oxygen during stress. It has been found that spherically shaped (11 nm) serum oxide nanoparticles quench the active forms of oxygen formed inside the chloroplasts during intense light, high temperature, and cooling in the dark, thus ensuring the normal course of photosynthesis [18].

It is known that salinity has a serious effect on plant development, high salinity stress slows down the growth of plants (root, seedling size, biomass decreases), the amount of photosynthetic pigments (chlorophyll, carotenoids) decreases, the activity of catalase enzymes decreases. It was found that when plants are treated (covered) with ZnO nanoparticles, the growth of plants exposed to salt stress is normal, the amount of photosynthetic pigments increases, the amount of enzymes and soluble organic compounds remains normal. ZnO nanoparticles are an effective strategy to increase salt resistance in plants [19]. In our experiments, Al nanoparticles have been shown to play an important role in increasing salt resistance in plants.

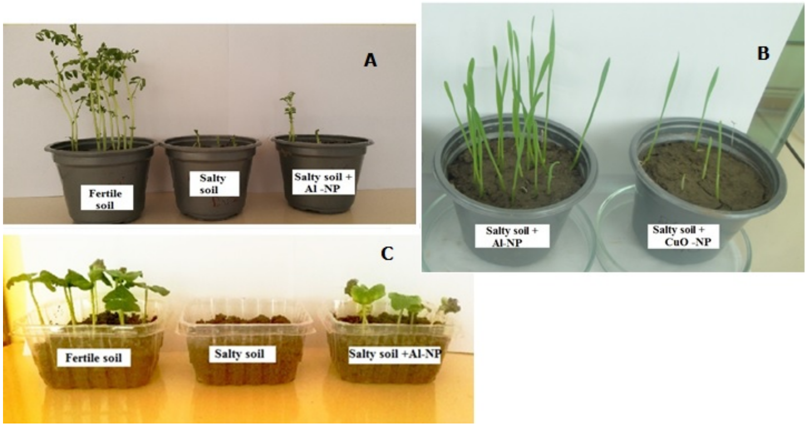

Fig. 5. The effect of Al and CuO nanoparticles on the growth and development of peas (A), wheat (B) and cotton (C) seedlings

Conclusion

Recent research shows that the interaction of nanoparticles with plants can have negative, insignificant and positive effects, depending on the type of nanoparticles.

These effects on plants can take the form of morphological, functional and structural changes. In addition to morphological changes in the root system and leaves of plants, nanoparticles can cause mineral nutrition, photosynthesis and biochemical changes. It has a significant effect on the cooling ability of seeds and germination. Some studies even provide information about genetic changes that occur as a result of plant-nanoparticle interactions. The bioaccumulation of nanoparticles in plants is specific to their type and depends on the physicochemical properties of the nanoparticles. Although the beneficial effects of nanoparticles on some plant species have been reported in experiments, the overall negative effects of the accumulation of these nanoparticles in soil and plants may outweigh the temporary and less beneficial effects. The main adverse effects identified to date are a decrease in seed germination rate, growth retardation, increased ROS, oxidative stress, and genetic changes.

Most nanoparticles can migrate and accumulate in plant organs and enter the food chain, move at trophic levels, become accessible for transfer, and are present in human and animal foods. Many nanoparticles have already been shown to be toxic to humans, and the ingestion of nanoparticles in plants poses major safety concerns. If these safety issues are not addressed properly now, nanomaterials can pollute the environment, causing irreversible or undesirable changes with potentially harmful consequences for both plants, animals and humans.

References

1. Liang X., Zhang L., Natarajan SK, et al. Antioxid Redox Signal 2013, v.19 (9), p. 998.
2. Prakash M.G., Chung I.M. Acta Biol Hung 2016, v. 67 (3), p. 286.
3. Lin D.H., Xing, B.S. Environmental Science & Technology 2008, v. 42 (15), p. 5580.
4. Wild E., Jones K.C. Environmental Science & Technology 2009, v. 43 (14), p. 5290.
5. Zhao L.J., Peralta-Videa J.R., Ren M.H., et al. Chemical Engineering Journal 2012, v. 184, p. 1.
6. Zhang Z.Y., He X., Zhang H.F., et al. Metallomics 2011, v. 3 (8), p. 816.
7. Lin S.J., Reppert J., Hu Q., et al. Small 2009, v. 5 (10), p. 1128.
8. Larue C., Laurette J., Herlin-Boime N., et al. Science of The Total Environment 2012, v. 431, p. 197.
9. Auffan M., Achouak W., Rose J., Roncato M.A., Chanéac C., Waite D.T., Masion A., Woicik J.C., Wiesner M.R., Bottero J.Y., Environmental Science & Technology 2008, v. 42, p. 6730.
10. Foley S., Crowley C., Smaihi M., Bonfils C., Erlanger B.F., Seta P., Larroque C. Biochem. Biophys. Res. Commun. 2002, v. 294, p. 116.
11. Kamat J.P., Devasagayam T.P., Priyadarsini K.I., Mohan H. Toxicology 2000, v. 155, p. 55.
12. Petersen E.J., Henry T.B., Zhao J., MacCuspie R.I., Kirschling T.L., Dobrovolskaia M.A., Hackley V., Xing B., White J.C. Environmental Science & Technology 2014, v. 48, p. 4226.
13. Ahmadov I.S., Ramazanov M.A., Sienkiewicz A., Forro L. Digest Journal of Nanomaterials and Biostructures, 2014, v. 9 (3), p. 1149.
14. Khodakovskaya M., Dervishi E., Mahmood M., Xu Y., Li Z. ACS Nano 2009, v. 3, p. 3221.
15. Chichiriccò G., Poma A. Nanomaterials 2015, v. 5 (2), p. 851. DOI:10.3390/nano5020851.
16. Judy J.D., Unrine J.M., Rao W., Wirick S., Bertsch P.M. Environmental Science & Technology 2012, v. 46 (15), p. 8467. DOI:10.1021/es3019397.
17. Cifuentes Z., Custardoy L., de la Fuente J.M., Marquina C., Ibarra M.R., Rubiales D., Pérez-de-Luque, A. Journal of Nanobiotechnology 2010, v. 8 (1), p. 26. DOI:10.1186/1477-3155-8-26
18. Wu H., Tito N., Giraldo J.P. ACS Nano, 2017, v. 11 (11), p. 11283. DOI:10.1021/acsnano.7b05723
19. Abdel Latef, AAH, Abu Alhmad, MF, Abdelfattah KE, Journal of Plant Growth Regulation 2017, v. 36, p. 60. https://doi.org/10.1007/s00344-016-9618-x

DYNAMICS OF AC SQUID ON JOSEPHSON JUNCTION WITH ANHARMONIC CURRENT-PHASE RELATION

IN ASKERZADE

Department of Computer Engineering and Center of Excellence of Superconductivity Research, Ankara University, Ankara, 06100, Turkey
Institute of Physics ANAS, 33, H.Cavid 33. Baku, AZ1143, Azerbaijan
E-mail: imasker@eng.ankara.edu.tr

The effective critical current of ac SQUID on Josephson junction with anharmonic current-phase relation is calculated. The influence of anharmonicity parameter of Josephson junction and geometrical inductance of ac SQUID on switching dynamics is analyzed.

Keywords: Josephson junction, current-phase relation, ac SQUID
PACS: 74.50.r, 85.25.Cp, 74.20.Rp

It is well known that ac SQUID consists of one Josephson junction, including to superconducting loop (Fig. 1a). Suppose that a magnetic flux Φ_e passes through the interior of the superconducting ring with inductance L. The flux on the superconducting ring is not equal to external magnetic flux Φ_e [1, 2]

$$\Phi = \Phi_e - LI \ . \tag{1}$$

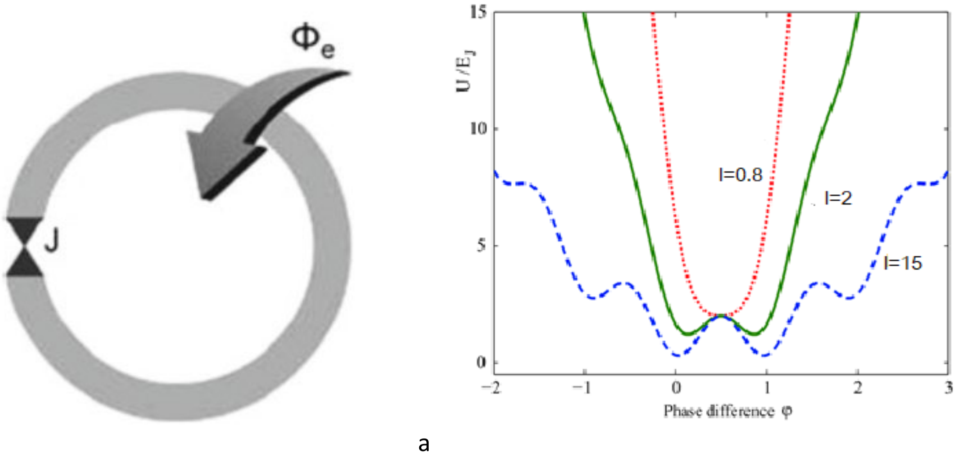

Fig. 1. Schematic presentation of ac SQUID (a) and Profile of potential energy of ac SQUID (b)

Their difference is due to the screening current circulating in the superconducting ring. Such rings with Josephson junction deserve as sensitive elements in magnetometers [1,2]. Detailed description of ac SQUID on junction with sinusoidal current-phase relation

$$I = I_c \sin\phi \tag{2a}$$

were presented in Refs. 1. Last year ac SQUID was used as flux superconducting qubits for quantum computation [3, 4]. Profile of potential energy in ac SQUID [1, 2]

$$U = E_J \left\{ 1 - \cos\phi + \frac{(\phi - \phi_e)^2}{2l} \right\}, \ E_J = \frac{\hbar I_c}{2e}, \tag{3}$$

presented in Fig. 1b. In last Eq. $\phi_e = 2\pi \frac{\Phi_e}{\Phi_0}$ is the normalized external magnetic flux, $l = 2\pi \frac{LI_c}{\Phi_0}$

the normalized geometrical inductance of superconducting ring.

The relationship (2a) is fulfilled with high accuracy for Josephson junctions on low-temperature superconductors [5]. In the case of high-temperature superconductors, the current-phase relation becomes anharmonic [6]

$$I = I_{c0} f_\alpha(\phi) = I_{c0}(\sin\phi + \alpha\sin 2\phi)\,, \tag{2b}$$

where anharmonicity parameter α depends on the junction preparation technology [3,7]. Dynamical properties of Josephson junctions with an anharmonic current-phase relation (2b) were previously studied in [8–11].

As shown in Ref. 12-13, the effective critical current $I_{ceff} = \max(I_{c0} f_\alpha(\phi))$ of a single junction with anharmonic current-phase relation small α can be presented as

$$I = I_{c0}(\phi) = I_{c0}(1 + 2\alpha^2)\,. \tag{4}$$

It is clear that in SQUIDs on junctions with anharmonic current-phase relation, loop inductance introduce additional anharmonism to current-phase relation [14,15]. In this short paper, we present the influence of anharmonism of current-phase relation on effective critical current and dynamics of ac SQUID.

It is well known that the dynamics of ac SQUID on a junction of harmonic current-phase relation (2a) can be written as [1,2]

$$\beta\ddot{\phi} + \dot{\phi} + \sin\phi + \frac{\phi}{l} = \frac{\phi_e}{l}\,. \tag{5}$$

In the case of anharmonic current-phase relation (Eq. (2b)) we can get similar Eq.

$$\beta\ddot{\phi} + \dot{\phi} + \sin\phi + \alpha\sin 2\phi + \frac{\phi}{l} = \frac{\phi_e}{l}\,. \tag{6}$$

Similarly to [12] calculations show that effective critical current reach at the

$$\cos\phi_c = 2\alpha - \frac{1}{l} \tag{7}$$

The final result for normalized effective critical current in superconducting loop is

$$i_{ceff} = \frac{I_{ceff}}{I_{c0}} = \left\{(1 + 2\alpha^2) + \frac{\pi}{2l} - \frac{2\alpha}{l}\right\} \tag{8}$$

The influence of anharmonicity parameter α for different geometrical inductance l in ac SQUID on effective critical current is presented in Fig. 2. As followed from Eq. (8) and Fig. (2), in the limit of very high inductance $l \to \infty$ our results coincide with the case of a single junction [12,13]. Generally, taking into account anharmonicity α and geometrical inductance l leads to increasing of effective critical current of a junction.

Calculation of switching time τ_s using Eq. (6) between neighboring states (in this states difference between numbers flux quantum is equal 1) in the case of overdamped Josephson junction ($\beta << 1$) similarly to Ref. [1] leads to expression

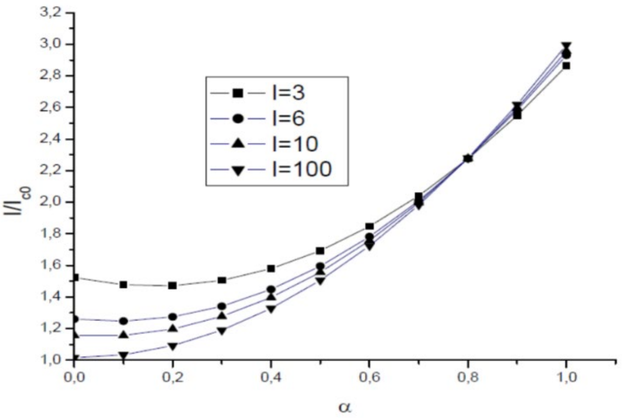

Fig. 2. Effective critical current Josephson junction in ac SQUID

$$\tau_s = \frac{l}{i_{ceff}(\alpha)} \tag{9}$$

Changing of switching time τ_s for different values of anharmonicity α of a junction and geometrical inductance of ac SQIUD l shown in Fig. 3a. It is clear a small effects of anharmonicity parameter α on switching time τ_s for ac SQUIDs with small geometrical inductance of superconducting ring.

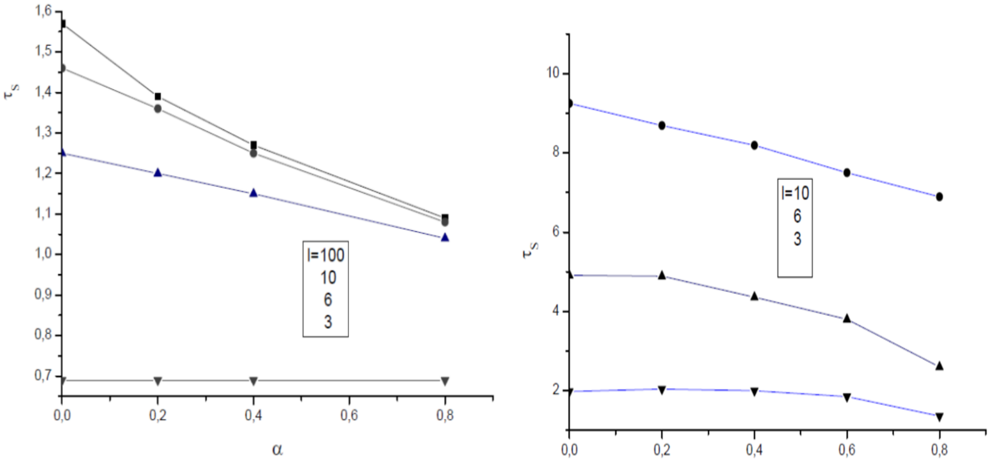

Fig. 3a. Switching time τ_s for the case a) $\beta << 1$ b) $\beta < 1$

Calculation of switching time τ_s between neighboring states in the case of Josephson junctions with $\beta < 1$ similarly to above calculations given by the expression

$$\tau_s = \frac{\pi}{2i_{ceff}(\alpha)}\,. \tag{10}$$

Changing of switching time τ_s for different values of anharmonicity parameter α of junction and geometrical inductance of ac SQUID l presented in Fig. 3.b. As you can see a small effects of anharmonicity parameter α for ac SQUIDs with small geometrical inductance of superconducting ring as in the limit $\beta < 1$. In high geometrical inductance increasing of anharmonicity parameter α leads to decreasing of switching time τ_s in superconducting rings.

Thus, in this study, it was calculated the effective critical current in ac SQUID with Josephson junction of anharmonic current-phase relation. It was shown that in all cases of the presence of additional terms in current-phase relation leads to a decrease of switching times with increasing of anharmonicity parameter α. It is also found that with increasing of the geometrical inductance of superconducting ring l effects of anharmonicity parameter on dynamics ac SQUIDs becomes important.

Acknowledgment

This study is supported by TÜBİTAK grant No 118F093.

References

1. Likharev K.K., Introduction into Dynamics of Josephson junctions and circuits, New York, Gordon Breach, 1986, 586 p.
2. Askerzade I., Bozbey A., Canturk M., Modern aspects of Josephson Dynamics and superconductivity electronics, 2017, 211 p. DOI: 10.1007/978-3-319-48433-4, (Springer, Berlin)
3. Wendin G., Shumeiko V.S. Low Temperature Physics 2007, v. 33 (9), p.724. DOI: 10.1063/1.2780165.
4. Wendin G. Reports on Progress in Physics 2017, v. 80, p. 106001. DOI: 10.1088/1361-6633/aa7e1a
5. Il'ichev Zakosarenko V., Fritzsch L., Stolz R., Hoenig H.E., Meyer H.-G. Rev. Sci. Instrum. 2001, v. 72, p. 1882. DOI: 10.1063/1.1347374.
6. Tsuei C.C., Kirtley J.R. Rev. Mod. Phys. 2000, v. 72, p. 969. DOI: 10.1103/RevModPhys.72.969.
7. Askerzade I.N. Unconventional Superconductors: anisotropy and multiband effects, (Springer, Berlin), 2012, 177 p.
8. Askerzade I.N., Technical Physics 2006, v. 51, p. 393. DOI: 10.1134/S1063784206040013.
9. Askerzade I.N., Low Temperature Physics, 2015, v. 41 (2), p. 241. DOI: 10.1063/1.4916071
10. Askerzade I.N., Kornev V.K. Radiotekhnika i Elektronika, 1994, v. 39, p. 869.
11. Canturk M., Askerzade I.N. IEEE Trans. Appl. Supercond. 2012, v. 22, p. 1400106. DOI: 10.1109/TASC.2012.2220762.
12. Goldobin E.et al. Phys Rev. B 2007, v. 76, p. 224523. DOI:https://doi.org/10.1103/PhysRevB.76.224523.
13. Askerzade I.N. J. Supercon and Nov. Mag. 2019, v. 32 (10), p. 3149. DOI: 10.1007/s10948-019-5112-6.
14. Askerzade I.N., Askerbeyli R. Low Temperature Physics 2020, v. 46 (9), p. 919. DOI: 10.1063/10.0001714.
15. Askerzade I.N., Askerbeyli R. Low Temperature Physics, 2021, v. 47 (5), p. 392. DOI: 10.1063/10.0004232.

POLARIZATION OF NUCLEON IN THE LOCAL POTENTIAL WITH SPIN-ORBITAL INTERACTION

IG AFANDIYEVA and RA AHMEDOV

Azerbaijan State University of Oil and Industry, Baku, Azerbaijan
E-mail: afandiyeva.irada@asoiu.edu.az; ahmedov.rasim@asoiu.edu.az

A study of the calculations of polarization effects associated with the scattering of hadrons on the nucleus in the pulse approximation. The local interaction potential includes the spin-orbit interaction. In this case, the transition occurs directly from the initial to the final state of the cluster transfer without changing the internal states of the nucleons. The scattering amplitude contains a term that depends on the spin orientation and a term that does not depend on the spin orientation, and the polarization occurs due to interference between these two parts of the scattering. The degree of polarization is proportional to the probability that the cluster "aimed" at the initial nucleus with the corresponding values of momentum and angular momentum are captured to form a composite nucleus. The polarization sign depends on the value of the incident particle energy. Depending on the energy, there is interference from positive and negative scattering angles and this affects the sign of polarization. It is of interest to study polarization for individual energy regions. This can monitor the change in the polarization sign.

Keywords: cluster, matrix element, impulse approximation, polarization.
PACS: 25.45.De, 24.50.+g, 21.60.Gx

Introduction

Theoretical and experimental studies on nucleon scattering show that particles are polarized after scattering. Polarization is a consequence of the fact that the nucleon-nucleus interaction can be represented by a complex spin-dependent potential. The presence of such a potential is indicated by the spin dependence of the nucleon-nucleon interaction. A particle with a nonzero rest mass and spin J (in units of the Planck constant) has $2J + 1$ quantum states corresponding to different spin orientations. The state of a particle is a superposition of these states. If the superposition coefficients are completely (pure state), the particles should be completely polarized. This polarization will on the average be parallel to the atomic planes and perpendicular to the momentum.

The experimental results allowed a new look at spin-dependent effects in the dynamics of direct nuclear reactions at large collision parameters, which can be successfully described using well-developed theoretical methods for evaluating the matrix elements of transitions (the distorted wave method, the coupled channel method).

The polarization effects usually are used for investigation spin-dependent interactions in the scattering processes and for checking the used model. Polarization of particles scattered from unpolarized nuclei can occur due to the spin–orbit interaction between the incident particle and the nuclei [1]. The theoretical analysis of the polarization effects in the scattering of hadrons showed that, in addition to the central interactions, must be considered also a spin-orbit interaction.

Early, it was shown [2] that the calculated in the quark cluster model real and imaginary parts of the leading asymptotic term of the spin-flip amplitude of the charge exchange reactions agree sufficiently well with the amplitude reconstructed by the model independent approach from the experimental data.

The polarization of scattered particles in the eikonal approximation has been reported in [2,3]. In this paper polarization effects in scattering processes with hadron are analyzed by means of the impulse approximation with Gauss, spin- orbital and residual pair potentials. Considered energy region lies below the threshold meson production and the impulse approximation is used. It is assumed that the amplitude of the interaction of nucleons of the incident nucleus with the nucleons of the target nucleus is the same as in the case of collision free nucleons.

The polarization function

Particle with a nonzero rest mass and spin *J* has 2*J*+1 quantum states corresponding to different spin orientations of the particle. The state of a particle is superposition of these states. If the particle completely polarized to mean superposition coefficients of these states are completely determined. If the superposition coefficients are specified only by certain statistical characteristics, then particle has partial polarization. The particle can be completely unpolarized when these coefficients are not determined.

Let us consider the production of transversely polarized hadrons in the scattering processes. Under the assumption that at high energies of incident hadrons, the kinetic energy of the hadrons is large in comparison with the binding energies of the nucleons, the interaction of the hadrons with the nucleons of the nucleus can be treated independently. With each nucleon, the hadrons interacts only once. For the high- energy scattering we will considered only nuclear potential, and don't consider magnetic interaction. To determine the polarization, it is necessary to determine the scattering amplitudes using the unitarity condition. For construction the scattering amplitude that satisfies at least the two-particle unitarity condition is the use of realistic potentials [4].

The Schrodinger equation for this system is:

$$\left[-\frac{\hbar^2}{2m_h}\Delta-\frac{\hbar^2}{2m_N}\Delta_N+V\right]\Psi(r_h r_N)=E\Psi(r_h,r_N)\,, \tag{1}$$

where

$$W(r)=V=V_{12}(r_{h,N})+V_{ls}+V_{pair}\,, \tag{2}$$

$V_{12}(r_{h,N})$ – interaction between hadrons and nucleus nucleons and is Gauss potential, V_{ls} is spin-orbital interaction and V_{pair} potential of the residual pair interaction.

We seek the solution $\Psi(r_h r_N)$, which containing the incident plane wave of the hadrons and the scattered waves. In the pulse approximation the wave function $\Psi(r_h r_N)$ is replaced by

$$\Psi(r_h r_N)\rightarrow\frac{1}{(2\pi)^3}\iint dKdre^{-ik_i r_h}\varphi_i(r)\psi_{k_i K}(r_h r_N)\,, \tag{3}$$

where k_i – initial pulse of the hadron, *K* – transferred pulse.

In scattering described by the Schrödinger equation, the amplitude *f* is a scalar. In the spherically symmetric central field, the scattering matrix elements has following view

$$f = \frac{1}{(2\pi)^6} \int e^{i(k_i - k_j + K)r} \, \psi_f^*(r) \psi_i(r) (k_f K' | V | k_i K) drdKdK' , \tag{4}$$

where

$$(\mathrm{k_f K'}|\mathrm{V}|\mathrm{k_i K}) = (2\pi)^3 \delta(\mathrm{k_f} + \mathrm{K}' - \mathrm{k_i} - \mathrm{K}) \int \mathrm{e}^{[\mathrm{i(K \; - k_i) r/2}]} \mathrm{V(r)} \varphi_{\mathrm{k_i - K}}(\mathrm{r}) \mathrm{dr} , \tag{5}$$

and k_f – is final impulse of the hadrons.

The mechanism that produces the polarization can be explained in the following manner.

The scattering amplitude is 2 x 2 elements of the matrix *f*, which may be expressed by the Pauli matrix and unit vector n

$$f = gn + (\mathrm{h}\sigma). \tag{6}$$

The multiples *g* in the (6) corresponding to the interaction, which don't depends on the spin, vector h – to the interaction under which reoriented the spin.

If the y-axis is chosen along the direction of the unit vector n($\varphi = 0$), then the wave function of the scattered particle initially located in the spin state χ_s

$$\chi_s = (n\boldsymbol{\sigma}) \; \chi_s , \tag{7}$$

where

$$\chi_s = c\chi_{1/2} + d\chi_{-1/2} , \tag{8}$$

and

$$c = \sqrt{\frac{1 + n_z}{2}}, \quad d = \frac{n_x + in_y}{\sqrt{2(1 + n_z)}} \tag{9}$$

The wave function has following view

$$\Psi = \begin{pmatrix} \sqrt{\dfrac{1 + n_z}{2}} \\ \dfrac{n_x + in_y}{\sqrt{2(1 + n_z)}} \end{pmatrix} e^{i\mathrm{kr}} + \begin{pmatrix} f^+(\theta) \\ f^-(\theta) \end{pmatrix} \frac{e^{ikr}}{r} , \tag{10}$$

where first term characterized plane wave, second spherical scattering wave, f^+ and f^- are the complex functions and depends on the scattering angle θ

$$f^+(\theta) = cg - idh , \; f^-(\theta) = dg + ich . \tag{11}$$

Usually for determination polarization double scattering is used:

$$\sigma(\theta_1, \theta_2, \varphi_{12}) = \left(1 + P_2 \mathbf{n_2} \langle \sigma \rangle_1 \right) I_2(\theta_2) I_1(\theta_1) = \{1 + P_2(\theta_2) P_1(\theta_1) \cos\varphi_{12}\} I_1(\theta_1) I_2(\theta_2) . \tag{12}$$

where indices 1 and 2 show single and double scattering. A beam of nucleons, scattering on one of the nuclei of the first target, is partially polarized. The degree of polarization is determined from the difference in the intensity of the beams scattered by the nuclei of the second target at the same angles to the right and to the left.

Dynamic polarization of particles, for example protons is carried out by the so-called solid-effect method. In this method, the nuclei of diamagnetic atoms are polarized in a diamagnetic substance containing a small amount (= 1%) of impurity magnetic atoms with an effective shell spin S = 1/2. The interaction of the magnetic moments of protons with the magnetic moments of the shells of magnetic atoms splits the EPR transition in an external magnetic field into three transitions: the allowed one, corresponding to the reorientation of only the spins of the shells of magnetic atoms, and two forbidden, corresponding to the simultaneous reorientation of the spins of the shells and the spins of protons.

In elastic scattering of particles on nucleons, polarization P of recoil nucleons arises, which is determined by the expression:

$$P\frac{d\sigma}{dt} \approx \operatorname{Im} A^{*}B\,, \tag{13}$$

where A is the scattering amplitude without spin flip; B - with a flip of the back. To test the interaction models, it is important to trace the course of polarization with the 4-momentum transferred to the nucleon. Since the interaction is spinning dependent, the effective cross section will also depend on polarization of the hadrons. Using the definition of the differential scattering cross section, we obtain that

$$\sigma(\theta,\varphi) = \{1 + P(\theta)\cos\phi\}\left(|g(\theta)|^2 + |h(\theta)|^2\right), \tag{14}$$

$$P(\theta) = 2\frac{\operatorname{Re}(g^{*}h)}{|g(\theta)|^2 + |h(\theta)|^2}\,. \tag{15}$$

To quantify the function $P(\theta)$, it can be represented as follows. In the Born approximation, taking into account the spin-orbit interaction, the scattering amplitude has the form

$$f = \frac{1}{2\pi\mu c^2}\int \exp[-i(\mathbf{k}' - \mathbf{k})r]\frac{1}{2ir}\frac{dV}{dr}(\sigma r \times \nabla)dr\,. \tag{16}$$

In the framework of pulse approximation, using the (16) we obtain:

$$h(\theta) = \frac{i}{2}\eta^2 \sin\theta \int \exp[-i(\mathbf{k}' - \mathbf{k})\mathbf{r}](V_{hn} + \frac{1}{2ir}(\sigma l)\frac{dV}{dr})\,, \tag{17}$$

and

$$P(\theta) = -\frac{\mu}{k^2 \sin^2\theta}(k' - k)(V_G + V_{sl} + V_{pair})\frac{d\sigma(\theta)}{d\theta} / \sigma(\theta) = \frac{(\hbar k/\mu c)^2 d \sin\theta V^2(|\mathrm{k} - \mathrm{k}'|)}{c^2 + d^2 + \frac{1}{4}d^2(\hbar k/\mu c)^4 \sin^2\theta}, \tag{18}$$

where $V(|k - k'|)$ is the Fourier transform of the function V(r).

From expression (18) it is seen that the polarization *P* vanishes if *d* equals zero. An important feature of this expression is that the polarization determined by it is completely determined by the relative values of the coefficients c and d.

It has been shown in the work [5] that a polarization effect arises from the quantum spin-entanglement of the projectile-target system in addition to the separable total spin depending on the collision energy and scattering angle.

Conclusion

Polarization effects are important of studying the structure of particles. The studies of nucleon polarization can illuminate some aspects of nuclear structure, since the polarization depends on the particular nucleus used as a target as well as upon of the interaction.

Orientation effects arise from the action of the spin-orbit term in the distorting potential and the kinematic polarization of the transferred angular momentum due to the gradual separation of the deflection from the far and near sides of the nucleus. The experimental results clearly support the presence of a spin-orbit term in the optical potential. But its intensity, obtained from inelastic scattering and transfer reactions, turns out to be much greater than could be expected on the basis of convolution with a realistic nucleon-nucleon interaction.

Comparison of the results of calculations in the framework of the considered potentials shows that these phenomenological potentials are capable of describing most of the transferred angular momentum in correlation with energy dissipation. On the other hand, it follows from studies within the framework of the nucleon exchange model that random nucleon transfer and the quantum Pauli exclusion effect play an important role in the interpretation of the value and orientation of the transferred spin, which is in agreement with experiment.

The results obtained above can be generalized to the cases when not only nucleons and compound particles, but also any elementary particles, for example, mesons or antinucleons, appear as particles.

References

1. Haque A.K.F. et al. J. Phys. Commun. 2017, v. 1, p. 035014. DOI:10.1088/2399-6528/aa8bf8
2. Ahmedov R.A. Cumhuriyet SCI. Journal 2016, v. 37, p. S56.
3. Abdulvahabova S.G. and Afandiyeva I.G. Journal of Qafqaz University 2015, v. 1 (1), p.61.
4. Abdulvahabova S.G. et.al. Cumhuriyet SCI. Journal 2019, v.40 (1), p. 79.
5. Blum Kand B. and Lohmann B. Phys. Rev. Lett. 2016, v. 116, p. 033201. DOI:10.1103/PhysRevLett.116.033201

MAGNETIC PROPERTIES of $Zn_{1-x}Fe_xSe$ COMPOUND

NA ISMAYILOVA [1] and II ABBASOV[2]

[1] Institute of Physics of the ANAS, 131 H. Javid Ave., Az-1143, Baku, Azerbaijan
[2]Azerbaijan State University of Oil and Industry, 20 Azadlig Street, Az-1010, Baku, Azerbaijan
E-mail: ismayilova_narmin_84@mail.ru

The magnetic propertie of Fe doped $Zn_{1-x}Fe_xSe$ have been investigated using the first-principle calculations within density functional theory. Our results reveal that the strong spin polarization of the 3d states of the Fe atoms is not affect to origin of ferromagnetism in $Zn_{1-x}Fe_xSe$. A decrease in the concentration of iron atoms in the supercell does not affect the stability of the AFM phase.

Keywords: DFT, DOS, band gap, magnetic moment
PACS: 29.30.Aj, 13.40.-f, 61.72.Vv

Introduction

Doped with Cr, Fe, Ni, Mn impurity atoms ZnSe material is considered promising materials at room temperature (RT), and recently the growth of active elements based on Fe^{2+} doped chalcogenide crystals has become the subject of intense research to create powerful and effective mid-IR lasers [1, 2].

In recent years a lot of work devoted to theoretical calculations for investigation of structural and electronic properties of ZnS compound [3-6, 7, 8]. By implementing empirical pseudopotential method electronic properties of ZnS and ZnSe, ZnTe was calculated [3, 4, 5].

Using correction mBJ potential electronic band structure where band gap value was 2.787eV calculated in ref. [7]. Forbidden band gap was found to be 2.84 and 2.82 in experimental works [9, 10, 11].

The authors of experimental works [12, 13, 14] investigated magnetic properties of $Zn_{1-x}Fe_xSe$. Their result reveal that this compound show paramagnetic properties at low temperatures and in low magnetic fields. In ref. [15] V and Cr-doped ZnS, ZnSe were investigated. It was obtained that ZnTe are ferromagnetic without p- or n-type doping treatment. However, Mn-, Fe-, Co- or Ni-doped ZnS, ZnSe and ZnTe are spin-glass states.

In this work, we study the electronic and magnetic properties of Fe-doped ZnSe samples based on DFT.

Method of calculation

We use spin-polarized density functional theory [16] (DFT) with generalized gradient approximation (GGA) [17], as implemented in the Atomistix Tool Kit program software (ATK, http://quantumwise.com/) [18]. In presented work pseudopotentials HGH [19], FHI [20], SG15 [21] were used. As correlation functional we used BLYP [22, 23]. The wave function was expanded taking into account plane waves with energies up to 150 Ry, which provided a good convergence of the total energy. The primitive and supercell were optimized with force and stress tolerances of 0.0001 eV/Å and 0.0001 eV/Å^3, respectively.

Result

First, we relaxed the unit cell of ZnSe, and the optimized lattice constants. Optimized lattice parameter is in in good agreement with the experimental value a^{opt}=5.658 Å, a^{exp}=5.662 Å [24]. Based on the optimized structure of ZnSe, we calculate the electronic band structure. The calculated bandgap in the GGA +FHI scheme is 0.81 eV, which is smaller than the experimental value. Now to improve the bandgap, we use the GGA + SG15 combination. The calculated bandgap is 2.82 eV, which is in good agreement with the experimental value. We can see that the conduction band minima (CBM) and valence band maxima (VBM) occur at the Γ symmetry point, demonstrating the direct bandgap nature of ZnSe.

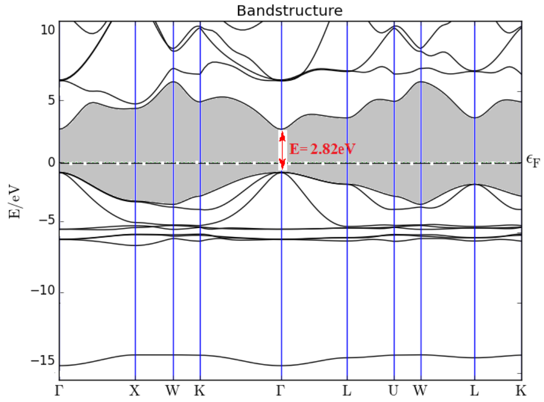

Fig. 1. Electronic structure of ZnSe

The introduction of Fe atomos can lead to the magnetization of the system due to the 3d electronic statet, thus study of the magnetization of the compound is of great interest. For Fe; ZnSe, we consider the Fe ion substituting for the Zn atom in different supercells 1×2×2, 2×2×2, 2×2×3, and 3×3×2, leading to 12.5%, 6.25%, 4.2%, and 2.7% Fe concentrations. From the energy difference $\Delta E = E(\mathrm{AFM}) - E(\mathrm{FM})$ it was abvious that FM state is favored over AFM state.

How we can see from Fig. 2 additional states are formed around the Forbidden band gap for doped Fe:ZnSe system. This state is mainly due to the d electrons states of the iron atoms. But all spin up and spin down states are similar.

This result reveal that $Zn_{1-x}Fe_xSe$ has antiferromagnetic properties for all supercells.

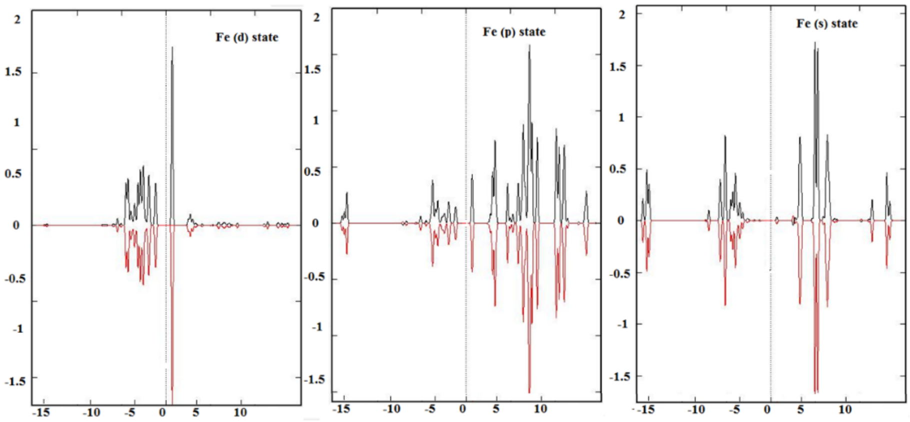

Fig. 2. Calculated DOS doped Fe:ZnSe system

Conclusion

We have evaluated the properties in terms of structural, electronic and magnetic features of the pure and Fe doped ZnSe system. In the calculated electronic structure by using of the exchange correlation functional GGA-SG15 observed a decrement in bandgap which is valued 2.82 eV. The electronic structure of the system is analyzed by the band structure and DOS plots. Density functional theory based calculations show ferromagnetic property in Fe doped ZnSe system.

Reference

1. Kulyuk L.L., Laiho R., Lashkul A.V., Lahderanta E., Nedeoglo D.D., Nedeoglo N.D., Radevici I.V., Siminel A.V., Sirkeli V.P., Sushkevich K.D. Physica B 2010, v. 405, p. 4330. https://doi.org/10.1016/j.physb.2010.07.036
2. Alekseev E.E., Kazantsev S.YU., Podlesnikh S.V. Optical Materials Express 2020, v. 10, p. 2075. https://doi.org/10.1364/OME.401095
3. Karazhanov S.Zh., Ravindran P., Kjekshus A., Fjellvag H., Svensson B.G. Physical Review B 2007, p. 75. ID: 155104.http://dx.doi.org/10.1103/PhysRevB.75.155104
4. Tsuchiya T., Ozaki S., Adachi S.J. Journal of Physics: Condensed Matter 2003, v. 15, p. 3717.
5. Walter J.P., Cohen M.L, Petroff Y., Balkanski M., Physical Review B 1970, v. 1, p. 2661. http://dx.doi.org/10.1103/PhysRevB.75.155104
6. Huang M.-Z., Ching, W.Y. Physical Review B 1993, v. 47, p. 9446.
7. Asadi Y., Nourbakhsh Z., Computational Condensed Matter 2019, v. 16, p. e0037.
8. https://doi.org/10.1016/j.cocom.2019.e00372
9. Rachidi A., Atmani E.H., Fazouan N., Boujnah M., Materials Sciences and Applications 2016, v. 7, p. 562. DOI: 10.4236/msa.2016.79047
10. Kayed T.S., Qasrawi A.F., Khaled A. Elsayed. Journal of Electronic Materials 2019, v. 45 (6), p. 2763. https://doi.org/10.1007/s11664-019-07055-3.
11. Bechiria A., Benmakhloufa F., Bouarissab N. Physics Procedia 2009, v. 2 (3), p. 803.
12. https://doi.org/10.1016/j.phpro.2009.11.028
13. Riippischer H., Jacobs J. and Navikov B. V. Phys. Staf. Solidi (A) 1975, v. 40 (2), p. 575.
14. Furdyna J.K., J. Appl. Phys. 1988, v. 64, p. R29. http://dx.doi.org/10.1063/1.341700.
15. Guldner Y., Rigauz C., Menant M., Mullin D.P., Furdyna J.K. Solid State Commun. 1980, v. 33, p. 133.
16. Serre H., Basterd G., Rigauz C., Mycielski J., Furdyna J.K.. Proceedings of the Fourth International Conference on the Physics of Narrow-Gap Semiconductors, Linz 1981, Lecture Notes in Physics, v. 52, Springer, Berlin, 1982, p. 321.
17. Katayama-Yoshidaa H., Sato K. Journal of Physics and Chemistry of Solids, 2003, v. 64, p. 447. https://doi.org/10.1016/S0022-3697(03)00126-4
18. Hohenberg P., Khon W., Phys. Rev. B 1964, v. 136, p. 864. https://doi.org/10.1103/PhysRev.136.B864
19. Perdew J., Burk K., Wang Y., Phys. Rev. B 1996, v. 54, p.16533. https://doi.org/10.1103/PhysRevB.54.16533
20. http://quantumwise.com/.
21. Hartwigsen C., Goedecker S., Hutter J. Phys. Rev. B 1998, v. 58, p. 3641.
22. https://doi.org/10.1103/PhysRevB.58.3641
23. Fuchs M.and M. Scheffler. Comput. Phys. Commun. 1999, v. 119, p. 67.
24. https://doi.org/10.1016/S0010-4655(98)00201-X
25. Martin S., François G. Comput. Phys. Commun. 2015, v. 196, p. 36.
26. https://doi.org/10.1016/j.cpc.2015.05.011
27. Becke A.D. J. Chem. Phys. 1993, v. 98 (7), p. 5648. doi:10.1063/1.464913.
28. Lee C., Yang W., Parr R.G., Phys. Rev. B 1988, v. 37, p. 785-789.
29. doi:10.1103/PhysRevB.37.785.
30. Ley L., Pollak R.A., McFeely F.R., Kowalczyk S.P., Shirley D.A. Phys. Rev. B 1974, v. 9, p. 600.

SPECTRAL STUDY OF THE NOVA ASASSN-17hx (SCT2017)

KM MIKAILOV[1], KI ALISHEVA[1,2], BN RUSTAMOV[1,2], IA ALAKBAROV[2] and AH ALILI

[1]Baku State University, Baku, Azerbaijan

[2] Shamakhy Astrophysical Observatory named after N. Tusi, Azerbaijan National Academy of Sciences, Baku, Azerbaijan

E-mail: kamalaalisheva@bsu.edu.az

We have carried out spectral observations of the Nova ASASSN-17hx during August-November for 15 nights with different intervals. The obtained spectra, with a resolution of R=28000 (λλ3900-8000Å Å), cover the moments of minimum and maximum on the light curve, the moment of the secondary outburst of SCT 2017. Measured the profiles of the spectral lines were constructed, the radial velocities of the stellar and interstellar spectral lines. It was found that the Balmer lines are more intense, the HeI lines are noticeable, the lines of ionized metals make up the majority. With the exception of HeI, all absorption lines show a two-component structure. The first narrow component arises during the outburst of 1 maximum, and the second broad component of absorption during the second outburst. This proves that there were 2 powerful ejections of matter on the star. The velocity of the first was -450 km/s, and the second -685 km/s. At the maximum, the lines show P-Cyg profiles. The absorption of the Hα line shows a five-component structure. This is due to layers, with different velocities. The profiles of the absorption lines of the interstellar medium NaI and CaII show an eight-component structure. This indicates that the interstellar medium in the direction of the star has a multilayer structure.

Keywords: Novae, cataclysmic variables, spectra

PACS: 97.30.Qt, 95.75.–z, 95.30.Ky

Introduction

The investigation of Novae means one of the urgent tasks of astrophysics. While Novae outburst are not a frequent event, they are of particular interest.

Novae are close binary systems, consisting of a main star, which is in the main sequence or is already in the stage of a red giant and a companion - a white dwarf. In such systems, the matter of the outer layers of the main star flows over to the white dwarf. The overflowing matter forms an accretion disk around the white dwarf, the accretion rate (speed) onto the white dwarf is stable and depends on the parameters of the main star and also on the ratio of the masses of the stars-components of the binary system.

Accretion gas accumulates on the surface of the white dwarf, forming a hydrogen-rich layer and is additionally heated by the high-speed flow from the accretion disk. This is also facilitated by the penetration into the degenerate surface layer of carbon from the underlying layers of the white dwarf. Under nondegenerate conditions, as a result of thermonuclear reactions, the release of energy leads to an increase in temperature, an increase in pressure and, accordingly, an expansion, a decrease in density and a decrease in the rate of nuclear reactions (proportional to density and temperature) - that means the establishment of a self-adjusting hydrostatic equilibrium. However, a feature of a nonrelativistic degenerate gas is an extremely weak dependence of pressure on temperature: The result is an explosive acceleration of fusion reactions in a hydrogen-rich envelope, the temperature rises sharply until the degeneracy is lifted at a given density, and is formed a shock wave, dumping the top layer of the white dwarf's hydrogen envelope into the surrounding space.

Soon after the outburst, a new accretion cycle begins on the white dwarf and accumulation of the hydrogen layer and, after a while, determined by the accretion rate and the properties of the white dwarf, the outburst is repeated.

The outburst of a Nova ASASSN-17hx (also called nova Sct 2017 and V612 Sct) was discovered using All Sky Automated Survey for SuperNovae (ASASSN) June 19, 41 UT as a bright new star candidate [1]. After there was a spectroscopic confirmation [2] together with the CTIO spectral classification [3,4]. We were informed about the outburst of the Nova Sct 2017 by an employee of the Nicolaus Copernicus University in Torun, prof. T.Tomov. Systematic observations of this object were carried out during August-November 2017.

Our goal is to trace the evolution of the spectrum during the outburst of a nova Sct 2017.

Observations and dats reduction

Spectral observations were carried out over 15 nights during August-November 2017, at the 2-meter telescope of the Shamakhy Astrophysical Observatory (SHAO) of the National Academy of Sciences of Azerbaijan on a fibre-optic echelle spectrograph ShaFES [5] of the Cassegrain focus. The spectra were obtained using a CCD array detector cooled with liquid nitrogen. Matrix size 4096x4096 pixels, 1 pix.=15 mic. Spectral resolution R=28000, wavelength range λλ 3800-8000 Å Å. Every night, at least two spectra of the object and the standard were obtained, including all calibration spectra. The obtained spectra cover the moments of minimum and maximum on the light curve, as well as the moment of the secondary outburst of the star ASASSN-17hx.

The spectra were reduced using the standard method using the DECH 30 program [6]. Spectra extractions were performed using an IRAF mask. The wavelength calibration of the spectra was carried out using the spectrum of a thorium-argon lamp. By combining all echelle orders, was created a single spectrum.

Also to build a complete picture of the processes taking place on the New ASASSN-17hx high resolution ESO spectra were used (R = 110,000) [7] and low resolution ARAS (R = 9000-11000) [8], obtained in July, August and October.

Also, a V-band light curve was plotted using the AAVSO photometric database (Fig. 1) [9].

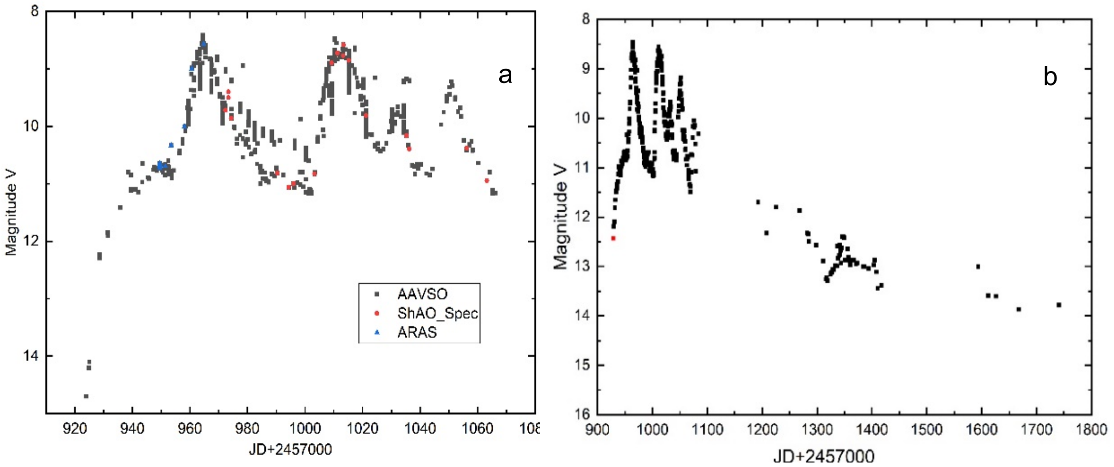

Fig. 1. Light Curve ASASSN-17hx: a – the points of observations carried out at the ShAO are marked in red.red point; b- shows the overall light curve from the day of the outburst to the given date.

Fig. 1a shows the ASASSN-17hx light curve. The abscissa shows the Julian date, on the ordinate axis is the apparent magnitude. The value of the obtained spectra lies in the fact that on certain dates the spectra were obtained only by us.

We have begun to observe the star during the recession after the first outburst, then, at a minimum, a secondary outburst and its decay, as well as the moments of decay after the third and fourth low-amplitude outbursts.

As you can see, the brightness of the star dropped to 15 magnitudes, that is, in fact, up to the brightness with which it started the outburst (Fig. 1b).

The study of the light curve showed that the Nova, during 37 days before the first outburst, increased its magnitude to 8m, 47 days after the first outburst, there was a second outburst with an amplitude of $2^{m}.6$. The brightness of the first outburst is almost equal to the brightness of the second outburst. 68 days later the first outburst, a low-amplitude third outburst ($0^{m}.7$) occurred, and 87 days later there were fourth outbursts with an amplitude of $1^{m}.65$.

Figure 2 shows the changes in the ASASSN-17hx spectrum at different brightness moments of the star.

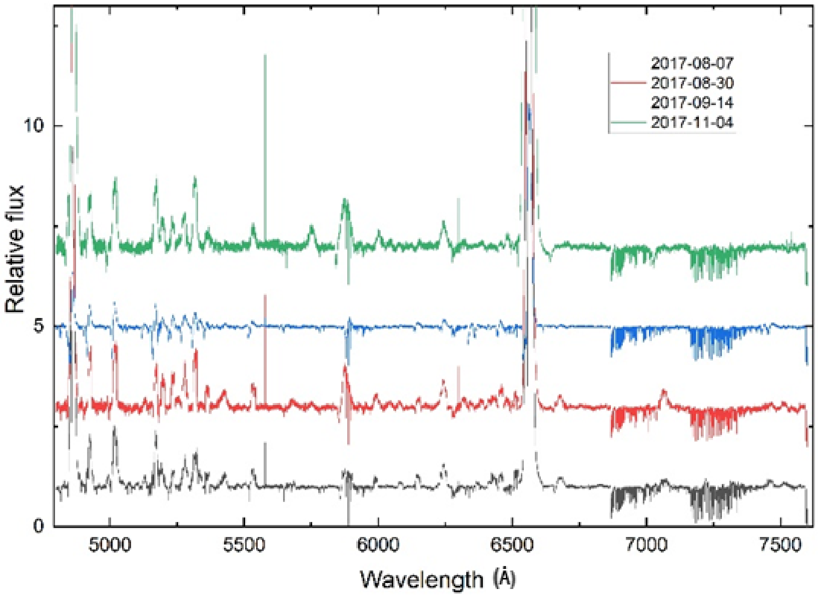

Fig. 2. Spectra of Nova ASASSN-17 hx obtained at ShAO at different dates: black color - decline after the first outburst; red is the first low; blue -maximum after the second outburst is; green color - low-amplitude third outburst

It was identified about 100 spectral lines (Table 1).

Table 1. Identification spectral lines

Wavelength, Å	Element	Wavelength, Å	Element	Wavelength, Å	Element
3933,664	CaII (k)	4468,493	TiII 31	5275,994	Fe II 49
3968,47	CaII (H)	4501,271	TiII 31	5316,609	Fe II 49
3970,074	Hepsi	4522,634	Fe II 38	5336,849	Ti II 69
4101,74	Hd	4534,166	Fe II 38	5362,864	Fe II 48
4163,659	Ti II 105	4549,467	Fe II 38	5381,02	Ti II 69
4178,855	FeII 28	4563,761	Ti II 50	5425,269	Fe II 49
4173,45	FeII 27	4555,89	Fe II 37	5397,131	Fe I 15
4233,127	FeII 27	4571,971	Ti II 82	5526,809	Sc II 31

Wavelength, Å	Element	Wavelength, Å	Element	Wavelength, Å	Element
4246,829	ScII 7	4583,829	Fe II 38	5577,35	[OI]
4273,317	FeII 27	4589,961	Ti II 50	5657,87	Sc II 29
4296,567	FeII 28	4616,64	Cr II 44	5793,932	Fe I 1086
4300,052	TiII 41	4629,336	Fe II 37	5875,63	He I 11
4301,928	TiII 41	4805,105	Ti II 92	5895,923	Na I D1
4303,166	FeII 27	4824,13	Cr II 30	5889,953	Na I D2
4307,9	TiII 41	4848,24	Cr II 30	6147,735	Fe II 74
4312,861	TiII 41	4861,337	Hb	6238,375	Fe II 74
4314,084	Sc II 15	4911,205	Ti II 114	6243	Fe II+ N II
4314,979	TiII 41	4923,921	Fe II 42	6300,697	Sc II 28
4320,965	TiII 41	5018,434	Fe II 42	6347,091	Si II 2
4325,01	Sc II 15	5031,019	Sc II 23	6371,359	Si II 2
4351,764	Fe II 27	5129,143	Ti II 86	6416,905	Fe II 74
4374,455	Sc II 14	5154,061	Ti II 70	6432,654	Fe II 40
4383,547	FeI 41	5169,03	Fe II 42	6238,375	Fe II 74
4385,381	Fe II 27	5172,684	Mg I 2	6456,376	Fe II 74
4395,031	TiII 19	5183,6042	Mg I 2	6516,053	Fe II 40
4400,355	Sc II 14	5188,7	Ti II 70	6562,816	Ha
4404,752	FeI 41	5197,569	Fe II 49	6678,149	He I 46
4417,718	TiII 40	5226,534	Ti II 70	7065,19	He I 10
4443,802	TiII 19	5234,62	Fe II 49	7423,63	N I 3
4450,487	TiII 19	5239,823	Sc II 26	7442,29	N I 3

The spectrum of one night with identified lines is shown in figure 3.

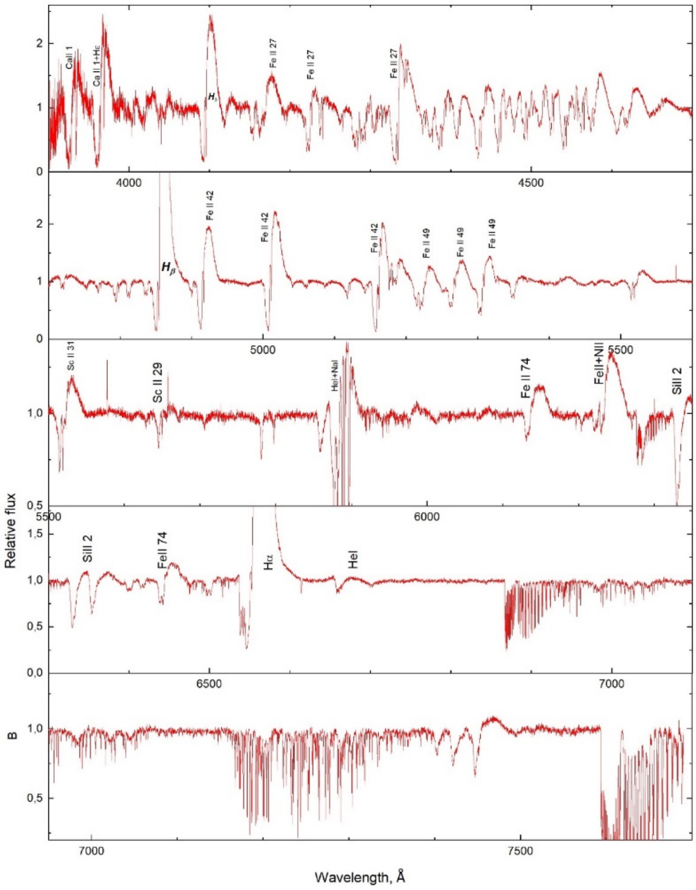

Fig. 3. The spectrum of one night with identified lines.

Discussion

The spectra of classical novae at the maximum luminosity can be attributed to the He/N type or Fe II type. As is known, the spectra of novae belonging to the Fe II type are formed in a large annular gas envelope, the source of which is a secondary star, and the He/N spectra are formed in the ejections of white dwarfs. In hybrid objects, both classes of spectra appear sequentially [10,11]. As shown by the analysis of the ASASSN-17hx spectrum, this star belongs to the hybrid type.

The evolutions of the profiles of the spectral lines Hα and Hβ, Fe II and HeI+NaI D were considered.

Profile Hα

During the first outburst, Hα shows a P Cyg profile. At the peak of the outburst, an absorption component appears, which increases. During the decay, Hα shows a two-emission component with central absorption, the absorption component turns out to be above the continuum. On the rise to the second flash, the profile is strongly broadened. At the moment of the second outburst, multicomponent broad absorption appears. And during the second recession, absorption gradually disappears and turns into a complex emission component.

Fig. 5. showns the cropped profile of the H$_\alpha$ line, where the multicomponent structure of the left wing of the line is clearly visible.

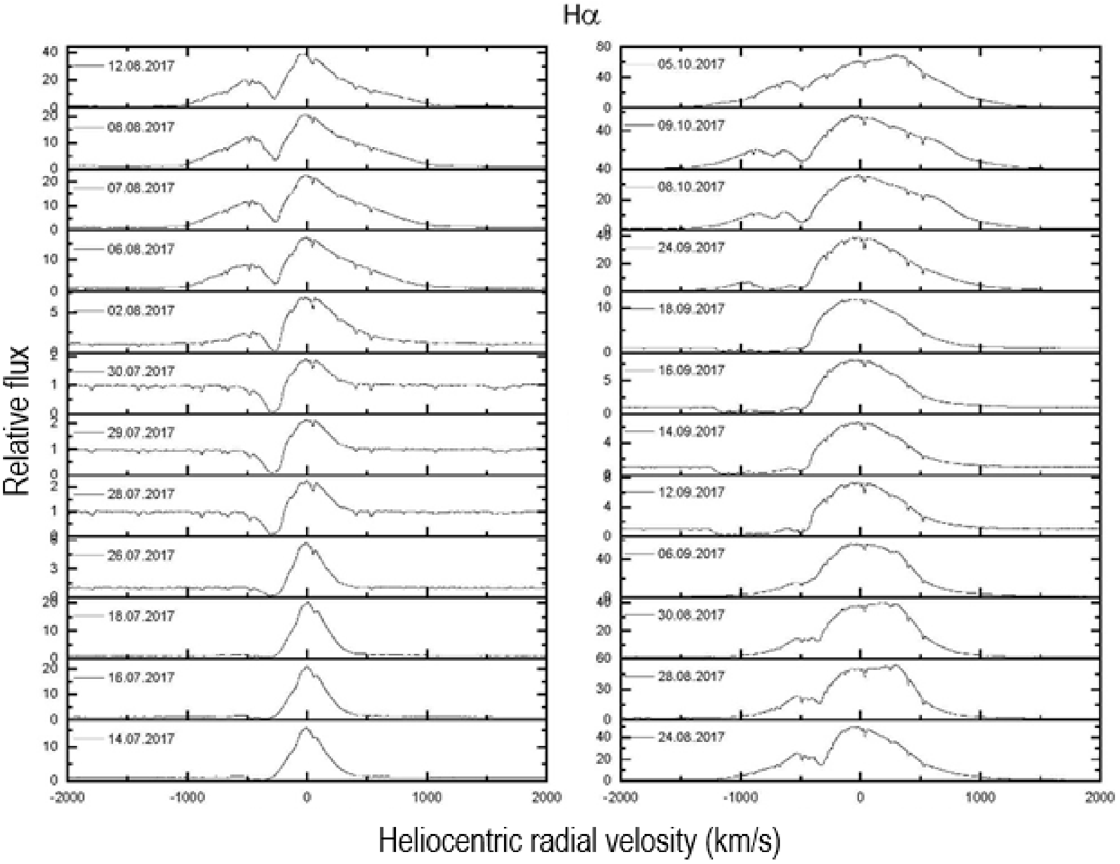

Fig. 4. The evolution of the profile of the Hα line at various dates

At the moment of the second outburst, the absorption of the H_{α} line shows a five-component structure, with corresponding radial velocities RV_1 = -1146 km/s, RV_2 = -1054 km/s, RV_3 = -972 km/s, RV_4 = -798 km/s, RV_5 = -508 km/s. This is due to different speeds in different layers.

Profile H_{β}

The Hβ line profile shows a more interesting change. During the ascent to the first outburst, the profile shows itself as P Cyg. An absorption component appears just before the first outburst. During a outburst, in contrast to $H\alpha$, the emission component completely disappears and reappears only during a recession. In the minimum between the first and second outburst, appears a very wide jagged emission, which is smoothed out during the second outburst. At the moment of the second outburst, multicomponent broad absorption appears. And during the second recession, absorption gradually disappears and turns into a complex emission component. Fig. 7. Shows the evolution of the profile of the $H\beta$ line at various dates.

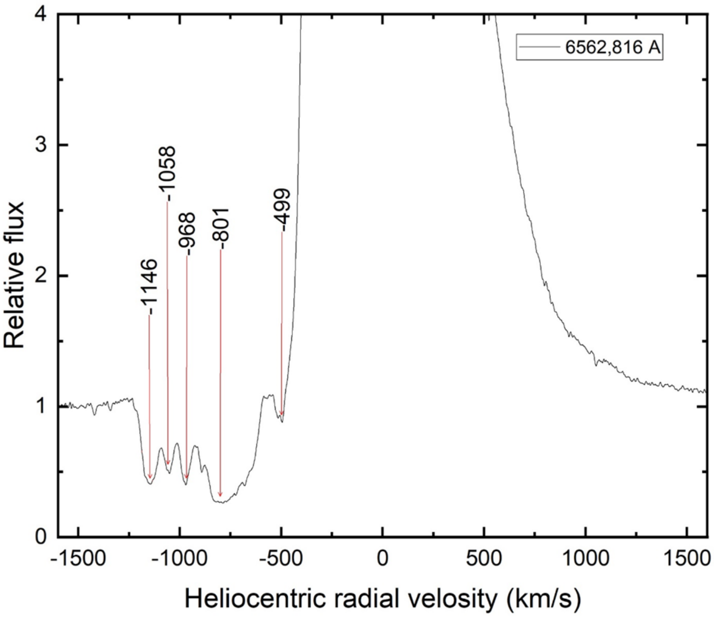

Fig. 6. The multicomponent structure of the left wing of the H_{α} line

Profile line Fe II

Spectrum ASASSN-17hx near the maximum on July 29, in H_{β} and Fe II show noticeable absorptions. The pre-maximum and maximum spectra of ASASSN-17hx show Fe II lines with P Cyg profiles, and the spectrum near the maximum is typical of a supergiant. After the July 29 outburst, the P Cyg profile disappears, and appears a complex emission profile. An emission rectangular toothed profile appears between the first and second outbursts. In anticipation of the second outburst, a broad absorption and emission P Cyg profile begins to be observed. After the second outburst, the emission rectangular serrated profile reappears at the minimum.

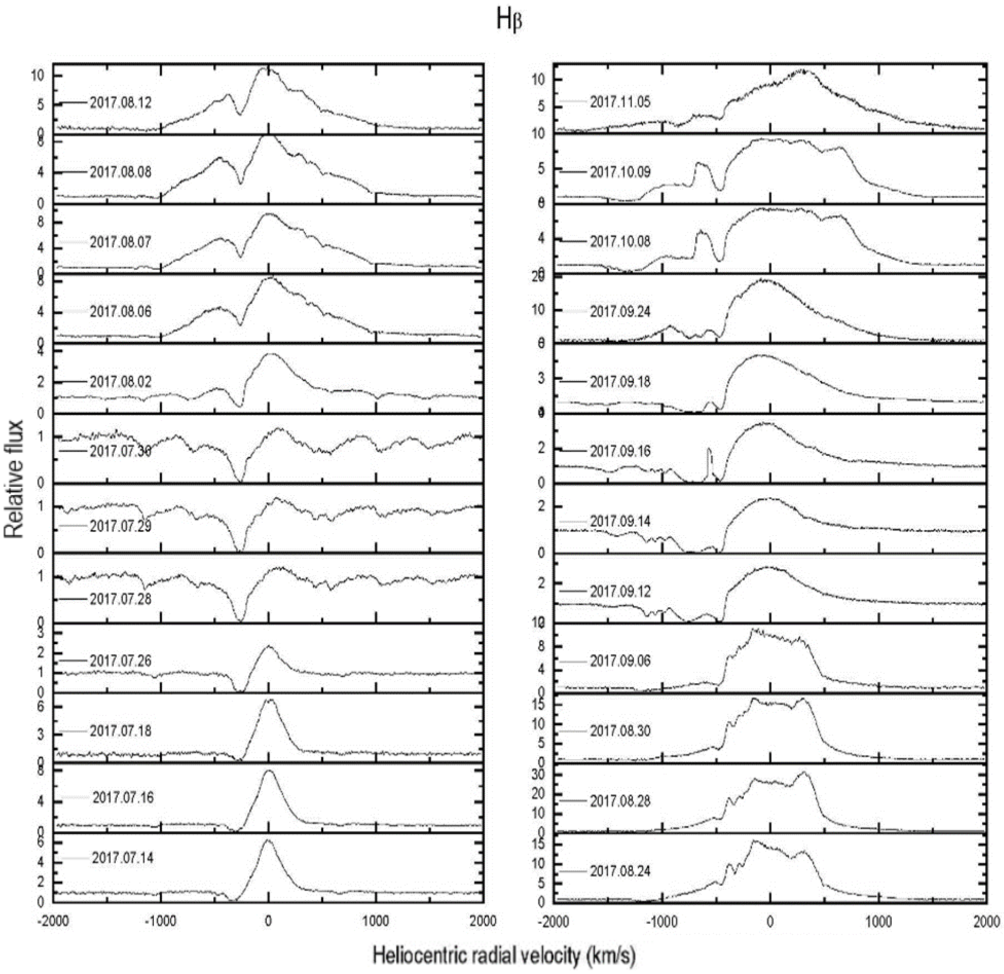

Fig. 7. The evolution of the profile of the Hβ line at various dates.

Figure 8. shows the evolution of the profile of the Fe II line at various dates.

HeI + NaI D line

The HeI emission component in the spectrum is "contaminated" with stellar and interstellar NaI D absorption lines. Therefore, it is very difficult to comment on the HeI 5876 emission component. The radial velocity of the HeI absorption component shows a strong change (from -600 km/s to -1700 km/s). Before the first outburst, it is not observed and appears only during the decline and is observed more intensely. The radial velocity reaches -1200 km/s. By the onset of the second outburst, both emission and absorption disappear again and reappear during the second minimum. The radial velocity increases and reaches -1700 km/s.

High-resolution ESO spectra showed that NaI D interstellar absorption lines have an 8-component structure with radial velocities -13.2 km/s; 8.3 km/s; 25.43 km/s; 48.5 km/s; 57.9 km/s; 63.6 km/s; 73.8 km/s; 102.3 km/s, respectively.

Conclusions

It was revealed that 4 outbursts were observed in the nova: two strong ones with amplitudes of 2.6 and two weaker ones with amplitudes of 0.7^m and 1^m. 65.

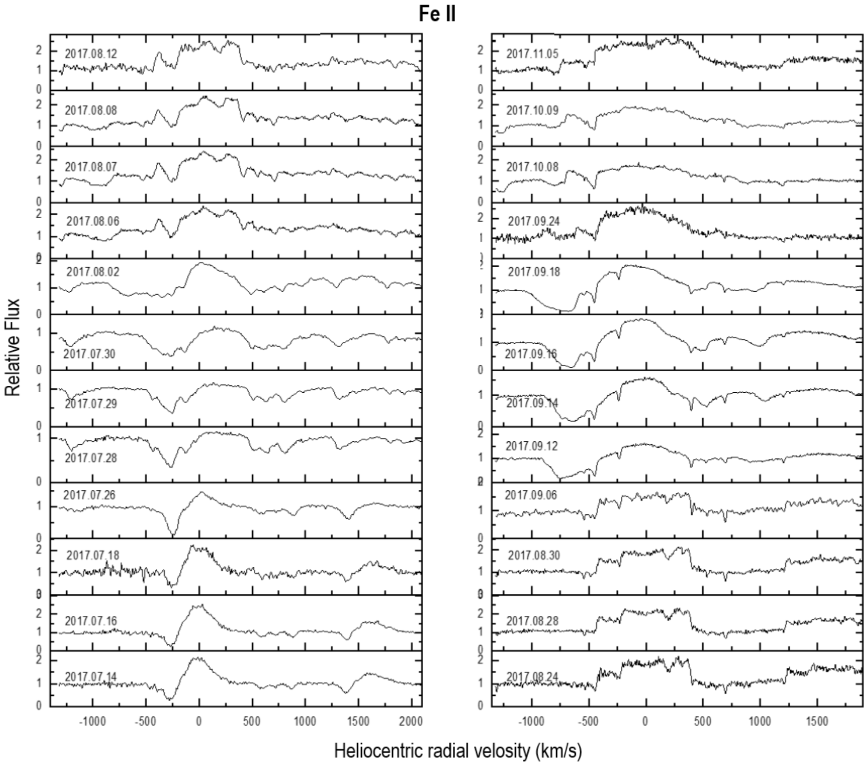

Fig. 8.The evolution of the profile of the FeII line at various dates

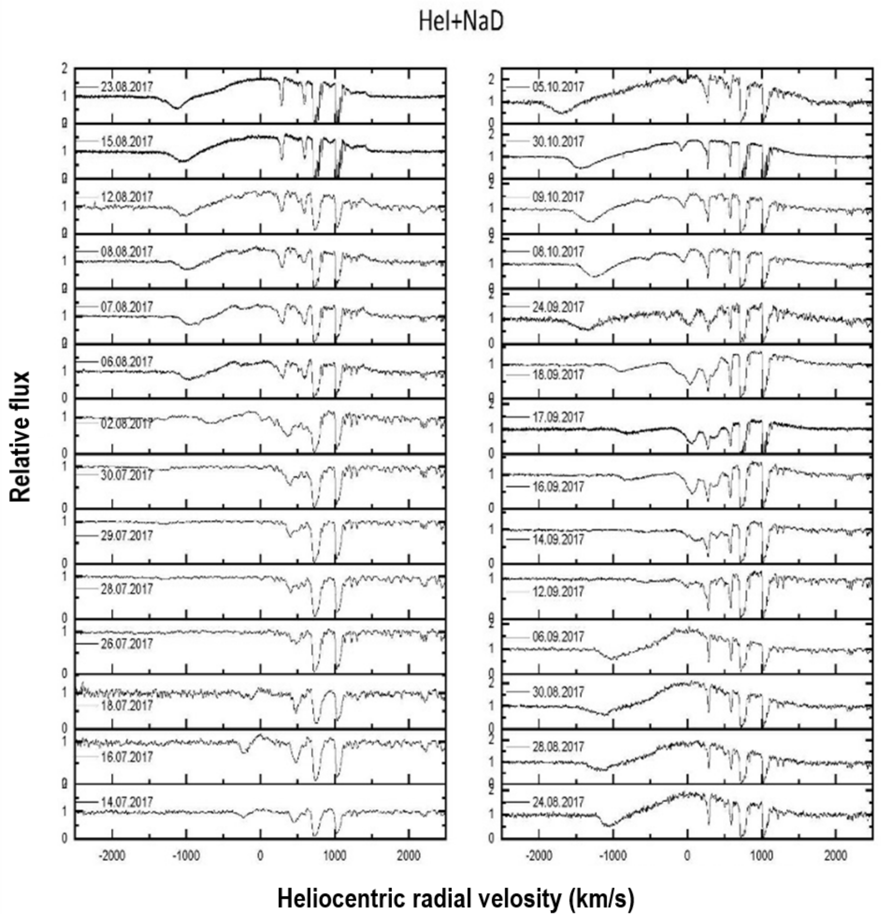

Fig. 9. shows the evolution of the profile of the HeI+NaI D line at various dates

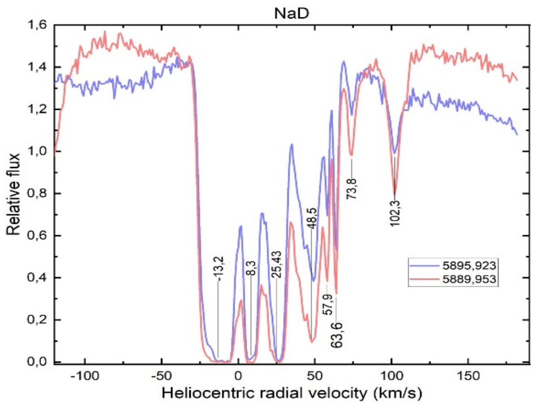

Fig. 10. NaI D interstellar absorption lines

An analysis of the Nova spectrum showed that it belongs to the hybrid class He/N and FeII, since the HeI (5875.63) lines are also observed at different stages, lines NI (7424, 7442, 7468), as well as FeII (5169, and etc.).

All lines, except for HeI and NI, show rather complex profiles at various stages.

Spectra obtained during the first and second outbursts showed that there were two atmospheric emissions. The speed of the first was -450 km/s (FWHM=30 km/s), and the second -685 km/s (FWHM = 130 km/s).

At the moment of the second outburst, the absorption of the H_α line shows a five-component structure, with corresponding radial velocities RV_1=-1146 km/s, RV_2=-1054 km/s, RV_3=-972 km/s, RV_4=-798 km/s, RV_5=-508 km/s. This is due to different speeds in different layers.

High-resolution ESO spectra showed that NaI D interstellar absorption lines have an 8-component structure with radial velocities -13.2 km/s; 8.3 km/s; 25.43 km/s; 48.5 km/s; 57.9 km/s; 63.6 km/s; 73.8 km/s; 102.3 km/s, respectively.

Acknowledgements. The authors are grateful to the people of the ARAS association and ESO for making freely available the spectra of their observations. We also thank the observers registered to the AAVSO database who contributed to the photometric monitoring of ASASSN-17hx.

References

1. Stanek K.Z. et al. The Astronomer's Telegram 2017, No 10523
2. Kurtenkov, A. et al. The Astronomer's Telegram, 2017, No. 10527
3. Williams, Robert E. Astronomical Journal 1992, v.104, p.725. DOI: 10.1086/116268
4. Williams, R.E. et al. Astrophysical Journal Supplement 1994, v. 90, p. 297. DOI: 10.1086/191864
5. Mikailov, Kh. M. et al. Kinematics and Physics of Celestial Bodies, 2020, v. 36 (1), p. 22. DOI: 10.3103/S0884591320010043
6. http: //www.gazinur.com/DECH-software.html
7. http://archive.eso.org/wdb/wdb/eso/eso_archive_main/query
8. http://www.astrosurf.com/aras/Aras_DataBase/Novae/2017_NovaSct2017.htm
9. https://www.aavso.org/www.aavso.org/LCGv2/index.html
10. Williams, R. The Astronomical Journal 2012, v. 144 (4), id. 98. DOI: 10.1088/0004-6256/144/4/98
11. Mason, E. et al. Astronomy & Astrophysics 2020, v. 635, id.A 115, 16 p. DOI 10.1051/0004-6361/201937025

SPATIAL STRUCTURE OF THE OCTAPEPTIDE MOLECULE

LI ISMAILOVA, RM ABBASLI and NA AKHMEDOV

Baku State University, Baku, Azerbaijan
E-mail: lara.ismailova.52@mail.ru, namiq.49@bk.ru, ranaabbasli54@mail.ru

Peptide molecules in the cell carry out all regulatory processes. Understand the mechanisms of action of these molecules can be, if you solve the problem of their structural and functional activity. The role of modern computer programs in studding of the spatial structure of the peptide molecules in living systems is very important. This work is devoted to study the spatial organization, conformational possibilities of the octapeptide molecule Pro-Pro-Gly-Leu-Gly-Pro-Leu-Arg. The calculations were carried out by the method of theoretical conformational analysis and a special computer program. The low-energy conformations of this molecule and the values of the dihedral angles of the main and side chains are founded. The energy of the intra- and inter-residue interactions is estimated. The conformational mobility of the amino acid side chains is investigated and the amino acids with specific interplays with different receptors are founded.

Keywords: molecule, peptide, conformation,structure, shape
PACS: 87.15 Aa, 87.15 He, 06.30.Bp

Introduction

The peptide molecules and thear biological functions in living systems are related with their specific spatial structures. Therefore, to understand the mechanism by whitch the peptides function it is necessary to know their three dimensional structures. It is important to know the full complement of low-energy conformational states. Peptides regulate all functions of a living organism. It is known, that proline and glysin containing peptides had a protective effect in microcirculatory dysfunction under conditions of inflammation and stress [1].

Using a radioimmunoassay against the C-terminal sequence Arg-Pro-NH_2 (RP amide) have isolated the peptide Leu-Pro-Pro-Gly-Pro-Leu-Pro-Arg-Pro-NH_2 (Antho-RP amide) from an extract of the sea anemone Anthoplaurelegutissima. It is active molecule. It is known that octapeptide molecule Pro-Pro-Gly-Leu-Gly-Pro-Leu-Arg. has no effect [2]. This work is devoted to study the spatial organization, conformational possibilities of the octapeptide molecule Pro-Pro-Gly-Leu-Gly-Pro-Leu-Arg. This molecule has three amino acids Pro, which have a rigid side chain, two Gly, which has no side chain, two amino acids Leu and one Arg, with have large and labile side chains. The calculations were carried out by the method of theoretical conformational analysis and a special computer program]. The potential energy of this molecule was chosen as the sum of the nonvalent, electrostatic and torsional interaction energies and the energy of hydrogen bonds. The low-energy conformations of this octapeptide molecule, the dihedral angles of the backbone and side chains of the amino acid residues of this molecule, and the energies of intra- and inter-residual interactions were determined. The present paper is an extension of our previous investigations of structural and functional organization of peptide molecules [3-6].

Section

Neuropeptides play an important role in all nervous systems and structure-functional studies of these peptides is one approach to understanding this role. Calculation of octapeptide molecule Pro-Pro-Gly-Leu-Gly-Pro-Leu-Arg has been carried out by the method of theoretical conformational analysis with regard to nonvalent, electrostatic and torsional interactions and energy of the hydrogen bonds. In presenting the results of the calculation of the spatial structure of the molecules we used the spatial classification. All structural versions according to it break down into shapes including certain forms of the main chain, each form is represented by a set of conformations. The conformations are determined by the number of rotational degrees of freedom of the side chains of the residues being included in the molecule. The conformational state of each amino residue is conveniently described by the backbone ϕ, ψ, ω and side chain χ_1, χ_2… dihedral angles. The terms “conformation” used in the following analysis will always imply exact quantitative characteristics of residue or fragment geometry. For a stable conformation, the ϕ and ψ dihedral angles are located in low-energy region R, B, L and P of the conformational map. We introduce the notion “form of a residue” to denote the region of its backbone dihedral angle. The conformation of the backbone forms of residue in a given amino acid sequence will specify the backbone form of a fragment. Forms belonging to a particular shape have an analogous peptide chain contour and a similar mutual arrangement of backbones and side chains. Designations indications of dihedral angles have been measured up to the generally accepted nomenclature [7].

The conformational possibilities of octapeptide molecule Pro-Pro-Gly-Leu-Gly-Pro-Leu-Arg. were studied in fragments. First, the conformational properties of the tetrapeptide Pro-Pro-Gly-Leu were determined based on the stable conformations of the monopeptides N-acetyl-L-proline, L-glycine and L-leysine. Then the spatial structure of the hexapeptide Pro-Pro-Gly-Leu-Gly-Pro was studied. At the final stage of the analysis, calculation of the octapeptide molecule Pro-Pro-Gly-Leu-Gly-Pro-Leu-Arg were investigated. The starting conformations of this were constructed from the low-energy conformations of the hexapeptide fragment and the stable conformations of the dipeptide fragment Leu-Arg. We carried out all of these structures by minimization over all the dihedral angles.

Discussion and conclusions

Tetrapeptide molecule Pro-Pro-Gly-Leu contains 60 atoms and 15 variable dihedral angles. The conformational possibilities of the N-terminal Pro-Pro-Gly-Leu tetrapeptide have been studied at the first step on the base of low energy conformations of appropriate amino acid residues. It is known that for any amino acid residue (with the exception Gly) present in front of Pro having all conformations with R-form of main chain are high-energy therefore such state for Pro1 is excluded from the calculation. Thus initial structural variants can obtain only the following four shapes of peptide skeleton: eee, eef, efe and eff. There are the energy differentiation both in respect of the conformations, and forms of the main chain and shapes. Falling within the range 0-5.0 kcal/mol are representatives of four shapes. The shapes eee, efe and eff have enthalpic and entropic preference; they are presented by many low-energy conformations

Hexapeptide Pro-Pro-Gly-Leu-Gly-Pro contains 81 atoms and 20 variable dihedral angles. The octapeptide Pro-Pro-Gly-Leu-Gly-Pro-Leu-Arg contained 124 atoms and 34 variable dihedral angles. The relative energy of the conformations of the octapeptide molecule varied within the range 0–11 kcal/mol.

Over 200 initial approximations were compiled for octapeptide molecule. All of them were minimized by energy, their geometric and energy parameters were estimated. The low-energy conformations of the octapeptide molecule are presented in Table 1.

Table 1. The energy parameters: relative energy (U_{rel}) and energy contributions of nonvalent (U_{nv}), electrostatic (U_{el}), torsion(U_{tors}) interactions of optimal conformations of the octapeptide molecule

№	**Shape**	**Conformation**	**U_{rel}**	**Energy range, kcal/mol**		
				U_{nv}	**U_{el}**	**U_{tors}**
1	eeeffff	BBBB$_{3222}$PRR$_{2122}$B$_{3222}$	0,0	-31,7	0,2	3,0
2	eeeffff	BBBB$_{3222}$PRR$_{2222}$R$_{3222}$	4,5	-29,1	0,8	5,0
3	eefeffe	BBPB$_{2122}$RRB$_{2322}$B$_{1222}$	4,9	-29,6	0,2	5,0
4	eeefffe	BBBB$_{3222}$PRB$_{1222}$B$_{3122}$	5,0	-29,6	-0,9	7,3
5	eeefffe	BBBB$_{3222}$PRB$_{1222}$B$_{3322}$	5,1	-28,5	0,1	5,3
6	effeffe	BBPB$_{2122}$RRB$_{2322}$B$_{1222}$	6,4	-27,1	0,3	5,0
7	eeeeffe	BBBR$_{3122}$PRB$_{3322}$R$_{3322}$	6,9	-27,8	-0,3	6,8
8	effefee	BBPB$_{2122}$RBB$_{3222}$B$_{1222}$	7,9	-23,0	0,7	2,0
9	eeeffee	BBBB$_{3222}$PBB$_{1222}$B$_{3322}$	10,4	-23,5	-0,9	6,1
10	eeeeffe	BBBR$_{3222}$PRB$_{3222}$R$_{3322}$	8,3	-26,7	-0,4	7,2
11	eefeefe	BBRB$_{2122}$BRB$_{1222}$B$_{3222}$	11,2	-23,0	-0,3	6,2

The global conformation of this molecule (U_{rel}=0 kcal/mol) is BBBB$_{3222}$PRR$_{2122}$B$_{3222}$. The contribution of the stabilizing nonvalent to this conformation is (–31,7) kcal/mol, where as electrostatic interactions account for 0,2 kcal/mol and torsion for 3,0 kcal/mol. This conformation is efficient both in nonvalent and in electrostatic interactions forming hydrogen bonds between atoms of main chain which make contribution (-2.1 kcal/mol) in total energy. The main contributions of the interresidual interactions in this conformation were dipeptide contributions (–4,6) kcal/mol, tripeptide (–3,0) kcal/mol, tetrapeptide (–4,2) kcal/mol, pentapeptide (–8,7) kcal/mol, hexapeptide (-2,1) kcal/mol and heptapeptide (-6,9) kcal/mol.

In this conformation, amino acid residues Leu-Gly-Pro-Leu-Arg form folded structure but Pro-Pro-Gly-Leu takes extended form. Side chains Arg8 is labile in space that forms subsequently efficient interactions with previous residues Arg8-Pro2 (-5.8 kcal/mol), Arg8-Gly3 (-1.0 kcal/mol), Arg8-Leu4 (-3.0 kcal/mol), Arg8-Gly5 (-2.4 kcal/mol) and Arg8-Pro6 (-0.5 kcal/mol).

The geometric parameters of the three low-energy conformations of the octapeptide molecule are presented in Table 2.

It is revealed that low energy conformations of this molecule have the folded and half folded types of backbone. These folded forms bring parts of the backbone and the side chains of the amino acids together, and they result in convenient interactions.

The results can be used to study the spatial structure of octapeptide molecule as well as to study the conformational capabilities of side chains when interacting with receptor molecules. The side chain of Arg8 have no conformational freedom in the low-energy structures of the octapeptide molecule. Thus, the theoretical conformational analysis of the octapeptide molecule led to such structural organizations of molecules that do not exclude the realization by the molecule of a number of various functions that require strictly specific interactions with various receptors.

Table 2. Geometric parameters (degree) of the optimal conformations of Pro1-Pro2-Gly3-Leu4-Gly5-Pro6-Leu7-Arg8 octapeptide molecule

Residues	Shape (conformation)		
	eeeffff $BBBB_{3222}PRR_{2122}B_{3222}$	eeefffe $BBBB_{3222}PRB_{1222}B_{3122}$	effeffe $BBPB_{2122}RRB_{2322}B_{1222}$
Pro1	-60 161 175	-60 161 175	-60 157 176
Pro2	-60 168 175	-60 167 175	-60 138 178
Gly3	-73 74 -177	-73 74 -177	83 -69 179
Leu4	-93 131 180 -53 176 -174 181	-91 143 -171 -54 177 -174 180	-107 93 -165 181 62 175 172
Gly5	133 -72 178	142 -66 171	-106 -85 -166
Pro6	-60 -48 180	-60 -51 170	-60 -47 176
Leu7	-93 -57 -176 180 69 -173 178	-107 151 179 89 167 -166 180	-106 109 180 -172 -69 173 -167
Arg8	-113 95 180 -50 -63 -177 180	-118 -55 177 -66 85 177 -174	-128 151 180 59 180 179 180
U_{rel} (kcal/mol)	0	5.0	6.4

Note: The values of dihedral angles are given in the sequence φ, ψ, ω, χ^1, χ^2,...

Figures 1(a,b) represent schematically the backbone forms and positions of residues in low-energy conformations $BBBB_{3222}PRR_{2122}B_{3222}$ and $BBPB_{2122}RRB_{2322}B_{1222}$ of Pro1-Pro2-Gly3-Leu4-Gly5-Pro6-Leu7-Arg8 octapeptide molecule.

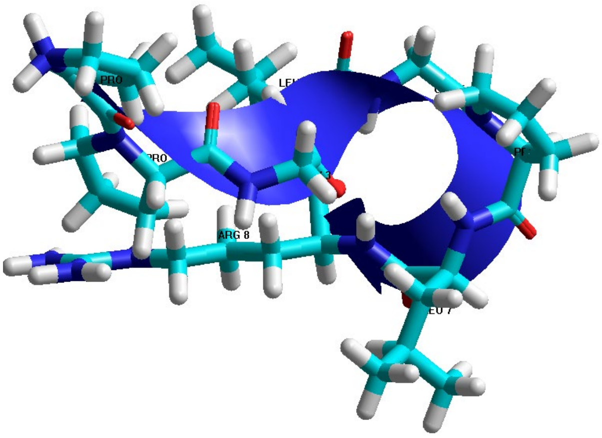

Fig. 1a. Spatial structure of the low energy conformational $BBBB_{3222}PRR_{2122}B_{3222}$ of the octapeptide molecule

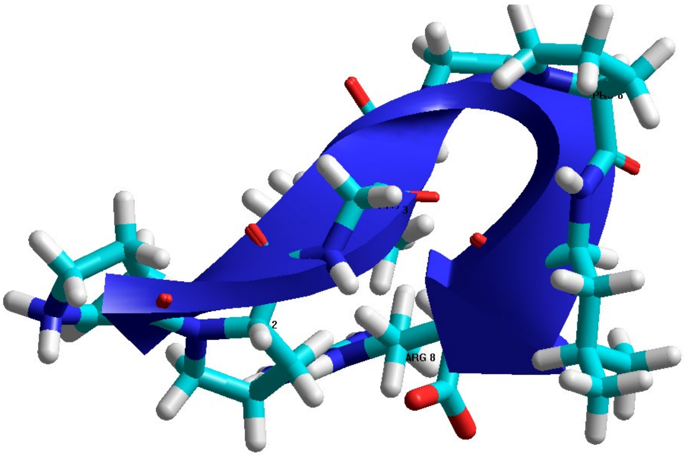

Fig. 1b. Spatial structure of the low energy conformational $BBBB_{3222}PRB_{1222}B_{3122}$ the octapeptide molecule.

The figures show that the octapeptide molecule has an extended N-terminal fragment and a folded C-terminal part of the molecule. Conformational possibilities of side chain of Arg8 in the best low energy conformations of octapeptide have been investigated by plotting conformational maps. The conformational maps show that side chain of Arg8 have no conformational free.

We have studied in detail the spatial structure and conformational properties of octapeptide molecule Pro1-Pro2-Gly3-Leu4-Gly5-Pro6-Leu7-Arg8. The relative energy of the conformations of the octapeptide molecule varied within the range 0–11 kcal/mol. Study of the spatial structure of the octapeptide have almost 11 low-energy conformations. It can be assumed that the low-energy folded form of the main chain of the molecule provides intramolecular interactions. Amino acid Arg8 lacks the ability to interact with the receptor. Therefore, the lack of activity of the octapeptide molecule can be associated with the folded form of the molecule and the lack of conformational freedom of amino acid residues.

References

1. Martinova K.B., Andreeva L.A., Klimova P.A. et al. Bioorg. Khim., 2009, v. 35, p. 165. DOI: 10.1134/s1068162009020022
2. Cartensen K., Kennth L. et al. Peptides 1992, v. 13, p. 851. DOI: 10.1016/0196-9781(92)90040-a
3. Akhmedov N.A., Ismailova L.I., Abbasli R.M., Agayeva L.N., Akhmedova S.R. IOSR JAP 2016, v. 8, p. 66. DOI: 10.9790/4861-08136670
4. Akhmedov N.A., Agayeva L.N., Akhmedova S.R., Abbasli R.M., Ismailova L.I. IOSR Journal of Applied Physics 2021, v. 13, p.62. DOİ:10.9790/4861-1305026267 www.iosrjournals.org.
5. Akhmedov N., Agayeva L., Akverdieva G., Abbasli R., Ismailova L. J.Chem.Soc.Pak. 2021, v. 43, p.500.
6. Ismailova L.I., Abbasli R.M., Akhmedov N.A. Proceedings of the 7-th International Conference on Control and Optimization with Industrial Applications 2020, v. 1, p. 218.
7. IUPAC IUB. Quantities, Units and Symbols in Physical Chemistry, Blackwell Scientific, Oxford 1993, DOI:10.1134,S0006350921040023.

INVESTIGATION OF ELECTROPHYSICAL PROPERTIES OF DEEPLY BURRIED AVALANCHE PHOTODIODES

EA JAFAROVA[1], AA DOVLATOV[2], LA ALIYEVA[1], RA ALIYEV[3] and ES TAPDYGOV[1]

[1] Institute of Physics of the NASA, Baku, AZ-1143, Azerbaijan
[2]Department of Physics, Azerbaijan State University of Oil and Industry, Baku, Azerbaijan
[3]Institute for Physical Problems of Baku State University, Baku, Azerbaijan
E-mail: celmira1@rambler.ru, lala1960@rambler.ru, alihuseyndovlatov@gmail.com

There have been investigated electric characteristics of avalanche photodiodes with deeply buried pixels (MAPD) at different polarities of potential applied to the n-Si substrate. It is shown that the optimal voltage of a structure with deeply buried pixels is higher than the breakdown voltage. The value of the maximum overvoltage at which the process of stable amplification of the photocurrent occurs is determined by the second inflection point of the volt-ampere characteristics (the first inflection point corresponds to the breakdown voltage and the onset of the avalanche process). An increase in the value of the optimal voltage significantly increases the multiplication factor of free charges, the magnitude of the photocurrent, and increases the energetic resolution of the photocurrent signal. At the forward bias of MAPD (negative potential is applied to n-Si substrate) the exponential rise of the current with the voltage Uf < 0.5 V ($I_{\mathrm{d}} = const \cdot \exp\frac{qU_f}{\beta kT}$, β~1.2) has been observed, what appropriate to diffusion mechanism of current leakage through p-n junction.

Keywords: micropixel avalanche photodiode, volt-ampere characteristic, breakdown voltage
PACS: 85.30.-z, 84.30.Jc, 85.30.Fg

Introduction

Recent years developed micropixel avalanche photodiodes have a wide application in creating devices and equipment for scientific research, radiation monitoring instruments, medical research equipment and other fields where supersensitive detectors are required.

MAPD constructions with high-density deeply buried n^+-regions (pixels) are described in details [1-4]. MAPD has a complex multilayered structure: in sections passing through n_{px}^+ -regions there are three p-n junctions, but in sections not passing through the said regions only one p-n junction (substrate-epitaxial layer) exists.

In works [2-5] there have been presented investigation results of photoelectric parameters of MAPD structure. Investigations of quantum efficiency show that high sensitivity of MAPD structures within short-wave length allows using these devices with scintillators and Cherenkov radiation detectors.

It is also established that MAPD structures have a wide range of photoresponse linearity ($5 \cdot 10^4$ photon/mm^2) based on the high pixel density [6]. Investigation of physical processes in multilayered MAPD structures at different polarities of potential to n- Si substrate is of interest.

Results and discussion

Total current passing through MAPD structure is defined as $I_{tot}=I_s+(I_d+I_{ph})\cdot M$, where I_s- is the surface current not participating in avalanche process, I_d - is the dark current generated in the volume depletion region, I_{ph}- is the photocurrent generated by the photons in depletion region, M- is the coefficient of avalanche charge carrier amplification.

The nature of occurrence of surface leakage current I_s in abrupt p-n junctions is related to the generation and recombination processes follow entere perimeter of photodiode. Its magnitude does not exceed 1 nA and depend on device area. The surface leakage current not crossing the avalanche region goes into the device contacts immediately and therefore it does not amplified.

For investigations there has been chosen MAPD- 3N (pixel density $4 \cdot 10^4$px /mm^2) sample with working voltage at room temperature U_f=90,2V and photodetection efficiency PDE=30%.

Volt-Ampere investigations show that at low reverse voltages (positive potential is applied to n-Si substrate) the observed slight rise in current is mainly related to the leakage current I_s. After free charge carriers are formed in the avalanche zone initiation the nature their generation is not important. At close to the breakdown voltages these charge carriers are accelerating in electric field and produce impact ionization, cause avalanche process. The latter brings about the sharp rise in current in structure under investigation.

In Fig. 1 there has been presented the dark current of MAPD-3N structures versus the applied reverse voltage. Two points of inflection are observed on the graph.

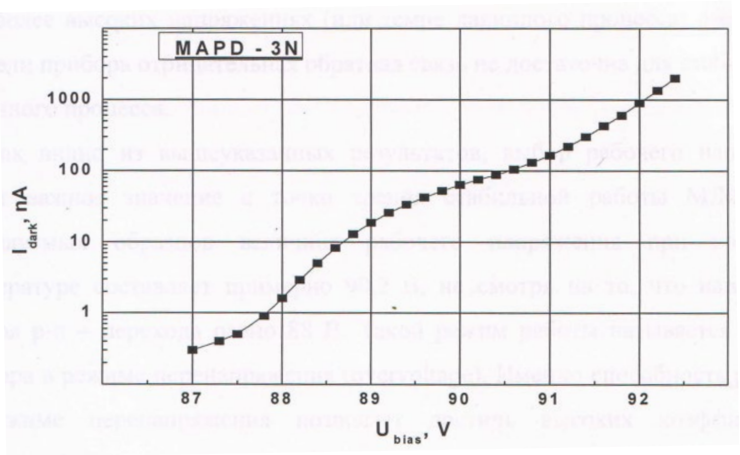

Fig. 1. Volt- Ampere characteristic of MAPD-3N with deeply buried pixels.

In figure 2 it is represented a graph of the differential volt-ampere dependence. It is seen that the inflection points coincide with the extremes of the differential current-voltage dependence. At low voltages down to 80V the magnitude of dark current I_d does not exceed 0.1nA and very slightly depends on the voltage. At U_f >87.5V there has been observed sharp rise in I_d (up to several orders) due to the high rate of avalanche process in the structure. By reaching U=88V (first of inflection) and above the rise in avalanche current retards because of negative feedback existing in each pixel (n_{px}^{+} - range) of MAPD (Fig. 1). This voltage is corresponding to the maximum point in Fig. 2 (88V) and its magnitude is the breakdown voltage. The second point of inflection In Fig. 1 is in agreement with the voltage 90.2 V, in this case the magnitude of current hardly depends on the voltage (minimum point in Fig. 2).

The calculations show that precisely this region of inflection is the optimum working voltage of micropixel avalanche photodiodes. At this value of overvoltage has been achieved the maximum amplification of photocurrent with mach possible stability of multiplication process. At higher voltages (91,5V) the instability of avalanche current is observed. It is explained of the fact that at higher overvoltage the negative feedback imbedded in the pixel's construction becomes not enough to stabilize avalanche process.

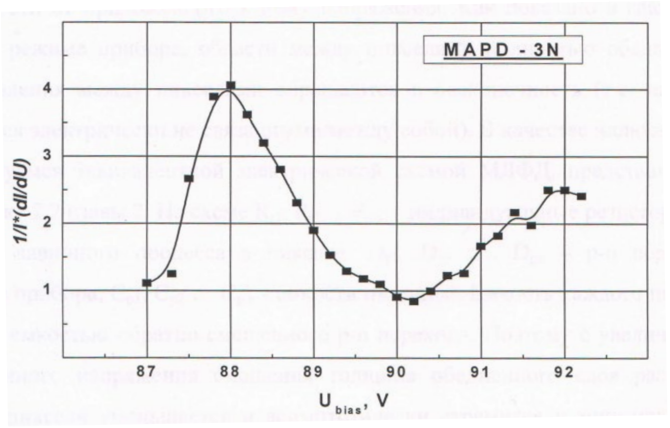

Fig. 2. Relative rate of change of the dark avalanche current as a function of the reverse voltage applied to the MAPD.

As it is seen from above the finding of working voltage is an important point for MAPD steady operation. For investigated samples the magnitude of working voltage at room temperature is about 90.2 V even though the breakdown voltage of p-n junction is 88V. The overvoltage capability allows high photocurrent gains to be achieved with low levels of excess noise factor in the MAPD. Traditional avalanche photodiodes cannot mainly work under the conditions like these because of danger of irreversible failure of semiconductor.

In works [7-9] there have been investigated the reactive properties of MAPD structures with deeply buried pixels by applying to the structure the negative potential to the substrate (n- Si). It is shown that by the voltage polarity like this the first p-n junction has a main part in physical processes going in investigated structures with three p-n junctions (in cross-sections passing through pixels).

To obtain the total information about the parameters of MAPD structures under investigation one can measure the current by applied the negative potential to n-Si substrate. In Fig. 3 there has been presented the dependence of current on direct bias in semi-logarithmic scale for one of the typical samples of MAPD-3N.

As it is seen from figure the exponential rise current with the voltage has been observed.

$$I_{\mathrm{f}} = const \cdot \exp\frac{qU_f}{\beta kT}$$

Within the low direct bias (0÷ 0.5) V the coefficient β derived from the slope of bias the given dependence weakens and β changes from the value ~2.8 to ~1.2.

Conclusion

It is shown that, in contrast to traditional avalanche photodiodes incapable of operating under overvoltage conditions (V_{over}) without irreversible damage and failure of the semiconductor device, MAPD structures with deeply buried pixels can operate at overvoltage and achieve maximum photocurrent amplification with the maximum possible stability of the amplification process. The exponential growth of the MAPD current with a forward bias voltage with a coefficient β ~ 1.2 at (U_f = 0 ÷ 0.5V) is associated with the diffusion mechanism of the leakage current.

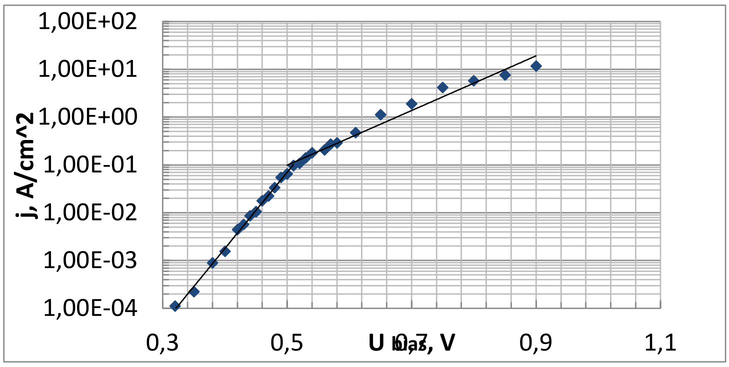

Fig. 3 Forward branch of Volt-Ampere characteristic of micropixel avalanche photodiodes (MAPD-3N) at T=300K (semi-logarithmic scale).

Acknowledgements

The authors are grateful to Dr. Z.Y. Sadygov for their helpful advice and comments at carrying out of experimental work and the writing this material.

References

1. Sadygov. Z., Micro-channel avalanche photodiode. Russian Patent №2316848, 2008, HOTL-31.06,Bul (4).
2. Anfimov N., Chirikov-Zorin I., Dovlatov A. et. al. Nucl. Instr. Meth. 2010, A. 617, p. 78.
3. Sadygov Z., Zerrouk F., Dovlatov A. et. al. Nucl. Instr. Meth. 2009, v. 610, p. 381.
4. Dovlatov A., Fizika 2009, v. 15(2) p. 180.
5. Jafarova E., Dovlatov A., Aliyeva L., Tapdyqov E., Askerova K. European Journal of Engineering Research and Science 2019, v. 4, p.108.
6. Sadygov Z. et.al. Pisma v JTF 2010, v. 36 (11), p.83.
7. Jafarova E., Sadygov Z., Dovlatov A., Aliyeva L., Tapdyqov E, Askerova K. Journal of Electrical Engineering 2017, v. 5, p.181.
8. Jafarova E., Iskenderzade Z., Dovlatov A., Aliyeva L., Tapdyqov E. ANAS Reports series of Phys-technical sciences, Physics and Astronomy 2013, v. 32, p. 526.
9. Jafarova E., Sadygov Z., Dovlatov A., Aliyeva L., Tapdyqov E. and Askerova K. European Journal of Engineering Research and Science 2018, v. 3(4), p. 61.
10. Sze S., Physics of Semiconductor Devices. Moscow, 1984, Mir, (1), p. 456.

ELECTRICAL PROPERTIES OF TWO-BARRIER SCHOTTKY DIODES

RK MAMEDOV and AR ASLANOVA

Baku State University, Baku, Azerbaijan
E-mail: rasimaz50@yahoo.com

An additional electric field (AEF) is localized at the edge of the interface of real Schottky diodes (SD) and it participates in the potential barrier formation. On the inner part of the SD contact, a potential barrier is formed according to the ideal Schottky model, and the real SD is characterized by a two-barrier energy structure. The forward branches of the I - V characteristic of the Au-nGaAs SD are shifted by a voltage value equal in magnitude to the voltage / -U$_C$ / AEF from the ordinate in the direction of increasing the voltage. At the initial values of the forward voltage, reverse currents flow through the SD, which also continue with reverse biases.

Keywords: real Schottky diode, additional electric field, voltage-current characteristic, potential barrier height
PACS: 72.40. +*w*, 72.80.Ey, 73.30.+y

Introduction

In connection with the development of modern measuring technology, especially scanning probe microscopy (SPM), some important features of the electronic processes occurring in real rectifying contacts of metals with semiconductors (CMS), i.e. SD. Using SPM measurement methods, the AEF was found in the edge region of the contact, which is well used for unambiguous interpretation of many features of real SDs, which are difficult to interpret with the theories of ideal SD [1-6]. AEF, which arises due to the potential difference between the interface surface and adjacent free surfaces of the semiconductor and metal, exists in almost all real CMS [1]. Unfortunately, the effect of AEF on the properties of SD is still poorly understood.

Figure 1 shows AFM images of the relief (*a*), potential (*b*), and profiles (*c*) of the metal cross sections and the surface potential of the Au-nGaAs Schottky contact [3].

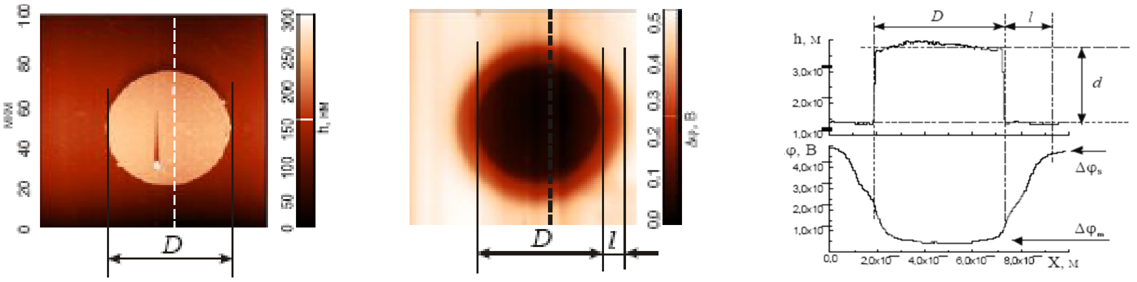

a) **b)** **c)**

Fig. 1. Atomic Force Microscopic relief (*a*), potential (*b*) and contour (*c*) cross-section of the space *h* and Δ*φ* Images of the surface Au-nGaAs contact with diameter of D = 50 µm.

Figure 1a shows that a round metal (Au) electrode with a diameter D on the surface of a semiconductor (nGaAs) plate has a clear circular boundary. Under the action of the AEF, a wheel-shaped transition region (areole) with a width (*l*) is formed around the contact on the semiconductor surface (figure 1*b*). The value of the potential along the width of the areole increases from the potential of the metal to the potential of the free surface of the semiconductor, and this is clearly seen in figure 1*c*.

AEF penetrates into the n-type semiconductor in depth and covers the edge near-contact region of wide contacts and the whole near-contact region of narrow CMS. Under the influence of AEF with a strength E_A, a redistribution of charges occurs and a space charge region (SCR) with an electric field strength E_I directed to the contact surface of the metal is formed. As a result of superposition of electric fields with strengths E_A and E_I, a resultant electric field (REF) with strength Er is formed in the SCR. The dependence of *Er* on the distance *x* is depicted by a curved line, where it has a low value near the interface and reaches a maximum at a sufficiently large distance from it. As a result, the metal and semiconductor in the depth of the SCR acquire the potentials φ_m and φ_s (where $\varphi_m < \varphi_s$). Thus, the SD under the influence of the resulting voltage drop ($-U_C$) due to the AEF becomes in a non-equilibrium state, where: $U_C = \varphi_s - \varphi_m$. In the event of a short circuit with a wire two ends of the SD with an area S_C and the potential barrier height of the Φ_B, in a closed external circuit under the influence of a negative voltage ($-U_C$) of the AEF in the absence of an external voltage, an electric current I_{Uc} can flow according to the thermionic emission theory [7].

$$I_{Uc} = S_C A T^2 \exp\left(-\frac{\Phi_B}{kT}\right)\left[\exp\left(-\frac{qU_C}{kT}\right)-1\right] \tag{1}$$

All designations are generally accepted.

Thus, the electrical properties of real SDs are determined by both the REF of the edge part and the SCR of the inner part of the near-contact region of the semiconductor, which determine the formation of the energy structure of the contact.

Two-barrier energy structure and current passage

Electronic processes in real SDs occur in the active participation of the electric field of the SCR of the inner part and the REF of the edge part of the contact. In wide SDs with a contact area S, the AEF is directed from the contact surface to the free surfaces of contacting materials and occupies a certain edge part with the potential barrier height Φ_{B2} and area S_2. The inner part of the SD contact with the potential barrier height Φ_{B1} and the area S_1 remains without AEF. As a result, the energy structure of a real SD in the absence of an external voltage *U* is depicted as shown in figere 2.

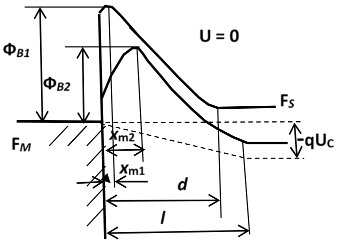

Fig. 2. Two-barrier energy structure of SD in the absence of external voltage.

The maximum barrier height Φ_{B1} of the inner contact surface is located from the contact surface of the metal at a distance x_{m1}, according to the Schottky model. In the equilibrium state, the saturation currents I_{S1} flowing in opposite directions over the barrier height Φ_{B1} become equal in magnitude to each other and, therefore, the current I_1 of the inner part of the contact becomes equal to zero. The edge part of the contact under voltage $(-U_C)$ of the AEB is in a non-equilibrium state and the maximum barrier height Φ_{B2}, formed on the basis of the REF, is located from the contact surface of the metal at a distance $x_{m2} > x_{m1}$. Through the edge part of the contact with S_2 and Φ_{B2}, a current flows in the opposite direction, which is determined by formula (1).

When a forward voltage is applied to the SD, its I – V characteristic, consisting of the sum of the currents of the internal I_{F1} and edge I_{F2} parts of the contact, is determined by the thermionic emission theory [2] and is expressed by the following formulas [8]:

at $0<U\leq/-U_C/$,

$$I_F = I_{F1} + I_{F2} = S_1AT^2\exp\left(-\frac{\Phi_{\mathrm{B1}}}{\kappa\mathrm{T}}\right)\left[\exp\left(\frac{qU}{n_{11}\kappa\mathrm{T}}\right) - \exp\left(-\frac{qU}{n_{12}\kappa\mathrm{T}}\right)\right] +$$
$$+ S_2AT^2\exp\left(-\frac{\Phi_{\mathrm{B2}}}{\kappa\mathrm{T}}\right)\left[\exp\left(\frac{-n_{21}qU_C + qU}{n_{21}\kappa\mathrm{T}}\right) - \exp\left(-\frac{qU}{n_{22}\kappa\mathrm{T}}\right)\right] \tag{2}$$

and at $U>/-U_C/$,

$$I_F = SAT^2\exp\left(-\frac{\Phi_{\mathrm{B}A}}{\kappa\mathrm{T}}\right)\left[\exp\left(\frac{qU}{n\kappa\mathrm{T}}\right) - \exp\left(-\frac{qU}{n'\kappa\mathrm{T}}\right)\right] \tag{3}$$

All designations are generally accepted.

The character of the initial section of the forward branch of the I - V characteristic of the SD is determined by the numerical values of S_1, S_2, Φ_{B1}, Φ_{B2} and the peculiarities of changes in Φ_{B1} and Φ_{B2} by $q\beta_1U$ and $q\beta_2U$, respectively. When the applied voltage becomes equal to the AEF voltage ($U=/-U_C/$), the current stops flowing through the edge part from S_2 of the contact. With a further increase in voltage ($U>/-U_C/$), currents begin to flow in the forward direction through both parts with Φ_{B1} and Φ_{B2} of the contact. A SD with a total contact area S has an effective potential barrier height Φ_{BA}, an ideality coefficient n, a dimensionless coefficient, n' and its I – V characteristic will be determined by formula (3).

When a reverse voltage ($U<0$) is applied to the SD, the current of the common contact is determined by the sum of the currents of the internal I_{R1} and edge I_{R2} parts of the contact and is determined by the following formula [8]:

$$I_R = I_{R1} + I_{R2} = S_1AT^2\exp\left(-\frac{\Phi_{\mathrm{B1}}}{\kappa\mathrm{T}}\right)\left[\exp\left(-\frac{qU}{n_{r11}\kappa\mathrm{T}}\right) - \exp\left(\frac{qU}{n_{r12}\kappa\mathrm{T}}\right)\right] +$$
$$+ S_2AT^2\exp\left(-\frac{\Phi_{\mathrm{B2}}}{\kappa\mathrm{T}}\right)\left[\exp\left(\frac{-n_{r21}qU_C - qU}{n_{r21}\kappa\mathrm{T}}\right) - \exp\left(\frac{qU}{n_{r22}\kappa\mathrm{T}}\right)\right] \tag{4}$$

The character of the reverse branch of the I - V characteristic of the SD is also determined by the numerical values of S_1, S_2, Φ_{B1}, Φ_{B2} and the features of changes

Results and discussion

From the two-barrier energy structure shown in figure 2 and analytical expressions for the I - V characteristics in the forward (2,3) and reverse (4) directions, it follows that the electrical properties of real SDs with AEF are determined by both their electrophysical and design-technological parameters. The interpretation of the published experimentally measured I - V characteristics of real SDs, which have certain deviations from the norm either in the forward or reverse direction, or in both directions, with the help of the Schottky one-barrier energy model and the thermionic emission theory, is often difficult, and usually no special attention is paid to these nuances. At the same time, the use of a two-barrier model of real SDs for a clear representation of electronic processes becomes more productive.

Figure 3*a* shows the I – V characteristics in the forward and reverse directions of an SD with a diameter of 1000 µm in a wide temperature range (100–320 K), made on the basis of the contact of an alloy (Au, Ag) with an n-type GaAs semiconductor [9]. It can be seen that the forward branches of the I - V characteristic of the (Au, Ag) -nGaAs SD are shifted by the voltage U_O, which is equal in modulus to / -U_C / AEF from the ordinate in the direction of increasing the voltage U. At the initial values of the forward voltage, reverse currents flow through the SD, which continue and with reverse biases (-U). The SD currents flow through the common contact area in the forward direction and the edge area in the reverse direction. The value of the short-circuit current I_{Uc} of the SD in the absence of voltage (U = 0) and the voltage U_C of the AEF at room temperature is about $1.2.10^{-9}$ A and 200 mV, respectively. With a decrease in temperature to 100 K, the current I_{Uc} decreases to 5.10^{-10} A (figure 3*a*) and the voltage U_C of the AEF increases to about 600 mV. The temperature dependence of the voltage / - U_C / of the AEF (Au, Ag) -nGaAs SD has a linear character.

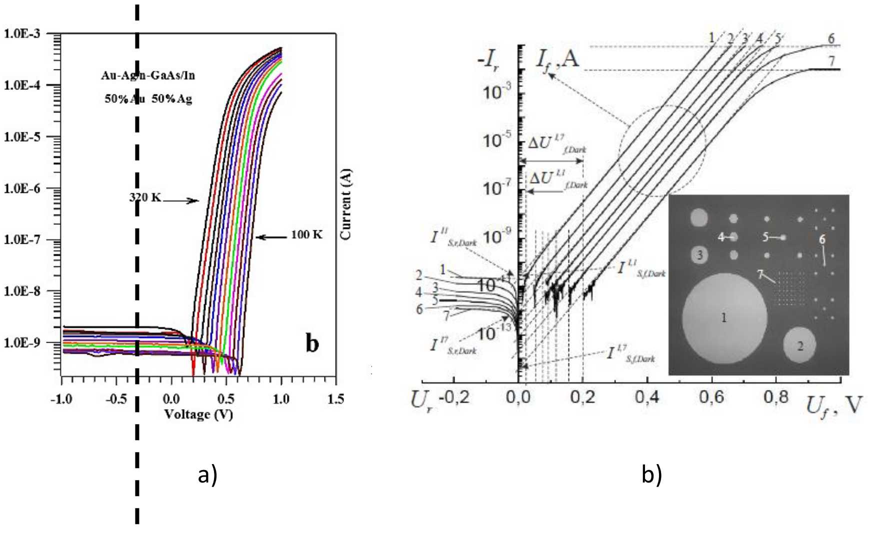

a) b)

Fig. 3. Temperature (a) and dimensional (b) dependences of the I-V characteristic. metal-nGaAs.

The results of measurements of the size dependences of the current passage into the metal - nSi SD with a potential barrier height of about 0.7 eV and different diameters (6-1000 µm) show [10] that the contribution of the edge current *Io* to the total diode current becomes insignificant at forward bias. With a reverse bias, it noticeably affects the current-voltage characteristic of the SD and causes a premature electrical breakdown of the junction. The breakdown voltage of the SD decreases with an increase in the contact diameter. However, the study of the current passage in Au - nGaAs SDs with a potential barrier height of about 1.1 eV and different diameters (5-500 µm) shows [11] that the contribution of the current Io to the total SD current significantly affects both the forward and reverse directions (figure 3*b*). The forward branches of the I - V characteristic of the Au - nGaAs SD are shifted by the U_C AEF in the direction of increasing voltage. The reverse branches of the I – V characteristic of the SD are almost entirely composed of the edge currents of the contact. The saturation currents of the SD in the forward and reverse directions differ significantly from each other and the difference between them increases with decreasing contact diameter and for SD with a diameter of 5 µm it is about 2 orders of magnitude.

Conclusion

The electrical properties of real SD with certain constructive structures have some specific features in the forward and reverse directions. At the edge of the SD interface, the AEF is localized and it participates in the formation of a potential barrier. A potential barrier is formed on the inner part of the SD contact according to the ideal Schottky model. The forward branches of the I – V characteristic of the Au-nGaAs SD are shifted by a voltage value equal in modulus to / $-U_C$ / AEF from the ordinate in the direction of increasing the voltage. At the initial values of the forward voltage, reverse currents flow through the SD, which also continue with reverse biases. The SD currents flow through the common contact area in the forward direction and the edge area in the opposite direction. The value of the short-circuit current I_{Uc} of Au - nGaAs SD in the absence of voltage (U = 0) and voltage U_C of the AEF at room temperature is about $1.2.10^{-9}$ A and 200 mV, respectively. The saturation currents of the SD in the forward and reverse directions differ and the difference between them increases with a decrease in the contact diameter from 500 to 5 µm, and for SD with a diameter of 5 µm it is about 2 orders of magnitude.

References

1. Mamedov R.K., Contacts metal-semiconductor with an electric spot field, Baku, BSU, 2003.
2. Zi S.M., Physics of Semiconductor Devices, Part 1. Moscow, Mir, 1984.
3. Torkhov N.A., Bozhkov V.G., Ivonin I.V., Journal of Surface Investigation 2009, v. 3 (6), p. 888.
4. Rhoderick E.H, Williams RH. Metal-Semiconductor Contacts. 2nd edn. Oxford, Claredon Press, 1988.
5. Mamedov R.K., News BSU 2013, v. 4, p. 128.
6. Tung RT. Phys Rev B 1992, v. 45, p. 13509.
7. Mamedov R.K., Aslanova A.R., J. Superlattices and Microstructures 2018, v. 118, p. 298.
8. Mamedov R.K., Aslanova A.R., J. Superlattices and Microstructures 2019, v. 136, p. 106297.
9. Küp S., Taşer A., Kanmaz İ., Güzeldir B., Sağlam M.. Materials Today: Proceedings 2019, v. 18, p. 1936.
10. Ismailov T.H., Aslanova A.R. Int. J. of Innovative Technology and Exploring Engineering 2015, v. 5, p. 1.
11. Torkhov N.A., Physics and Technology of Semiconductors 2018, v. 52 (10), p. 1150.

PHOTOLUMINESCENCE OF $CdGa_2Se_4$ and $ZnGa_2Se_4$ DOPED WITH Nd ATOMS

IA MAMEDOVA[1], AN NABIYEVA[1], TG KERIMOVA[1] and NA ABDULLAYEV[1,2]

[1]Institute of Physics of ANAS, Baku, Azerbaijan
[2]Baku State University, Baku, Azerbaijan
E-mail: irada_mamedova@yahoo.com

The photoluminescence spectra of $ZnGa_2Se_4$: Nd^{3+} and $CdGa_2Se_4$: Nd^{3+} at room temperature are studied. temperature. For the first time, emission lines were discovered in the photoluminescence spectra of $ZnGa_2Se_4$: Nd^{3+} and $CdGa_2Se_4$: Nd^{3+} in the range 880–920 nm, which are associated with transitions in the Nd^{3+} ion.

Keywords: Photoluminescence, intracenter transitions, $ZnGa_2Se_4$, $CdGa_2Se_4$, Nd
PACS: 78.55.-m, 82.60.Nh, 68.49.-h

Introduction

The study of the radiative characteristics of wide-gap semiconductors makes it possible to create various optoelectronic devices on their basis. The introduction of rare-earth activators makes it possible to obtain efficient luminescence with a sufficiently high quantum yield.

Compounds $A^2B^3{}_2C^6{}_4$ are characterized by bright luminescence, high photosensitivity, significant values of the band gap ~ 2.4 ÷ 4 eV, which is of interest for use as a matrix for doping with rare earth elements. It should be noted that there is a small number of works in which the results of studying of luminescence characteristics of $A^2B^3{}_2C^6{}_4$ compounds using REEs as activators are presented [1, 2]. We have previously investigated the photoluminescence of $ZnGa_2S_4$ <Nd> [3]. In the spectral range 400–1100 nm at 300 K, bands with split lines were observed, which belong to the intracenter luminescence of the Nd^{3+} ion.

In this work, as a matrix for doping with Nd^{3+} ions, we used compounds that are representatives of ternary semiconductors of the $A^2B^3{}_2C^6{}_4$ group, $CdGa_2Se_4$, and $ZnGa_2Se_4$.

Experimental technique

Samples for measurements were synthesized from the initial components Zn, Cd, Ga, and Se taken in a stoichiometric ratio in graphitized quartz ampoules. An impurity of the rare earth element Nd was introduced during the synthesis. X-ray diffractometric studies were carried out on a Bruker D8 Advance instrument. Lattice parameters a = b = 5.571 Å, c = 10.759 Å, c / a = 1.931. $CdGa_2Se_4$ and $ZnGa_2Se_4$ crystallize in a tetragonal structure (space group S_4^2) (Fig. 1). The photoluminescence spectra were measured on a Nanofinder 30 confocal laser microspectrometer (Tokyo Instr., Japan). A femtosecond tunable Ti-doped sapphire laser (Spectra Physics, USA) with a second harmonic wavelength of 400 nm and a maximum power of 10 mW and a Nd: YAG laser with an output radiation wavelength λ = 532 nm were used as a source of exciting light.

Discussion

As it is known, $CdGa_2Se_4$ and $ZnGa_2Se_4$ compounds belong to tetrahedral ordered vacancy

$A^{II}B_2^{III}C_4^{VI}$ compounds. These compounds usually have tetragonal lattice structure with space groups: S_4^2 or D_{2d}^{11} [4]. The Brillouin zone for the $A^{II}B_2^{III}C_4^{VI}$ lattice shown in Fig. 1 (b) four times less than the Brillouin zone of sphalerite [5].

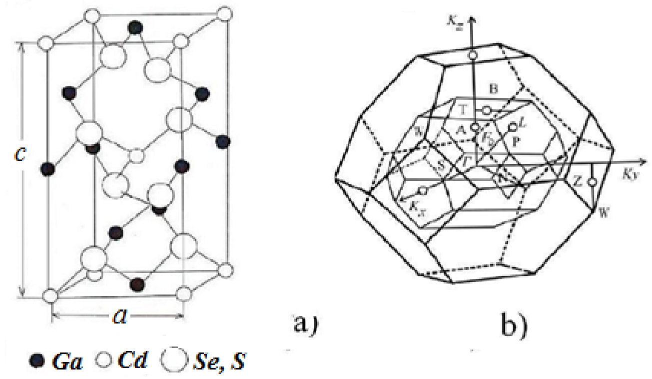

Fig. 1. Crystal lattice (a) and Brillouin zone (b) of $A^{II}B_2^{III}C_4^{VI}$ group compounds

Figures 1, 2 show Raman spectra of $CdGa_2Se_4$ and $ZnGa_2Se_4$.

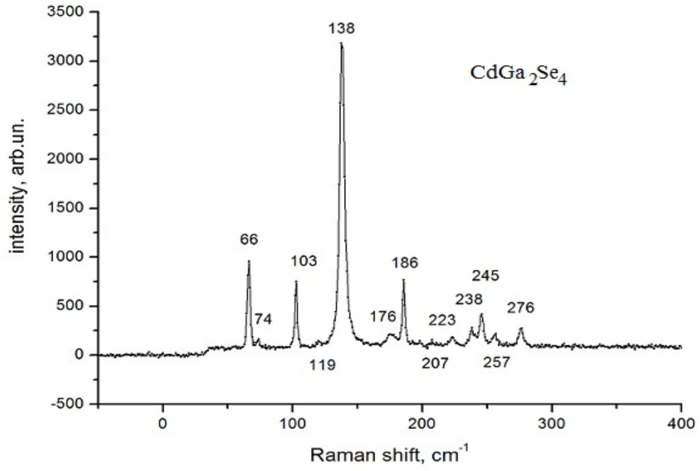

Fig. 1. Raman spectrum of $CdGa_2Se_4$

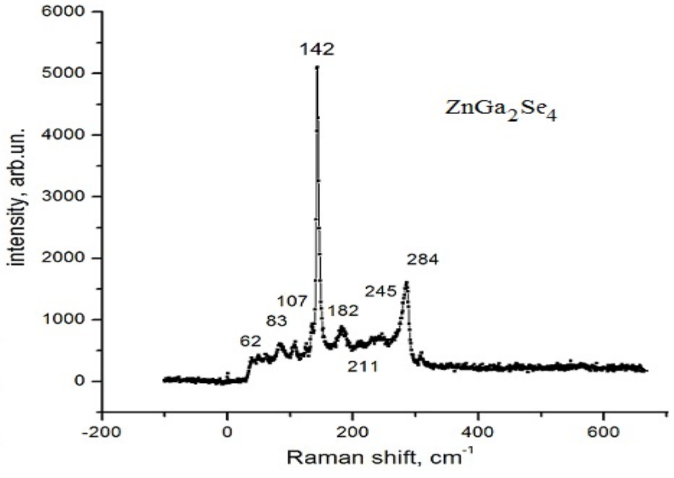

Fig. 2. Raman spectrum of $ZnGa_2Se_4$

The observed frequencies of the phonons $CdGa_2Se_4$ and $ZnGa_2Se_4$ and the determination of their symmetry are widely discussed in [6, 7].

Semiconducting compounds with a band gap of more than 2 eV are promising materials for use as a matrix for doping with rare earth elements. The value for band gaps of $CdGa_2Se_4$ and $ZnGa_2Se_4$ were determined in [8, 9] as 2,32 eV and 2, 45 eV, respectivly.

Figure 3 shows the PL spectrum of $ZnGa_2Se_4$: Nd^{3+} upon laser excitation at 532 nm at 300 K. It should be noted that Nd atoms have good solubility in $ZnGa_2Se_4$ and $CdGa_2Se_4$. As can be seen from the figure, the PL spectrum consists of an emission band, which is split by the crystal field into sublevels, where more intense emission lines are observed at 880 nm, 898 nm, and 906 nm.

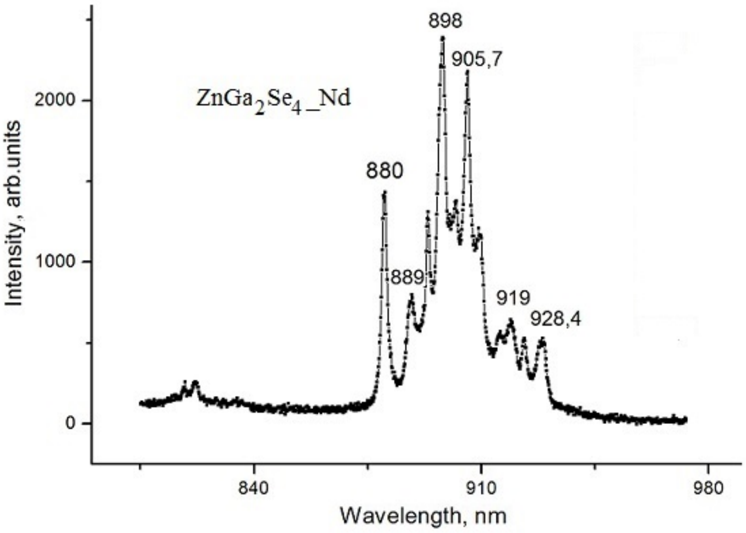

Fig. 3. Photoluminescence spectrum of $ZnGa_2Se_4$: Nd^{3+}

The photoluminescence spectrum of $CdGa_2Se_4$:Nd^{3+} (Fig. 4) also exhibits narrow equidistantly spaced lines at 886nm, 902nm, and 920nm.

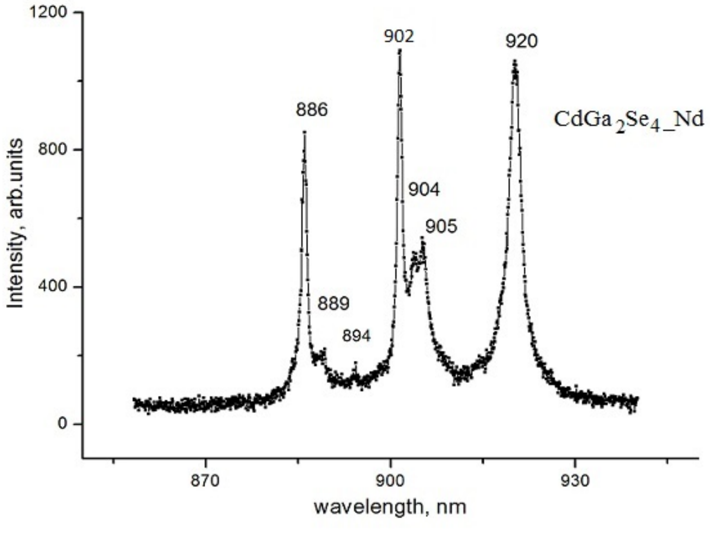

Fig. 4. Photoluminescence spectrum of $CdGa_2Se_4$: Nd^{3+}

Comparison with the literature [10, 11] and tabular data of the values of the frequencies of electronic transitions in the neodymium atom suggests that these bands with split lines are related to the intracenter luminescence of the Nd^{3+} ion. These lines are laser in nature due to radiative transitions between the $^4F_{3/2}$ → $^4I_{9/2}$ levels. The half-widths of all lines observed in the PL spectrum of $ZnGa_2Se_4$: Nd^{3+} and $CdGa_2Se_4$: Nd^{3+} are in the order of 1–2 nm. Table 1 shows the identification of the Nd^{3+} lines in $ZnGa_2Se_4$ and $CdGa_2Se_4$.

Table 1. PL bands of the Nd^{3+} ion in $CdGa_2Se_4$ and $ZnGa_2Se_4$

Compound	**$CdGa_2Se_4$: Nd^{3+}**	**$ZnGa_2Se_4$: Nd^{3+}**
Wavelength, nm	886 902, 904, 905 920	880, 888, 893, 898, 901, 906, 909, 915, 918, 923, 928
Transition	$^4F_{3/2}$ → $^4I_{9/2}$	

Conclusion

The photoluminescence spectra of $ZnGa_2Se_4$: Nd^{3+} and $CdGa_2Se_4$: Nd^{3+} at room temperature are studied. The temperature upon excitation of light is 532nm. The emission lines in the photoluminescence spectra of $ZnGa_2Se_4$: Nd^{3+} and $CdGa_2Se_4$: Nd^{3+} in the range 880–920 nm, which are associated with the $^4F_{3/2}$ → $^4I_{9/2}$ transitions in Nd^{3+} ion, have been found.

Acknowledgment

This work was carried out with financial support from the Foundation for the Development of Science under the President of the Republic of Azerbaijan (Grant No. EIF-BGM-3-BRFTF-2 + / 2017-15 / 02/1)

References

1. Tagiev B.G., Guseinov G.G., Jabbarov. R.B. et al. Izv. RAS. Inorganic materials 2000, v. 36 (12), p. 1415.
2. Claudia W., Shuang Zh. and Hartmu H. Kristallograf. 2005, v. 220, p. 277.
3. Mamedova I.A. Transactions of ANAS 2017, v. 37, p. 21.
4. Hahn H., Frank G., Klinger W. and et al, Storger A. D. and Storger G. Zeitschrift fur Anorganische und Allgemeine Chemie 1955, v. 279 (5-6), p. 241.
5. Kerimova T.G. Doc. Thesis. Phys.-mat. Science, Baku, 1966.
6. Jahangirli Z.A., Kerimova T.G., Abdullaev N.A. et al. Physics and Technology of Semiconductors 2017, v. 51, p. 585.
7. Kerimova T.G., Mamedova I.A., Abdullaev N.A. et al. Physics and Technology of Semiconductors 2014, v. 48, p. 894.
8. Chang-Dae K., Tong-San Ch., Wha-Tek K. et al. Solid State Communication 1987, v. 63 (9), p. 871.
9. Lee Y.-L. and Kim W.-T. Phys. Rev. B 1994, v. 50, p. 10672.
10. Rasuleva A.V., Solomonov V.I. Solid State Physics 2005, v. 47, p. 1432.
11. Kaminskiy 3.A., Sarkisov S., Chan H. and etc. J. Inorganic materials 1980, v. 16, p. 1333.

Ab INITIO STUDIES OF ELECTRONIC BAND STRUCTURE OF DEFECTS IN CdMnS

MA MEHRABOVA[1], NT PANAHOV[2] and NH HASANOV[3]

[1]Institute of Radiation Problems, ANAS, Baku, Azerbaijan
[2]Azerbaijan University of Architecture and Construction, Baku, Azerbaijan
[3]Baku State University, Baku, Azerbaijan
E-mail: m.mehrabova@science.az

Ab initio calculations are performed in the Atomistix Toolkit program within the DFT and LSDA on DZDP basis to calculate the electronic band structure of ideal and defective $Cd_{1-x}Mn_xS$ semimagnetic semiconductors. Supercell of $Cd_{1-x}Mn_xS$ of 8 and 64 atoms was constructed, atom relaxation and optimization of the crystal structure were carried out. We have used Hubbard U potential U_{Mn} = 3.59 eV for *3d* states for Mn atoms. Electron band structure, density of states, total energy were calculated. Our calculations show that the band gap increase with the increase in Mn concentration. It was defined that defects as interstitial Cd (S) atom or Cd(S) vacancy in the crystal structure lead to increasing of band gap, shifting of Fermi level towards the valence or conduction band. We can manage the physical properties of $Cd_{1-x}Mn_xS$ SMSC by variation of Mn ion concentration and defects in the crystal structure.

Keywords: Ab initio calculations, DFT, semimagnetic semiconductors, electronic band structure, interstitial atom, vacancy
PACS: 42.70.Nq, 71.20.-b, 75.50.Gg

Introduction

Room temperature CdS based semimagnetic semiconductors (SMSC), such as Mn doped CdS is a very good photo-luminance compound due to *d* states at the top of the valence band and intra-*d* shell transitions [1]. The ternary nature of CdMnS SMSC gives us the possibility of tuning the lattice constant and band parameters by varying the composition of the material. The substitutional Mn atoms in the CdS lattice are also characterized by highly efficient electroluminescence, which makes this material important in the context of optical flat panel display applications [2,3].

The Mn-CdS sheet with 16 atom supercell is analyzed by Kumar et al. [4]. Nabi [5] investigated electronic and magnetic properties of Mn doped CdS in wurtzite phase, using ab-initio calculations based on LDA, GGA and LDA + U exchange and correlation functionals. Ahmed et al. [1] investigated electronic band structure of $Cd_{1-x}Mn_xS$ (x = 6.25 %) using spin-polarized Density Functional Theory (DFT) within the framework of Generalized Gradient Approximation (GGA), its extension via on-site Hubbard U interactions (GGA + U) and a model for exchange and correlation potential TB-mBJ. The electronic band structure of wurtzite CdS calculated by Rantala et al. using two different self-consistent ab initio LDA methods [6].

The purpose of this work was to calculate the electronic band structure of defects as interstitial Cd (S) atom and Cd(S) vacancy in $Cd_{1-x}Mn_xS$ SMSC.

Methods and results

Ab initio calculations are performed in the Atomistix Toolkit (ATK) program within the DFT and LSDA on DZDP basis. We have used Hubbard U potential U_{Mn} = 3.59 eV for 3*d* states for Mn atoms [2,7,8]. An ideal supercells of 8 (Figure 1) and 64 (Figure 2) atoms were constructed. After the construction of $Cd_{1-x}Mn_xS$ (x = 0; 6.25 %; 25%) supercells, atom relaxation and optimization of the crystal structure were carried out to eliminate forces and minimize stresses. Electron band structure, density of states were calculated, total energy have been defined in antiferromagnetic (AFM) and ferromagnetic (FM) phases. The band gap for the $Cd_{1-x}Mn_xS$ with x=0.25 supercells is equal to E_g=1.6 eV and total energy is equal to E_t=-6698.61546 eV. For the x=0.0625 supercell band gap is equal to E_g=1.25eV and total energy is equal to E_t=59267.92943 eV. Calculations show that the band gap increase with increase in Mn ion concentration (Table 1).

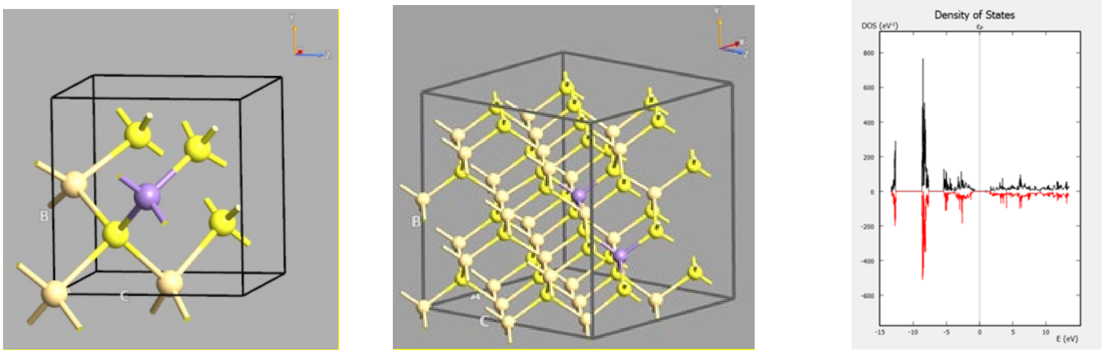

a) b) c)

Fig. 1. $Cd_{1-x}Mn_xS$ *a*) x=0.25, bulk configuration; *b*) x=0.0625, bulk configuration; c) x=0.0625, density of states.

Table 1. Band gap and total energy for $Cd_{1-x}Mn_xS$, $0 \le x \le 0.25$

x	E_g, eV	E_t, eV
0	0.83	-1910,95
0.0625	1.25	-59267,93
0.25	1.6	-6698,62

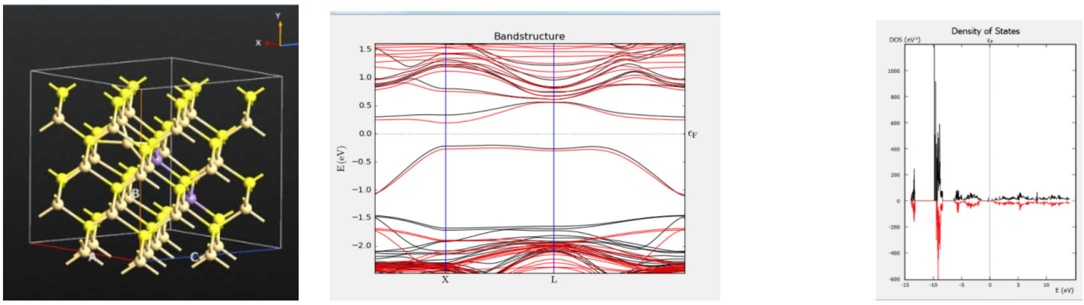

a) b) c)

Fig. 2. Interstitial Cd atom in $Cd_{1-x}Mn_xS$, a) bulk configuration; b) electronic band structure; c) density of states

Supercell of $Cd_{1-x}Mn_xS$ of 64 atoms with interstitial Cd ($I_{Cd)}$ atom and interstitial S (I_S) atom were constructed. After the construction of $Cd_{1-x}Mn_xS$ (x=6.25 %) supercell with interstitial Cd or S atom, atom relaxation and optimization of crystal structure were carried out. Electron band structure, density of states were calculated, total energy have been defined (Figure 2, Figure 3). In the case of Interstitial Cd atom, the band gap is equal to E_g=1.35 eV, total energy is equal to E_t=-60817.72528 eV (Figure 2).

For the interstitial S atom the band gap is equal to E_g=1.75 eV, total energy is equal to E_t=-59624.67318 eV (Figure 3). It can be concluded that Interstitial Cd or S atom in crystal structure leads to an increase in the band gap and total energy, Fermi level shifts towards the valence or conduction band (Table.2).

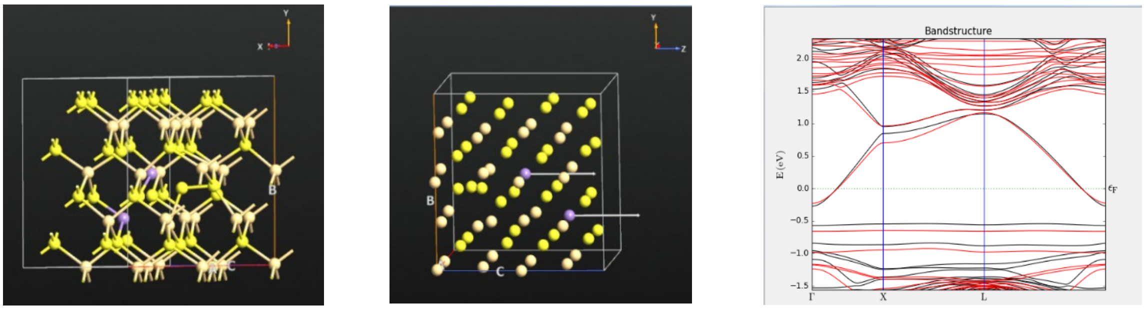

a) b) c)

Fig. 3. Interstitial S atom in $Cd_{1-x}Mn_xS$:
a) bulk configuration; b) magnetic momentsin FM phase; c) electronic band structure

In the case of S vacancy (V_S), the band gap is equal to E_g=1.3eV, total energy is equal to E_t=-58907.646 eV (Figure 4); for Cd vacancy (V_{Cd}) the band gap is equal to E_g=1.55 eV, total energy is equal to E_t=-57712.50684 eV (Figure 5).

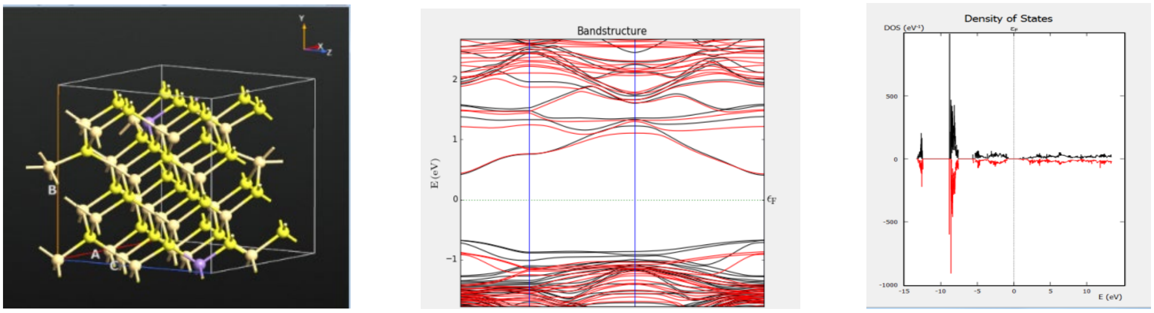

a) b) c)

Fig. 4. S vacancy in $Cd_{1-x}Mn_xS$, x=0.625 a) bulk configuration; b) electronic band structure; c) density of states

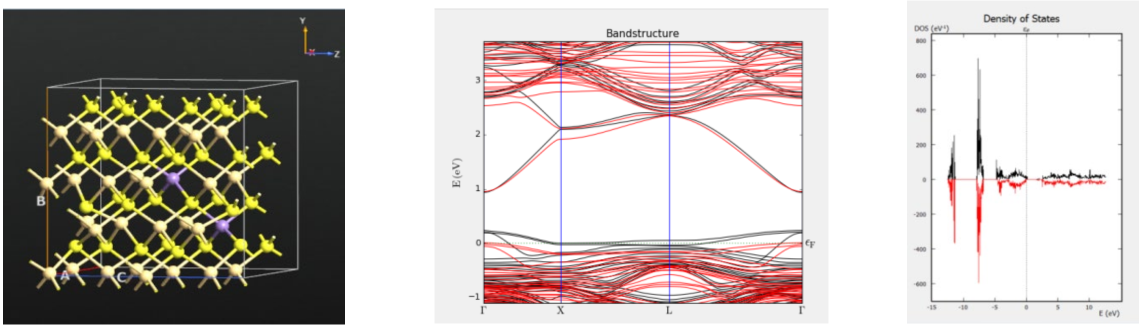

a) b) c)

Fig. 5. Cd vacancy in $Cd_{1-x}Mn_xS$, x=0.625 a) bulk configuration; b) EBS; c) DOS

It can be concluded that Cd or S vacancy in crystal structure leads to an increase in the band gap, decrease in the total energy, Fermi level shifts towards the valence or conduction band (Table.2).

Table 2. Band gap and total energy for Interstitial Cd (S) atom and Cd (S) vacancy in $Cd_{1-x}Mn_xS$, x=0.25

x=0.0625	Ideal	V_{Cd}	V_S	I_{Cd}	I_S
E_g, eV	1.25	1.55	1.3	1.35	1.75
E_t, eV	-59267.93	-57712.5	-58907.646	-60817.73	-59624.67

Conclusion

Ab initio calculations have been performed to analyze electronic band structure of ideal and defective $Cd_{1-x}Mn_xS$ SMSC (x =0.25; 0.0625). It has been defined that with an increase in Mn ion concentration in the $Cd_{1-x}Mn_xS$, there is an increase in the band gap. Based on the results obtained we can state that defects in crystal such as interstitial atom and vacancy lead to an increase in the band gap, change in the total energy, shifting of Fermi level towards the valence or conduction band. Thus, we can manage the physical properties of $Cd_{1-x}Mn_xS$ SMSC by variation of Mn ion concentration and defects in the crystal structure.

References

1. Ahmed N., Nabi A., Nisar J., Tariq M., Javid M.A., Nasim M.H. Materials Science 2017, v. 35 (3), p. 479. DOI: https://doi.org/10.1515/msp-2017-0084
2. Mehrabova M.A., Orujov H.S., Hasanov N.H., Kazimova A.I., Abdullayeva A.A. Mechanics of Solids 2020, v. 55 (1), p.108. DOI: 10.3103/S0025654420010021
3. Nazir S., Ikram N., Tanveer M., Shaukat A., Saeed Y., Reshak A.H. J. Phys. Chem. A. 2009, v. 113, p. 6022. DOI: 10.1021/acs.jpca.1c06685
4. Kumar S., Kumar A., Ahluwalia P.K. AIP Conference Proceedings, New York. 2014, p. 1732.
5. Nabi A. Computer Matererial Science A 2016, p.210.
6. Rantala T.T., Rantala T.S., Lantto V., Vaara J. Surface Science 1996, v. 352, p.77.
7. Mehrabova M.A., Hasanov N.H., Huseynov N.I., Kazimova A.I. Journal of Radiation Researches 2020, v. 7 (2), p. 39.
8. Mehrabova M.A., Orujov H.S., Hasanov N.H. International Journal of Materials Science and Applications 2014, v. 3 (6-1), p.24. DOI: 10.11648/j.ijmsa.20211004.11.

VAPOR SYNTHESIS OF ZnO NANOCRYSTAL-BASED HOLLOW MICROSPHERES

A.JISHIASHVILI, A.CHIRAKADZE, Z.SHIOLASHVILI, N.MAKHATADZE,
V.GOBRONIDZE and D.JISHIASHVILI

Georgian Technical University, V. Chavchanidze Institute of Cybernetics. 5, Z. Andjaparidze St., 0186, Tbilisi, Georgia
E-mail: ajishiasvili@gmail.com

The hollow micro- and nanostructures have shown high optical, catalytic, sensing and other activities. In this paper, we have developed the ammonium chloride (NH_4Cl) based technology for the vapor synthesis of ZnO and Zn-based nano- and micromaterials. We have shown that using NH_4Cl, ZnO and Zn powders as a source powders, the layered microspheres can by synthesized, having diameters up to 100 micrometers. The layers were synthesized at 410°C. They were contained Zn plates with embedded, 100-200 nm sized ZnO nano crystals. The annealing of these spheres at the same temperature in an oxygen deficient environment caused the outdiffusion of Zn from the layer to the surface, oxidation and formation of a shell, which was encapsulating the Zn-rich spherical core. Further annealing resulted in the increase of Zn internal pressure in the core, followed by the micro-explosion of a shell and the formation of hollow ZnO microspheres.

Keywords: ZnO, ammonium chloride, hollow microsphere
PACS: 81.07.-b, 68.37.Hk, 81.15.Gh

Introduction

Benefiting from the wide direct band-gap (3.5 eV at 300K), lasing ability, piezoelectric properties, high thermal and chemical stability, low toxicity, biocompatibility, and other unique properties the ZnO nanomaterials can be considered as one of the popular and most studied semiconductors. [1-4].

As is well-known, the morphology of nanomaterials strongly affects their properties [5-8]. This enables the tailoring of nanomaterial functionality by controlling their shape. Recently, the hollow nano- and microspheres attracted great attention due to their out-standing properties [9-11]. They have a high specific surface area, a low density, a high surface-to-bulk ratio, and a high density of surface active sites. According to these unique properties, the hollow ZnO micro-and nanospheres are highly desirable materials to be used as catalysts and materials for surface effect-based devices, including different gas- and biosensors, UV photodetectors, catalysts etc.

The purpose of this work was to develop the new technology for the growth of ZnO nanomaterials, including hollow microspheres and to study the mechanism of their formation. The technological novelty of this work is in the application of ammonium chloride (NH_4Cl) thermal decomposition products for producing ZnO micro- and nanomaterial.

Experimental

Microspheres were produced in a vertical quartz reactor. It was first evacuated to 2.10-5 Torr and then isolated from the vacuum pumps. Its bottom was loaded with a mixture of ZnO (0.9g), Zn (0.4mg), and NH_4Cl (0.8g) powders and heated by an external furnace up to 550°C. The substrate was at a 2 cm distance above the source and was heated by the convective flow at a rate of 11°C/min. At the beginning of heating, as the source temperature reached 195°C, NH_4Cl decomposed into ammonia and HCl, which reacted with ZnO to form volatile $ZnCl_2$ and

H_2O [12]. The maximum substrate temperature of 410°C was reached and stabilized after 40 minutes of heating (Fig. 1). We selected the weight of ammonium chloride in such a way that approximately at that time, it would be completely decomposed and evaporated. The selected substrate temperature was close to the melting point of Zn (419°C). This was the first stage of the growth, after which no oxidizing H_2O molecules and $ZnCl_2$ precursors were produced (Fig. 1). Beginning from this point, the Zn powder in the source was the only supplier of Zn vapor, and the residual air and air leakage in the sealed reactor were the only suppliers of oxide molecules. In this oxygen-deficient atmosphere, the Zn-rich material was deposited on the Si substrate, forming the layered spheres. This was the second growth stage. The Zn powder in the source was completely consumed in 70 min. From this point on, the third growth stage was started, which was the simple annealing of the spheres in the residual air for extra 20 minutes (Fig. 1). All three growth stages were performed sequentially in one closed technological cycle.

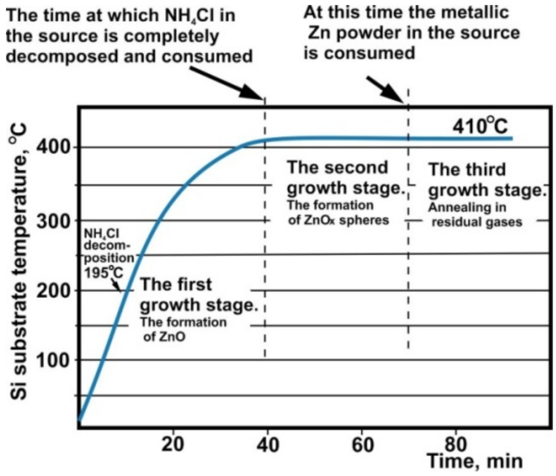

Fig. 1. The time-temperature graph of the growth process.

Results and discussion

In the first growth stage, which proceeded in the presence of oxidizing water molecules and a gradually raising substrate temperature, the dense nanocrystalline ZnO layer was formed on Si. The sizes of ZnO crystals varied in the range of 0.5-2.0 micrometer. Most of them had hexagonal bases and prism, pyramid, or truncated pyramid habits. After 40 minutes of growth, the temperature was stabilized at 410°C. SEM image and corresponding XRD pattern of deposited granular ZnO crystals are represented in Fig. 2. No phases other then ZnO were found in the XRD pattern.

The crystalline Zn and ZnO both have hexagonal structures. However, there is a great difference in the surface properties of their facets. The Zn terminated basal (0001) facet of ZnO has the highest surface energy and chemicall activity [13]. ZnO crystals usually grow along *c*-axis, which is perpendicular to Zn (0001) surface. In contrast to this, the {0001} facets of metallic Zn have a lowest surface energy. They are chemically inert, more stable, and resistive to oxidation [14-16]. Accordingly, the metallic Zn nano- and microcrystals naturally grow laterally by expanding their chemically active $\{10\bar{1}0\}$ or $\{11\bar{2}0\}$ facets and forming plate-like layers.

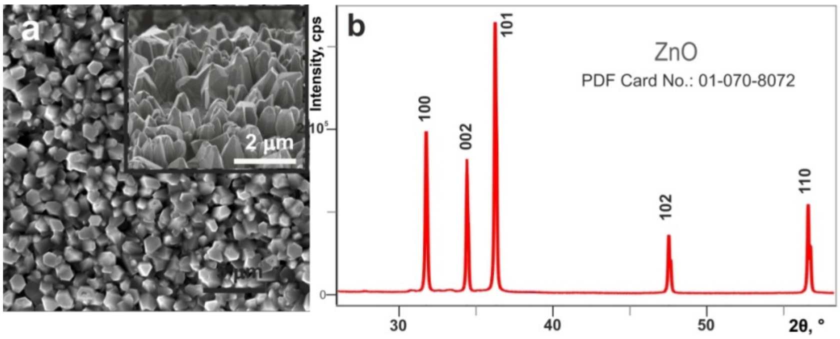

Fig. 2. The granular layer of ZnO nanocrystals, formed at the end of the first growth stage (a); XRD pattern of this layer (b).

The solubility of oxygen in Zn is extremely low. Besides, a small enrichment of ZnO with Zn, even at the level of few atomic percents, first causes the appearance of oxygen vacancies and then the segregation of Zn and ZnO phases [17]. Hence, if the Zn vapor condenses in the oxygen-deficient atmosphere, then the formation of Zn and ZnO phases is expected to emerge. This was confirmed by our results on the growth of Zn-based nanomaterials in conditions when the weight of NH_4Cl in the source was decreased by twice, as compared to conditions described in the experimental section. The synthesized micrometer size hexagonal layered icosahedron is shown in Fig. 3 a. The vapor pressure of Zn at this temperature is sufficiently high (P_{Zn}=0.12 Torr). The pores in thee Zn layer are clearly seen in the inset of Fig. 3 a, indicating that at 410°C a part of Zn is evaporated from the layer. The completed Zn layers are stacked together forming rough hexagonal icosahedron. The Zn surface, which is very close to molten state at this temperature, serves as an ideal nucleation site for the growth of ZnO crystals, and even the epitaxial growth of ZnO may take the place in Zn-ZnO system [18,19]. The small amount of oxygen in the reactor is sufficient to grow some ZnO nanostructures like one dimensional micro-rod, shown in the inset of Fig. 3 a (the composition was analyzed by EDS method and the results are not presented here).

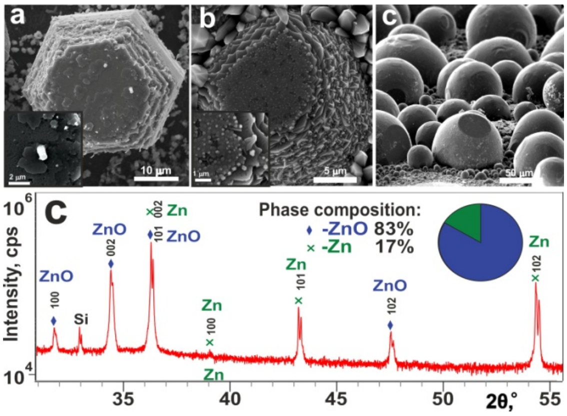

Fig. 3. The hexagonal layered Zn icasahedron formed when the NH_4Cl content in the source was decreased to 0.4 g (a); the layered microsphere produced in case, when the content of NH_4Cl was twice increased (b,c) and XRD pattern of this material (d).

The same oxygen deficient environment was formed at the end of the first growth stage, when the formation of oxidizing water molecules was ceased due to the complete decomposition of NH_4Cl powder in the source. In the second growth stage the Zn powder in the source was the only supplier of Zn vapor to the substrate surface. The layered spheres with diameters varying in the wide range from a few micrometers up to 100 micrometers were produced on the substrate, as is indicated in Fig. 3 b, c. The XRD pattern of the grown material shows the presence of Zn and ZnO phases (Fig. 3 d).

The layers, formed in the second growth stage (the inset in Fig. 3 b), differs from that produced at low NH_4Cl content (inset in Fig. 3 a). The former comprised 100-200 nm thick merged Zn plates with a high number of embedded ZnO nanocrystals having the same lateral sizes. In contrast to this, the later layer has few ZnO nanocrystals. We assume that the reason for this difference was the low concentration of oxidizing species in the process performed at decreased NH_4Cl content in the source.

As it was mentioned above, at the end of the second growth stage, the ammonium chloride and Zn powder in the source were completely consumed. The formation of hollow microspheres started in the third growth stage, which was proceeding as a simple annealing process at a constant temperature of 410°C in the atmosphere of residual gases (including air that was leaking in the reactor from the environment). At first, the rough surfaces of a spheres were oxidized and a thin irregular oxide layer was produced.

Zn atoms can easily diffuse through the irregular oxide layer. At its surface, they can be oxidized, forming the ZnO nanocrystal shell. The initial stage of this process is illustrated in Fig. 4 a. This process goes on very intensively until there are holes between ZnO nanocrystals in the shell. However, with time, it may happen that the growing shell will hermetically encapsulate and seal the inner sphere. If such happened in our process, then the vapor pressure inside the shell was gradually increasing and when it was reaching a certain critical value, the shell exploded, releasing the extra pressure (Fig. 4 c,d).

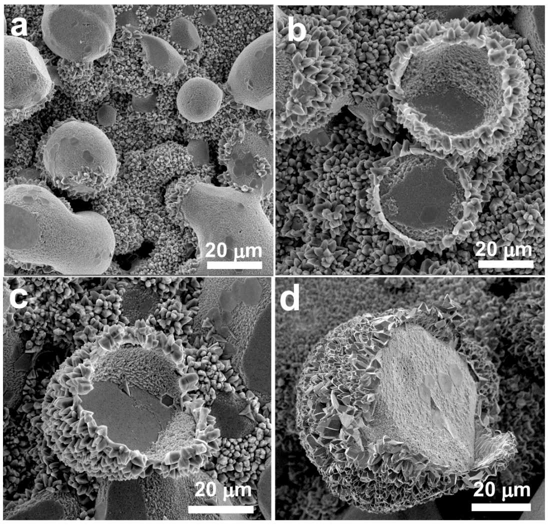

Fig. 4. The initial stage of the hollow microsphere formation and produced hollow microsphere (a,b); the “real" hollow micro-sphere with empty cavity and one, which still keeps a part of its inner Zn-rich sphere (c,d).

After the nanocrystalline ZnO shell broke, the Zn vapor freely sublimated out of the sphere and caused a gradual decrease in the core volume. Fig. 4 c,d illustrates two spheres, one of them is a "real" hollow sphere (Fig. 4 c), while another still keeps a half of its internal content. Fig. 5 illustrates some morphologies of hollow spheres, synthesized in the third growth stage.

Taking into consideration the results of this work, we proposed the following possible growth mechanism of ZnO hollow spheres (Fig. 6).

The hollow microspheres were produced by transformations that take place during the annealing of layered Zn enriched spheres at 410°C in the residual gases containing a low oxygen concentration. At first, the Zn atoms were outdiffusing to the surface of a layered sphere, forming a thin nanocrystalline ZnO shell around it. The process of Zn outflow continued and, with time, a thick shell of ZnO nanocrystals with sizes in the range of 0.5-2.0 micrometer was formed. This shell was hermetically encapsulating the inner sphere. As the annealing was continued, the internal pressure of Zn was gradually increasing, causing the burst up of a ZnO outer shell. After this, the internal sphere was evaporating, thus producing the hollow ZnO microsphere.

According to our preliminary results, the synthesized ZnO spheres, together with the granular ZnO layer deposited in the first growth stage, show high activity in photocatalytic degradation of methylene blue.

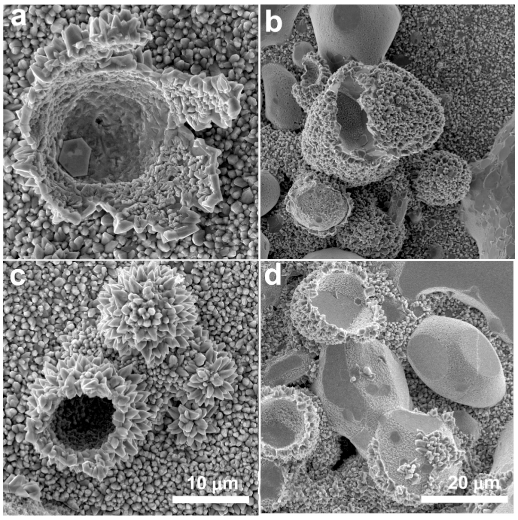

Fig. 5. Some examples of hollow microspheres, produced by the developed technology.

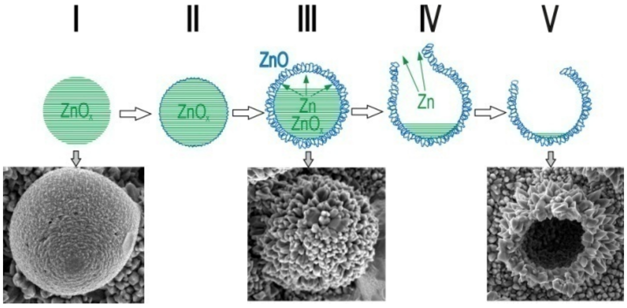

Fig. 6. The proposed mechanism of the hollow microsphere formation.

Conclusions

The new technology was developed for the synthesis of nanocrystalline ZnO based hollow microspheres. Its novelty was in the application of ammonium chloride decomposition products for producing nanomaterials. NH_4Cl, ZnO and Zn powders were used as source materials. The growth proceeded in three stages.

In the first stage, during 40 minutes, the Si substrate was gradually heated up to 410°C. As a result the nanocrystalline ZnO layer was produced with sizes in the range of 0.5-2.0 micrometer. ZnO was synthesized due to the chemical reactions between $ZnCl_2$ and Zn vapor with water molecules, formed after interaction of ZnO in the source with ammonium chloride. This stage ended with complete consumption of NH_4Cl in the source.

The Zn powder in the source was the only supplier of Zn atoms to the Si substrate in the second growth stage. The oxygen deficient environment, formed in this stage, facilitated the growth of a layered micrometer sized spheres. The layers were formed by merging and lateral growth of Zn plates with 100-200 nm thickness. These layers contained the embedded ZnO crystals of sizes up to 200 nm. The stage ended when Zn powder in the source was consumed.

In the third stage the microspheres were annealed in the environment of residual gases with low oxygen content. This caused the outdiffusion of Zn from the microsphere, its oxidation at the surface and formation of the nanocrystalline shell which gradually encapsulated the inner Zn-rich microsphere. The sizes of ZnO crystals were up to 2.5 micrometer. In cases when the outer shell was hermetically inclosing the inner sphere, the internal pressure of Zn was slowly rising with time. At a certain Zn pressure, the outer shell was exploding, producing the hollow microspheres.

Acknowledgment

This work was supported by Shota Rustaveli National Science Foundation of Georgia (SRNSFG) [grant number YS-19-087].

References

1. Galdámez-Martinez A., Santana G., Güell F., Martínez-Alanis P. R., Dutt A. Nanomaterials 2020, v.10 (23), p. 857. DOI:10.3390/nano10050857
2. Barzinjy A., Hamad S., Azeez H. Jordan Journal of Applied Science 2020, v.13 (2), p. 123.
3. Piqueras J., Hidalgo P. Physica Status Solidi A 2021, p. 2100323.
4. Borysiewicz M.A. Crystals 2019, v. 9, p. 505. DOI:10.3390/cryst9100505
5. Melegari S.P., Fuzinatto C.F., Gonçalves R.A., Oscar B.V., Denice Schulz Vicentini D.S., Matias W.G. Chemosphere 2019. v. 224, p. 237.
6. Afolalu S. A., Soetan S.B., Ongbali S.O., Abioye A.A., Oni A.S. IOP Conference Series: Materials Science and Engineering 2019. v. 640, p. 012065.
7. Abdelmohsen A.H., Waleed M. A., El Rouby; Ismail N., Farghali A.A. Scientific Reports 2017. v. 7, p. 5946.
8. Sulciute A., Nishimura K., Gilshtein E., Cesano F., Viscardi G., Nasibulin A.G., Ohno Y., Rackauskas S. Journal of Physycal Chemistry C 2021. v.125, p. 1472.
9. Wang Sh., Qiao G., Chen X., Wang Z., Cui H. Crystals 2020, v. 10, p. 1010.
10. Guang Sh-K., Xie X-J., Zheng J. et al. Journal of Materials Science 2020, v. 55, p. 11938.
11. Chen X., Yang Z-T., Wang N., et al. Nanotechnology Reviews 2021. v.10, p. 1349.
12. Borisov V. A., D'yachenko A. N., Kraidenko R. I. Russian Journal of Inorganic Chemistry 2012 v. 57 (4), p.

499. https://doi.org/10.1134/S0036023612040043

13. Wilson H.F., Tang Ch., Barnard A.S. Journal of Physical Chemistry C 2016. v.120 (17), p. 9498. https://doi.org/10.1134/S0036023612040043
14. Jabbari V., Foroozan T., Shahbazian-Yassar R. Advanced Energy and Sustainability Research 2021, p. 2000082.
15. Gao P.X., Lao Ch.Sh., Ding Y., Wang Z.L. Advanced Functional Materials 2006, v. 16, p. 53.
16. Guo Ch. F., Wang Y., Jiang P., Cao S., Miao J., Zhang Zh., Liu Q. Nanotechnology 2008. v. 19, p. 445710.
17. Wriedt H.A. Journal of Phase Equilibrium 1987, v. 8 (2), p. 166.
18. Zheng J., Archer L.A. Science Advances 2021, v. 7, 19 p.
19. Xiang Yang Kong X.Y., Ding Y.,Wang Zh.L. Journal of Physical Chemistry B 2004, v. 108, p. 570.

SIMPLE SYNTHESIS METHOD OF TIN DIOXIDE NANOPARTICLES FOR GAS SENSING APPLICATION

DA AHMADOVA and NN MUSAYEVA

Institute of Physics of the Azerbaijan National Academy of Sciences, 131, H.Javid ave., AZ1143, Baku, Azerbaijan
E-mail: sedefahmadova@gmail.com

In this work, nanosized particles of SnO_2 are synthesized by a simple Sol- gel method. After mixing $SnCl_2{\cdot}2H_2O$ and isopropyl alcohol (C_3H_8O) at 100°C for 40 minutes, the resulting solution was stored at room temperature for 24 hours. The solution, which completely turned into a gel during this period,it was then thermal treated at 400°C for 2 hours. The powder was analyzed by X-ray diffraction, scanning electron microscopy (SEM), IR and Raman spectroscopy methods. The size of the obtained tetrogonal nanocrystalline nanoparticles is 13 nm, which is determined by the Scherrer equation and the results were confirmed by SEM observation images.

Keywords: sensor, SnO_2, Raman, SEM, nanoparticles
PACS: 61.46+w, 61.82.Fk, 07.07.Df

Introduction

Metal oxides (mainly tin oxide) have been studied for many years and are used in the electronics industry (sensors, batteries, transistors) [1-3]. Tin dioxide (SnO_2) based sensors, which is able to detect variety of gases, have domestic and industrial applications [4]. This is due to their electronic structure, chemical and mechanical stability, and their sensitivity to the environment. SnO_2 structure has excellent sensitivity and stability due to its large specific surface area, high porosity and good permeability. [5-7]. Therefore, improving their sensory properties remains a priority.

The most important characteristics of sensors are sensitivity, selectivity, working temperature and fast recovery time. Since the sensitivity of the sensor is related to the processes occurring on the surface of the material on which it is formed, it is assumed that the sensitive element's surface area increasing will lead to an increase of the sensor's sensitivity. The optimal way to increase the surface area is to reduce the size of the oxide particles

There are different technologies for the synthesis of SnO2 nanosize particles as hydrothermal, spray pyrolisys, Sol-gel [8-10]. The simplicity of the method and the reduction in the cost of synthesis are important.

In this work, we used a simple and cheap method for the synthesis of SnO2 nanoparticles. The resulting powdery nanomaterial was characterized by XRD, SEM, Raman, and IR spectroscopy.

Experiment

For this purpose 25 ml isopropyl alcohol (C_3H_8O) was added to $SnCl_2{\cdot}2H_2O$. The solution was stirred at 100 ^{0}C for 40 minutes. After mixing then resulting solution was stored at room temperatures for 24 hours. The solution completely turned into a gel. After gel formation it was drying and then termal treated at 400 ^{0}C for 2 hours. As a result the crystalline nano powder was obtained. The synthesis process is illustrated in the Fig. 1

For structural characterization of the synthesized powder material X-ray diffraction method was used. For morphology observation of the samples by Scanning electron microscope (SEM) the powder was put directly on the Carbon tape and taken the images, Raman and IR spectroscopy analysis were carried out at room temperature.

Fig. 1. Synthesis method of tin dioxide nanoparticles.

Rezult and discussion

The XRD specter of obtained tin oxide sample is shown at Fig. 2. The peaks at scattering angles of 26.6°, 34°, 38°, 52°, 54.8°,57.8°, 62°, 64.6°, 66°, 71°, 79° which corresponds to (110), (101), (200) (211) (220), (102), (310), (112), (301), (202) and (321) crystal plane respectively.

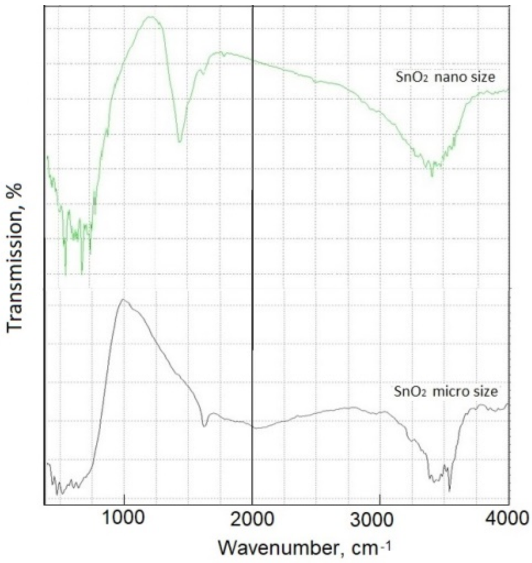

Fig. 2. XRD patterns of SnO_2 nanoparticles

The peak and relative intensities obtained for the SnO_2 match with the literature values [11], so that the intense peaks are indicating that the SnO_2 nanoparticles were highly crystallized and it is confirmed that the synthesized material has a tetragonal SnO_2 phase. There were no characteristic peaks of impurity observed, confirming the high purity of the synthesized materials. The particles size of the SnO_2, which have the average value 13 nm was calculated using Debye Scherer formula:

$$D = \frac{\mathrm{k}\lambda}{\beta\cos\theta},$$

D is the average particle size, λ is the wavelength of X- ray used, K is the shape factor, β is the full line width at the half-maximum elevation of the main intensity peak and θ is the Bragg angle.

Fig. 2. presents SEM images of the nanoparticles. The magnification value is 20 nm. As it can be seen from the figure, the average size of the observed nanoparticles corresponds to the results obtained by XRD.

The synthesized SnO_2 nanoparticles were subjected to FT-IR analysis to detect the various characteristic functional groups related with the synthesized nanoparticles and the results are compared with microcrystal SnO_2 (Fig. 3)

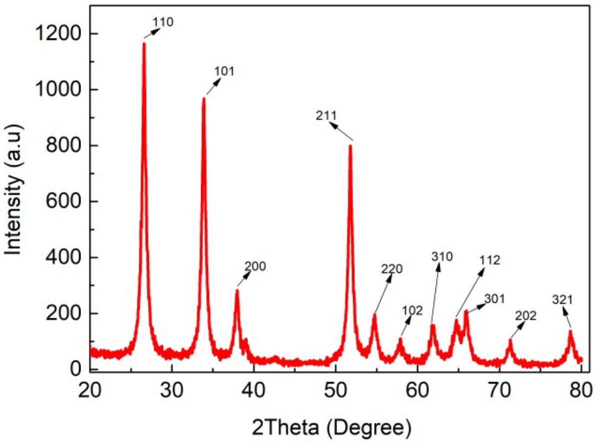

Fig. 3. SEM images of the nanoparticles SnO_2

The specimen from nanosize SnO_2 have IR peaks in the range of 582 cm^{-1}, 757 cm^{-1}, 880 cm^{-1}, 1441 cm^{-1}, 1557 cm^{-1}, 1628 cm^{-1}, 1781 cm^{-1}, 3401 cm^{-1} and 3442 cm^{-1}, while the microcrystal demonstrate not all these peaks. The absorption peak at 582 cm^{-1} corresponds to metal-oxygen (O-Sn-O) vibration mode. The peak at 880 cm^{-1} is ascribed to the stretching vibration of Sn-O bond. The strong broad peaks in higher region at 3401 and 3442 cm^{-1} are due to the stretching vibration of hydroxyl (OH) groups. The spectrum of tin dioxide nanoparticles showed the bands for the C=O and C-H functional groups located at 1441 cm^{-1}, 1557 cm^{-1} and 1781 cm^{-1}. The peak at 1628 cm-1 corresponds to Sn-OH [11].

The Raman spectra, where recorded from different places on the sample show five fundamental Raman scattering peaks at 471 cm^{-1}, 498 cm^{-1}, 540 cm^{-1}, 627 cm^{-1}, 676 cm^{-1}, 763 cm^{-1}, which are related to typical rutile phase of the synthesized SnO_2 nanoparticles [12].

Conclusions

This work is reported the simple synthesize of SnO_2 nanoize particles by simple Sol gel method. X-Ray diffraction analysis of the powder shows that the particle size is approximately 13 nm. This value is confirmed by SEM observation of the morphology. The peaks on IR specter of nanosize particles informed the presence of OH (3400-3441) cm-1, O-Sn-O (582 cm-1), C-H (1441 cm-1), 880 (Sn-O), Sn-OH (1628 cm-1) bonds. Raman spectroscopic analysis confirmed good crystallization of obtained SnO_2 in rutile tetragonal structure. All this parameters of synthesized SnO_2 is open a new opportunity to apply them in different (depending from doping) high effective, low cost gas sensors.

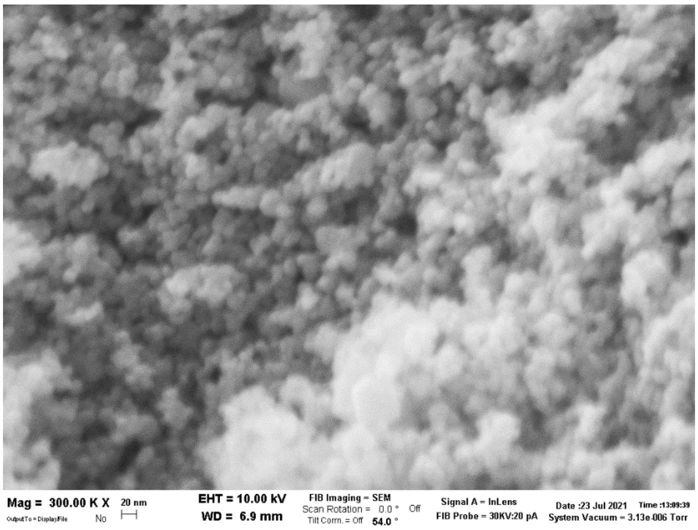

Fig. 4. FTIR spectra of SnO_2 nanoparticles.

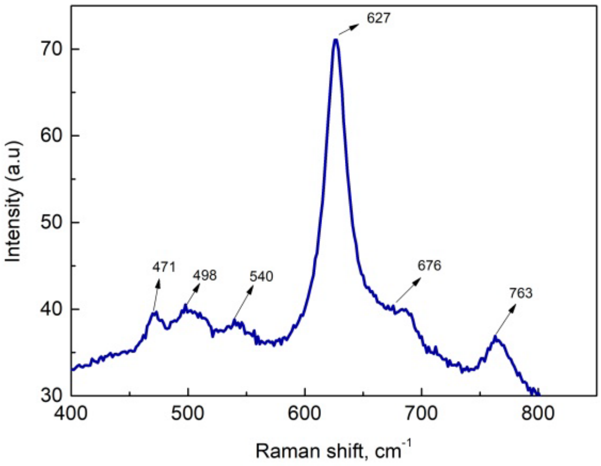

Fig. 5. Raman spectra of nanocrystalline SnO_2

Acknowledgment

Authors would like to thanks to Dr. Giovana Trevisi from IMEM-CNR for SEM analysis and prof.Imameddin Amiraslanov, Institute of Physics, ANAS for X-ray Diffraction analysis.

References

1. Yu-Feng Sun, Shao-Bo Liu, Fan-Li Meng, Jin-Yun Liu, Zhen Jin, Ling-Tao Kong and Jin-Huai Liu. Sensors 2012, v. 12, p. 2610. doi: 10.3390/s120302610
2. M.A. Kebede. Current Opinion in Electrochemistry 2020, v. 21 (6), p. 182. DOI:10.1016/j.coelec.2020.02.003

3. Hongtao Cao Lingyan Liang. Synthesis, Properties, and Applications Metal Oxides 2020, p 441. DOI: 10.1016/b978-0-12-815924-8.00015-3
4. Ding, C.-F., Lin, Y.-C., Yang, C.-C., Huang, K.-C., Hsiao, Y.-J., & Hsiao, W.-T. Fabrication of Tin Oxide Based Gas Sensor in Ethanol Gas Sensing 2020, IEEE Sensors Applications Symposium (SAS). DOI: 10.1109/SAS48726.2020.9220020
5. Kim, H., Kim, M.-C., Kim, S., Kim, Y.-S., Choi, J.-H., & Park, K.-W. RSC Advances 2020, v.10 (18), p.10519. doi.org/10.1039/D0RA00531B
6. Zou, Y., Chen, S., Sun, J., Liu, J., Che, Y., Liu, X.,Yang, D. ACS Sensors 2017, v. 2 (7), p. 897. DOI: 10.1021/acssensors.7b00276
7. Qinqin Z., Lisha M., Qiang Z., Chenggang W., Xijin X. Journal of Nanomaterials 2015, Article ID 850147, 15 p. DOI: 10.1155/2015/850147
8. Talebian N. and Jafarinezhad F. Ceramics International 2013, v. 39 (7), p. 8311. DOI: 10.1016/j.ceramint.2013.03.101
9. Hong Y.J., Yoon J.W., Lee J.H., Kang Y.C. Chemistry 2014, v. 20 (10), p. 2737. DOI: 10.1002/chem.201304502
10. Nuțescu D.C., Barrena Pérez M.I., Gómez de Salazar J.M., Carcea I., Chicet D.L., Palamarciuc, I. Solid State Phenomena 2016, v. 254, p. 200. DOI:10.4028/www.scientific.net/SSP.254.200
11. Ahmad Khoudro Samia Haj Najeeb. Chemistry and Materials Research 2020, v.10 (5), p. 9. DOI: 10.7176/CMR/10-5-02
12. Mariammal R.N., Ramachandran K., Renganathan B., Sastikumar D. Sensors and Actuators B: Chemical 2012, v. 169, p. 199. DOI: 10.1016/j.snb.2012.04.067

THREE-DIMENSIONAL STRUCTURE OF GLUTEOMORPHIN MOLECULE

NA AKHMEDOV, LN AGAYEVA, RM ABBASLI and LI ISMAILOVA

Baku State University, Baku, Azerbaijan
E-mail: Namiq.49@bk.ru, https://orcid.org/0000-0002-0181-0465

A number of exogenous peptides obtained from food have opioid-like properties. These peptides were called exorphins. The first known exorphins were obtained by in vitro pepsin hydrolysis of α-casein and wheat glutone. The conformational capabilities of the gluteomorphin molecule (Tyr1-Pro2-Gln3-Pro4-Gln5-Pro6-Phe7-OH) have been studied by the method of theoretical conformational analysis. The potential function of the system is chosen as the sum of non-bonded, electrostatic, torsion interactions and the energy of hydrogen bonds. Low-energy conformations of the gluteomorphin molecule and the dihedral angles of the main and side chains of amino acid residues included in the molecule were found, the energy of intra- and intersubstance interactions was estimated. It has been shown that the spatial structure of the gluteomorphin molecule is represented by eight structural types. It can be assumed that the molecule performs its physiological functions in these structures. These three-dimensional structures make it possible to propose synthetic analogs for a given molecule. The results obtained can be used to elucidate the structural and structure-functional organization of gluteomorphin molecule.

Keywords: exorphin, gluteomorphin, opioid, structure, conformation
PACS: 87.15 Aa, 11.55.-m, 82.80.-d

Introduction

Gliadorphin (also known as gluteomorphin) is an opioid peptide that is formed during digestion of gluten protein. Gluteomorphins are derived from gliadin, one of the main proteins found in gluten. It is usually broken down into asmailovamino acids by digestion enzymes. Both caseomorphins (derived from digestion of milk products) and gluteomorphins are morphine-like opioids that have been likened to drugs like LSD. They can be very sedating and addictive and help to explain why 75% of the calories in the standard American diet (S.A.D.) come from wheat and dairy alone. Food addiction is a very real thing, and these opioids play a huge role [1].

We have investigated the structural and functional organizations of the opioid peptides. This work is a continuation of our previous research [2-4]. The molecule was calculated using the method of theoretical conformational analysis. The potential function of the system is chosen as the sum of non-bonded, electrostatic and torsion interactions and the energy of hydrogen bonds. Nonvalent interactions were assessed by Lennard-Jones potential. Electrostatic interactions were calculated in a monopole approximation according to the Coulomb's law using partial charges on atoms. The conformational possibilities of the gluteomorphin molecule were studied under the conditions of the water environment. The energy of hydrogen bonds was estimated using the Morse potential.

Section

In presenting the calculation results, we used the classification of peptide structures by conformations, forms of the main chain, and shapes of the peptide backbone. Conformational states are completely determined by the values ϕ, ψ of the dihedral angles of the main and side chains of all amino acid residues included in a given molecule. Forms of the main chain of a fragment are formed by combinations of forms of R, B, L residues in a given sequence. Forms of the main chain of a dipeptide can be divided into two classes - folded (f) and unfolded (e) forms, which are called shapes. All conformations are grouped by backbone shape, and backbone shapes are grouped by shape. To designate the conformational states of the residues, identifiers of the X_{ij} type are used, where X defines the low-energy regions of the conformational map φ–ψ: R(φ, ψ=–180°–0°), B(φ=–180°–0°; ψ=0°–180°), L(φ,ψ=0°–180°) and P(φ=0°–180°; ψ=–180°–0°) ij... = 11..., 12..., 13..., 21... define the position of the side chain (χ_1, χ_2, ...) with the index 1 corresponding to the angle value in the range from 0 to 120°, 2 – from 120° to -120°, and 3 – from -120° to 0°. The designations and readings of the angles of rotation correspond to the IUPAC-IUB nomenclature [5].

Discussion and conclusions

The three-dimensional structure of the gluteomorphin molecule (Tyr1-Pro2-Gln3-Pro4-Gln5-Pro6-Phe7-OH) was investigated based on the low-energy conformations of the corresponding amino acid residues. The heptapeptide molecule of gluteomorphin contains three proline amino acid residues. It is known that for the amino acid preceding proline, the R form of the backbone is high-energy. Therefore, for the residues Tyr1, Gln3, Gln5, only B form of the main chain was selected, and the conformations of eight shapes were calculated for this gluteomorphin molecule. The calculation results show that the conformations of eight shapes efeeee, efefef, efefee, eeefef, efeeef, eeefee, eeeeee, and eeeeef fall into the energy range 0 - 3 kcal/mol. The energy range 0 - 3.0 kcal/mol includes 8 conformations of the efeeee shape, 9 conformations of the efefef shape, 5 conformations of the efefee shape, 7 conformations of the eeefef shape, 2 conformations of the efeeef shape, 2 conformations of the eeefee shape, 1 conformation of the eeeeee shape, and 3 conformation of the eeeeef shape (Table 1). The most stable conformations of the gluteomorphine molecule were selected from each shape, which are presented in table 2. Here, the energy contributions of non-valent ($U_{nv.}$), electrostatic ($U_{el.}$), torsion ($U_{tors.}$) interactions and the relative ($U_{rel.}$) energy of the optimal conformations of the gluteomorphine molecule are indicated. The energies of intra- and intersubstituted interactions, the geometric parameters of five conformations, the relative energy of which is less than 1.6 kcal/mol, are presented in Tables 3 and 4. Figure 1 shows the spatial arrangement of amino acid residues in these low-energy conformations of the heptapeptide molecule.

The energy of non-valent interactions in low-energy conformations changes in the energy range (-29.9) - (-27.1) kcal/mol, electrostatic interactions (-3.8) - (-2.5) kcal/mol, torsion interactions (3.2) - (5.2) kcal/mol (Table 2).

The global conformation of the gluteomorphin molecule is the $B_1RB_{12}BB_{12}BB_3$ conformation of the efeeee shape. The conformation is advantageous for non-bonded and electrostatic interactions. Effective di-, tri- and tetrapeptide interactions arise in this conformation, Tyr1 effectively interacts with the Pro2-Gln3-Pro4 fragment, which contribution is (-7.7) kcal/mol, Gln3 with Pro4-Gln5, which contribution is (-8.7) kcal/mol, Gln5 with Pro6-Phe7, which contribution is (-8.7) kcal/mol. In this conformation, a hydrogen bond arises between the C = O atoms of the main chain of Gln3 and the N-H of the side chain of Gln5(Table 3).

The relative conformation energy of $B_1RB_{11}RB_{13}RR_3$ is 0.3 kcal/mol higher than in the global conformation. Here, semi-folded forms of the main chain alternate. In this conformation, the stabilizing electrostatic interactions are the largest (Table 2), but it loses 0.6 kcal/mol in non-valence interactions. The contribution of Tyr1 with the Pro2-Gln3-Pro4 tripeptide site is (-10.9) kcal/mol, Gln3 with the Pro4-Gln5-Pro6 tripeptide site is (8.2) kcal/mol, Gln5 with the Pro6-Phe7 dipeptide site is (-6.5) kcal/mol (Table 3). The $B_1RB_{13}RB_{12}BB_3$ conformation differs from the previous conformation in the shape of the chain of the Pro6-Phe7 residues and has a relative energy of 1.1 kcal/mol (Table 3).

Table 1. The energy distribution of the conformations of the gluteomorphin molecule

№	Shapes	Energy range, kcal/mol							
		0-1	1-2	2-3	3-4	4-5	5-6	6-7	>7
1	efeeee	3	3	2	3	-	-	-	12
2	efefef	1	2	6	2	3	1		13
3	efefee	-	4	1	-	1	-	-	12
4	eeefef	-	2	5	2	2	1	-	15
5	efeeef	-	1	1	2	-	1	2	12
6	eeefee	-	1	1	1	1	-	2	14
7	eeeeee	-	-	1	-	1	4	3	44
8	eeeeef	-	-	3	2	2	2	-	12

Table 2. Energy contributions of non-valent (U_{nv}), electrostatic (U_{el}), torsional (U_{tors}) interactions and the relative energy (U_{rel}) of the optimal conformations of the gluteomorphin molecule

№	Shapes	Conformation	U_{nv}	U_{el}	U_{tors}	U_{tot}	U_{rel}
1	efeeee	$B_1 R B_{12} B B_{12} B B_3$	-29.9	-3.3	4.5	-28.6	0
2	efefef	$B_1 R B_{11} R B_{13} R R_3$	-29.3	-3.8	4.8	-28.3	0.3
3	efefee	$B_1 R B_{13} R B_{12} B B_3$	-28.9	-3.0	4.4	-27.5	1.1
4	eeefef	$B_2 B B_{12} R B_{13} R R_3$	-28.4	-3.0	4.3	-27.1	1.5
5	efeeef	$B_1 R B_{12} B B_{12} R R_3$	-27.1	-3.2	3.2	-27.0	1.6
6	eeefee	$B_2 B B_{12} R B_{12}B B_3$	-27.6	-2.9	3.8	-26.7	1.9
7	eeeeee	$B_2 B B_{12} B B_{12} B B_3$	-28.8	-2.8	5.2	-26.4	2.2
8	eeeeef	$B_2 B B_{12} B B_{12}R R_3$	-27.4	-2.5	3.9	-26.0	2.6

Table 3. Energy inside and between residual interactions in the conformations of the gluteomorphin molecule $B_1RB_{12}BB_{12}BB_3$ (U_{rel}=0 kcal/mol, first line), $B_1RB_{11}RB_{13}RR_3$ (U_{rel}= 0.3 kcal/mol, second line), $B_1RB_{13}RB_{12}BB_3$ (U_{rel}= 1.1 kcal/mol, third line), $B_2BB_{12}RB_{13}RR_3$ (U_{rel}=1.5 kcal/mol, fourth line), $B_1RB_{12}BB_{12}RR_3$ (U_{rel}=1.6 kcal/mol, fifth line)

Tyr1	**Pro2**	**Gln3**	**Pro4**	**Gln5**	**Pro6**	**Phe7**	
2.1	-3.4	-2.2	-2.1	-0.7	-0.1	-3.0	Tyr1
2.1	-3.7	-3.4	-3.8	-0.2	0	-1.5	
2.1	-3.3	-3.1	-2.2	-0.1	0	-1.4	
2.3	-5.6	-5.5	-0.2	0	0	-1.5	
2.0	-3.5	-2.1	-2.4	-0.7	-0.1	-2.5	
	0.2	-2.2	-0.3	-1.1	0	-0.2	Pro2
	0.3	-3.2	-0.3	0	0	0	
	0.2	-3.6	-0.3	0	0	0	
	0.3	-0.9	-0.3	0	0	0	
	0.3	-2.3	-0.3	-1.1	0	-0.1	
		-0.3	-3.7	-5.0	0	-0.2	Gln3
		1.1	-3.5	-2.7	-2.0	-0.3	
		0.8	-3.7	-2.8	-1.0	-0.7	
		-0.4	-3.4	-2.3	-1.9	0.1	

Tyr1	Pro2	Gln3	Pro4	Gln5	Pro6	Phe7	
		-0.4	-3.7	-4.8	0	0.1	
			0.3	-1.0	-0.3	-0.2	Pro4
			0.3	-3.8	-0.3	-0.1	
			0.3	-2.6	-0.3	-0.9	
			0.3	-3.5	-0.3	-0.1	
			0.3	-1.0	-0.3	-0.1	
				-0.3	-4.4	-4.3	Gln5
				0.7	-3.3	-3.2	
				-0.3	-4.3	-4.1	
				0.6	-3.5	-3.1	
				-0.3	-2.9	-2.0	
					0.3	-1.8	Pro6
					0.3	-3.3	
					0.4	-1.7	
					0.3	-3.4	
					0.3	-3.3	
						0.6	Phe7
						0.7	
						0.6	
						0.6	
						0.7	

Table 4. Geometric parameters (in degrees) of low energy conformations of the molecule gluteomorphin (the values of the dihedral angles are given in the sequence ϕ, ψ, w, χ1, χ2...)

	$B_1RB_{12}BB_{12}BB_3$	$B_1RB_{11}RB_{13}RR_3$	$B_1RB_{13}RB_{12}BB_3$	$B_2BB_{12}RB_{13}RR_3$	$B_1RB_{12}BB_{12}RR_3$
Tyr1	-73 131 175 61 92 0	-71 140 174 51 83 0	-72 132 175 56 89 0	-73 122 175 171 69 0	-72 133 175 60 91 0
Pro2	-60 -47 177	-60 -48 174	-60 -46 179	-60 116 -175	-60 -48—178
Gln3	-147 152 174 60 180 90	-144 147 179 29 60 70	-152 157 173 76 -68 109	-149 149 172 62 -168 82	-148 151 174 62 -173 82
Pro4	-60 115 -172	-60 -52 173	-60 -48 -176	-60 -63 172	-60 117 -171
Gln5	-155 153 168 65 -170 90	-156 150 180 74 -69 107	-154 154 169 63 -172 89	-160 149 178 74 -68 107	-153 148 -178 61 -170 91
Pro6	-60 137 175	-60 -57 -177	-60 138 173	-60 -57 -175	-60 -60 177
Phe7	-124 150 - -66 96	-102 -68 - -58 91	-124 149 - -65 98	-104 -65 - -59 91	-100 -68 - -59 90
ΔU	0	0.3	1.1	1.5	1.6

The energetic contribution of Tyr1 - followed by a tripeptide site is (-8.6) kcal/mol, Gln3 with a Pro4-Pro6 site (-7.5) kcal/mol, Gln5 with a dipeptide site Pro6-Phe7 (-8.4) kcal/mol (Table 3). The $B_2BB_{12}RB_{13}RR_3$ conformation differs from the second conformation only in the shape of the main chain of the second amino acid residue of proline and has a relative energy of 1.6 kcal/mol. The $B_1RB_{12}BB_{12}RR_3$ conformation, which differs only in the shape of the Pro4 backbone, has a relative energy of 1.6 kcal/mol.

The conformation of the fully unfolded form of the main chain $B_2BB_{12}BB_{12}BB_3$ has a relative 2.2 kcal/mol. This conformation is stabilized by tripeptide interactions between residuals. The $B_2BB_{12}BB_{12}RR_3$ conformation, which differs from the previous conformation in the shape of the main chain, has a relative energy of 2.6 kcal / mol, while the nature of the forces stabilizing this conformation is similar.

Thus, the spatial structure of the gluteomorphin molecule can be represented by eight structural types. It can be suggested that the molecule performs its physiological functions in these structures. Based on these structures, synthetic analogues of the molecule can be proposed. The theoretical conformational analysis of the gluteomorphin heptapeptide has led to such a structural organization of the molecule that does not exclude the implementation by the molecule of a number of functions that require strictly specific interactions with various receptors.

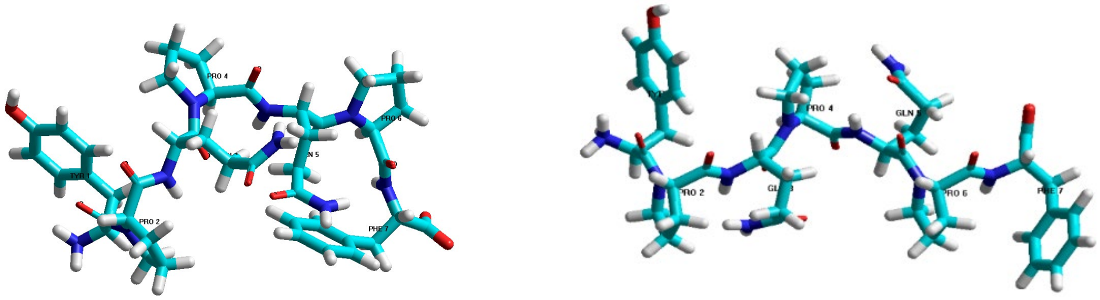

a) $B_1RB_{12}BB_{12}BB_3$ **b)** $B_1RB_{11}RB_{13}RR_3$

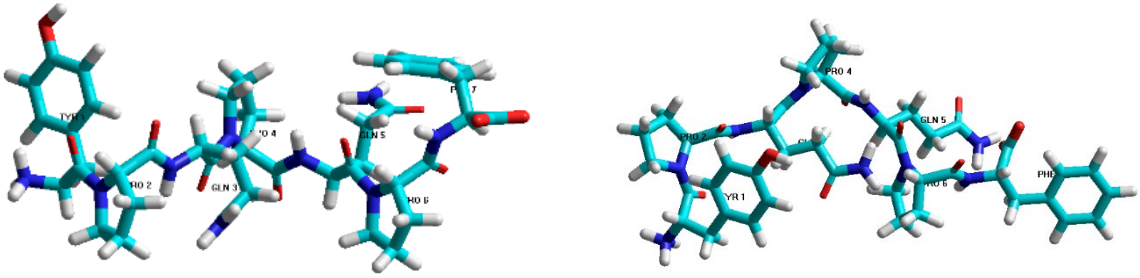

c) $B_1RB_{13}RB_{12}BB_3$ **d)** $B_2BB_{12}RB_{13}RR_3$

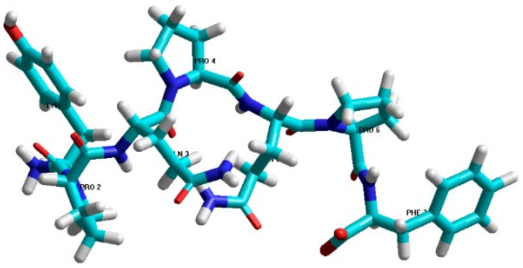

e) $B_1RB_{12}BB_{12}RR_3$

Fig. 1. Atomic model of spatial structure of the gluteomorphine molecule a), b), c), d) and e) corresponded to the structures with the relative energies 0 kcal/mol, 0.3 kcal/mol, 1.0 kcal/mol, 1,5 kcal/mol and 1.6 kcal/mol, respectively.

References

1. Chesnokova E.A., Sarycheva N.Y., Dubynin V.A. and et al. Physiological Sciences 2015, v. 46, p. 22.
2. Akhmedov N.A., Agayeva L.N., Akverdieva G.A., Abbasli R.M., Ismailova L.I. J.Chem.Soc.Pak. 2021, v. 43, (5), p. 500.
3. Akhmedov N.A., Agayeva L.N., Akhmedova S.R., Abbasli R.M., Ismailova L.I. Journal of Applied Physics (IOSR-JAP) 2021, v. 13 (5), p. 62. DOİ:10.9790/4861-1305026267 www.iosrjournals.org.
4. Agayeva L.N., Abdinova A.A., Akhmedova S.R., Akhmedov N.A. Biophysics, 2021, v. 66 (4), p. 531. DOI https://doi.org/10.1134/S0006350921040023
5. IUPAC IUB. Quantities, Units and Symbols in Physical Chemistry, Blackwell Scientific,Oxford 1993, https://old.iupac.org/publications/books/gbook/greenbook2ed.pdf DOI:10.1134,S0006350921040023.

PROMPT PHOTONS PRODUCTION IN PROTON-PROTON COLLISION AT HIGH ENERGIES

MR ALIZADA[1], AI AHMADOV[2,3] and AB ARBUZOV[2]

[1]Baku State University, str. Z.Khalilov, 23, Az-1148 Baku, Azerbaijan
ORCID: 0000-0002-9664-5465
[2]Bogoliubov Laboratory of Theoretical Physics, Joint Institute for Nuclear Research, Dubna, Moscow region, str. Curi 6, 141980, Russia
ORCID: 0000-0001-9326-6905
[3] Institute of Physics of the Azerbaijan National Academy of Sciences, H.Javid str. 33, Baku Az-1143, Azerbaijan
ORCID: 0000-0003-4848-2531
E-mail: mohsunalizade@gmail.com, arbuzov@theor.jinr.ru, ahmadov@theor.jinr.ru

In this paper, we have determined the differential cross section of the prompt photons production in sub-processes: Compton scattering of quark-gluon ($qg \to q\gamma$) and annihilation of quark-antiquark pair ($q\bar{q} \to g\gamma$) without and take into account polarization of colliding protons. It has been showed, the differential cross section is decreases with increasing energy of colliding protons. The value of the differential cross section of the prompt photons production in the annihilation of quark-antiquark subprocess is larger than the differential cross section of the prompt photons production in the Compton scattering of quark-gluon subprocess. Double spin asymmetry these subprocesses are calculated. Double spin asymmetry of Compton scattering of quark-gluon subprocess is zero. Double spin asymmetry of annihilation of quark-antiquark pair subprocess linearly depends on the product of the polarization degrees of colliding protons.

Keywords: Compton scattering of quark-gluon, annihilation of quark-antiquark pair, differential cross section, double spin asymmetry
PACS: 21.10.–k, 12.39.–x, 12.38.Mh

Introduction

The study of the phase diagram of strongly compressed baryonic matter is one of the main problems of elementary particles and nuclear physics. It is believed that immediately after the Big Bang, the universe existed in the form of a quark-gluon plasma (QGP) [1]. With the advent of modern accelerators, at the Relativistic Heavy Ion Collider (RHIC) and the *Large Hadron Collider* (LHC) and others, ultra-relativistic collisions of heavy ions made it possible to create high-density materials in laboratory conditions [2,3].

Prompt photons carry information about the nucleon, such as: the distribution of partons (quarks and gluons) inside the nucleon; the temperature of the nucleus; the collective expansion, as well as the spatial and temporal evolution of the medium. Prompt photons are produced in such processes as: Compton scattering; $q\bar{q}$ annihilation; bremsstrahlung of quarks experiencing hard scattering; γ photon emission from intermediate vector bosons [4].

The study of photon radiation is also interesting because in most hadron interactions, photons escape as a background to other signals under study. The experiments planned at the Nucleotron-based Ion Collider Facility (NICA) complex will have a great advantage over RHIC, LHC experiments, since the low energy obtained for the collision of heavy ions will reduce the number of additional particles production.

At present paper, prompt photons production in Compton scattering of quark-gluon ($q\bar{q} \to g\gamma$) and annihilation of quark–antiquark ($q\bar{q} \to g\gamma$) subprocesses are investigated.

Differential cross section of subprocesses

The Feynman diagrams of prompt photons production in Compton scattering of quark-gluon ($qg \to q\gamma$) and in annihilation of quark-antiquark ($q\bar{q} \to g\gamma$) subprocess are constructed and the matrix elements are written in the form:

$$M_{11} = \bar{U}(p_2)\hat{\varepsilon}_\nu^\gamma \left(i\frac{\hat{p}_a + m_a}{p_a^2 - m_a^2} \right) \hat{\varepsilon}_\mu^g U(p_1) T_{ij}^a,\ M_{12} = \bar{U}(p_2)\hat{\varepsilon}_\mu^g \left(i\frac{\hat{p}_b + m_b}{p_b^2 - m_b^2} \right) \hat{\varepsilon}_\nu^\gamma U(p_1) T_{ij}^a$$

and

$$M_{21} = -iee_q g_s \bar{\upsilon}(p_2)\gamma_\mu \left(\frac{\hat{p}_a + m_a}{p_a^2 - m_a^2} \right) \gamma_\nu U(p_1) \varepsilon_\mu^g \varepsilon_\nu^\gamma T_{ij}^a,\ M_{22} = -iee_q g_s \bar{\upsilon}(p_2)\gamma_\nu \left(\frac{\hat{p}_b + m_b}{p_b^2 - m_b^2} \right) \gamma_\mu U(p_1) \varepsilon_\nu^\gamma \varepsilon_\mu^g T_{ij}^a$$

respectively.

Calculation of the matrix elements are preformed using FeynCalc. The phase volume of the subprocesses is calculated as [5]. The differential cross section is evaluated at the values [6].

In the Fig. 1(a,b) are presented the dependencies of the differential cross sections of the photons production in the Compton scattering of quark-gluon and annihilation of quark-antiquark subprocesses from the energy of colliding protons(a) and the dependence of the differential crosss section of the photons production in the process of annihilation of quark-antiquark on the energy of colliding protons at the different values of the products of the polarization degrees of colliding protons: $1 - \lambda_1 \lambda_2 = 0$, 2^+, 2^{--} - ± 0.25, 3^+, 3^{--} $-^-$ ± 0.81.

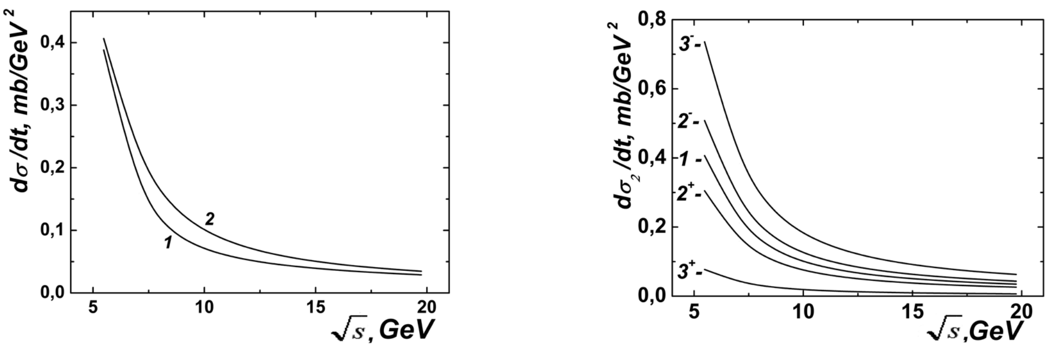

a b

Fig. 1. The dependencies of the differential cross-sections of the photons production in the Compton scattering of quark-gluon and annihilation of quark-antiquark from the energy of colliding protons (a), the dependence of the differential cross section of the photons production in the process of annihilation of quark-antiquark on the energy of colliding protons at the different values of the products of the polarization degrees of protons 1- $\lambda_1 \lambda_2$ = 0, 2+, 2- - ± 0.25, 3+, 3- -- ± 0.81 (b).

As can be seen from Fig. 1(a) the differential cross section decreases with increasing energy of colliding protons. The values of the differential cross section of the production of photons in the annihilation process of quark-antiquark (curve 2) are larger than the differential cross section of the production of photons in the Compton scattering process of quark-gluon (curve 1). This means that the probability of the production of photons during the annihilation of quark-antiquark is greater than the probability of the production of photons in the Compton process of scattering quark-gluon. With an increase values of the Mandelstam invariant variable *u* the differential cross section of subprocess increases.

Calculation showed that squares of the matrix element of the Compton scattering without and taking into account the polarization of colliding protons are identical. The coincidence of the squares of the matrix elements indicates that law of the parity of the system is preserved.

The differential cross section of the photons production in the annihilation process of quark-antiquark depends on the value of the product of the polarization degrees of colliding protons and decreases with increasing value of product of polarization degrees (Fig. 1b).

The dependence of differential cross sections of the Compton scattering of quark-gluon subprocess from the energy of colliding protons has been considered at collisions of "*u*", "*d*" quarks with gluon: $ug \to u\gamma$ and $dg \to d\gamma$. Has been showed, the dependence the differential cross sections of the Compton scattering of quark-gluon subprocess from the energy of colliding protons for a "*u*" quark is less than "*d*" quark.

The dependence of differential cross sections of the Compton scattering of quark-gluon subprocess on the energy of colliding protons at values of the Mandelstam invariable *u* E_u=10, 40, 70 and 100 *GeV* has been calculated. It decreases with decreasing values of the Mandelstam invariable *u.*

Double spin asymmetry

The double spin asymmetryof the process with polarized protons is determined by the formula [5]. At an early stage, it was shown that the squares of matrix elements for Compton scattering without and taking into account polarization are identical. Because of double spin asymmetry of this subprocess is zero. It is known that in any unipolarization processes with photons, the squares of matrix elements without and taking into account polarization coincide, that is, the terms in the square of the matrix element with a degree of polarization are zero [5]. The coincidence of the squares of the matrix elements indicates that law of the parity of the system is preserved.

The double spin asymmetry of annihilation of quark-antiquark subprocess linearly depends on the product of the polarization degrees of colliding protons. The value of the double spin asymmetry is maximal when the polarization of colliding protons is opposite and minimal when they are identically directed.

Conclusion

The differential cross-section of subprocesses are decreases with increasing energy of colliding protons. The values of the differential cross section of the production of prompt photons in the annihilation process of quack-antiquark are larger than the differential cross section of the production of photons in the Compton scattering process of quark-gluon. This means that the probability of the production of prompt photons in the annihilation of quark-antiquark process is greater than the probability of the production of photons in the Compton scattering of quark gluon. The values of the differential cross-section of the production process of photons in the annihilation process of quack-antiquark depend on the value of the product of the polarization degrees of colliding protons. With increasing value of product of polarization degrees differential cross section increases.

The value of the double spin asymmetry of Compton scattering process of quark-gluon is zero. Taking into account the polarization of only the initial quarks and gluons in Compton scattering does not contribute to the differential cross-section of the subprocess. The value of the double spin asymmetry of annihilation of quark-antiquark subprocess linearly depends on the product of the polarization degrees of colliding protons. The value of the double spin asymmetryis maximal when the polarization of colliding protons is opposite and minimal when they are identically directed.

References

1. Masson E., on behalf of the ALICE Collaboration Direct photon measurements with the ALICE experiment at the LHC 2018, arXiv:1811.02220v1 [hep-ex], DOI: 10.3390/proceedings2019010001
2. Acharya S. et al. (ALICE Collaboration) Phys.Rew C, 2019, v. 99, p. 024912-1. DOI: 10.1103/PhysRevC.99.024912
3. The ATLAS Collaboration Measurement of the cross section for isolated-photon plus jet production in pp collisions at p s = 13 TeV using the ATLAS detector, Phys. Lett. B, 2018, p. 780 578, DOI:10.1016/j.physletb.2018.03.035.
4. Greiner W., Schramm S., Stein E. Quantum chromodynamics. 3nd Edition, Springer, Germany, 1989.
5. Zyla P.A., Barnett R.M., Beringer J., Dahl O. et al Particle physics booklet. 2020.

ELECTRON MOTION IN A CONTINUOUS MEDIA WITH EXTERNAL MAGNETIC FIELD

JM ABBASZADE[1], CHV ABDULLAZADE[1], UF AGAYEVA[1], GT AHMADOVA[1], AY ALİYEVA[1], NE ALİYEVA[1], RR ALİ[1], RK ASLANOVA[1], KL DAVUDOVA[1], GE ISMAYİLOVA[1], KHD JAFARLİ[1], LG MAHARRAMOVA[1], SM MURADOVA[1], SHSH PİR-MAHAMMAD ABDULLAHİ[1], AM SULEYMANLİ[1], CHA ZEYNALOVA[1] and RG JAFAROV[2]

[1]Baku State University, Baku, Azerbaijan
[2]Theoretical Physics Department and Institute for Physical Problems of Baku State University, Baku, Azerbaijan
E-mail: fizing08@mail.ru, r.g.jafarov@gmail.com

This article is a theoretical-methodological investigation in nature, where we study the propagation of small perturbations of an electron in a continuos media (with neglect of all dissipation processes in it), i.e. in an ideal liquid (or gas), located in a uniform constant magnetic field B. The wave function of an electron is found in states in which it has certain values of momentum and angular momentum along the direction of the field. The energy spectrum and wave function are calculated.

Keywords: Magneto-hydrodynamics, Alfven waves, spectral problem, electron precession.
PACS: 52.30.Cv, 95.30.Ky, 96.50.Ry

Introduction

An electromagnetic processes have a fundamental sense for a number of natural phenomena. The combination of the classical electrodynamics with hydrodynamics has resulted in magnetic hydrodynamics, which is directly related to plasma physics. When solving magnetic hydrodynamics equations in the form of a plane wave $\exp\{i(\vec{k}\vec{r}-\omega t)\}$ for electron precessions propagating in the continuos media located in the external uniform magnetic field, according to the dispersion law, the electron precession frequency ω substantially depends on the direction of the wave vector $\vec{k}$ as $\omega=(4\pi\rho)^{-1/2}\vec{H}\vec{k}$. I.e., the electron motion in the ideal-like continuous media which located in the constant magnetic field is an electron spontaneous moving and precession in the Alfven wave [1, 2] propagating in the constant magnetic field, in principle.

To study this problem, we determine the energy levels of the electron in the constant magnetic field as following by L.D. Landau [3] with separated method for solution of radial Schrödinger equation, firstly and then calculate the energy levels of electron precession and the lifetime of the electron residence at the corresponding quantum levels.

Consider the problem of the electron motion in the continuous media (in Alfven wave) in a constant magnetic field, The Hamilton operator according of the simple postulations of quantum mechanics is

$$\hat{H}=\frac{1}{2M}\left(\hat{\vec{p}}+\frac{e}{c}\vec{A}\right)^2+\frac{M\omega_A^2\vec{r}^2}{2},$$

where M is a electron mass, $\left(\hat{\vec{p}}+\frac{e}{c}\vec{A}\right)^2$ – Lorentz postulate for relativistic electron momentum, $e>0$ is the electron charge,

$$\omega_A=\frac{1}{\sqrt{4\pi\rho_{Fl}}}\vec{B}\vec{k} \tag{1}$$

– the Alfven frequency [1, 2], $\vec{B}$ – magnetic field intensity, ρ_{Fl} is a fluid density of continuous media, $\vec{k}$ – Alfven wave vector, $\frac{M\omega_A^2\vec{r}^2}{2}$ – plasma potential for electron precession in a continuous media (i,e, in the Alfven wave, where potential takes the form $\frac{M\omega_A^2\vec{r}^2}{2} = \frac{M\vec{r}^2}{8\pi\rho_{Fl}}(\vec{B}\vec{k})^2$.

In expanding the square $\left(\hat{\vec{p}} + \frac{e}{c}\vec{A}\right)^2$, we must bear in mind that $\hat{\vec{p}}$ does not in general commute with the vector $\vec{A}$, which is the function of the coordinates. Hence we must write $\left(\hat{\vec{p}} + \frac{e}{c}\vec{A}\right)^2 = \hat{\vec{p}}^2 + \frac{e}{c}(\hat{\vec{p}}\vec{A} + \vec{A}\hat{\vec{p}}) + \frac{e^2}{c^2}\vec{A}^2$. According to the quantum mechanical commutation rules of the momentum operator with any function of the coordinates, we have $\hat{\vec{p}}\vec{A} - \vec{A}\hat{\vec{p}} = -i\hbar\, div\vec{A}$. Thus $\hat{\vec{p}}$ and $\vec{A}$ commute if $div\vec{A} \equiv 0$. Thus holds, in particular, for a uniform field, if its vector potential is expressed in the form $\vec{A} = \frac{1}{2}[\vec{B}\vec{r}]$. Accordingly above mentioned discussion for Hamilton operator we have

$$\hat{H} = \frac{1}{2M}\left(\hat{\vec{p}}^2 + \frac{e}{c}\hat{\vec{p}}[\vec{B}\vec{r}] + \frac{e^2}{c^2}\frac{1}{4}[\vec{B}\vec{r}]^2\right) + \frac{M\vec{r}^2}{8\pi\rho_{Fl}}(\vec{B}\vec{k})^2.$$

Using relation between coordinate and momentum operators for $\hat{\vec{p}}[\vec{B}\vec{r}] = \vec{B}\hat{\vec{L}}$ ($\hat{\vec{L}}$ – angular momentum operator) and $\hat{\vec{p}}^2 = -\hbar^2\vec{\nabla}^2 = -\hbar^2\Delta$, according $\hat{\vec{p}} = -i\hbar\vec{\nabla}$ (see [4], also), Hamilton operator

$$\hat{H} = \frac{1}{2M}\left(\hat{\vec{p}}^2 + \frac{e}{c}\vec{B}\hat{\vec{L}} + \frac{e^2}{c^2}\frac{1}{4}\left[\vec{B}\vec{r}\right]^2\right) + \frac{M\vec{r}^2}{8\pi\rho_{Fl}}\left(\vec{B}\vec{k}\right)^2,$$

in cylindrical polar coordinates ($x, y, z \to \rho, \varphi, z$) [5] with the z-axis in the direction of the magnetic field, when wave vector $\vec{k}$ coincide with the direction of the vector $\vec{B}$ (using relation $\hat{\vec{L}} \equiv \hat{L}_z = -i\hbar\frac{\partial}{\partial\varphi}$ and de Broglie postulate between momentum and wave vector ($\vec{p} = \hbar\vec{k}$), for z-projections of the $\vec{k}$, momentum operator $\hat{p}_z = -i\hbar\frac{\partial}{\partial z}$ ($k_z^2 = \left(\frac{\hat{p}_z}{\hbar}\right)^2 = -\frac{\partial^2}{\partial z^2}$) and magnetic field intensity $\vec{B} \equiv B_z$ according gauge condition $div\vec{A} = 0$ [3] (when the vector potential has component $A_\varphi = \frac{1}{2}B\rho$, $A_z = A_\rho = 0$ and Laplace operator is $\Delta = \frac{\partial^2}{\partial\rho^2} + \frac{1}{\rho}\frac{\partial}{\partial\rho} + \frac{1}{\rho^2}\frac{\partial^2}{\partial\phi^2} + \frac{\partial^2}{\partial z^2}$), we determine Schrödinger equation $\hat{H}\psi(\rho,\phi,z) = E\psi(\rho,\phi,z)$ in the form:

$$-\frac{\hbar^2}{2M}\left[\frac{\partial^2}{\partial\rho^2} + \frac{1}{\rho}\frac{\partial}{\partial\rho} + \frac{1}{\rho^2}\frac{\partial^2}{\partial\phi^2} + \frac{\partial^2}{\partial z^2}\right]\psi(\rho,\phi,z)$$

$$\left[-i\hbar\frac{eB_z}{2Mc}\frac{\partial}{\partial\phi} + \frac{e^2B_z^2}{8Mc^2}\rho^2 - \frac{MB_z^2}{8\pi\rho_{Fl}}\rho^2\frac{\partial^2}{\partial z^2}\right]\psi(\rho,\phi,z) = E\psi(\rho,\phi,z), \qquad (2)$$

Let’s rewrite the equation (2) as following

$$[\hat{D}_0(\rho,z) + \hat{D}_1(\rho,z)]\psi(\rho,z)\,exp\{\,im\phi\} = \left(E + i\hbar\frac{\omega_B}{2}\frac{\partial}{\partial\phi}\right)exp\{\,im\phi\}\psi(\rho,z), \qquad (3)$$

where we using for wave function a form

$$\psi(\rho,\phi,z)=\frac{exp\{im\phi\}}{\sqrt{2\pi}}\psi(\rho,z) \tag{4}$$

(here m is magnetic quantum number) and introduce the following notations,

$$\widehat{D}_0(\rho,z)=-\frac{\hbar^2}{2M}\left[\frac{\partial^2}{\partial\rho^2}+\frac{1}{\rho}\frac{\partial}{\partial\rho}+\frac{1}{\rho^2}\frac{\partial^2}{\partial\phi^2}+\frac{\partial^2}{\partial z^2}\right]+\frac{M\omega_L^2}{8}\rho^2, \tag{5}$$

$$\widehat{D}_1(\rho,z)=-\frac{Mv_A^2}{2}\rho^2\frac{\partial^2}{\partial z^2} \tag{6}$$

(Here $\omega_L=\frac{eB_z}{Mc}$- Larmor frequency and $v_A=\frac{B_z}{\sqrt{4\pi\rho_{Fl}}}$ is Alfven speed).

A solution of Schrödinger equation (3) at low Alfven velocity.

Under the assumption for low propagation velocity of Alfven wave (i.e. in very small intensity B_z external magnetic field) according as a some analogy of perturbation theory, we neglect the term $\widehat{D}_1(\rho,z)=-\frac{Mv_A^2}{2}\rho^2$ for perspective calculation δE correction to electron energy levels

$$E=E_o+\delta E, \tag{7}$$

via the equation for finding eigenfunction and eigenvalue for $\hat{D}_1(\rho,z)$ operator,

$$\widehat{D}_1(\rho,z)\psi_0(\rho,z)=\delta E\psi_0(\rho,z), \tag{8}$$

Then we rewrite the equation (3) as following

$$-\frac{\hbar^2}{2M}\left\{\left[\frac{\partial^2}{\partial\rho^2}+\frac{1}{\rho}\frac{\partial}{\partial\rho}+\frac{1}{\rho^2}\frac{\partial^2}{\partial\phi^2}+\frac{\partial^2}{\partial z^2}\right]+\frac{M\omega_L^2}{8}\rho^2\right\}exp\{im\phi\}\psi_0(\rho,z)$$
$$=\left(E_0+i\hbar\frac{\omega_L}{2}\frac{\partial}{\partial\phi}\right)exp\{im\phi\}\psi_0(\rho,z), \tag{9}$$

A second equation is homogeneous second order linear and its solution is well known from the courses of the non-relativistic quantum mechanics (see, for example [4]). We choice a solution for this equation in the form

$$Z(z)=exp\left\{\frac{i}{\hbar}p_z z\right\}. \tag{14}$$

The result for λ_z is

$$\lambda_z=\frac{p_z^2}{2M}, \tag{15}$$

i.e. electron have a spontaneity forward and back motion along axis z.

Let us now detail investigate a solution of the first equation from the system (13).

Defining a new independent variable

$$\xi=\frac{M\omega_L}{2\hbar}\rho^2, \tag{16}$$

we can write the first equation in system (13) in the form

$$\xi\frac{\partial^2R(\xi)}{\partial\xi^2}+\frac{\partial R(\xi)}{\partial\xi}+\left(\frac{1}{\hbar\omega_L}\lambda_\rho-\frac{1}{4}\xi-\frac{m^2}{4\xi}\right)R(\xi)=0. \tag{17}$$

The solution of equation (17) well known (see, for example, [3], or [4]). At $\xi\to\infty$ the desired function behaviors as $e^{-\xi/2}$, and at $\xi \to 0$ as $\xi^{\frac{m}{2}}$. According to this considerations, we search the solution of (16) in the form

$$R(\xi) = e^{-\frac{\xi}{2}}\xi^{\frac{|m|}{2}}w(\xi). \tag{18}$$

The solution of equation (17) takes the form [6]

$$w(\xi) = F\left(-\left(\frac{\lambda_\rho}{\hbar\omega_L} - \frac{|m|+1}{2}\right), |m|+1, \cdot\, \xi\right). \tag{19}$$

If the wave function is everywhere finite, the quantity $\frac{\lambda_\rho}{\hbar\omega_L} - \frac{|m|+1}{2}$ must be a non-negative integer n_ρ. In this case, the energy levels are given by the formula

$$\lambda_\rho = \hbar\omega_L\left(n_\rho + \frac{|m|+1}{2}\right), \tag{20}$$

Which equivalent to expression for the energy levels of a electron in uniform magnetic field: $E = \hbar\omega_L\left(n_\rho + \frac{1}{2}\right)$, which here gives the discrete energy values corresponding to motion in a plane perpendicular to the field – Landau levels [3]. According (7), (13), (15) and (20) total energy levels of electron motion into Alfven wave with external uniform constant magnetic field as the following:

$$E = \frac{\hbar\omega_L m}{2} + \hbar\omega_L\left(n_\rho + \frac{|m|+1}{2}\right) + \frac{p_z^2}{2M} + \delta E. \tag{21}$$

where the solution of $\delta E = \int_0^\infty \rho d\rho \int_{-\infty}^{\infty} dz\, \psi_0^+(\rho, z)\widehat{D}_1\psi_0(\rho, z)$ is our future elaboration.

The corresponding radial wave function is:

$$R_{n_\rho m}(\rho) = \left(\frac{M\omega_L}{\hbar}\right)^{\frac{|m|+1}{2}} \frac{1}{|m|!}\left[\frac{(|m|+n_\rho)!}{2^{|m|}n_\rho!}\right]^{1/2} e^{-\frac{M\omega_L}{4\hbar}\rho^2}\rho^{|m|}F\left(-n_\rho, |m|+1, \frac{M\omega_L}{2\hbar}\rho^2\right), \tag{22}$$

These are normalized by the condition $\int_0^\infty R^2\rho d\rho = 1$.

The hypergeometric function is here a generalized Laguerre polynomial.

According (4), (11), (14), (18), (19) and (22) total wave function is:

$$\psi(\rho, \phi, z) = \left(\frac{M\omega_L}{\hbar}\right)^{\frac{|m|+1}{2}} \frac{1}{|m|!}\left[\frac{\left(|m|+n_\rho\right)!}{2^{|m|+1}\pi n_\rho!}\right]^{1/2} exp\left\{im\phi + \frac{i}{\hbar}p_z z - \frac{M\omega_L}{4\hbar}\rho^2\right\}\rho^{|m|}$$

$$F\left(-n_\rho, |m|+1, \frac{M\omega_L}{2\hbar}\rho^2\right). \tag{23}$$

Research of lifetime of electron in n_ρ quantum levels during the precession around of ρ is our future elaboration, also.

Author Contributions: Jafarov R.G. is author of idea of the problem and method of solution of the equations, and other coauthors contributed equally to this work.

Acknowledgments

We would like to thank Organizing Committee for hospitality. Conflicts of interest: The authors declare no conflict of interest.

References

1. Landau L.D., Lifshits E.M. Electrodynamics of Continuous Media. Moscow: Nauka, 1982 (Second Edition), 620 p.
2. Alfven G., Felthammar K.-G. Space Electrodynamics. Moscow: Mir, 1967 (Second Edition), 260 p.
3. Landau L.D., Lifshits E.M. Quantum Mechanics (Nonrelativistic Theory). Moscow: Nauka, 1989 (Fourth Edition), v. III, 495 p.
4. Jafarov R.G. Quantum Mechanics (Lectures notes). Baku: ISAAC Group Publ., 2021,195 p.
5. Madelung E. Die Mathematischen Hilfsmittel des Physikers. Berlin: Spinger-Verlag. 1957, 618 p.
6. Beitman G., Erdeyi A. Higher Transcendental Functions. Moscow: Nauka, 1973, v.1, 294 p.

ELECTRICAL AND GALVANOMAGNETIC PROPERTIES OF CHALCOGENIDE SPINEL CONTAINING $Ni_{0.25}Cu_{0.05}Fe_{0.70}Cr_2S_4$

AI AHMEDOV

Institute of Physics of the National Academy of Sciences of Azerbaijan, Baku, Azerbaijan
E-mail: susenahmedli@gmail.com

Electrical and galvanomagnetic studies were carried out at low temperatures, which showed that $Ni_{0.25}Cu_{0.05}Fe_{0.70}Cr_2S_4$ is a semiconductor ferromagnet. It was found that the anomalous Hall coefficient R_a is three orders of magnitude higher than the normal Hall coefficient R_0, and that both coefficients take on a maximum value around the Curie temperature. Then they drop sharply. As in the case of substances with spontaneous magnetization, in this substance EMF Hall increases sharply linearly in the field of technical magnetization. The temperature dependence of the electrical conductivity σ of the compound $Ni_{0.25}Cu_{0.05}Fe_{0.70}Cr_2S_4$ indicates a semiconductor type of conductivity. The coefficient of thermal EMF decreases with increasing temperature, and its slow growth begins in the region of magnetic transformation. In this case, the thermal EMF α around T ~ 130K changes sign from positive to negative. The effect of a magnetic phase transition on charge transfer in the ferromagnet $Ni_{0.25}Cu_{0.05}Fe_{0.70}Cr_2S_4$ has been found.

Keywords: magnetization, $Ni_{0.25}Cu_{0.05}Fe_{0.70}Cr_2S_4$, Curie temperature, electrical conductivity
PACS: 64.70.kg, 75.50.Dd, 75.50.Pp

Introduction

It is known that isovalent substitution of ions in tetra and octahedral sites of spinel with the formation of solid solutions proceeds quite easily if the ion sizes are not too different [1, 2, 3].

Based on this, in order to obtain semiconductor compounds with high Curie temperatures, $FeCr_2S_4$ was partially replaced by Ni, Cu and a composition of the $Ni_{0.25}Cu_{0.05}Fe_{0.75}Cr_2S_4$ type was prepared. Such a solid solution is a convenient object for elucidating the relationship between electrical and magnetic properties. It is known from magnetic studies that the composition $Ni_{0.25}Cu_{0.05}Fe_{0.75}Cr_2S_4$ has a ferromagnetic structure [2, 3, 4].

Synthesis, preparation of samples and research methods

The calculated amount of the initial components of high purity was placed in an evacuated quartz ampoule, which was slowly heated to 900° C. After 3 days, the temperature slowly dropped to room temperature. The resulting compositions were thoroughly ground in an agate mortar and pressed under a pressure of 2.5 GPa. Annealing was carried out at 800° C in vacuum for 8 days. X-ray analysis showed that the obtained sample is single-phase and has a spinel structure.

Measurements of electrical conductivity and thermo-EMF were carried out by the compensation method at direct current.

Experimental results and their discussion

This work is devoted to the study of the dependence of the Hall EMF on the strength of the external magnetic field at different temperatures, as well as the temperature dependences of the electrical conductivity and thermo-EMF of $Ni_{0.25}Cu_{0.05}Fe_{0.75}Cr_2S_4$ crystals.

The Hall EMF dependences for $Ni_{0.25}Cu_{0.05}Fe_{0.70}Cr_2S_4$ samples at different temperatures are shown in Fig. 1.

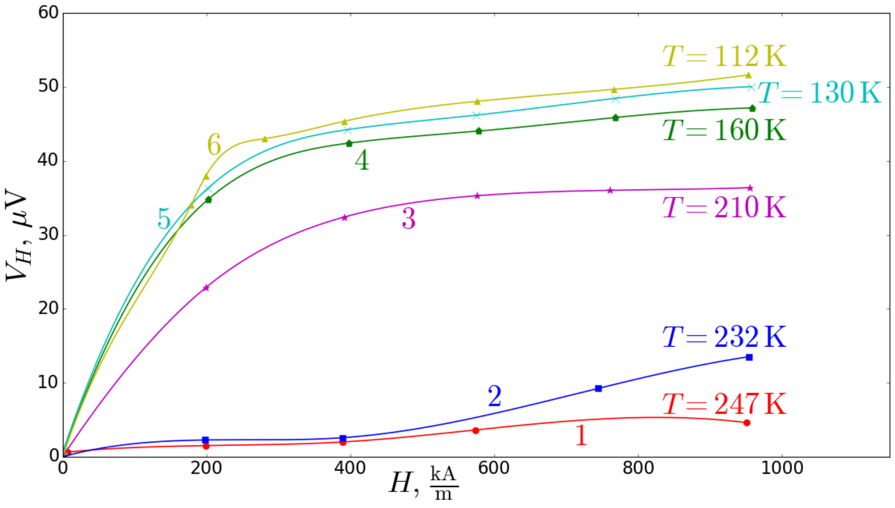

Fig. 1. Dependences of the Hall EMF for a $Ni_{0.25}Cu_{0.05}Fe_{0.70}Cr_2S_4$ crystal at different temperatures.

As can be seen from the figure, at low values of the magnetic field strength, the Hall EMF grows strongly with an increase in the strength of the external magnetic field, but later this growth slows down sharply. It is also seen that with an increase in temperature, the growth of the Hall EMF decreases. Above $T > T_\mathrm{C}$ ($T_\mathrm{C} \approx 225$ K), the dependence $E_x \sim f(H)$ is linear and this indicates the absence of spontaneous magnetization. To calculate the normal (R_0) and anomalous Hall coefficient (R_A), we used the standard formula [2]

$$E_x = \frac{d}{I} U_x = R_0(H + 4\pi M) + R_A M \tag{1}$$

Where d is the size of the sample in the direction of the magnetic field,, I is the current through the sample, M is the magnetization at given temperatures T and field H.

In the detuned region of fields $M = M_s + \chi H$ and according to [3], depends on H in the linear approximation in the field

$$R_A = R_s + \left(\frac{dR_A}{dH}\right)_H \tag{2}$$

In these expressions, M_s is the spontaneous magnetization, χ is the differential susceptibility, R_s is the spontaneous part of the anomalous Hall coefficient. Replacing, in (1) M by its expression, we get for E_x:

$$E_x = \left(R_0 + \frac{\chi E_0}{M_s}\right) H + E_0 \tag{3}$$

Here E_0 is a segment cut off on the E_x axis by extrapolation to $H = 0$ of the linear part $E_x(H)$, moreover

$$E_0 = M_s(4\pi R_0 + R_A) \tag{4}$$

Therefore

$$R_A = \frac{E_0}{M_s} - 4\pi R_0 \tag{5}$$

From these expressions it can be obtained that

$$\frac{E_x - E_0}{H} = R_0 + \chi \frac{E_0}{M_s} \tag{6}$$

The left side of this equation is the tangent of the slope of the linear part $E_x = f(H)$, obtained in the region of strong fields. From equation (6) for the normal Hall coefficient we obtain

$$R_0 = \frac{E_x - E_0}{H} - \chi \frac{E_0}{M_s} \tag{7}$$

Therefore, having data for χ and M_s, it is possible to determine the magnitude and sign of R_s, and hence R_0, since R_A at $H = 0$ turns into a spontaneous coefficient R_s. The data required for calculating R_A, for magnetization M and susceptibility were taken from [3].

The calculated values of R_0 and R_A depending on the temperature for the compositions $Ni_{0.25}Cu_{0.05}Fe_{0.70}Cr_2S_4$ are given in the table.

Table

$Ni_{0.25}Cu_{0.05}Fe_{0.70}Cr_2S_4$		
T, K	$R_0 \cdot 10^9\ \frac{\Omega \cdot sm}{Gs}$	$R_0 \cdot 10^6\ \frac{\Omega \cdot sm}{Gs}$
112	1.69	0.70
130	-1.43	1.17
177	-4.53	1.62
209	-7.35	1.83
232	-1/48	0.94

The table shows that for the composition $Ni_{0.25}Cu_{0.05}Fe_{0.70}Cr_2S_4$ at low temperatures both R_0 and R_A have a positive sign, at $T \geq 130$ K R_0 changes sign to negative, which is consistent with the behavior of the thermo - EMF coefficient (see Fig. 2.).

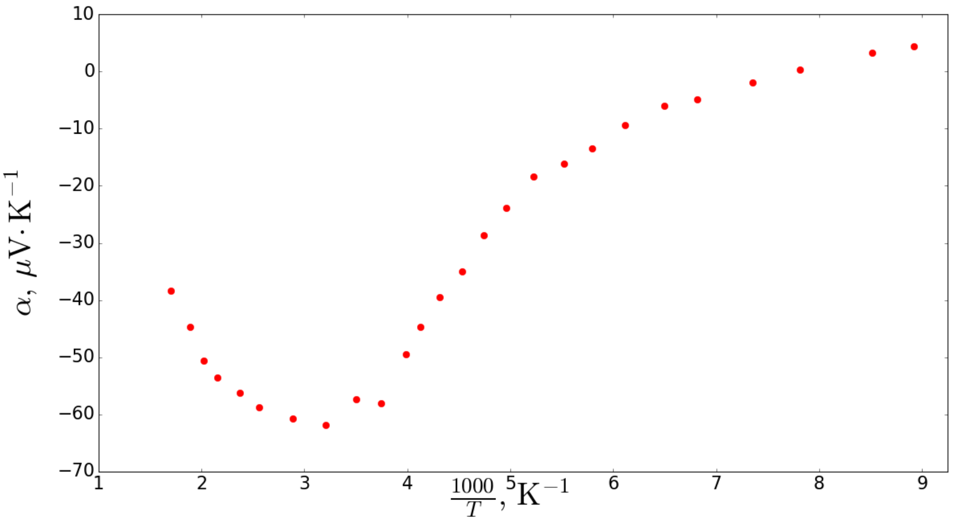

Fig. 2. Dependence of thermo-EMF on temperature ($\alpha \cdot T = f(T)$) for $Ni_{0.25}Cu_{0.05}Fe_{0.70}Cr_2S_4$ crystals.

The temperature dependence of the electrical conductivity for the sample (see Fig. 3.) $Ni_{0.25}Cu_{0.05}Fe_{0.70}Cr_2S_4$ shows that, before the magnetic phase transition for the studied composition, starting from 100 K, a metallic behavior of the conductivity is observed with increasing temperature.

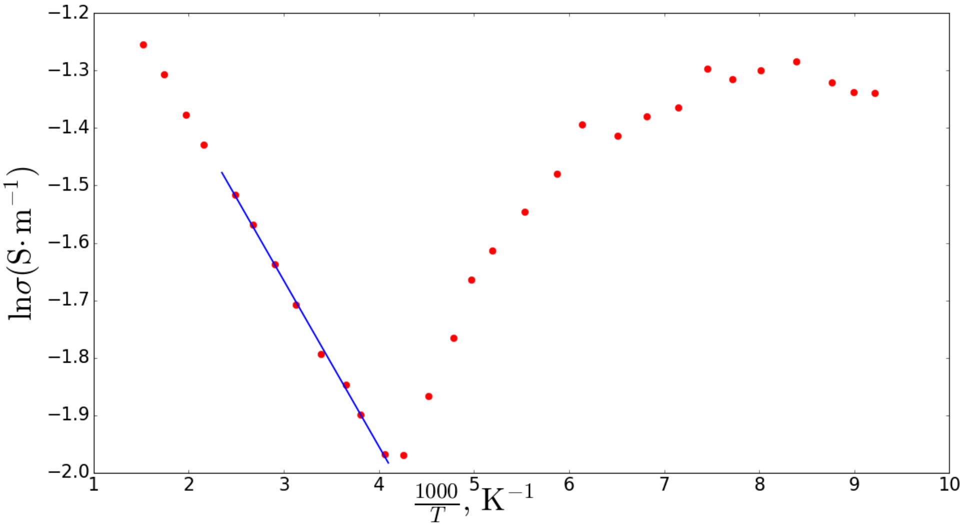

Fig. 3. Dependence of specific electrical conductivity on temperature $\left(\ln\sigma = f\left(\frac{1000}{T}\right)\right)$ for Ni0.25Cu0.05Fe0.70Cr2S4 crystals.

Above the temperature of the magnetic phase transition for the composition $Ni_{0.25}Cu_{0.05}Fe_{0.70}Cr_2S_4$, a semiconductor behavior of the conductivity is observed. The corresponding changes are also observed on the temperature dependence of the thermal EMF coefficient. This is apparently due to the scattering of charge carriers on spin inhomogeneities formed during the transition of a spin system from a magnetically ordered state to a disordered one [5]. Above 250 K, the intrinsic conductivity region is realized in the $Ni_{0.25}Cu_{0.05}Fe_{0.70}Cr_2S_4$ crystal.

The activation energy found from the slope of the curves $\ln\sigma = f\left(\frac{1000}{T}\right)$ in the high-temperature region for the composition $Ni_{0.25}Cu_{0.05}Fe_{0.70}Cr_2S_4$ is $2.35 \cdot 10^{-2}$ eV [6].

Figure 2 shows that with an increase in temperature, the thermo-EMF coefficient decreases and a sign inversion occurs. At low temperatures, p-type conductivity is observed in this sample [7].

Conclusion

Thus, studies of the magnetic and electrical properties of the compound in the temperature range 113–660 K have shown that this compound is a ferromagnet and has a semiconducting character of electrical conductivity. The effect of the magnetic phase transition on charge transfer in the ferromagnet $Ni_{0.25}Fe_{0.75}Cr_2S_4$ has been found. Electrical studies have shown that at low temperatures $Ni_{0.25}Fe_{0.75}Cr_2S_4$ is a p-type semiconductor.

References

1. Steinbeiss E., Dintner H., Annalen der Physik 7 Folge, Band 27, Heft. 1, 1971, p. 119. DOİ: 10.1002 / andp. 19714820115
2. Treitinger L., Göbel H., Pink H. Mat. Res. Bull., 1976, v. 11, p. 1375.
3. Sadikhov R.Z., Namazov A.D. J. Tech.Phys. 1989, v. 31 (1), p. 314. https://journals.ioffe.ru/articles/viewPDF/28331
4. Akhmedov A., Aldzhanov M. A., Najafzade M. D., Ibragimov I. N., Sultanov G. D. AJP Fizika, 2018, v.XXIV (3), p. 67.
5. Loseva G.V., Ovchinnikov S.G. In collection: Physics of magnetic materials, ed. V. A. Ignatchenko, G. A. Petrakovsky (Novosibirsk, Nauka, 1983, p. 60.
6. Neumann H. Phys. Stat. Sol. (a) 1979, v. 56, p. 137.
7. Shalimova KV. Physics of semiconductors, 2010. 400 p.

THE PUGMY DIPOLE REZONANCE OF ^{164}Dy NUCLEUS

E GULIYEV[1], H QULIYEV[2] and AA KULIEV[2]

[1]State Agency on Nuclear and Radiological Activity Regulation, Ministry of Emergency Situations, N.Rafiyev 66, Baku, Azerbaijan
[2]National Aviation Academy of Azerbaijan, Baku, Azerbaijan
E-mail: ekuliev@yahool.com

The excitation of pygmy dipole resonance (PDR) in even-even ^{164}Dy nucleus is examined through quasiparticle random-phase approximation (QRPA) with the effective interactions that restores the broken translational and Galilean invariances. Where, the transition cross sections, probabilities, photon strength functions and isospin character of the predicted resonance were studied.

Keywords: PDR, QRPA, ^{164}Dy, cross-section
PACS: 24.60.Dr, 07.57.Pt, 25.12.-m

Introduction

Presence of low lying E1 resonance is well identified in nuclei and named pygmy dipole resonance (PDR) [1].This low-lying dipole excitation mode has been center of interest from theoretical and experimental perspective due to its close relations with the neutron skin, the symmetry energy in the equation of state and astrophysical r-process [2-5]. Despite the PDR is widely accepted as a common mode of excitation for many atomic nuclei [3, 5], however, its nature is still under discussion. PDR had been investigated mostly for nuclei sitting at least one closed shell [3, 5]. Recently, nuclei far from shell closure have been examined from PDR window from theoretical point of view [6-11], but experimental effort for the PDR in heavy, strongly deformed nuclei is still inadequate [12, 13].

In this study, the excitation energies, transition probabilities, splitting behaviors of E1's into K=0 and K=±1, and other related properties of the 164Dy isotopes were investigated using the translational and Galilean invariances quasiparticle random-phase approximation (TGI-QRPA) up to particle threshold energy. This model satisfactorily described the electric and magnetic dipole strength in various nuclei [6,8].

Theory

The electric dipole strength calculations were carried out with a translational and Galilean symmetric Hamiltonian of the form.

$$H = H_{sqp} + h_0 + h_{\Delta} + W_{dip} \tag{1}$$

here H_{sqp} is the Hamiltonian for the single-quasiparticle motion

$$H_{sqp} = \sum_{s} \varepsilon_s(\tau) B_{ss}(\tau) \tag{2}$$

Here

$$W_{dip} = \frac{3}{2\pi}\chi_1 \left(\frac{NZ}{A}\right)^2 \left(\vec{R}_n - \vec{R}_p\right)^2 \tag{3}$$

is interaction that represent the coherent isovector dipole vibrations of protons and neutrons, the centre-of-mass (c.m.) of the nucleus being at rest. Where, $\varepsilon_s(\tau) = \sqrt{\Delta_\tau^2 + (E_s(\tau) - \lambda_\tau)^2}$

is the quasiparticle energy of a nucleon where Δ_τ is the BCS paring energy gap, λ_τ is the chemical potential. Here, $B_{ss}(\tau) = \sum_{\rho=\pm} \alpha_{s\rho}^{+}(\tau)\alpha_{s\rho}(\tau)$ where $\alpha_s^{+}(\alpha_s)$ are quasiparticle creation (annihilation) operator and $\rho = \pm 1$ represents time reversal states. $\vec{R}_n$ and $\vec{R}_p$ so $R_\mu = \sum_{k=1}^{A} r_k Y_{lm}(\Theta_k, \Phi_k)$ are the centre of mass (c.m.) coordinates of the neutron and proton systems. The term χ_1 denotes the isovector dipole -dipole coupling constant.

The broken translational and Galilean invariance of the single-quasiparticle Hamiltonian can be restored with the aid of h_0 and h_D of interactions of the form [14-16].

$$h_0 = -\frac{1}{2\gamma}\sum_{\mu}[H_{sqp}, P_\mu]^{+}[H_{sqp}, P_\mu] \tag{4}$$

$$h_\Delta = -\frac{1}{2\beta}\sum_{\mu}[U_\Delta, R_\mu]^{+}[U_\Delta, R_\mu] \tag{5}$$

Here, $\gamma = \langle 0|[P_\mu^{+}, [H_{sqp}, P_\mu]|0\rangle$ and $\beta = \langle 0|[R_\mu^{+}, [U_\Delta, R_\mu]|0\rangle$ are extracted from the mean field and pairing potentials. The P_μ is the spherical components of the linear momentum for the $J^\pi = 1^-$ excitations, and $\mu = \pm 1$. The U_Δ is pairing potential.

The reduced probabilities of E1 transitions for even-even deformed nuclei can be obtained using the mathematical expression within the framework of TGI-QRPA, is as follows:

$$B(E1, 0^{+}0 \to 1^{-}K) = (1 + \delta_{K,1})\frac{1}{Y(\omega_i)}\left|(e_{eff}^{p} M_p + e_{eff}^{n} M_n)\right|^2 \tag{6}$$

where

$$Y(\omega_i) = Y_n(\omega_i) + Y_p(\omega_i),\ Y_\tau(\omega_i) = 2\omega_i \sum_{ss'}(\tau)\frac{\varepsilon_{ss'}^{5} r_{ss'}^{2} u_{ss'}^{2}}{(\varepsilon_{ss'}^{2} - \omega_i^{2})^2} \tag{7}$$

$$M_\tau = 2\sum_{ss'}^{(\tau)} r_{ss'} u_{ss'} g_{ss'}, \tag{8}$$

Where M_t is electric dipole operators for neutron and proton systems, and $g_{ss'}$ is the sum of two quasiparticle amplitudes ($\psi_{ss'}$ and $\varphi_{ss'}$) in the even-even nucei ($g_{ss'} = \psi_{ss'} + \varphi_{ss'}$).For the E1 transitions, $e_{eff}^{p} = N/A$ is the effective charge for protons and $e_{eff}^{n} = -Z/A$ for neutrons.

The one of the nuclear quantities that can be calculated and observed is the photon strength function. The strength function from ground to excited states for E1 transitions with Lorentzian weight of deformed nuclei can be calculated within the TGI-QRPA using the following equation [17-19].

$$S_{E1}(\omega_i) = \frac{1}{2\pi}\sum_{i}\frac{\Delta}{(\omega_i - \omega_0)^2 + \left(\frac{1}{2}\Delta\right)^2} B(E1; 0^{+} \to 1^{-}) \tag{9}$$

where

$$\delta_{\Delta}(\omega_i-\omega_0)=\frac{1}{2\pi}\frac{\Delta}{(\omega_i-\omega_0)^2+\left(\frac{1}{2}\Delta\right)^2} \tag{10}$$

$\delta(\omega_i-\omega_0)$ is Lorentz function with the averaging parameter Δ in MeV. From here, the strength function takes the form

$$S_{E1}(\omega_i)=\sum_n \delta_{\Delta}(\omega_i-\omega_0)\cdot B(\lambda,n) \tag{11}$$

Photo-absorption cross section is vital for electric dipole mode, and it is expressed for a nucleus as follows [20].

$$\sigma_{E1}(E)=\frac{4\pi^2e^2}{\hbar c}(\omega_i-\omega_0)\sum \quad |\langle\Psi_i|M|\Psi_0\rangle|^2\delta_{\Delta}(\omega_i-\omega_0) \tag{12}$$

Depending on the strength function of the electric dipole photo-absorption cross section, it is written as follows [21, 22]:

$$\sigma_{E1}(\omega_i)=\frac{16\pi^3e^2}{9\hbar c}\omega_i S_{E1}(\omega_i) \tag{13}$$

Another important quantity is the related widths for ground state transitions that can be calculated with formulas [23]:

$$\Gamma_0(E1)=0.349\cdot\omega_i^3\cdot B(E1) \tag{14}$$

$$\Gamma_0(M1)=3.86\cdot\omega_i^3\cdot B(M1) \tag{15}$$

Where the B(M1) values for the magnetic dipole excitation calculated using the rotational invariant RI-QRPA model presented in Refs [16, 24-26].

Results and discussion

We have performed the calculations for the ^{164}Dy nucleus using QRPA employing deformed Wood-Saxon potential with a well depth of 6 MeV [27]. The pairing parameters Δ_n (Δ_p) and chemical potentials λ_n (λ_p) were obtained using the method given by Soloviev [28], the deformation parameters δ_2 were extracted as Refs in [19, 29] from measured quadrupole moments [30]. Table 1 shows the pairing parameters, chemical potentials, and deformation parameters, of the ^{164}Dy isotope.

The strength parameter χ_1 was chosen as $400/A^{-5/3}$ MeV fm^{-2} for the isovector dipole-dipole interaction which is suggested for the isovector dipole-dipole interaction in order to describe the centroid of the giant dipole resonance of the dysprosium isotopes. Its magnitude is related to the isovector symmetry potential, and the chosen value is in close agreement with the analysis of Bohr and Mottelson [19].

Table 1. Pairing correlation parameters (in MeV) and *δ*₂ values

Nuclei	**Δn**	**Δp**	**ln**	**lp**	**δ2**
164Dy	0.95	1.03	-7.000	-7.974	0.304

The Energy Weighted Sum Rule (EWSR) is very useful for verifying the accuracy of the QRPA calculation. Therefore, we calculated EWSR in QRPA and compared it with the model-independent EWSR. Where, the energy weighted sums of the QRPA strength depending on the model's transition matrix elements were calculated and compared with the model-independent, classical energy-weighted sum rule (EWSR). The model-independent classical Thomas-Reiche-Kuhn (TRK) sum rule [19] is given:

$$TRK = 14.8\frac{NZ}{A}(e^2 fm^2 \cdot MeV) \tag{16}$$

The EWSR expression according to TGI-QRPA theory is as follow

$$EWSR = \sum_i \omega_i \cdot B(E1)(e^2 fm^2 \cdot MeV) \tag{17}$$

Figure 1 shows a comparison of the model-independent, classical TRK sum rule with the model-dependent sum rule.

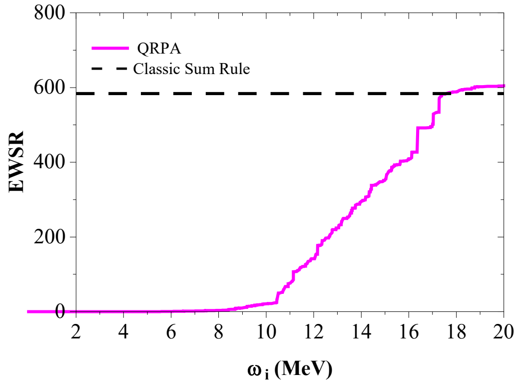

Fig. 1. EWSR of dipole strength function of ^{164}Dy isotope

In general, comparison of the sum rules show that GDR mode consumes approximately 100% of EWSR. The results of the model dependent EWRS reveal that the summed transition strengths up to 25 MeV exhaust about 101–108% of the classical TRK sum rules, while below 10 MeV (i.e., the PDR region), it exhausts about 6.0% of the classical TRK sum rule for the investigated Dy isotopes. Comparison of model-dependent and independent EWSR show QRPA based EWSR nice reflect classical TRK sum rule.

Now we will discuss the prediction of our calculations for the pygmy energy region for the ^{164}Dy nucleus. Figure 2 shows the distribution of a photo-absorption cross-section calculated using TGI-QRPA.

Figure 2 indicates that the photo-absorption cross section for nuclei of interest increase as a function of energy within the 5 to 10 MeV energy region.

In recent years, the photon strength function (γSF) has become one of the crucial quantities that provide information for understanding the structure of the nucleus [31]. Photon strength function can be measured by transfer reactions such as (^{3}He, αγ), (p, tγ) and inelastic scattering reactions, e.g., (^{3}He, ^{3}He'γ), (p, p'γ) [32]. The photon strength function is directly proportional to the cross section and the relationship between these two quantities is as follows [33, 34]:

$$f(E_\gamma) = \frac{\sigma(E_\gamma)}{3E_\gamma(\pi\hbar c)^2} \tag{18}$$

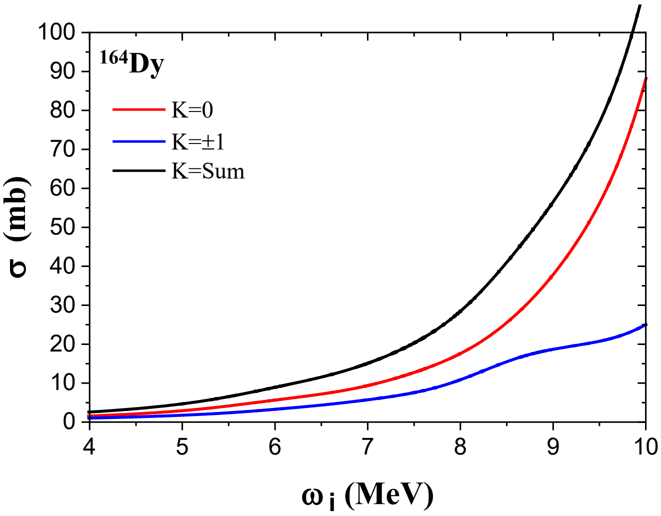

Fig. 2. (Color online) The photo-absorption cross section for even-even ^{164}Dy

Using the Eq (18), it is possible to obtain γSF for investigeted nucleus via the photo-absorption cross sections calculated in the TGI-QRPA. For ^{164}Dy isotope the experimental data on γSF exist more than cross sections.

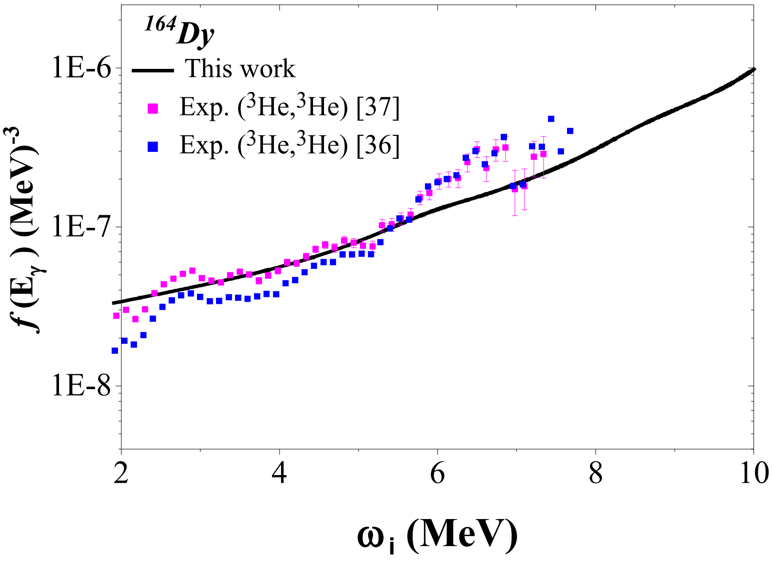

Fig. 3. Calculated photon strength functions for the even-even ^{164}Dy nucleus compared with measured primary photon strength functions [36,37] for the ^{164}Dy (n, γ) reaction.

Therefore, comparing of experimental γSF with the ones calculated in this work, gives valuable information for PDR region [35-37] and shed light on the future experiemnts. In Figure 3, our calculations of the photon strength function for even-even ^{164}Dy nucleus and available experimental data were compared. The calculations show that there is a smooth increasing of strength function up to 5 MeV for investigated nucleus. It is evident that experimental results from Ref [37] are described more accurately by our model. The explanation for the similarity of our results with Ref [37] and deviations from Refs [35, 36] could be the fact that no extracting magnetic dipole strength, hidden weaker transitions in the atomic background, and different types of backgrounds are challenges for presenting pure SF for E1 excitations in earlier experiments. Therefore if one takes into account the inclusion of several improvements in a new experiment, consistent of our prediction with new observation are founded.

Let's now discuss the energy distribution of calculated transition probabilities. The computed transition probabilities for E1 spread over energy region of 5≤E≤10 MeV with a structure similar to resonance. The results extracted from our calculations agree well with those nuclei that having PDR in the neighborhood of Dy isotopes of interest [10, 38].

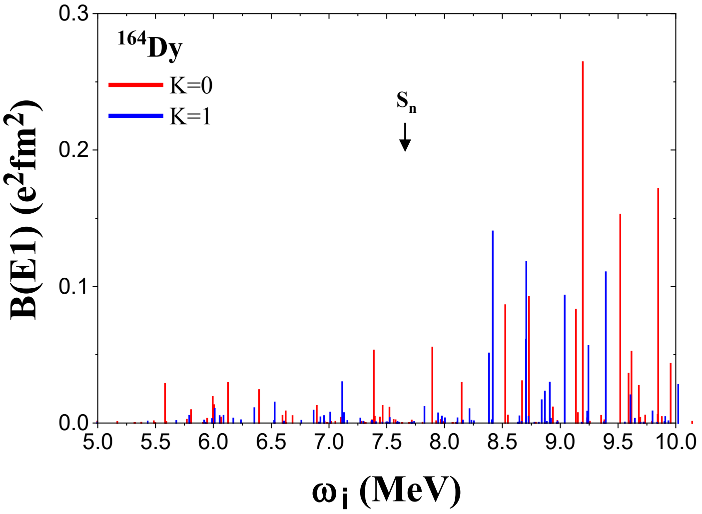

Fig. 4. (Color online) The electric dipole distribution of low-energy region in ^{164}Dy isotope extracted from TGI-QRPA. The threshold energy for neutrons (S_n) taken from [39] are shown with vertical arrows.

Recently, the structure of E1 excitations under the particle threshold energy has become the subject of theoretical studies [4]. Analyzing the structure of E1 excitations is possible through two-quasiparticle (neutron or proton) configurations of the one-phonon wave functions of the E1 excitations [40, 41]. Thought such analyses it is also possible to test macroscopic depiction of PDR which describes the neutron skin oscillates versus the saturated core including proton-neutron. With investigating the structure and collectivity of the PDR for the ^{164}Dy nucleus, we examined the phonon two-quasiparticle structure of E1 excitations in the range for PDR region using the QRPA.

Table 2 shows the excitation energies ω_i, the reduced B(E1) probabilities, the two-quasiparticle amplitudes, the single-particle structure of the states with asymptotic Nilsson quantum numbers ($Nn_z\Lambda\Sigma$), the contributions of neutrons and protons configurations wave functions to their sum wave functions $\psi^i_{ss'}$, in percent, and contribution of the sums of electric dipole operators of neutron (proton) systems M_t of the most pronounced of 1^-0 and 1^-1 dipole excitations the sum includes the 2qp amplitudes, which have a value greater than 0.05.

From the Table 2, it can be understood that for both K=0 and K=±1 components below the particle threshold energy the electric dipole excitations are mainly formed by only-neutron-neutron or only-proton-proton configurations. Our results indicated that the two-quasiparticle configurations of the E1 excitations below the particle threshold energy are inherent the mono-nucleon behavior. These results shown a simple geometrical macroscopic interpretation of the structure of the PDR mode is not valid microscopically. This prediction is supported by other microscopic studies [42]. As can be seen from the Table 2, several excitations above particle threshold energies with the same character are also predicted.

It is well known that spin-flip resonance (SFR) shares almost the same energy interval with PDR and may overlap with it. To investigate role of SFR in formation of excitations below particle threshold energy, here we studied the contribution of M1 excitations in the ^{164}Dy spectrum below 10 MeV. The transition strengths for the M1 excitation, obtained using the rotational invariant QRPA [16]. Due to the different measure units of E1 and M1 transition strengths, we calculated the ground-state transition widths of the low-lying dipole excitations (see Eq (14) and Eq (15)) for the ^{164}Dy isotopes in the 5–10 MeV energy region in order to picture the impacts of the E1 and M1 excitations. We display them for comparison in *Figure 5,* where the grey histogram corresponds to the E1 transition widths while the purple one indicates M1 transition widths, both in 200 keV steps.

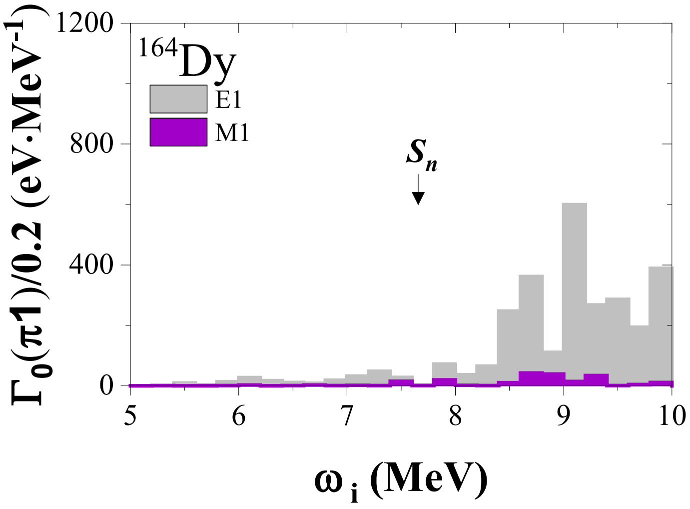

Fig. 5. B(E1) (gray) and B(M1) (purple) strength distributions for the even-even $^{154\text{-}164}$Dy nuclei below 10 MeV in 200 keV steps

Figure 5 shows that the E1 and M1 strengths occupy same energies, but compared to the high E1 strength distribution, the M1 excitations make a relatively small contribution for all nuclei of interest.

Table 2. Two-quasiparticle structure of the several $K^{\pi}=0;\pm1$ states with the highest B(E1) values of ^{156}Dy calculated with TGI-QRPA

K=0					K=1				
ωi (MeV)	**B(E1) (e2fm2)**	$\psi^{i}_{ss'}$	**NnzΛΣ**	**%cont**	**ωi (MeV)**	**B(E1) (e2fm2)**	$\psi^{i}_{ss'}$	**NnzΛΣ**	**%cont**
6.125	0.029	-0.785	nn 530↑-660↑	61.554	6.012	0.010	-0.994	pp 651↑-532↑	98.803
		-0.243	nn 512↑-402↑	5.881	6.355	0.011	-0.997	nn 514↑-624↓	99.400
7.389	0.053	0.225	nn 750↑-640↑	5.055	6.53	0.015	0.895	pp 640↑-510↓	80.102
		-0.260	nn 732↓-651↑	6.750			-0.432	pp 541↓-422↓	18.662
		0.147	nn 761↑-651↑	2.162	7.116	0.030	0.886	pp 550↑-640↓	78.499
		-0.302	pp 550↑-640↑	9.129			0.347	pp 411↓-301↑	12.040
		0.149	pp 550↑-431	2.224	7.826	0.012	0.968	nn 640↑-761↑	93.702
		-0.219	pp 530↑-420↑	4.798	8.215	0.010	0.706	nn 400↑-501↑	49.843
		-0.233	pp 541↓-651↓	5.435			0.236	nn 400↑-761↑	5.569
		-0.326	pp 532↓-422↓	10.599			-0.356	nn 651↑-752↑	12.673
		-0.170	pp 521↑-411↑	2.894			0.298	nn 532↓-642↑	8.880
		-0.130	pp 303↓-413↓	1.688			0.437	nn 402↑-503↑	19.096
		-0.195	pp 532↓-642↓	3.817	8.417	0.140	0.286	nn 400↑-501↑	8.179
		-0.271	pp 523↑-413↑	7.346			-0.234	nn 651↑-752↑	5.475
		-0.534	pp 523↓-633↓	28.549			-0.651	nn 402↑-503↑	42.380
7.893	0.055	-0.121	pp 550↑-640↑	1.461			-0.331	nn 642↓-743↓	10.956
		0.865	pp 550↑-431↓	74.740			-0.254	pp 400↓-541↓	6.451
		-0.105	pp 541↓-651↓	1.094	8.703	0.061	-0.289	nn 642↓-743↓	8.352
		0.330	pp 532↓-422↓	10.874			-0.803	nn 622↑-514↓	64.480
		0.103	pp 303↓-413↓	1.052			-0.345	pp 422↑-523↑	11.902
		0.228	pp 523↑-413↑	5.182	8.708	0.118	-0.229	nn 411↑-512↑	5.244
		0.123	pp 523↓-633↓	1.523			-0.331	nn 642↓-743↓	10.956
8.148	0.029	0.131	nn 521↓-631↓	1.709			0.594	nn 622↑-514↓	35.283
8.526	0.086	-0.101	nn 550↑-660↑	1.010			-0.503	pp 422↑-523↑	25.300
		0.125	nn 550↑-651↓	1.570			-0.239	pp 404↑-505↑	5.712
		-0.152	nn 532↑-642↑	2.303	8.867	0.023	0.602	nn 532↓-642↑	36.240
		-0.227	nn 521↑-411↑	5.167			-0.380	nn 411↑-512↑	14.440
8.670	0.031	0.130	nn 550↑-651↓	1.678			0.628	nn 523↓-633↑	39.438
		-0.173	nn 532↑-642↑	2.994	8.910	0.030	0.445	nn 550↑-651↑	19.802
		-0.160	nn 521↑-411↑	2.560			-0.705	nn 532↓-642↑	49.702
8.730	0.092	-0.103	nn 550↑-660↑	1.056			-0.309	nn 411↑-512↑	9.548
		0.358	nn 550↑-651↓	12.789			0.224	nn 512↑-413↑	5.017
		-0.517	nn 532↑-642↑	26.708			0.234	pp 633↑-514↑	5.475
		0.182	nn 521↑-411↑	3.309					
		0.107	pp 532↓-422↓	1.145					

Conclusion

The analysis of the evolution of the pygmy dipole resonances along a dysprosium isotopic chain confirms that the TGI-QRPA reproduces the basic features of these resonances very well. We established that PDR states exhaust up to 0.8% of the classic TRK sum rule for the investigated Dy isotope.

Comparison of the theoretical and experimental cross sections show consistent with each other. In general, a comparison of the theoretical strength functions with experimental ones was showed modern measurements are more satisfying.

According to our calculations, we have seen the splitting of K=0 and K=±1 modes due to the deformed structure of Dy isotopes. The results reveal that the E1 transition strengths in ^{164}Dy nucleus below the particle threshold show structural differences in microscopic and macroscopic interpretations.

In addition, the results indicate a dominant E1 contribution, with there being no considerable predicted spin-flip contribution to the dipole strength in the PDR region.

References

1. Brzosko J et al, Canadian Journal of Physics 1969, v. 47, p. 2849.
2. Pickstone S et al. EPJ Web of Conferences 2015, v. 93, p. 01053.
3. Bracco A et al, Progress in Particle and Nuclear Physics 2019, v. 106, p. 360.
4. Paar N et al, Reports on Progress in Physics 2007, v. 70, p. 691.
5. Savran D et al, Progress in Particle and Nuclear Physics 2013, v. 70, p. 210.
6. Tabar E et al, Physica Scripta 2021, v. 96, p. 075303.
7. Tabar E et al, Nuclear Physics A 2021, v. 1008, p. 122138.
8. Quliyev H et al, Nuclear Physics A 2021, v. 1014, p. 122239.
9. Tamkas M et al, Nuclear Physics A 2019, v. 987, p. 79.
10. Yoshida K and Nakatsukasa T, Physical Review C 2011, v. 83, p. 021304.
11. P apst O et al, Physical Review C 2020, v. 102, p. 034323.
12. Kneissl U et al, Progress in Particle and Nuclear Physics 1996, v. 37, p. 349.
13. Von Neumann-Cosel P, Progress in Particle and Nuclear Physics 1997, v. 38, p. 213.
14. Guliyev E et al, Physics Letters B 2002, v. 532, p. 173.
15. Pyatov N I and Salamov D I, Nukleonika 1977, v. 22, p. 127.
16. Kuliev A A et al, The European Physical Journal A 2010, v. 43, p. 313.
17. Malov L A et al, Zeitschrift für Physik A Atoms Nuclei 1985, v. 320, p. 521.
18. Soloviev V G et al, Nuclear Physics A 1980, v. 342, p. 261.
19. Bohr A and Mottelson B. *Nuclear Structure vol.2,* Benjamin: New York, USA, 1975
20. Ring P and Schuck P. *The nuclear many-body problem,* Springer Science: New York, USA, 2004
21. Ponomarev V Y et al, Nuclear Physics A 1994, v. 569, p. 333.
22. Litvinova E et al, Physical Review C 2008, v. 78, p. 014312.
23. Kneissl U et al, Progress in Particle and Nuclear Physics 1995, v. 34, p. 285.
24. Guliyev E et al, Central European Journal of Physics 2010, v. 8, p. 961.
25. Guliyev E et al, Nuclear Physics A 2013, v. 915, p.78.
26. Tabar E et al, Nuclear Physics A 2018, v. 979, p. 143.
27. Dudek J and Werner T, Journal of Physics G: Nuclear and Particle Physics 1978, v. 4, p. 1543.
28. Soloviev V G. *Theory of Complex Nuclei,* Pergamon Press: New York, USA, 1976
29. Ertuğral F et al, Acta Physica Polonica A 2015, v. 128, p. 254.
30. Pritychenko B et al, Atomic Data and Nuclear Data Tables 2016, v. 107, p. 1.

31. J Rekstad et al, Physica Scripta 1983, v. 1983, p. 45.
32. Larsen A et al, Physical Review C 2011, v. 83, p. 034315.
33. Brits C et al, Nuclear Physics A 2019, v. 99, p. 054330.
34. Bartholomew G et al. Chapter 4-Gamma-ray strength functions. In Advances in Nuclear Physics, Springer: New York, USA,1973
35. Guttormsen M et al, Physical Review C 2003, v. 68, p. 064306.
36. Nyhus H et al, Physical Review C 2012, v. 85, p. 014323.
37. Renstrøm T et al, Physical Review C 2018, v. 98, p. 054310.
38. Guliyev E et al, Journal of Physics G: Nuclear and Particle Physics 2020, v. 47, p. 115107.
39. Wang M et al, Chinese Physics C 2012, v. 36, p. 1287.
40. Colo G and Bortignon P, Nuclear Physics A 2001, v. 696, p. 427.
41. Vretenar D et al, Nuclear Physics A 2001, v. 692, p. 496.
42. Co' G et al, Physical Review C 2009, v. 80, p. 014308.

CIRCULAR (LINEAR) POLARIZATION OF THE γ-QUANTUM IN THE REACTION $\mu^-\mu^+ \to H\gamma$

SK ABDULLAYEV, MSH GOJAYEV and AK GULAYEVA

Baku State University, Baku, Azerbaijan
E-mail: macidqocayev@bsu.edu.az, ORCID: 0000-0001-7372-3283

The process of the joint generation of a Higgs boson and a γ-quantum in muon-antimuon collisions investigated within the framework of the Standard Model: $\mu^-\mu^+ \to H\gamma$. Taking into account the longitudinal polarizations of the muon-antimuon pairs and the circular (linear) polarization γ-quantum, expressions for the differential and integral cross sections of the process are obtained. Expressions for the degrees of circular and linear polarization γ-quantum are found. The dependence of these characteristics, as well as the effective cross-section of the process on the departure angle θ_γ and the energy $\sqrt{s}$ of the muon-antimuon pair is studied in detail.

Keywords: muon-antimuon pair, γ-quantum, Higgs boson, degree of circular polarization, degree of linear polarization.
PACS: 14.60.Ef, 14.70.Bh, 14.80.Bn

Introduction

In 2012, ATLAS and CMS collaborations discovered the Higgs boson in the Large Hadron Collider (LHC) [1, 2] (see reviews [3-5]). The Higgs boson was discovered at the LHC by studying its decays into two photons $H \to \gamma\gamma$ and two lepton-antilepton pairs $H \to ZZ^* \to 4\ell$, where Z^* – virtual Z-boson, $\ell = e^\mp$ or $\mu^\mp$. Decays were also detected in the LHC according to the scheme $H \to WW^* \to \ell\nu\ell\nu$, where W – a charged boson, ν – a muon or electron neutrino. According to the CMS collaboration data, it was determined that the mass of the Higgs boson is $M_H = 125.3 \pm 0.4(stat.) \pm 0.5(syst.)$ GeV, and according to the ATLAS collaboration data, it is $M_H = 126.0 \pm 0.4(stat.) \pm 0.4(syst.)$ GeV.

The study of the physical properties of the Higgs boson and the study of the mechanism of spontaneous violation of electroweak symmetry is one of the main tasks of future high-energy electron-positron and muon-antimuon colliders [6-11].

In electron-positron (muon-antimuon) collisions, the interaction constants of the Higgs boson with massive W- and Z-bosons can be measured with high accuracy in the main channels of its birth: during the emission of the Higgs boson $e^-e^+ \to Z^* \to ZH$ [12-14], in the mechanisms of fusion of W^+W^-- and ZZ-bosons $e^-e^+ \to W^*\nu_e W^*\bar{\nu}_e \to H\nu_e\bar{\nu}_e$, $e^-e^+ \to Z^*e^-Z^*e^+ \to He^-e^+$ [12-14].

The interaction constant of the Higgs boson with the top quark is measurable in the process $e^-e^+ \to t\bar{t}H$ [15].

The most important interaction constants of the Higgs boson are associated with the vertices $H\gamma\gamma$ and $HZ\gamma$. To measure these interaction constants, the study of the reaction of the joint generation of a γ-quantum and the Higgs boson in electron-positron (muon-antimuon) collisions $e^-e^+ \to H\gamma$ is of particular interest. Within the framework of the Standard Model (SM), this process was studied in [16, 17] without taking into account the polarization states a e^-e^+-pair and a photon. The processes $e^-e^+ \to H\gamma$, $e^-e^+ \to H^0(h;A)\gamma$, taking into account the longitudinal polarizations of the electron-positron pair, were studied in [18] (here, H^0, h and A – the Higgs bosons of the Minimal Supersymmetric Standard Model [19, 20].

In this paper, we investigate the degrees of circular and linear polarization γ-quantum in the process of

$$\mu^- + \mu^+ \to H + \gamma\,. \tag{1}$$

Radiation of γ-quantum by a muon-antimuon pair

The process of co-generation of the Higgs boson and the γ-quantum during the collision of a muon-antimuon pair is described by the Feynman diagrams shown in Fig. 1. Diagrams a) and b) correspond to the radiation of the γ-quantum and the Higgs boson by a muon-antimuon pair. Diagrams c) and d) are fermionic and W-bosonic loop diagrams (cross-channel diagrams are added to them). The remaining diagrams are t-channel vertex diagrams containing exchanges $Z - \mu$ and $W^{\pm} - \nu_\mu$ (it is necessary to add cross-channel diagrams to them).

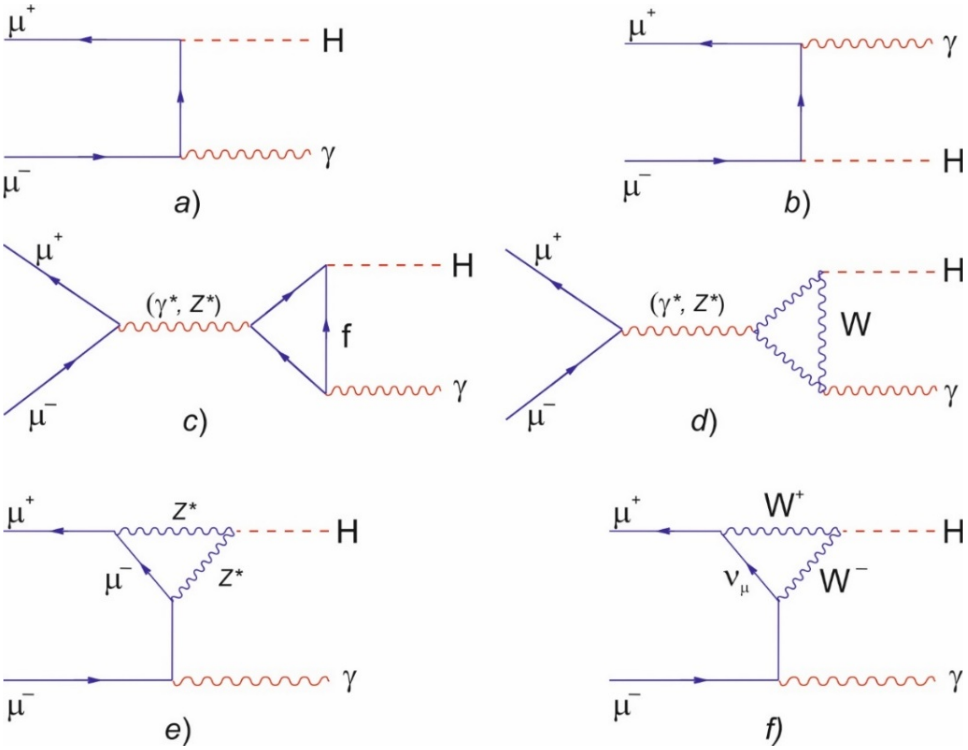

Fig. 1. Feynman diagrams of the process $\mu^-\mu^+ \to H\gamma$

First, let's consider the Feynman diagrams a) and b), where the Higgs boson and the γ-quantum are emitted by a muon-antimuon pair. According to Feynman's rules, the amplitude corresponding to these diagrams, in SM, can be written as follows:

$$M_{i\to f} = ieg_{H\mu\mu}[\overline{\upsilon}(p_2,\lambda_2)R_0u(p_1,\lambda_1)], \tag{2}$$

where

$$R_0 = \frac{\hat{p}_1-\hat{k}+m_\mu}{(p_1-k)^2-m_\mu^2}\cdot\hat{e}^* - \hat{e}^*\frac{\hat{p}_2-\hat{k}-m_\mu}{(p_2-k)^2-m_\mu^2}; \tag{3}$$

$g_{H\mu\mu} = \frac{m_\mu}{v} = (\sqrt{2}G_F)^{1/2}m_\mu$ – the interaction constant of the Higgs boson with the muon-antimuon pair; $\upsilon(G_F)$ – the vacuum value of the Higgs boson field (the Fermi constant of weak interactions); p_1, p_2, p and k – 4-impulses of the muon, antimuon, Higgs boson and γ-quantum, respectively; m_μ – the mass of the muon; λ_1 and λ_2 – the helicity of the muon and antimuon; $\hat{e}^* = \gamma_\mu e_\mu^*$; e_μ^* – the 4-polarization vector of the γ-quantum.

I'll use Dirac's equations the amplitude (2) is reduced to the form:

$$M_{i\to f} = -ieg_{H\mu\mu}[\bar{\upsilon}(p_2,\lambda_2)Ru(p_1,\lambda_1)], \tag{4}$$

where

$$R = \frac{2(e^*\cdot p_2)-\hat{e}^*\hat{k}}{2(p_2\cdot k)} - \frac{2(e^*\cdot p_1)-\hat{k}\hat{e}^*}{2(p_1\cdot k)}. \tag{5}$$

For the square of the amplitude modulus (4) in the center of mass system, the expression was obtained:

$$|M_{i\to f}|^2 = \frac{e^2g_{H\mu\mu}^2}{2}\left(\frac{1}{(p_1\cdot k)}+\frac{1}{(p_2\cdot k)}\right)^2\{(1+\lambda_1\lambda_2)[M_H^2(e\cdot p_1)(e^*\cdot p_1)+(p_1\cdot k)(p_2\cdot k)]$$

$$-(\lambda_1+\lambda_2)[(e\cdot p_1)(p_1p_2ke^*)_\varepsilon - (e^*\cdot p_1)(p_1p_2ke)_\varepsilon + (p_2\cdot k)(p_1kee^*)_\varepsilon]\}, \tag{6}$$

where $(abcd)_\varepsilon = \varepsilon_{\mu\nu\rho\sigma}a_\mu b_\nu c_\rho d_\sigma$ – the designation is entered.

When obtaining formula (6), we neglected the mass of the muon compared to its energy ($m_\mu^2 << s$) and used the projection operators of the muon and antimuon [21]:

$$u(p_1,\lambda_1)\bar{u}(p_1,\lambda_1) = \frac{1}{2}\hat{p}_1(1-\lambda_1\gamma_5), \qquad \upsilon(p_2,\lambda_2)\bar{\upsilon}(p_2,\lambda_2) = \frac{1}{2}\hat{p}_2(1+\lambda_2\gamma_5). \tag{7}$$

In the center of mass system, the differential cross-section of the process $\mu^-\mu^+ \to H\gamma$ is related by the square of the amplitude modulus by the ratio

$$\frac{d\sigma}{d\Omega_\gamma} = \frac{|M_{i\to f}|^2}{64\pi^2s^2}(s-M_H^2). \tag{8}$$

Here $d\Omega_\gamma = d(cos\theta_\gamma)\,d\phi_\gamma$ – is the solid angle of departure of the γ-quantum, θ_γ – the angle between the directions of the γ-quantum and muon impulses, $s=(p_1+p_2)^2$ – the square of the total energy of the muon-antimuon pair.

The differential effective cross-section of the annihilation process (1) has the form:

$$\frac{d\sigma}{d(cos\theta_\gamma)} = \frac{\sqrt{2}G_F\alpha_{KED}m_\mu^2}{4s(1-\upsilon^2\cos^2\theta_\gamma)^2}\left\{(1+\lambda_1\lambda_2)\left[\frac{2x}{1-x}\upsilon^2\sin^2\theta_\gamma + (1-x)(1-\upsilon^2\cos^2\theta_\gamma)\right]\right.$$

$$\left. -s_\gamma(\lambda_1+\lambda_2)[2\upsilon^2\sin^2\theta_\gamma-(1-x)(1-\upsilon^2\cos^2\theta_\gamma)]\right\}, \tag{9}$$

where $\upsilon = \sqrt{1 - 4\frac{m_\mu^2}{s}}$ – is the muon velocity, $x = \frac{M_H^2}{s}$ – is the ratio of the squares of the Higgs boson mass to the square of the total energy of the muon-antimuon pair.

Using the standard formula, we determine the degree of circular polarization a γ-quantum in the reaction $\mu^- \mu^+ \to H\gamma$ (averaging is performed on the polarization states of the antimuon):

$$P_\gamma(\sqrt{s}, \theta_\gamma) = -\lambda_1 \cdot \frac{2\upsilon^2 \sin^2\theta_\gamma - (1-x)(1-\upsilon^2\cos^2\theta_\gamma)}{(2x/(1-x))\upsilon^2\sin^2\theta_\gamma + (1-x)(1-\upsilon^2\cos^2\theta_\gamma)}\,. \qquad (10)$$

At zero departure angle of the γ-quantum, the degree of its circular polarization is maximal and does not depend on the energy of the muon-antimuon pair

$$P_\gamma(\theta_\gamma = 0; \pi) = \lambda_1 = \pm 1\,.$$

At the departure angles of a γ-quantum $0 < \theta_\gamma < \pi$, the degree of its circular polarization is equal to (we neglected the mass term of the muon in terms of velocity $\upsilon^2 = 1 - \frac{4m_\mu^2}{s} \approx 1$ compared to unity):

$$P_\gamma(0 < \theta_\gamma < \pi) = -\lambda_1 \cdot \frac{1-x^2}{1+x^2}\,.$$

In this case, the degree of circular polarization of the γ-quantum does not depend on the angle θ_γ, but depends on the energy $\sqrt{s}$ of the muon-antimuon pair. With an increase in the energy of the muon-antimuon pair, the degree of circular polarization of the γ-quantum increases and at $\sqrt{s} >> M_H$ reaches its maximum value

$$P_\gamma(\sqrt{s} >> M_H) = -\lambda_1 = \mp 1\,.$$

In Fig. 2 shows the energy $\sqrt{s}$ dependence of the degree of circular polarization of the γ-quantum at 15°<θ_γ<165°. It follows from the figure that with increasing energy $\sqrt{s}$, the degree of circular polarization P_γ increases (decreases) and reaches a maximum (minimum) at the end of the spectrum at $\lambda_1 = -1$ ($\lambda_1 = +1$).

Integrating expression (9) over the angles of emission of the γ-quantum, for the total cross section of the reaction $\mu^- \mu^+ \to H\gamma$ we find the formula:

$$\sigma = \frac{\sqrt{2}G_F \alpha_{KED}}{4s} m_\mu^2 \left\{ (1+\lambda_1\lambda_2)\left[\frac{x}{1-x}(L(1+\upsilon^2)-2) + (1-x)L\right] - s_\gamma(\lambda_1+\lambda_2)[(x+\upsilon^2)L-2] \right\}, \qquad (11)$$

where the notation is introduced

$$L = \frac{1}{\upsilon}\ln\left|\frac{1+\upsilon}{1-\upsilon}\right|\,. \qquad (12)$$

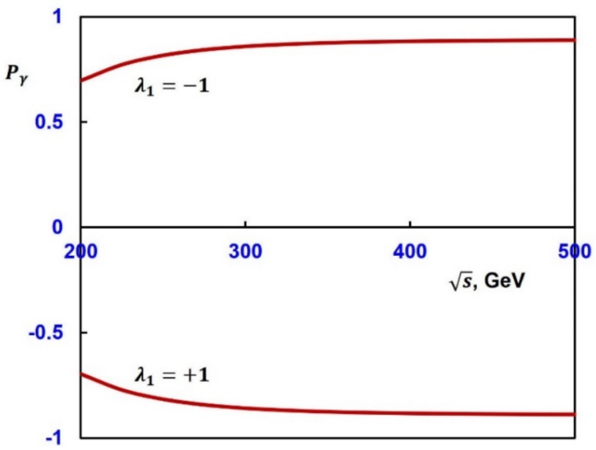

Fig. 2. Energy dependence of the degree of circular polarization of the γ-quantum

The degree of circular polarization of the γ-quantum in this case is determined by the formula (at $\upsilon^2 \approx 1$)

$$P_\gamma(\sqrt{s}) = -\lambda_1 \cdot \frac{(1-x)[(1+x)L-2]}{(1+x^2)L-2}. \tag{13}$$

The differential cross section of the reaction $\mu^-\mu^+ \to H\gamma$ for a linearly polarized γ-quantum is expressed by the formula (averaged over the polarization states of the muon-antimuon pair):

$$\frac{d\sigma(\vec{e})}{d\Omega_\gamma} = \frac{\sqrt{2}G_F\alpha_{KED}m_\mu^2}{8\pi s(1-\upsilon^2\cos^2\theta_\gamma)^2}\left[\frac{4x}{1-x}\upsilon^2(\vec{e}\vec{n})^2 + (1-x)(1-\upsilon^2\cos^2\theta_\gamma)\right]. \tag{14}$$

At the birth of a γ-quantum linearly polarized along the axis X, the differential effective cross section will be:

$$\frac{d\sigma(\vec{e}_x)}{d\Omega_\gamma} = \frac{\sqrt{2}G_F\alpha_{KED}m_\mu^2}{8\pi s(1-\upsilon^2\cos^2\theta_\gamma)^2}\left[\frac{4x}{1-x}\upsilon^2\sin^2\theta_\gamma\cos^2\phi_\gamma + (1-x)(1-\upsilon^2\cos^2\theta_\gamma)\right]. \tag{15}$$

If the γ-quantum is linearly polarized along the axis Y, the differential cross section is:

$$\frac{d\sigma(\vec{e}_y)}{d\Omega_\gamma} = \frac{\sqrt{2}G_F\alpha_{KED}m_\mu^2}{8\pi s(1-\upsilon^2\cos^2\theta_\gamma)^2}\left[\frac{4x}{1-x}\upsilon^2\sin^2\theta_\gamma\sin^2\phi_\gamma + (1-x)(1-\upsilon^2\cos^2\theta_\gamma)\right]. \tag{16}$$

Using the standard formula, we determine the degree of linear polarization of the γ-quantum

$$P(\sqrt{s},\theta_\gamma) = \frac{2x\upsilon^2\sin^2\theta_\gamma\cos 2\phi_\gamma}{2x\upsilon^2\sin^2\theta_\gamma + (1-x)^2(1-\upsilon^2\cos^2\theta_\gamma)}. \tag{17}$$

The degree of linear polarization of the γ-quantum is maximum at the azimuthal angle $\varphi_\gamma = 0;\pi$ of departure and vanishes at $\phi_\gamma = \frac{\pi}{4};\frac{3\pi}{4}$. At a polar angle $\theta_\gamma = 0(\pi)$ of emission of a γ-quantum, the degree of its linear polarization is zero (it was noted above that the degree of circular polarization of a γ-quantum is maximum in this case):

$$P_\gamma(\theta_\gamma = 0) = \lambda_1 = \pm 1.$$

At $15^\circ \leq \theta_\gamma \leq 165^\circ$, the degree of linear polarization of the γ-quantum is expressed by the formula

$$P(\sqrt{s}, \theta_\gamma) = \frac{2x}{1+x^2}. \tag{18}$$

With an increase in the energy $\sqrt{s}$ of the muon-antimuon pair, the degree of linear polarization of the γ-quantum decreases, while the degree of its circular polarization increases.

In Fig. 3 illustrates the dependence of the degree of linear polarization of a γ-quantum on the energy of a muon-antimuon pair. As can be seen, with increasing energy $\sqrt{s}$, the degree of linear polarization of the γ-quantum decreases.

The total cross section of process (1), integrated over the angles of emission of the γ-quantum, has the form:

$$\sigma = \frac{\alpha_{KED} G_F m_\mu^2}{\sqrt{2}s} \left\{ \frac{x}{1-x} [(1+v^2)L - 2] + (1-x)L \right\}. \tag{19}$$

In Fig. 4 illustrates the dependence of the effective cross section (19) on the energy of the muon-antimuon pair. It is seen that with increasing energy $\sqrt{s}$, the cross section increases.

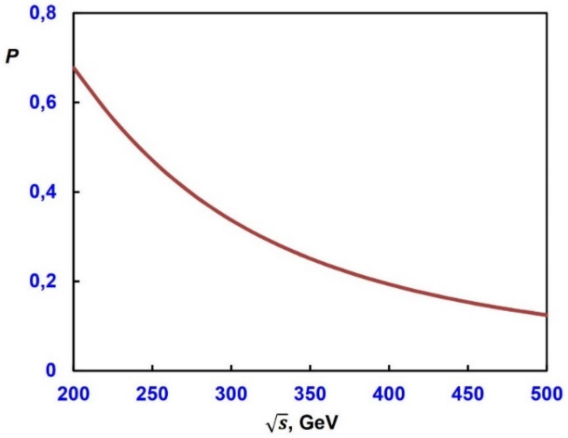

Fig. 3. Energy dependence of the degree of linear polarization of the γ-quantum

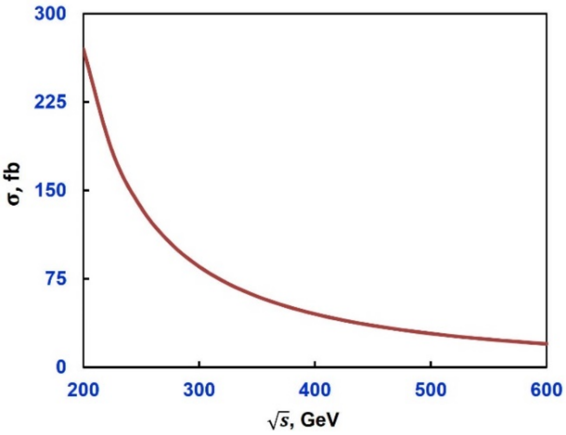

Fig. 4. Dependence of the reaction $\mu^-\mu^+ \to H\gamma$ cross section on energy $\sqrt{s}$.

Calculation of fermionic and W-boson loop diagrams

Now we turn to the calculation of the Feynman diagrams c) and d) Fig. 1 with fermionic and W-bosonic loops (cross-channel diagrams are added to them). These diagrams contain γ- and Z-poles with a virtual boson.

Suppose that annihilation of a longitudinally polarized muon-antimuon pair produces a circularly polarized γ-quantum. In this case, the differential cross section of the process $\mu^-\mu^+ \to H\gamma$ can be written in the form:

$$\frac{d\sigma}{d(\cos\theta_\gamma)}=\left(\frac{\alpha_{KED}^2 M}{\sqrt{x_W}}\right)^2\cdot\frac{(s-M_H^2)^3}{2048\pi s}\left\{\frac{|F_\gamma|^2}{s^2}[(1-\lambda_1\lambda_2)(1+\cos^2\theta_\gamma)+2s_\gamma(\lambda_1-\lambda_2)\cos\theta_\gamma]+\right.$$

$$+\frac{4|D_Z(s)|^2}{x_W^2}|F_Z|^2[((1-\lambda_1\lambda_2)(g_V^2+g_A^2)+(\lambda_1-\lambda_2)2g_Vg_A)(1+\cos^2\theta_\gamma)+((1-\lambda_1\lambda_2)2g_Vg_A+$$

$$+(\lambda_1-\lambda_2)(g_V^2+g_A^2))2s_\gamma\cos\theta_\gamma]-\frac{4\,\mathrm{Re}\,D_Z(s)}{x_W s}\mathrm{Re}(F_\gamma F_Z^*)[((1-\lambda_1\lambda_2)g_V+(\lambda_1-\lambda_2)g_A)\times$$

$$\left.\times(1+\cos^2\theta_\gamma)+((1-\lambda_1\lambda_2)g_A+(\lambda_1-\lambda_2)g_V)2s_\gamma\cos\theta_\gamma]\right\}. \tag{20}$$

It follows from this formula for the differential effective cross section that the colliding muon and antimuon must have opposite helicities $\lambda_1=-\lambda_2=\pm1$. If the muon is polarized to the right $\lambda_1=+1$, then the antimuon should be polarized to the left $\lambda_2=-1$ $(\mu_R^-\mu_L^+)$, and vice versa, if the muon has left helicity $\lambda_1=-1$, then the antimuon should have right helicity $\lambda_2=+1$ $(\mu_L^-\mu_R^+)$. This is due to the conservation of the total angular momentum in the transitions $\mu^-\mu^+\to\gamma^*$, $\mu^-\mu^+\to Z^*$.

It was established above that the differential effective section corresponding to diagrams a) and b) in Fig. 1 differs from zero only if the muon and antimuon have the same helicities $\lambda_1=\lambda_2=\pm1$ ($\mu_L^-\mu_L^+$ or $\mu_R^-\mu_R^+$). Therefore, by the spiral properties of the muon-antimuon pair, we can distinguish the contributions to the cross section of diagrams a) and b) from the contribution of diagrams c) and d). Indeed, in the annihilation of a left- or right-handed muon and antimuon ($\mu_L^-\mu_R^+$ or $\mu_R^-\mu_R^+$), the differential cross section is determined by diagrams a) and b), while in the collision of an $\mu_L^-\mu_R^+$ or $\mu_R^-\mu_L^+$-pair, the contribution to the cross section only of diagrams c) and d) differs from zero.

Let us now consider the case when the muon and the γ-quantum are polarized, and over the polarization states of the antimuon is averaged

$$\frac{d\sigma(\lambda_1,s_\gamma)}{d(\cos\theta_\gamma)}=\left(\frac{\alpha_{KED}^2 M_W}{\sqrt{x_W}}\right)^2\cdot\frac{(s-M_H^2)^3}{2048\pi s}\left\{\left[\frac{|F_\gamma|^2}{s^2}+\frac{4|D_Z(s)|^2}{x_W^2}|F_Z|^2(g_V^2+g_A^2+2g_Vg_A\lambda_1)-\right.\right.$$

$$\left.-\frac{4\,\mathrm{Re}\,D_Z(s)}{x_W s}\mathrm{Re}(F_\gamma F_Z^*)(g_V+g_A\lambda_1)\right](1+\cos^2\theta_\gamma)+$$

$$\left.+\left[\frac{|F_\gamma|^2}{s^2}\lambda_1+\frac{4|D_Z(s)|^2}{x_W^2}|F_Z|^2(2g_Vg_A+(g_V^2+g_A^2)\lambda_1)-\frac{4\,\mathrm{Re}\,D_Z(s)}{x_W s}\mathrm{Re}(F_\gamma F_Z^*)(g_A+g_V\lambda_1)\right]\cdot 2s_\gamma\cos\theta_\gamma\right\}. \tag{21}$$

Let us determine the degree of circular polarization of a γ-quantum in the annihilation of a longitudinally polarized muon and an unpolarized antimuon:

$$P_\gamma(\sqrt{s},\theta_\gamma,\lambda_1)=\frac{2\cos\theta_\gamma}{1+\cos^2\theta_\gamma}\times$$

$$\times\left\{\frac{|F_\gamma|^2}{s^2}\lambda_1+\frac{4|D_Z(s)|^2}{x_W^2}|F_Z|^2(2g_Vg_A+(g_V^2+g_A^2)\lambda_1)-\frac{4\mathrm{Re}D_Z(s)}{x_W s}\mathrm{Re}(F_\gamma F_Z^*)(g_A+g_V\lambda_1)\right\}\times$$

$$\times\left\{\frac{|F_\gamma|^2}{s^2}+\frac{4|D_Z(s)|^2}{x_W^2}|F_Z|^2(g_V^2+g_A^2+2g_Vg_A\lambda_1)-\frac{4\mathrm{Re}D_Z(s)}{x_W s}\mathrm{Re}(F_\gamma F_Z^*)(g_V+g_A\lambda_1)\right\}^{-1}. \quad (22)$$

In Fig. 5 shows the dependence of the degree of circular polarization of a γ-quantum on the angle of its emission at $\sqrt{s}=2M_H=250$ GeV and the helicities of the muon $\lambda_1=+1$ and $\lambda_1=-1$. As follows from the figure, at $\lambda_1=+1$ ($\lambda_1=-1$) the degree of circular polarization of the γ-quantum at $\theta_\gamma=0^\circ$ is positive (negative), with increasing angle θ_γ it decreases (increases) and reaches zero at $\theta_\gamma=90^\circ$. A further increase in the angle θ_γ leads to a decrease (increase) in the degree of circular polarization of the γ-quantum.

Due to the weak neutral currents (Z-boson pole $\mu^-\mu^+\to Z^*\to H\gamma$), the γ-quantum can be circularly polarized. In this case, the differential cross section of the process $\mu^-\mu^+\to H\gamma$ is as follows:

$$\frac{d\sigma(s_\gamma)}{d(\cos\theta_\gamma)}=\frac{1}{2}\frac{d\sigma_0}{d(\cos\theta_\gamma)}[1+s_\gamma P_\gamma(\sqrt{s},\theta_\gamma)], \quad (23)$$

where

$$P_\gamma(\sqrt{s},\theta_\gamma)=\frac{2\cos\theta_\gamma}{1+\cos^2\theta_\gamma}\left\{\frac{4|D_Z(s)|^2}{x_W^2}|F_Z|^2\cdot 2g_Vg_A-\frac{4\mathrm{Re}D_Z(s)}{x_W s}\mathrm{Re}(F_Z^*F_\gamma)g_A\right\}\times$$

$$\times\left\{\frac{|F_\gamma|^2}{s^2}+\frac{4|D_Z(s)|^2}{x_W^2}|F_Z|^2(g_V^2+g_A^2)-\frac{4\mathrm{Re}D_Z(s)}{x_W s}\mathrm{Re}(F_\gamma F_Z^*)g_V\right\}^{-1} \quad (24)$$

– degree of circular polarization of the γ-quantum.

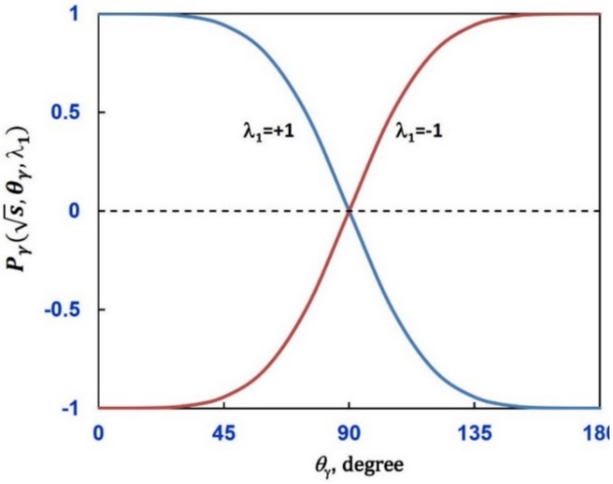

Fig. 5. Angular dependence of the degree of circular polarization of the γ-quantum

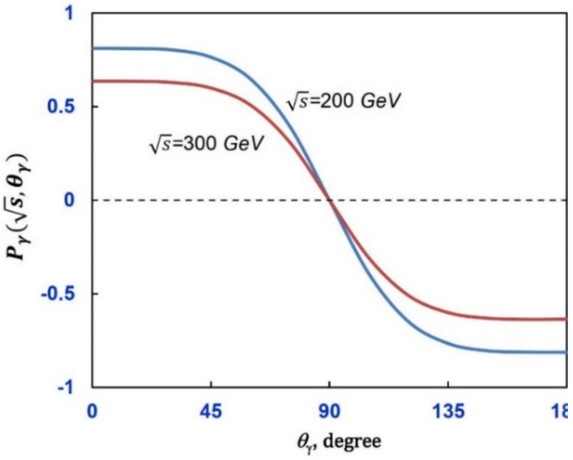

Fig. 6. Angular dependence of the degree of circular polarization of the γ-quantum

In Fig. 6 shows the dependence of the degree of circular polarization of a γ-quantum on its emission angle at $x_W = 0.2315$ and different energies of the muon-antimuon pair $\sqrt{s} = 200$ GeV, $\sqrt{s} = 300$ GeV. As can be seen from the figure, with an increase in the angle θ_γ, the degree of circular polarization of the γ-quantum decreases. An increase in energy $\sqrt{s}$ leads to a decrease in the degree of circular polarization of the γ-quantum.

We now turn to the study of the degree of linear polarization of the γ-quantum. In the case of the production of a linearly polarized γ-quantum along the axis X and along the axis Y, the differential effective cross section of the process $\mu^- \mu^+ \to H\gamma$ is expressed by the formula

$$\frac{d\sigma\begin{pmatrix}\vec{e}_x \\ \vec{e}_y\end{pmatrix}}{d\Omega_\gamma} = \left(\frac{\alpha_{KED}^2 M_W}{\sqrt{x_W}}\right)^2 \cdot \frac{(s - M_H^2)^3}{2048\pi s} \times$$

$$\times\left[\frac{\left|F_\gamma\right|^2}{s^2} + \frac{4\left|D_Z(s)\right|^2}{x_W^2}\left|F_Z\right|^2 (g_V^2 + g_A^2) - \frac{4\,\mathrm{Re}\,D_Z(s)}{x_W s}\mathrm{Re}(F_\gamma F_Z^*) g_V\right]\begin{pmatrix}1 - \sin^2\theta_\gamma \cos^2\varphi_\gamma \\ 1 - \sin^2\theta_\gamma \sin^2\varphi_\gamma\end{pmatrix}, \tag{25}$$

Using the standard formula, we determine the degree of linear polarization of the γ-quantum

$$P(\theta_\gamma) = -\frac{\sin^2\theta_\gamma}{1 + \cos^2\theta_\gamma} \cdot \cos 2\varphi_\gamma . \tag{26}$$

The degree of linear polarization of a γ-quantum reaches its maximum value at its azimuthal angle of departure $\varphi_\gamma = 0$ and π. At a polar angle of emission of the γ-quantum $\theta_\gamma = 0$ and π the degree of linear polarization vanishes. However, in this case, as noted above, the degree of circular polarization of the γ-quantum in absolute value reaches its maximum value. If the γ-quantum flies out at an angle $\theta_\gamma = \frac{\pi}{2}$, then the degree of its linear polarization in absolute value is maximum: $\left|P\left(\frac{\pi}{2}\right)\right| = 1$, and the degree of circular polarization of the γ-quantum vanishes.

In Fig. 7 shows the angular dependence of the degree of linear polarization of the γ-quantum at $\varphi_\gamma = 0$. As can be seen from the figure, the degree of linear polarization of the γ-quantum is negative, decreases with increasing angle θ_γ and reaches a minimum at $\theta_\gamma = 90^\circ$, a further increase θ_γ leads to an increase in the degree of linear polarization of the γ-quantum.

The total cross section of the process $\mu^- \mu^+ \to H\gamma$, integrated over the angles of departure of the γ-quantum, is determined by the formula

$$\sigma_0 = \left(\frac{\alpha_{KED}^2 M_W}{\sqrt{x_W}}\right)^2 \cdot \frac{(s - M_H^2)^3}{384\pi s}\left[\frac{|F_\gamma|^2}{s^2} + \frac{4|D_Z(s)|^2}{x_W^2} \cdot |F_Z|^2 (g_V^2 + g_A^2) - \frac{4\,\mathrm{Re}\,D_Z(s)}{x_W s}\mathrm{Re}(F_\gamma F_Z^*) g_V\right]. \quad (27)$$

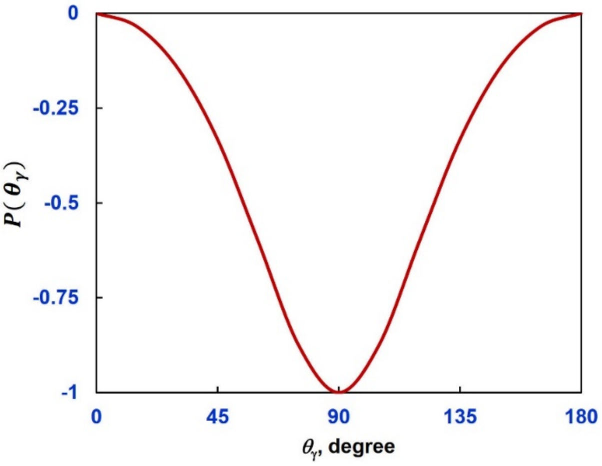

Fig. 7. Angular dependence of the degree of linear polarization of the γ-quantum

Conclusion

We discussed the process of co-production of the Higgs boson H and γ-quantum in muon-antimuon annihilation. Within the framework of the SM and taking into account the helicities of the muon-antimuon pair and the circular (linear) polarization of the γ-quantum, the differential cross section of the process $\mu^- \mu^+ \to H\gamma$ corresponding to the emission of a photon by the muon-antimuon pair and the W-boson, top-quark loop diagrams was obtained. The degrees of circular and linear polarization of the γ-quantum are determined. The dependence of these characteristics, as well as the effective cross section of the process on the emission angle θ_γ and the energy $\sqrt{s}$ of the muon-antimuon pair, is studied in detail. The calculation results are graphically illustrated.

References

1. ATLAS Collaboration. Phys. Letters, 2012, B716, p. 1.
DOI: https://doi.org/10.1016/j.physletb.2012.08.020
2. CMS Collaboration. Phys. Lett., 2012, B716, p. 30.
DOI: https://doi.org/10.1016/j.physletb.2012.08.021
3. Rubakov V.A. UFN, 2012, v. 182 (10), p. 1017 (in Russian). DOI: 10.3367/UFNe.0182.201210a.1017.
4. Lanev A.V. UFN, 2014, v. 184 (9), p. 996 (In Russian). DOI: 10.3367/UFNe.0184.201409i.0996.
5. Kazakov D.I. UFN, 2014, v. 184 (9), p. 1004 (in Russian). DOI: 10.3367/UFNe.0184.201409j.1004.
6. Shiltsev V.D. UFN, 2012, v. 182 (10), p. 1033 (in Russian). DOI: 10.3367/UFNe.0182.201210d.1033.
7. Peters K. Prospects for beyond Standard Model Higgs boson searches at future LHC runs and other machines. arXiv:1701.05124v.2 [hep-ex], 21 Feb. 2017. DOI: 10.22323/1.286.0028.
8. Poklonskiy A.A., Neuffer D. International Journal of Modern Physics A 2009, v. 25 (5), p. 959.
9. Delahaye J.P. Mod. Phys. Lett. 2011, v. A26, p. 2997.
DOI: https://doi.org/10.1142/S0217732311037303
10. Geer S. Ann. Rev. Nucl. Part. Sci. 2009, v. 59, p. 347.
DOI: https://doi.org/10.1146/annurev.nucl.010909.083736
11. Shiltsev V.D. Mod. Phys. Lett. 2010, v. A25, p. 567. DOI: https://doi.org/10.1142/S0217732310032949.

12. Barger V. et al. Phys. Rev. 1994, v. D 49 (1), p. 79. DOI:https://doi.org/10.1103/PhysRevD.49.79.
13. Kilian W., Kramer M., Zerwas P.M. Higgs-strahlung and WW fusion in e+e–-collisions. arXiv:hep-ph/9512355, 1995. DOI: 10.1016/0370-2693(96)00100-1.
14. Abdullayev S.K., Agamaliyeva L.A., Gojayev M.Sh., Saddigh F.A. GESJ: Physics 2015, v. 1 (13), p. 36.
15. Abdullayev S.K., Gojayev M.Sh., Nasibova N.A. Russian Physics Journal, 2019, v. 61 (10), p. 1838. DOI: https://doi.org/10.1007/s11182-019-01607-0
16. Abbasabadi A., Bowser-Chao D., Dicus D.A., Repko W.W. Phys. Rev. 1995, v. D52 (7), p. 3919. DOI: 10.1103/PhysRevD.52.3919
17. Bergstrom L., Nucl. Phys. 1985, v. B259, p. 137. DOI:10.1016/0550-3213(85)90302-5.
18. Djouadi A., Driesen V., Hollik W., Rosiek J. Preprint KA-TP-21-96, 1996. DOI: 10.1016/S0550-3213(96)00711-0
19. Djouadi A. The Anatomy of Electro-Weak Symmetry Breaking. Tome II: The Higgs boson in the Minimal Su-persymmetric Standard Model. arXiv: hep-ph/0503172v2, 2003; DOI: 10.1016/j.physrep.2007.10.004. DOI: 10.1016/j.physrep.2007.10.005.
20. Gunion J.F., Haber H.E. Nuclear Phys, 1986, v. B272, p. 1. DOI: https://doi.org/10.1016/0550-3213(86)90340-8
21. Abdullayev S.K. Standard Model, properties of lepton and quarks. Baku, Zaka Print, 2017, 276 p. (in azerb.)

FEATURES OF X-RAY DIFFRACTION AND OPTICAL ABSORPTION OF Sb-Se CHALCOGENIDE GLASS SYSTEM

SI MEKHTIYEVA[1], AI ISAYEV[1], RI ALEKBEROV[1,2], RF SADIKHLI[1], HI MAMMADOVA[1],
SN GARIBOVA[1,3] and SM MAMMADOV[1]

[1]Institute of Physics of ANAS, G. Javid ave 131, AZ1143 Baku, Azerbaijan
[2]Azerbaijan State University of Economics (UNEC), st.Istiqlaliyyat 6, Baku, AZ 1001, Azerbaijan
[3]Khazar University, 41 Mehseti str, Baku, AZ1096, Azerbaijan
E-mail: ramida_sadikhli@mail.ru

$Se_{33}Sb_{67}$, $Se_{50}Sb_{50}$, $Se_{60}Sb_{40}$, $Se_{70}Sb_{30}$, $Se_{80}Sb_{20}$ chalcogenide glass compositions was studied by X-ray diffraction and optical spectroscopy methods. Parameters first sharp diffraction peak (FSDP), which width half of the FSDP maximum (ΔQ) and local structure parameters - "quasi-period" of density fluctuations (d), size of medium range order(L) and optical band gap (E_g), average cordination number(Z), cohesive energy (CE) was calculated for studied compositions. It was determined that is not observed significant change in the value of d, but value of L is higher in materials more relative number of Se atoms.

Keywords: Chalcogenide, glass, amorphous, medium range order
PACS: 71.35.Cc, 61.43.Dq, 77.84.Bw

Introduction

Chalcogenide glasses are promising for use in optoelectronics, fiber optics, nonlinear optical systems and in memory devices [1-3]. The presented paper is devoted to the study of local structural parameters of the amorphous Se-Sb system of different composition, the optical absorption coefficient and determination of possible correlations between them. The reason for choosing the amorphous Se-Sb system as an object of study is that it allows obtain chemically different substances with different coordination numbers due to the variety of coordination numbers of the constituent elements. This is should lead to variation in physical properties. On the other hand, it is known that selenium (Se) is not resistant to crystallization, which limits its field of application. Addition antimony (Sb) to selenium can solve this problem, which can cause a connection between selenium chains three valence Sb and the large size and poor mobility of the structural elements.

Experimental details and sample preparation

$Se_{33}Sb_{67}$, $Se_{50}Sb_{50}$, $Se_{60}Sb_{40}$, $Se_{70}Sb_{30}$, $Se_{80}Sb_{20}$ chalcogenide glass compositions were synthesized by the conventional melt-quenching method. The components of a proper composition were placed in a quartz ampoule, which was evacuated to a residual pressure of 10^{-3} Pa. The synthesis were performed in a rotary furnace as the ampoules were heated at ~ 900 ^{0}C and kept at this temperature for 12 h, the furnace was rotated for homogeneous melting. After finishing the synthesis ampoules were quenched in air and samples are powdered for the X-ray diffraction studies. The chalcogenide compositions have been thermally evaporated with an evaporation rate of ~0,2 ÷ 0,4 mkm/san in vacuum of ~10^{-4} Pa. Thickness of thin films is d=1÷3 µm. The amorphous of the films was checked by X-ray diffraction analysis. The broad maxima observed in the diffraction curves are indicated by the absence of crystallized areas (Fig. 1). The absorption spectra of thins films were studied in the range of 190-1100 nm with

SPECOL -1500 spectrophotometer.

Results and discussion

Fig. 1 shows the intensity distribution curves the X-ray diffraction of Se-Sb thin films with different chemical compositions.

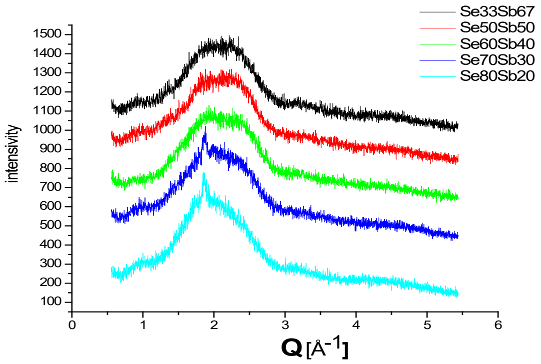

Fig. 1. X-ray diffraction curves of Se33Sb67, Se50Sb50, Se60Sb40, Se70Sb30, Se80Sb20 chalcogenide glass compositions.

The absence of sharp maxima in the diffraction curves proves their amorphousness. It can be seen from the curves that the first sharp diffraction peak (FSDP) was observed in the diffraction distribution of the studied samples. According to the X-ray curves the parameters of FSDP are calculated by the formula $Q_0 = 4\pi \sin\theta/\lambda$ (Q_0 -scattering vector, λ = 1,54056 Å), the width half of the FSDP maximum (ΔQ) and local structure parameters - "quasi-period" of density fluctuations (d) and the size of medium range order region was calculated based on them ((1) and (2) formulas), which the periodicity of density fluctuations and values of the correlation distance (L) are given in Table 1 [4, 5].

$$d = \frac{2\pi}{Q_0} \tag{1}$$

$$L = \frac{2\pi}{\Delta Q} \tag{2}$$

It can be seen from the table that in the absence of a significant change in the value of d. Value of L is higher in materials more relative number of Se atoms.

Table 1: Local structure parameters (d, L)

Compositions	**Q0, Å^{-1}**	**ΔQ, Å^{-1}**	**d,Å**	**L,Å**
Se33Sb67	0.99	0.72	6.34	7.72
Se50Sb50	1.01	0,68	6.21	9.235
Se60Sb40	1.002	0.61	6.267	10.3
Se70Sb30	1	0.586	6.28	10.71
Se80Sb20	1.009	0.55	6.224	11.418

From this it can be concluded that the correlation between the structural elements of the studied compositions is due to Se-Se bonds.

In the presented paper, the optical absorption spectra were measured of Se33Sb67, Se50Sb50, Se60Sb40, Se70Sb30, Se80Sb20 chalcogenide glass compositions films and have been shown in Fig. 2. It was found that the optical absorption spectrum of the studied materials consists of three parts; The weak absorption region (α<1 cm-1), which absorption coefficient is very weak dependence on the energy of the photon, the region of exponential absorption obeying the Urbach rule (α=1÷103 cm-1) and region dependence obeying to Taus' law(α≥ 104 см-1) [6]. The dependence of the absorption coefficient (α) on the energy photon(hν) in the region obeying Taus' law [6].

$$\alpha h\nu = A\left(h\nu - E_g\right)^2 \tag{3}$$

which A – constant is weakly dependent on temperature.

The dependence of $(\alpha h\nu)^{1/2}$ on hν was defined and by extrapolating the linear part of the graph to the zero value of the absorption coefficient was determined optical band gap (E_g) for studied compositions (Table2).

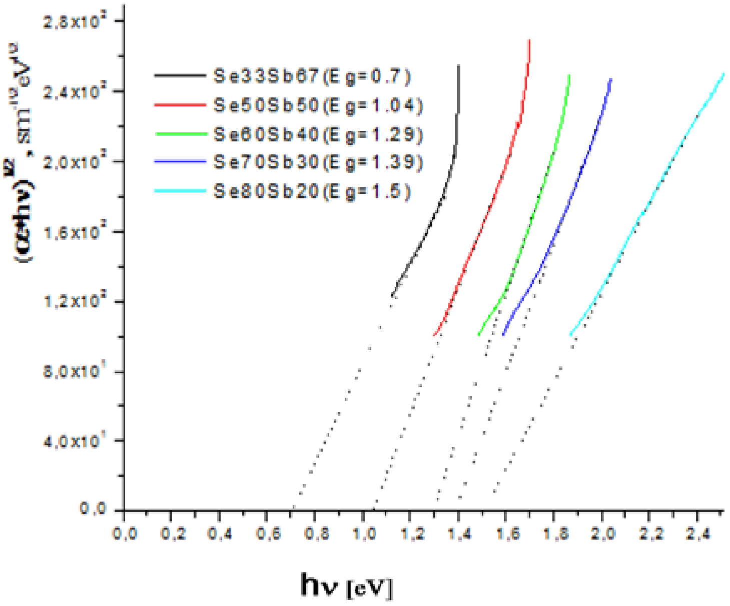

Fig. 2. Optical absorption spectra of Se-Sb thin films have different chemical compositions.

The presence of a linear dependence on a sufficiently wide range of photon energy indicates that the electronic transitions correspond to allowed indirect transitions. In order to determine relationship between the optical absorption coefficient and the near order parameters characterizing the amorphous matrix and other physical quantities was calculated the mean coordination number (Z), cohesive energy (CE) according to the following formula (Table2).

$$Z = 3X_{Sb} + X_{Se} \tag{4}$$

$$CE = \sum_i c_i E_i \tag{5}$$

Which, X is molar fraction of chemical elements in matter, c_i is the relative amount of chemical bonds determined according to the chemical bond approach (CBA), E_i is the energy of the chemical bonds. The relative amount of chemical bonds in compositions with different chemical compositions is determined by the ratio R - the ratio of the number of possible covalent bonds between chalcogen atoms to the number of covalent bonds between non-chalcogen atoms.

Table 2. Parameters of cohesive energy (CE), optical band gap (E_g), average coordination number (Z)

Compositions	**CE, kC/mol**	**E_g, eV**	**Z**
$Se_{33}Sb_{67}$	154,5	0.7	2,67
$Se_{50}Sb_{50}$	172	1.04	2,5
$Se_{60}Sb_{40}$	183,8	1.29	2,4
$Se_{70}Sb_{30}$	183,9	1.39	2,3
$Se_{80}Sb_{20}$	183,9	1.5	2,2

The value of R=1 corresponds only to the stoichiometric composition of heterepolar bonds ($Se_{60}Sb_{40}$). In compostions rich with chalcogen atoms ($Se_{70}Sb_{30}$, $Se_{80}Sb_{20}$), the value of R is greater than 1, but in compostions with chalcogen deficiency ($Se_{33}Sb_{67}$, $Se_{50}Sb_{50}$) is less than 1. The optical band gap(Eg) continues to increase with the increase of R in compositions corresponding to the values of R> 1. A possible interpretation of this fact is that the boundaries of the permissible zones in these compositions are formed mainly due to orbits of the selenium atom and therefore the value of Eg approaches the width optical band gap (Eg) of the selenium.

Conclusion

In this paper $Se_{33}Sb_{67}$, $Se_{50}Sb_{50}$, $Se_{60}Sb_{40}$, $Se_{70}Sb_{30}$, $Se_{80}Sb_{20}$ chalcogenide glass compositions was studied by X-ray diffraction and optical spectroscopy methods. Parameters first sharp diffraction peak (FSDP), which width half of the FSDP maximum (ΔQ) and local structure parameters - "quasi-period" of density fluctuations (d), size of medium range order(L) and optical band gap (E_g), average coordination number(Z), cohesive energy(CE) was calculated for studied compositions. It was determined that is not observed significant change in the value of d, but value of L is higher in materials more relative number of Se atoms. It was determined that, value of R=1 corresponds only to the stoichiometric composition of heterepolar bonds ($Se_{60}Sb_{40}$). In compostions rich with chalcogen atoms ($Se_{70}Sb_{30}$, $Se_{80}Sb_{20}$), the value of R is greater than 1, but in compostions with chalcogen deficiency ($Se_{33}Sb_{67}$, $Se_{50}Sb_{50}$) is less than 1.

References

1. Zakery and Elliott S., J. Non-Crystalline Solids 2003, v. 330 (1), p. 1.
2. Sanghera J. S., Aggarwal I. D., J. Non-Crystalline Solids 1999, v. 256–257, p. 6.
3. Semencha A.V., Kurushkin M.V., Markov V.A., Advanced Materials Research 2015, v. 1061, p. 987.
4. Lee J. H., Elliott S. R., J. Non-Crystalline Solids 1995, v. 192-193, p. 133.
5. Elliott S.R., Physical Review 1995, v. 51, p. 8599.
6. Tauc J., The optical properties of solids, North, Holland Amsterdam. 1970, 277 p.

METAL-CONTAINING NANOCOMPOSITES BASED ON ISOTACTIC POLYPROPYLENE AND BUTADIENE–ACRYLONITRILE RUBBER

NI KURBANOVA[1], TM GULIYEVA[1], GM EYVAZOVA[2], ZA AGAMALIYEV[2] and MB MURADOV[2]

[1] Institute of Polymer Materials of ANAS, Laboratory of Nanopolymer Composites, Sumgait, Azerbaijan
[2] Baku State University, Baku, Azerbaijan
E-mail: kurbanova.nushaba@mail.ru, ipoma@science.az

The effect that nanofillers containing copper and zinc oxides stabilized with a maleinized low-density polyethylene matrix and prepared mechanochemical exert on the structure and properties of metal-containing nanocomposites based on isotactic polypropylene and butadiene–acrylonitrile rubber was studied by X-ray diffraction and differential thermal analysis, a scanning electron microscope, as well as dielectric properties. The filling improves the strength, deformation, and rheological characteristics of the nanocomposites and enhances their resistance to thermal oxidation, which is probably due to the synergistic effect caused by interaction of copper and zinc containing nanoparticles with maleic groups of maleinized low-density polyethylene, dielectric properties practically did not change upon the introduction of copper and zinc oxide nanoparticles into the composition The nanocomposites based on isotactic polypropylene and butadiene–acrylonitrile rubber can be processed not only by pressing, but also by pressure casting and extrusion, which expands their application field. The nanofiller containing copper and zinc oxide nanoparticles stabilized by the maleinized matrix and prepared mechanochemically show promise as an additive to a compound of isotactic polypropylene with butadiene–acrylonitrile rubber. This favors the creation of the finely crystalline structure of the compound and to the improvement of its properties, which, in turn, expands the possible applications of the nanocomposite in automobile industry, mechanical and electrical engineering, medicine, petrochemical industry, and building.

Keywords: nanocomposites, isotactic polypropylene, butadiene–acrylonitrile, copper and zinc oxide nanoparticles, mechano-chemical method
PACS: 61.46.w, 82.35.Np, 71.38.k

Introduction

The modern stage of development of chemistry and technology of the composition materials is largely determined by the search for ways of creation of materials with an improved complex of properties. The intensive development of the world petrochemical industry intends a constant search for new materials possessing high consumer properties, ecological safety and simplicity of processing. Such materials are not without reason the thermoplastic elastomers (TPE). The creation of TPE is a priority direction of work in the field of polymer materials science [1, 2].

The most perspective direction of preparation of new types of TPE is the mixing of elastomers with plastics with simultaneous vulcanization of the elastomer, which leads to a high degree of dispersity of the rubber phase in the materials. TPEs obtained by this method were called thermoplastic vulcanizates (TPV). A distinctive peculiarity of TPV is the combination of the properties of vulcanized rubbers during exploitation and thermoplastics in the processing. Owing to the complex of high physical-mechanical properties, wide temperature range of working capacity, lower cost of finished products, TPVs are considered one of the most perspective classes of the polymer composite materials. Their application areas are very various [3, 4].

A large number of works on TPE and TPV has been obtained with use of polypropylene (PP) as thermoplastics, and SKEPT, natural rubber, butadiene nitrile rubber (BNR), etc. – as elastomers. In use of various fillers or compatibilizers for improvement of the compatibility, physical-mechanical and technological properties of the compositions [5-8].

The use of solid nanoparticles (NP) of various form and chemical nature as fillers of the polymer materials opens up new possibilities of modification of the latter ones, since the surface properties of the nano-sized substance are differed by high surface energy and adsorption activity. The composition materials containing NP have a high adhesive strength of the polymer matrix with NP [9].

Experimental

The following materials were used in work: isotactic PP "Kaplen" (Russia) of mark 01 030 with a molecular weight ~ 2- 3×10^5, polydispersity index – 4.5, MFI – 2.3-3.6 g/10 min.

BNR – butadiene nitrile copolymer of mark NB 192 HF, containing 27% of acrylonitrile, firm BSL Olefinverbund GmbH Shckopau, d=0.98g/cm^3 (Germany).

Nanoparticles (NP) of the zinc oxide (ZnO) and copper oxide (Cu_2O) stabilized by polymer matrix of maleinized high-pressure polyethylene manufactured of firm Olenta (Russia), obtained by a mechano-chemical method in a polymer melt, were used as NF. A content of nanoparticles – 5 mass %, size – 26±1.0 nm, degree of crystallinity – 35 ÷ 45% [12]. A ratio of components of composition (mass %): PP/BNR/NF=50/50/ (0.3; 0.5; 1.0)

The nanocomposite polymer materials have been obtained by mixing of PP with BNR and zinc and copper containing NF on laboratory rollers at temperature 160-165°C for 15 min. For carrying out of mechanical testing, the obtained mixtures were pressed in the form of plates with a thickness of 1 mm at 190°C and a pressure of 10 MPa.

The physical-mechanical indices of the obtained compositions were determined on the device PMI-250. The melting flow index (MFI) was determined on the device IIRT at T=230°C, load – 5.0 kg.

The X-ray phase (RPhA) of the obtained compositions has been carried out on the device “D2 Phaser” of firm Bruker (Germany).

Thermal stability of the investigated samples of thermoelastoplasts was studied on the derivatograph of mark Q-1500D of firm MOM (Hungary). The tests were carried out in the air atmosphere in the dynamical regime at heating of the samples 5 degr·min^{-1} from 20 to 500°C, weight – 100 mg, sensitivity of the channels DTA-250mcV, TG-100, DTG-1 mV.

SEM – analysis of the obtained compositions has been carried out on the device JEOL (USA).

Results and discussion

The nanocomposite polymer materials on the basis of PP/BNR with zinc and copper containing nanofiller have been obtained.

The physical-mechanical, rheological, heat-physical and thermal properties of the obtained nanocomposites have been investigated.

In Table 1 the physical-mechanical and rheological indices of the obtained nanocomposites are presented.

Table 1. Physical-mechanical and rheological indices of the composition materials

Composition (mass %.), PP/BNR/NF	Tensile strength at break, MPa	Specific elongation, %	Vacate heat stability, °C	MFI, g/10 min
PP/BNR/NF (ZnO)				
50/50/0	5.04	16	87	0.089
50/50/0.3	6.65	36	120	0.127
50/50/0.5	6.94	40	127	0.155
50/50/1.0	6.51	32	115	0.287
PP/BNR/NF (Cu_2O)				
50/50/0	5.04	16	87	0.089
50/50/0.3	5.55	20	110	0.114
50/50/0.5	6.15	24	115	0.123
50/50/1.0	5.51	21	105	0.169

As is seen from data of Table 1, an introduction of 0.3 –0.5 mass % of NF into composition leads to an increase of strength index from 5.04 to 6.94 NF (ZnO) and 6.15 MPa NF (Cu_2O). An increase of concentration of NF more than 0.5 mass % leads to the decrease of the composite strength (6.51 and 5.51 MPa), which has been probably stipulated by aggregation of nanoparticles leading to the formation of microdefects in a volume of the polymer matrix. An increase of NF concentration from 0.3 to 0.5 mass % leads to the decrease of deformation value at break of the composite in 2.25÷2.5 times NF (ZnO), nd 1.25÷1.5 times NF(Cu_2O), which has been apparently connected with the synergetic effect connected with availability of zinc-containing nanoparticles in matrix of MPE containing maleic groups, the mutual influence of which favors an increase in both deformation value and strength index. The investigation of Vicat heat stability of the obtained compositions showed that an introduction of nanofillers into composition of PP/BNR leads to the increase of heat-resistance index from 87 to 127°C NF (ZnO) and 115ºC NF (Cu_2O) in introduction of 0.5 mass % of NF, a further increase of quantity of NF leads to some decrease of heat-resistance index, which has been probably stipulated by microdeficiency of the obtained composite. At the same time, an increase of content of nanofiller (0.5-1.0 mass %) favors the increase of melting flow index (MFI) to 0.155 (0.5 mass %) and 0.287(1.0 mass %) NF (ZnO) and 0.123(0.5 mass. %) и 0.169(1.0 mass. %) NF(Cu_2O) g/10 min, which evidences about improvement of composition fluidity and possibility of its processing by casting under pressure and extrusion.

Fig. 1-3 presents the diffractograms of RPhA of the initial PP/BNR and PP/BNR with zinc and copper containing nanofillers. There have been shown the reflexes corresponding to PP: d_{hkl} 6.19929; 5.17135; 4.73608; 4.48713; 4.17687; 4.03424; 3.47038; 3.11297; 2.11651 Å and a halo image is given for an amorphous BNR. On the diffractogram of the sample PP/BNR/NF (ZnO) (Fig. 2) there are also observed reflexes characteristic for zinc-containing NP: d_{hkl} 2.46563; 2.12992; 1.50595; 1.28812 Å, which corresponds to the series of d_{hkl} of zinc oxide – ZnO according to ASTM card file. On the diffractogram of the sample PP/BNR/NF (Cu_2O) (Fig. 3) there are also observed reflexes characteristic for copper-containing NF: d_{hkl} 3.02053; 2.46563; 2.12992; 1.74331; 1.50595; 1.28812 Å, which corresponds to the series of d_{hkl} of copper oxide – Cu_2O according to ASTM card file. [d-Spacings (20) – 01-071-3645 (Fixed Slit Intensity) - Cu Kα1 1,54056 A. Entry Date:11/19/2008 Last Modification Date: 01/19/2011].

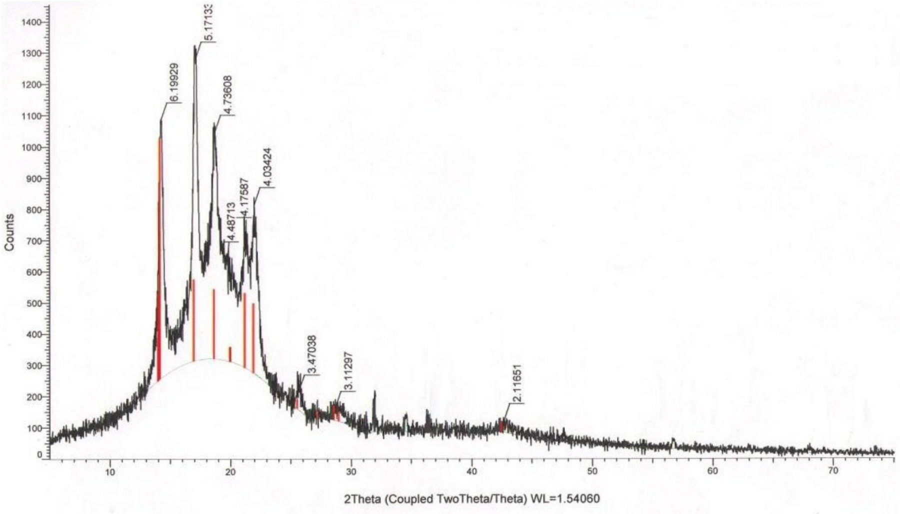

Fig. 1. Diffractogram of PP/BNR sample

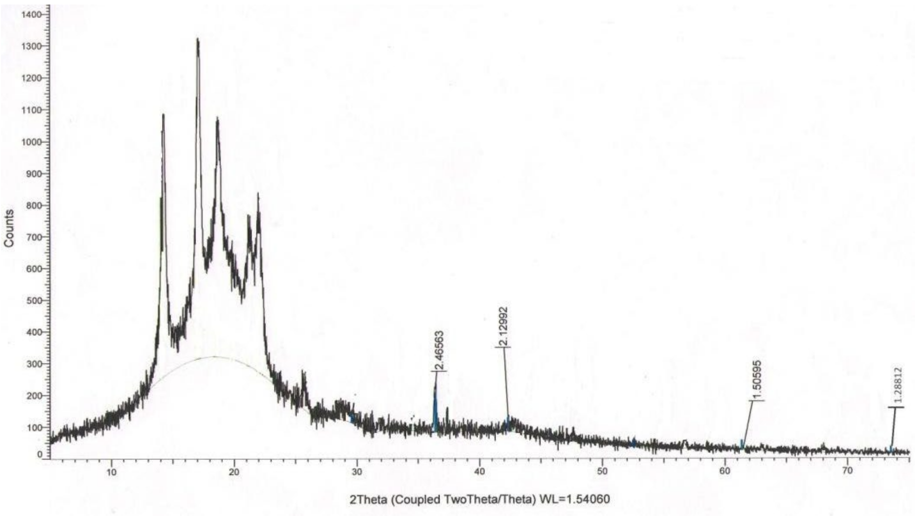

Fig. 2. Diffractogram of PP/BNR/NF(ZnO) sample

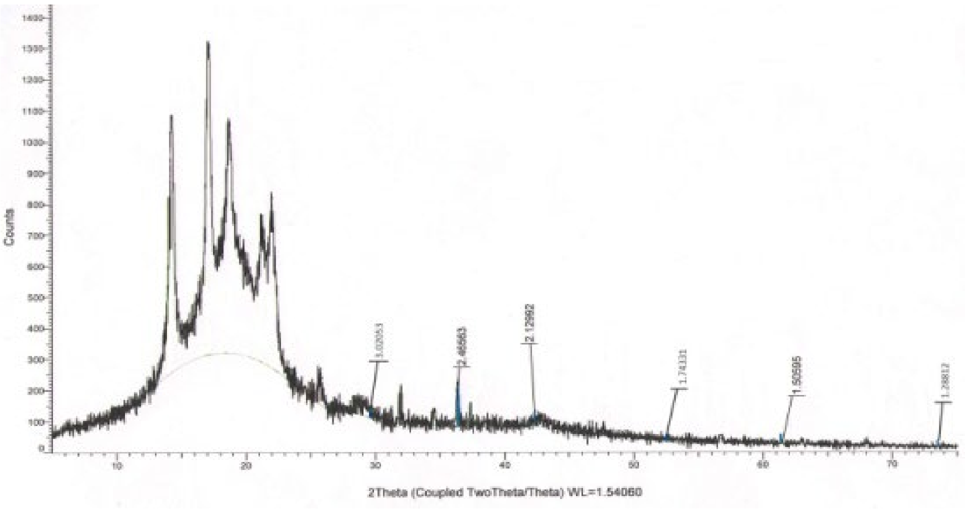

Fig. 3. Diffractogram of PP/BNR/NF(Cu_2O) sample.

Thermal stability of the investigated samples of mixed TPE on the basis of PP/BNR and

PP/BNR/NF containing NF with NP of zinc and copper oxide was estimated on activation energy (E_a) of thermal-oxidative destruction calculated by a method of double logarithm on TG curve on methodology [13], on temperature of 5% (T_5), 10% (T_{10}), 20 (T_{20}), 50% (T_{50}) decay of the investigated samples of TPE and also on their half-decay time – $Ʈ_{1/2}$. The data obtained as a result of derivatographic investigations are presented in Table 2.

Table 2. Thermal properties of the investigated samples of TPE

Composition (mass %.) of PP/BNR/NF	**M.p.,° C**	**T_5,°C**	**T_{10},°C**	**T_{20},°C**	**T_{50},°C**	**$Ʈ_{1/2}$, min..**	**E_a, kJ·mol^{-1}**
PP/BNR/NF (ZnO)							
50/50/0	150	210	225	250	300	62.8	124.48
50/50/0.3	150	240	260	305	370	75.1	186.32
50/50/0.5	150	250	270	315	380	80.3	204.77
50/50/1.0	150	235	255	300	365	72.4	172.45
PP/BNR/NF (Cu_2O)							
50/50/0	150	210	225	250	300	62.8	124.48
50/50/0.3	150	240	280	310	370	66.5	165.39
50/50/0.5	150	250	290	320	375	72.9	176.49
50/50/1.0	150	235	270	300	360	65.4	163.51

As can be seen from the data in Table 2, an introduction of HF containing NP of the zinc and copper oxide into the composition of mixed thermoelastoplasts favors the considerable increase of decay temperature of the samples: T_5 at 30-40°C, T_{10} at 35- 45°C, T_{20} at 55-65°C, T_{50} at 70-80°C; half-decay time $Ʈ_{1/2,}$ is increased from 62.8 to 80.3 min., and activation energy (E_a) of decay of thermal-oxidative destruction of the obtained nanocomposites is increased by 52-80 kJ/mol, while T_m is maintained on the level 150°C. The derivatographic investigations showed that an introduction of HF containing NP of the zinc and copper oxide into the composition of mixed thermoelastoplasts favors the improvement of thermal-oxidative stability of the obtained nanocomposites.

The numerous experimental data on mechanical, strength, relaxation and other properties of polymer-polymer and polymer- filler mixtures are explained within the framework of the concepts of the availability of interphase layer [14].

The permolecular structure of the polymer (size of spherulites, degree of crystallinity, availability of C=O groups and various branches, etc.) and the interphase interaction at the interface influences noticeably on properties of the polymer composites.

The metal-containing nanoparticles used in this work, being located at the interface of the interphase layer of the structural elements of PP, BNR and MPE favor the formation of composition of heterogeneous nucleation centers in a melt, which in the process of stepwise cooling of the nanocomposite favor the increase in crystallization centers, leading to an improvement in the crystallization process and the formation of a relatively fine-spherolite structure on the whole.

SEM analysis of the obtained composites has been carried out (Fig. 3, 4).

Figure 3. the electronic and multilayer images of the PP / BNR sample are presented.

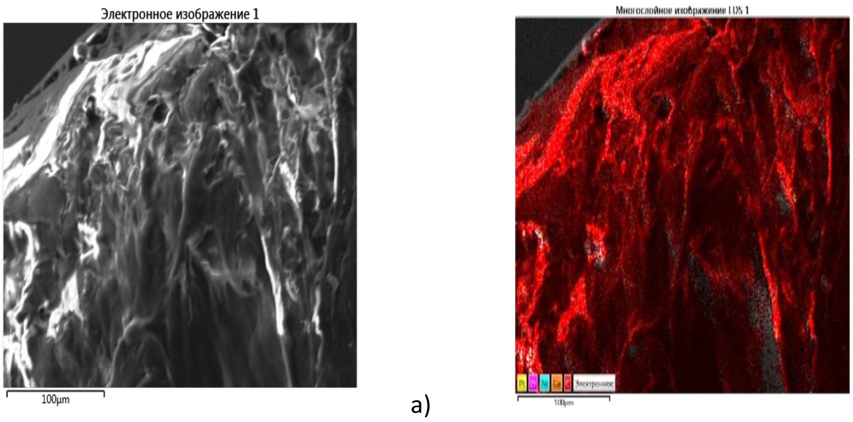

a) b)

Fig. 3. The electronic(a) and multilayer (b) images of the PP / BNR sample.

Figure 4 (a, b) shows micrographs of PP / BNK and PP / BNK / NN samples. It is seen that the structure of the composite (Fig. 4 a) is quite loose with large shapeless formations. An introduction of nanofillers into the PP/BNR composition favors the formation of a fine- spherulite layered structure, which leads to an increase in the fluidity of the nanocomposite (Fig. 4 b).

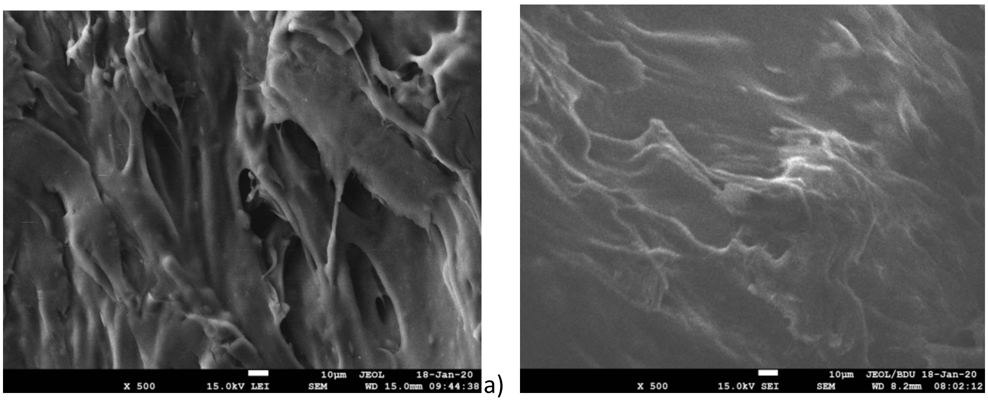

a) b)

Fig. 4. Micrographs of PP / BNK (a) and PP / BNK / NN samples.

SEM-analysis of the obtained nanocomposites showed that small amounts of nanofillers (0.3 – 0.5 mass %) introduced into the polymer, obviously play the role of structure-forming agents – artificial nuclei of crystallization, which favors the appearance of a fine-spherulite layered structure in the polymer, characterized by improved physical-mechanical, rheological and thermal properties of the obtained nanocomposite [15, C.80,328].

Conclusion

The influence of nanofiller containing nanoparticles of the zinc and copper oxide stabilized by matrix of maleinized polyethylene (MPE), obtained by mechano-chemical method on properties of composites on the basis of PP/BNR has been investigated.The RPhA diffractograms confirm the availability of the zinc and copper oxide nanoparticles in the composition of composites on the basis of PP/BNR.

It has been revealed the improvement of the strength, deformation and rheological indices and also the thermal-oxidative stability of the obtained nanocomposites, which has been apparently connected with the synergetic effect of the interaction of the zinc-, copper containing nanoparticles with maleic groups of MPE.

It has been shown that the nanocomposites on the basis of PP/BNR can be processed both by pressing method and by methods of casting under pressure and extrusion.

It has been shown the prospectivity of use of the nanofiller containing zinc and copper oxide NP, stabilized by a matrix of maleinized polyethylene, obtained by a mechano-chemical method as an additive to PP/BNR, which favors the creation of a fine- crystalline structure of the composition, in connection with which its properties are improved and thereby the areas of application of the obtained nanocomposite is expanded.

References

1. Polymer mixtures, Moscow, Mir, 1981, v. 2. p. 312.
2. Polymer Blends, Eds. by Paul D.R., Bucknall C.B.. New York; Chichester; Weinheim; Brisbane; Singapure; Toronto: Wiley, 2000, 1224 p.
3. Thermoplastic Elastomers, Ed. by Holden G., Kricheldorf H.R., Quirk R.P.. Munich: Hanser Publishers, 2004. p. 63.
4. Ashpina O. The Chemical Journal 2011, v. 1-2, p. 58.
5. Karger-Kocsis J., Thermoplastic rubbers via dynamic vulcanization, in Polymer blends and alloys, Shonaike G.O. and Simon G.P., Eds. New York:Marcel Dekker, 1999, p. 125-140.
6. Medintseva T.I., Prut E.V., Erina N.A. Polymer Science. Series A 2008, v. 50, p. 647.
7. Volfson S.I., Okhotina N.A., Nigmatulina A.I., Sabirov R.K., Kuznescova O.A., Achmerova L.Z., Plast. Massy 2012, v. 4, p. 42.
8. Karpov A.G., Zaikin A.E., Bikmullin R.S. Bull. Kaz. Technol. University 2008, v. 5, p. 124.
9. Mikhaylin Yu.A., Polymer materials 2009, v. 7, p. 10.
10. Pomogaylo A.D., Rozenberg A.S., Uflyand I.E., Nanoparticles of metals in polymers. Moscow, Khimiya, 2000, 672 p.
11. Gubin S.P., Yurkov G.Yu., Kosobudsky I.D. International Journal of Materials and Product Technology 2005, v. 23 (1-2), p. 2.
12. Kurbanova N.I., Aliyev A.T., Guliyeva T.M., Ragimova C.K., Axmadbekova C.F.,. Ishenko N.Y., Nurullayeva D.R., Metal- containing nanoparticles in maleinized polyethylene matrix, in PolyChar 26 World Forum on Advanced Materials. Tbilisi, 2018, p. 59.
13. Technical properties of polymer materials: Teaching-reference book, Edited by Prof. V.K.Krizhanovsky. Saint Petersburg: Profession, 2007, 240 p.
14. Pomogaylo A.D. Russian Chemical Reviews 2002, v. 71 (1), p. 1.
15. Encyclopedia of polymers, Moscow, Soviet. Encyclopedia, 1974, v. 2, p. 80.

KINETICS OF FORMATION AND DESTRUCTION OF THE DIELECTRIC GAP ON THESURFACE OF THE IONIC MATERIAL IN THE EXTERNAL ELECTRIC FIELD

VI ORBUKH, NN LEBEDEVA and GM EYVAZOVA

Baku State University, Baku, Azerbaijan
E-mail: vorbukh@gmail.com

A dielectric gap is formed in a material with ionic conduction (in an external electric field), which significantly affects the dielectric spectra and current transfer. In this work, for the process of gap formation, the time dependence of the parameters of this gap and the total current in the circuit was established. The destruction of the gap after switching off the electric field is considered in a similar way.

Keywords: nanoparticles, plants, stress, plant tolerant
PACS: 87.15.Kg, 87.16.Gj, 87.50.yg

Introduction

One of the trends in modern physics is the study of new materials. One of these materials is zeolite. This material has been widely and successfully used in medicine and purifications systems. Zeolite has been studied as an object of physics for the last ten years. Quite interesting results were obtained, such as, for example, anomalously high dielectric constant.

The study of their physical properties has been stimulated by the use of solid materials with ionic conduction. Zeolite is one of such widely used material. For example, it was founded in [1] that, in the contact of a zeolite with a metal electrode, the transfer of the electrode material to the zeolite occurs in weak electric fields. In [2], direct experimental evidence of a gas discharge in nanopores of natural zeolite in a constant electric field was obtained. It was found in [3] that at low frequencies the dielectric constant is anomalously high. In this work this phenomenon is explained by the presence of a dielectric gap at the sample boundary. Therefore, the question of the mechanism of the formation of a dielectric gap on the boundary of an ionic gap is still valid at present.

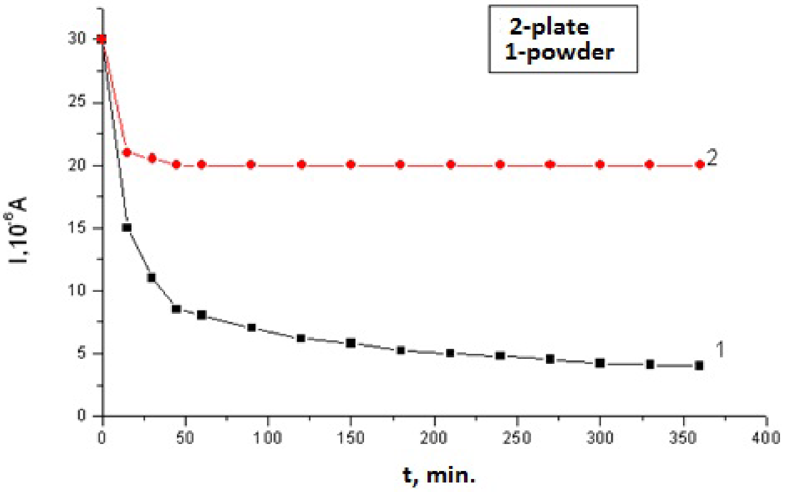

Fig. 1. 1-pure zeolite powder; 2-zeolite powder with added metal particles (from work [6])

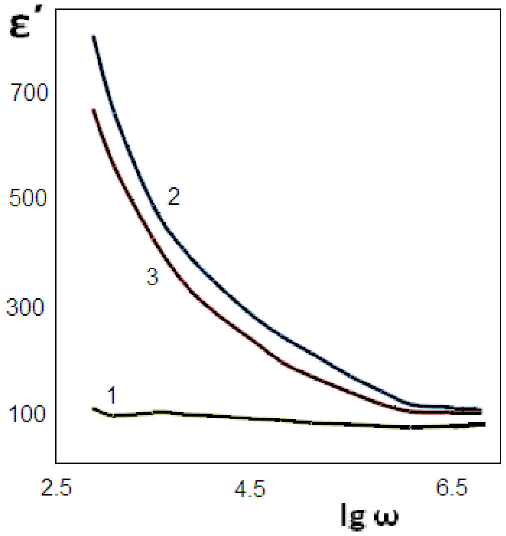

Fig. 2. Frequency dependence of the dielectric constant for natural zeolite (1)

Zeolite modified with silver ions (2) and zeolite modified with partially neutralized ions (3). A long-term decreasing current in a constant electric field was discovered in work [4]. The fundamentals of current transport in ionic materials are outlined in [5]. An abnormally high value of the dielectric constant at low frequencies was found [6].

Kinetics of formation of a dielectric gap in an external electric field

To study the electrical properties of the zeolite, the current was measured at constant voltage. It was found, that in zeolite and zeolite powder, the current falls out very slowly (on a scale of hours).Another measurement method consisted of measuring the resistance and capacitance of the sample in a week electric field (dielectric spectra). Unusual was the abnormally high dielectric constant (determined from measured capacitance) at low frequencies (Fig. 2).

The features of the electrical properties of material with ionic conductivity are determined by the fact that an excess of ions occurs near the one electrode, and their deficiency near the other. These features include the nonstationarity of current in a constant electric field and the abnormally high dielectric constant, measured at low frequencies. The nonstationarity of current can be explained by the fact that this is a transient current of the formation process of an insulating layer from the side of one electrode. The abnormally high dielectric constant is also explained by the formation of an insulating layer. At low frequencies, for most of the period the electric field is in the insulating layer, the capacity of which is inversely proportional to the thickness of the insulating layer, i.e. abnormal great. Using the example of zeolite, where the current carriers are positive ions, it was obtained the time dependence of the total current during the formation of a shut-off contact in ionic materials. In the process of current transfer, positive ions arriving at the cathode are compensated or neutralized by electrons from the anode and a shut-off contact is formed on the anode side (a charged layer without mobile carriers). Consider a sample with ionic conductivity, to which a voltage U_0 is applied. At the left end the electric potential is zero, and at the right – U_0. The current of positive ions is directed to the right side, that is, along the electric field. Since the diffusion of mobile ions is not taken into account, the boundary between the forming layer of positive charge (localized on the walls of the zeolite pore) and the conducting area is the plane parallel to the electrodes. This boundary will move towards the cathode until all the voltage is transferred to the space charge region. The length of the sample – *L*; the thickness of the layer of a stationary negative charge – *d*(*t*); the density of a stationary negative charge –*ρ* (*ρ*< *0*).

Since the charge density is constant, the potential ψ as a function of the coordinate (the axis is directed to cathode), has the form:

$$\varphi(\mathrm{x}) = -\frac{\rho \mathrm{x}^2}{2\varepsilon_0} - C(t)x \tag{1}$$

Accordingly, the electric field strength in the space charge region has the form:

$$E = \frac{\rho x}{\varepsilon_0} + C(t) \tag{2}$$

Since the conduction region (the length of which *L*- *d*(*t*)) is neutral, the electric field in it is the same as on the moving boundary, i.e. (2) for *x*= *d*(*t*)*:*

$$E(t) = \frac{\rho d(t)}{\varepsilon_0} + C(t) \tag{3}$$

(3) is also a uniform electric field in the region where there is a conductivity. This is due to the fact that the region is neutral. Consider the condition for the continuity of the charge on the moving boundary. Before the application of the electric field, the entire sample was neutral, so the rate of increase of the stationary negative charge $\rho\, d(t)' S$ is equal to the rate of decrease of the positive charge –jS (*j=σE; S*- area of the border; σ- specific conductivity). Thus, we get the equation (prime means differentiation):

$$-\rho d(t)' = j = \sigma E(t) \tag{4}$$

To obtain a closed differential equation for d(t), we equate both expressions for the electric field in the conducting region:

$$\frac{\rho d(t)}{\varepsilon_0} + C(t) = -\frac{-U_0 + \frac{\rho d^2(t)}{2\varepsilon_0} + C(t)d(t)}{L - d(t)} \tag{5}$$

The left side (5) is the formula for the electric field (3); the numerator of the right side is the potential difference in conducting region, the denominator is the width of this region. From (5) we obtain:

$$\frac{\rho d(t)}{\varepsilon_0} + C(t) = \frac{1}{L}\left(U_0 + \frac{\rho d(t)^2}{2\varepsilon_0}\right) \tag{6}$$

From (3) and (6), taking into account the fact, that ρ = -IρI, we obtain;

$$E(t) = \frac{U_0}{L}\left(1 - \left(\frac{d(t)}{d_\infty}\right)^2\right) \tag{7}$$

where $d_\infty = \sqrt{2U_0\varepsilon_0/|\rho|}$ – is the value of the gap width at large times.

Substituting (4) into (6), we obtain a differential equation for d(t):

$$\frac{d(t)'}{d_\infty}=\frac{2}{\tau}\left(1-\left(\frac{d(t)}{d_\infty}\right)^2\right), \tag{8}$$

where:

$$\tau=\frac{L|\rho|d_\infty}{\sigma U_0} \tag{9}$$

The solution of this differential equation with the initial condition d(0)=0 has the form:

$$d(t)=d_\infty\frac{e^{\frac{2t}{\tau}}-1}{e^{\frac{2t}{\tau}}+1} \tag{10}$$

Make sure, that the total current in the conductive and non-conductive parts of the system is the same. In the shut-off gap the potential is (1). For electric field we obtain:

$$E(x)=-\varphi(x)=\frac{\rho x}{\varepsilon_0}+C(t) \tag{11}$$

The current density is determined only by the bias current. From (11) it follows that

$$J=\varepsilon_0 C(t)' \tag{12}$$

In the conducting area, the electric field is determined from (3). Let us calculate the displacement current in this area, taking into account (4):

$$\varepsilon_0 E'=-j+\varepsilon_0 C(t)' \tag{13}$$

Adding the conduction current density to the displacement current (12), we obtain that the total current is still equal $\varepsilon_0 C(t)'$.

So we made sure that the total current in the sample is the same along the entire length and is equal $\varepsilon_0 C(t)'$.

To determine the dependence of the total current on time during the formation of the shut-off contact, we calculate the derivative of the left and right sides (6). Then taking into account (10), we get:

$$J(t)=\frac{\sigma U_0}{L}\frac{4e^{\frac{2t}{\tau}}}{\left(e^{\frac{2t}{\tau}}+1\right)^2}\left(1-\frac{d_\infty}{L}\frac{e^{\frac{2t}{\tau}}-1}{e^{\frac{2t}{\tau}}+1}\right) \tag{14}$$

From (14) it follows that when t ≤ τ, then practically this is a constant current in an ideal sample. At t ≥ τ the current decreases exponentially as $exp(-2t/\tau)$. These conclusions follow from the first factor in (14). The second factor for the entire reaction time varies from 1 to $1-d_\infty/L$, i.e. insignificantly in actual cases (d≤ L). From the above formula for (9) we obtain:

$$\tau\sim\frac{1}{\sigma\sqrt{U_0}} \tag{15}$$

It follows from (15) that relaxation time is inversely proportional to the conductivity and the square root of the applied voltage. (15) describes the process of zeroing the current with simultaneous formation of a shut-off contuct, to which the entire applied voltage passed. This type of gap is realized only in the presence of an external electrical voltage.

Kinetics of the disappearance of the dielectric gap after switching off the external electric field

Let the sample be kept at voltage U_0 until the current stops. If the voltage is turned off and the sample is short-circuited, then the recovery process begins, in which the charge dielectric layer disappears, and conductivity is restored throughout the entire volume of the sample. Then (7) takes the form

$$E = -\frac{\rho d^2}{2\varepsilon_0 L} \tag{16}$$

By turning formula(16) into (4), we$'$ will get:

$$d^{/} = -\frac{d^2}{\tau d_{\propto}} \tag{17}$$

Solving (17) with the initial condition $d(0) = d_{\propto}$, we obtain

$$d(t) = \frac{d_{\propto}}{1 + \frac{t}{\tau}} \tag{18}$$

In order to find an explicit expression for the dependence of the current on time during the destruction of the dielectric gap (in accordance with (11), it is necessary to find $C'(t)$. From(3) and (16), we obtain:

$$\frac{\rho d(t)}{\varepsilon_0} + C(t) = -\frac{\rho d(t)^2}{2\varepsilon_0 L} \tag{19}$$

Differentiating the left and right sides in time in (18), substituting the obtained expression for $C'(t)$ into (12), we obtain the formula for the total current density:

$$J = \frac{\sigma U_0}{L} \frac{1 - \frac{d_\infty}{L} \frac{1}{1 + \frac{t}{\tau}}}{\left(1 + \frac{t}{\tau}\right)^2} \tag{20}$$

This formula describes the relaxation process of destruction (disappearance) of the dielectric gap. When the equilibrium gap length is significantly less than the crystal length, then (20) (at large times) decreases in inverse proportion to the square of the time.

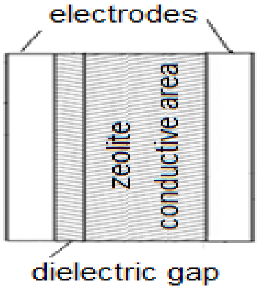

Conclusion

It is found that the formation of a dielectric gap is accompanied by an exponentially decreasing current. The time constant of this process is inversely proportional to the conductivity and the square root of the applied voltage. After switching off the external voltage (so that the potential difference at the ends of the sample is zero), the dielectric gap is destroyed. This process is also accompanied by a decreasing current. But now the current is inversely proportional to the square of the time (the time constant is the same as in section 1).

References

1. Orbukh V.I., Lebedeva N.N., Agamaliyev Z.A., Eyvazova G.M., Salamov B.G., J of Tech. Phys. 2020, v. 90, p. 325.
2. Lebedeva N.N., Orbukh V.I., Sultanov Ch.A. J of Tech. Phys. 2010, v. 80, p. 134.
3. Orbukh V.I., Eyvazova G.M., Lebedeva N.N., Muradov M.B., Salamov B.G. Trans. of ANAS 2015, v. 31, p. 100.
4. Veysman V.L., Markov V.N., Nikolayeva L.V., Pankova S.V., Solovyov V.G., Russian J of Solid State Physics 1993, v. 35, p. 1390.
5. Lidyard A., Moskva, Inostr. lit., 1962, 222 p.
6. Gavrilyachenko V.G., Kabirov YU.V., Panchenko Ye.M., Sitalo Ye.I., Gavrilyachenko T.V., Milov Ye.V., Lyanguzov N.V., Russian J of Solid State Physics 2013, v. 55, p. 1540.

PLASMONICS FOR SAFETY, SECURITY AND DEFENCE

L ILYASHENKO-RAGUIN[1], S PETRYCHENKO[2] and O KOVALEV[2]

[1] Department of Design and Operation of Electronic DevicesKharkiv National University of Radio Electronics, Kharkiv, Ukraine
[2] National Academy of the National Guard of Ukraine, Kharkiv, Ukraine
E-mail: mila.illyashenko@gmail.com

The current intense interest in the properties of silver nanoparticles for their applications in safety, security and defence is currently based on their resonantly enhanced scattering properties, including the sensitivity change in external environment. When silver nanoparticles are put in degraded environments, it results in differently colored scattered light, so that it is possible to notice the change of color. The initial color for resonantly enhanced scattered light is found by means of calculation for Total Scattering Cross-Section using spectral Boundary Integral Equation method with analytical regularization based on singularity subtraction improved by Fast Fourier Transform, that is proved to be appropriate to solve this kind of electromagnetic transmission problem providing fast and highly accurate results, which is required to enable knowledge, that is crucial for developing capabilities to address today's security challenges and for anticipating tomorrow's threats. Developed algorithm allows calculations of far-field scattering characteristics for silver nanoparticles as well as investigation for near-field characteristics in presence of opportunities for appearance of high amplitude enhancements for various wavelength of the nanoparticle illumination, while integration of human experts in the investigative analysis is done for fast innovative applications to fight illegal trafficking and criminal activities helping citizens to increase their security.

Keywords: Plasmonics, localised surface plasmon resonance, degraded environments, electromagnetic transmission problem, total scattering cross-section, spectral boundary integral equation method
PACS: 68.49.Uv, 87.52.-g, 05.40.-a

Introduction

The continued rise in terrorism has created a need for new and innovative applications of photonic technologies in very unconventional ways. They are based on the use of metal nanoparticles (NPs). When NPs are illuminated by the light source, they may exhibit a lot of interesting phenomena, including Localized Surface Plasmon Resonances (LSPRs). They result in resonantly enhanced scattering and resonantly enhanced absorption. Both phenomena already proved their usefulness for various civil applications.

Resonantly enhanced scattering

LSPRs depend on properties of materials, from those NPs are made. Among various materials, which came in research, there are iron (Fe), nickel (Ni), titanium (Ti), cobalt (Co), molybdenum (Mo), vanadium (V), wolfram (W), lead (Pb), platinum (Pt), aluminum (Al), palladium (Pd), gold (Au), silver (Ag) and copper (Cu). LSPRs of the last three listed metals, namely gold (Au), silver (Ag) and copper (Cu), fall in visible part of electromagnetic (EM) spectrum. This fact brings the ability to see and even to distinguish color of the light, scattered by them during LSPR. That gives opportunity to determine the LSPR wavelength using the color. Since LSPRs depend on properties of medium, in which NP is situated, color may change when the properties of external environment changes. Thus, presence of some contaminants in medium can be detected using color of light, scattered by NP, which is situated in this medium. Thus, resonantly enhanced scattering, which accompanies LSPR in NPs, is useful for applications, based on the use of color of reflected light, such as chemical sensing and biological imaging, while one of the most important applications to solve main socio-economic challenges with these light effects is medical diagnostics.

Resonantly enhanced absorption

The use of resonantly enhanced absorption is even more promising, because absorption results in heat, so that metal NP may become hot enough to fry ill cells of human body without affecting healthy cells. Thus, using resonantly enhanced absorption it is possible to make medical treatment of various diseases, including those for which helping should be imperative, especially in cases such as cancer, when other methods including radio-therapy, surgery and chemotherapy are not able to do so [1].

Resonantly enhanced scattering and resonantly enhanced absorption.

The use of those LSPR nanoparticles, which may have both, huge resonantly enhanced scattering and resonantly enhanced absorption simultaneously, gives opportunity to make medical diagnostics and medical treatment simultaneously, by using the same NP. But design, manufacturing and utilization of such a NP is very complicate task.

Due to the reason that LSPR of NPs depend on the size and shape of NP, the optimal choice of these parameters leads to design of NPs to be suitable for various applications, including those in sectors of Information and Communication; Industrial Manufacturing and Quality; Life Sciences and Health; Emerging Lighting, Electronics and Displays; Security, Metrology and Sensors; Design and Manufacturing of Components and Systems; Photonics Research, Education and Training; Agriculture and Food; Automotive and Transport (Fig. 1).

Fig. 1. Areas of applications for the Localized Surface Plasmon Resonance nanoparticles.

While the area for application of LSPR NPs is very broad, in this work we will focus on their use for safety, security and defence. We are motivated by the fact that, besides the dependence of LSPR wavelength, resonantly enhanced scattering and absorption properties on size, shape and materials of NP, LSPR properties of NPs strongly depend on properties of that environment, in which NP is situated, that gives the opportunity to use NP in testing for environmental contaminants [2]. This idea enables to design a diversity of imaging and non-imaging sensors for the security screening of packages, people and their bags, and may provide imagery in visually degraded environments, such as those of fog, cloud, rain and smoke, and solve other problems for homeland security, defence and counterterrorism.

While achieving specified effects is possible by using solid gold nanoparticles [medical applications] in civil defense applications, such as the health care, there are needs to address size, weight, and manufacturing cost issues when NPs are designed to be used under the difficult conditions, encountered in military environments. Emerging concepts with using core-shell NPs [1, 3] can support the realization of low-cost solutions, since not whole NP is made on noble metal, rather only its external part, which is deposed on the glass core. Thus, in this work the use of core-shell NP is investigated. While in fabrication of sensors different communities are involved including those, who are investigating topics that range from big data to robotics, electronics, fibre and materials, interdisciplinary collaboration is essential in particular those, which bring together achievements of computer science, mathematics, nanoengeneering, physics, optics, electromagnetism, biology, chemistry and medicine (Fig. 2) with purpose to use them for countering terrorism and crime, providing support to forensics, surveillance, security and defence forces.

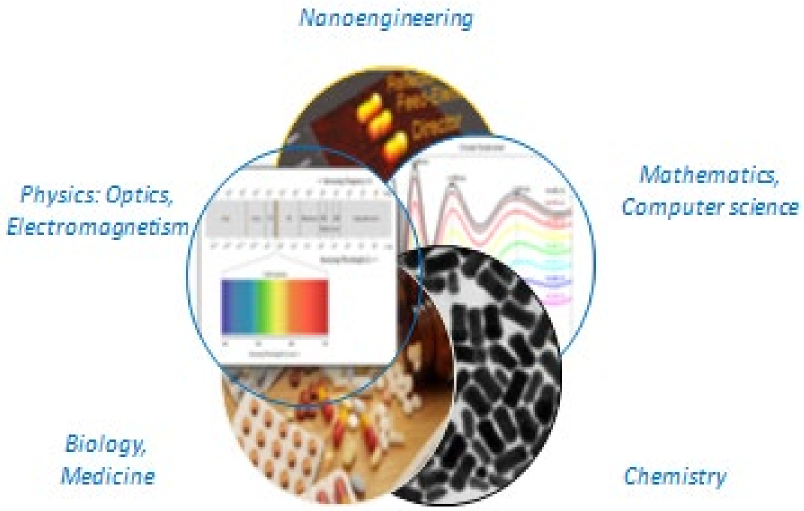

Fig. 2. Interdisciplinary of plasmonics.

It will also give opportinity for make leading-edge research in software development and implementation for industrial applications and scientific innovation in nanotechnology, which requires involvement and cooperation along the whole value chain from the exploration of the underlying techniques to the development of industrial products, enabling technical innovation to respond to the changing drivers from the world of security and defence, to offer unique selling propositions for sensors in this spectral band for the benefit of society.

Methodology

Hypotheses

The idea is following: when dangerous gas comes to environment, the dielectric permittivity of external environment changes, thus LSPR wavelength of NP, which is in this environment will change also. This change is possible to be noticeable. The color of reflected light will change, and new color will correspond to new wavelength of plasmon resonance in polluted environment. Thus by means of the light color, reflected by NP, presence of dangerous gases in environment may be detected.

The Color Prediction

The color of scattered light is possible to predict calculating Total Scattering Cross-Section (TSCS) as function on wavelength in visible part of EM spectrum. Having specified function and inspecting its graph, one must find maximums. The wavelengths, which correspond to maximums, are those of LSPRs. The color, corresponding to LSPR wavelength is that, which must appear when NP is in environment without contaminants.

Methods for TSCS calculations

To calculate TSCS is possible not only by means of new methods, by also using developed earlier numerical simulation tools based on the algorithms, made on known mathematical methods. This, however, require deep insight in the physical nature of the problem.

Common size of plasmonic NP is 5 nm < R < 100 nm, while wavelength of illumination is 300 nm < λ < 900 nm, thus, normalized wavenumber is 0.1 nm < *a* < 2.09 nm, where

$$a = kR = \frac{2\pi}{\lambda} R$$

and nanoparticle may be much smaller than the wavelength if illumination, thus, knowing techniques for so called *low frequency*, *medium frequency* and *high frequency* settings (Table 1), one may mistakenly select low frequency methods for TSCS calculation.

Table 1. Numerical methods

Number	Table Column Head	
	Kind of methods	**Definition**
1	Low frequency methods	Methods for objects, which are much smaller than wavelength of their EM wave illumination.
2	Medium frequency methodsa	Methods for objects, which are comparable with wavelength of their EM wave illumination.
3	High frequency methods	Methods for objects, which are much bigger than wavelength of their EM wave illumination.

Used when object is dielectrically big.

But despite of the fact that the object, is smaller than wavelength of illumination, object is dielectrically big due to high values of dielectric permittivity for materials to be involved manufacturing of photonic devices, in particular gold, silver and copper [4]. Then medium frequency methods must be used to calculate TSCS. In addition, arranging values of dielectric permittivity for silver as plot of function (Fig. 3) one may notice that real part of dielectric permittivity for silver may be negative, meaning that material exhibit negative refraction, at the same time imaginary part of this function for silver is not very small, meaning that absorption is not negligible. Since dielectric permittivity varied when wavelength is varied, one needs solving of the problem over whole range of possible excitation wavelength changing value of dielectric permittivity. Thus, we need fast numerical method.

Shapes of objects are smooth, because it is difficult to produce NP with complicated shapes, and mostly NP with simple shapes as spheres and ellipses as well as tubes with circular and elliptical cross-section came in research. Thus to calculate TSCS one needs method which takes into account the fact that boundary are smooth, in particular because of the possibility to have local near-field enhancements, with amplitudes reaching hundreds of those of illumination, when details smaller than a wavelength may make strong impact on the near-field behavier.

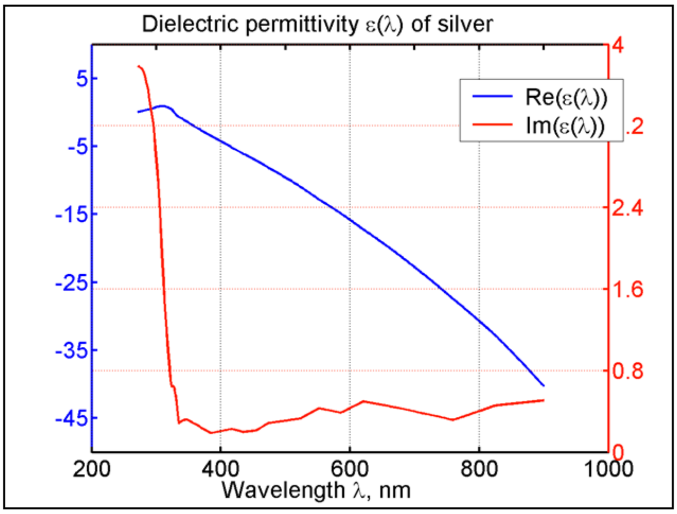

Fig. 3. Dielectric permittivity of silver as function on wavelenth of illumination from visible part of electromagnetic spectrum.

Thus, smooth boundary must be well described without approximation and simplification. We therefore opt on Spectral Fourier-Galerkin Method of Boundary Integral Equations (BIE), which must meet the following requirements:

- it may include near- and far-field visualizations to provide information on the LSPR effects, which are not available from measurements since it is much easier to see the process solving two-dimensional problem instead of three-dimensional problem;
- it may provide fast and accurate calculation of far-field characteristics due to automatically satisfied outgoing wave conditions;
- it is flexible dealing with complex valued wavelength-dependent material parameters of silver;
- it may accommodate accurately the smooth NP shape without simplifications to study a shape tunability of LSPR wavelength;
- it is flexible dealing with near-field effects of NPs at LSPR.

Calculation of TSCS must be done with high accuracy to enable knowledge, that is crucial for developing capabilities to address today's security challenges, to anticipating tomorrow's threats. Thus, Fast Fourier Transform (FFT) based method may provide needed results, especially because spectral Fourier-Galerkin BIE, when used in conjunction with FFT, may involve analytical regularization based on singularity subtraction to provide high accuracy in addition to fast result. Thus, summarizing chosen methods and techniques, obtained algorithm may be called as spectral Fourier-Galerkin Boundary Integral Equation method with analytical regularization based on singularity subtraction improved by Fast Fourier Transform.

Results and discussion

Calculation of far-field characteristics: Total Scaterring Cross-Section for solid silver nanoparticle

One of the most practical shape to be produced is starshaped nanoparticle. It at the same time incorporate in the same structure both tips and gaps. The results of calculation for 5-pointed nanostars and 6-pointed nanostars are presented in Fig. 4.

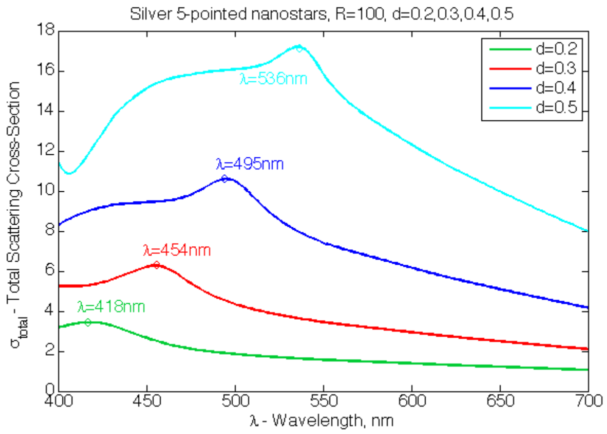

(a)

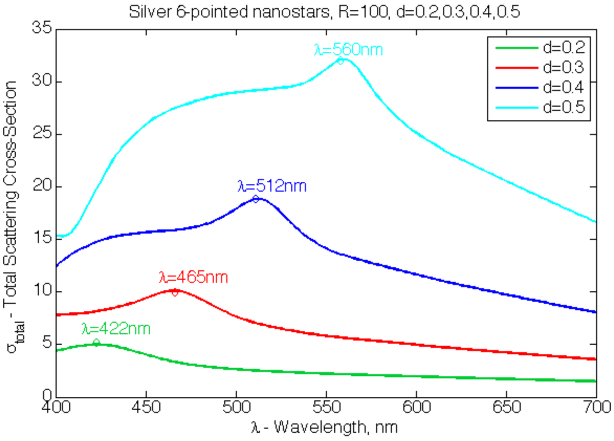

(b)

Fig. 4. Total scattering cross-section as function of excitation wavelength for silve nanoparticles with (a) 5-pointed nanostar shape; (b) 6-pointed nanostar shape.

Calculation of the near-fieldcharacteristics

Since the numerical results of TSCS calculations are done for investigation of their properties, which concerns plasmonic NP sensors within the context of their associated applications for safety, security and defence application., we presented near-field distribution during the resonance such as λ=418 nm and λ=536 nm (Fig. 5) and λ=422 nm and λ=560 nm (Fig. 6) because, it needs to know how thick may be layer of metal, i.e. metal shell, to provide best possible sensor properties.

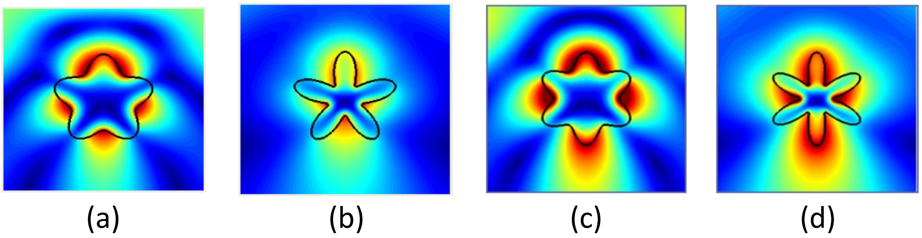
(a) (b) (c) (d)

Fig. 5. Near-field intensity pattern for 5-pointed starsduring resonance when (a) λ=418 nm; (b) λ=536 nm, (c) λ=422 nm; (d) λ=560 nm.

Results presented in Fig. 5 and Fig. 6 demonstrate, that success in producing core-shell dielectric-metal NP with the same properties as metal NP without affecting LSPR properties depends on penetration depth of plasmon mode inside the metal NP. Thus, when size of nanoparticle is such as radius R=100 nm, radius of embedded core in must be much smaller for cases when petals of nanostars are chosen to be narrow.

Conclusion

In this work the initial color for resonantly enhanced scattered light is found by means of calculation for TSCS using spectral BIE method with analytical regularization based on singularity subtraction improved by Fast Fourier Transform, that is proved to be appropriate to solve this kind of electromagnetic transmission problem, which is required to enable knowledge, that is crucial for developing capabilities to address today's security challenges and to anticipate tomorrow's threats. The set of numerical results demonstrate opportunity to have core from another material, embedded inside NP without affecting resonantly enhanced scattering.

References

1. Rastinehad A.R., Anastos H., Wajswol E., Winoker J.S., Sfakianos J.P., Doppalapudi S.K., Carrick M.R., Knauer C.J., Taouli B., Lewis S.C., Tewari A.K., Schwartz J.A., Canfield S.E., George A.K., West J.L., Halas N.J. Proceedings of the National Academy of Sciences 2019, v. 116 (37), p. 18590. DOI: 10.1073/pnas.1906929116.
2. Yu Z., Lim C.-K., Chan W. K.t, Chen Y., Shao W., Zhang Y., Prasad P.N., Tan T.T.Y., ACS Appl. Nano Mater. 2021. https://doi.org/10.1021/acsanm.1c03376.
3. Raguin L., Leuchtmann P., Hafner Ch., J. Comput. Theor. Nanoscience 2011, v. 8 (8), p. 1590. DOI:10.1166/jctn.2011.1853.
4. Johnson P.B., Christy R.W. Phys. Rev. B, 1972, v. 6 (12), p. 4370. doi: https://doi.org/10.1103/PhysRevB.6.4370.

ANTI-STOKES COMPONENT OF LASER IMPULSE IN THE OPTICAL FIBER AT CARs

RJ KASUMOVA[1], NV KERIMLI[1,2] and GA SAFAROVA[1]

[1]Baku State University, Baku, Azerbaijan
[2]Azerbaijan Medical University, Baku, Azerbaijan
E-mail : nazaket_kerimli@mail.ru

It has been analyzed nonstationary interaction of waves in optical fibers. Based on dispersion theory in the first approach it has been analyzed the nonlinear interaction between long impulse of strong pumping wave and super short impulse of Stokes wave with quadratic phase modulation. It has been examined the influence of different parameters of regime on spectrum of anti-Stokes wave within optical fiber. It has been shown that the phase modulation of excitatory laser impulse leads to widening of central maximum of anti-Stokes component.

Keywords: biological and medical applications, stimulated Raman scattering, CARS, optical fiber
PACS: 42.62.Be; 42.65.Dr; 42.81.Qb

Introduction

The last 20 years have seen an enormous upsurge in the number of publications reporting findings obtained by Raman spectroscopy, a non-invasive, non-destructive method which uses the inelastic scattering of light to provide a ‘fingerprint’ of the sample’s chemical composition and constituents [1]. Long neglected because of practical difficulties, the technique has been transformed by recent technological advances into a powerful analytical tool capable of opening avenues of investigation that were previously out of the reach of biomedical scientists. Beyond introducing the approach and describing its relative merits and weaknesses, it may become an invaluable tool for biomedical investigations [2].

Beginning with simple characterizations of biologically and medically important substances, aided by increasing technological sophistication, the use of Raman spectroscopy in biomedicine has quickly expanded to the investigation of complex biochemical interactions, the assessment of organelles and now the evaluation of living cells and tissue [1-3]. The first Raman investigations of reproductive organs were primarily oncological in nature; however, the past few years have seen an increase in the application of the technique for the assessment and evaluation of both male and female gametes. In particular, progress has been made in the characterization, identification and localization of sperm nuclear DNA damage [3].

Till presented analytical solving of component of scattering was done mainly by method of constant filed approximation (CFA) due to which the changing phase of interacted waves was neglected [4-6]. The changing of phase is taken into account in method of constant intensity approximation (CIA). Raman spontaneous scattering were analyzed by based on CIA in two versions: active medium within laser resonator and within external resonator [7-8]. Nonstationary case of generation of scattering component was analyzed in [4].

Based on CFA it was examined by us nonstationary optical process in metamaterials at three waves interaction [9-11]. Nonlinear optical process of generation of second harmonic [12-13], CARS [14] within optical fiber was learned by us based on CIA.

Theory

It was analyzed by us nonstationary generation of anti -Stokes component by method of CFA at CARS within optical fiber.

Based on CFA, for the spectral power density of anti-Stokes emission at first approximation of dispersion theory we got

$$S_a(z,\omega) = F \cdot \frac{1}{\sqrt{1+k^2\tau^4}} z^2 \cdot \mathrm{sinc}^2 \lambda' z \exp\left(-\frac{\omega^2\tau^2}{1+k^2\tau^4} - 2\delta\, z\right),$$

where τ-is duration of impulses, k-is coefficient of phase modulation

$$F = (cn_a/8\pi)\, |\gamma_a^{sa}|^2\, I_{po}^2 I_s(0) \cdot \tau^2/2\pi,$$

$$\lambda' = \sqrt{\frac{\left[(\gamma_a+\gamma_s^*)I_{po}+\Delta+\nu\, \omega\right]^2}{4} - \Gamma_p^2},\ \Gamma_p^2 = \gamma_a^{sa}\gamma_s^{sa} I_{po}^2.$$

$$\lambda = \sqrt{-\gamma_a^{sa}(\gamma_s^{sa})^* I_{po}^2 - \frac{\left[\delta_a-\delta_s+i(\gamma_a+\gamma_s^*)I_{po}+i(\nu\, \omega+\Delta)\right]^2}{4}},\ \nu = 1/u_s - 1/u_a.$$

Here I_{po} is the pump wave intensity and I_{so} is the Stokes compponent imtensity at the entrance to the medium. γ_i $(i = s, a)$ and $\gamma_p^{s,a}$ are the nonlinear coupling coefficients for stimulated Raman scattering of the Stokes and anti-Stokes components, and $\gamma_{p,s,a}^{sa}$ are the nonlinear coupling coefficients between the Stokes and anti-Stokes components, $u_{p,s,a}$ are the group velocities of the corresponding waves.

Results and discussion

As seen from Fig. 1. the component of dissipation and correspondingly the shape of spectrum is changed at various contributions of group velocities within conventional medium. Based on examination of nonlinear process at parameters taken from experiment, the changing of l_{NL}/l_ν and correspondingly ν which characterizes matching of group velocities doesn't lead to significantly changing of spectrum. At the same time during increasing of coefficient of phase modulation k, the widening of spectrum takes place, when p is ranging between 0 and 6.

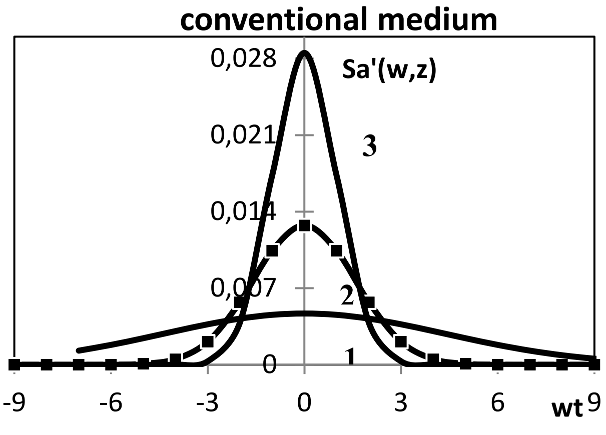

Fig. 1. Dependency of reduced spectral density of anti-Stokes component on parameter of $\omega\,\tau$ at z =0.6 m, for intensity of pumping wave I_{po} =10^8 W/cm^2, for phase mismatch Δ =8 m-1, l_{NL}/L_V= 3. Value of parameter $p = k^2\tau^4$ has been taken 0 (curve 3), 2 (curve 2) and 6 (curve).

Conclusion

Ultimately in presented paper the nonstationary generation of anti-Stokes component at CARS has been examined. It has been got the spectrum of anti-Stokes wave, it has been examined effect at different parameters of impulse regime (coefficient of phase modulation, parameter $p = k^2\tau^4$). Learning the spectrum of anti-Stokes regime with considering the matching of group velocities shows that the spectral dependency are symmetrical. With increasing of mismatching of group velocities the spectrum of exited impulse becomes narrow. In presented paper the calculated model is applied to optical fiber but can be used for other nonlinear materials.

References

1. Ramirez M.G, Gonzalez F.J. Raman spectroscopy in Vivo Medical Diagnosis, IntechOpen, 2018, 342 p. DOI: 10.5772/intechopen.72933
2. Kong K., Kendall C., Stone N., Notingher L. Advanced Drug Delivery Reviews 2015, v. 89, p.121.
3. McGregor H., Wang W., Short M., Zeng H. Advanced Health Care Technologies 2015, v. 2, p. 13.
4. Tolles W.M., Nibler J.W., McDonald J.R., Harvey A.B. Applied Spectroscopy 1977, v. 31 (4), p. 253.
5. Vermeulen N., Debaes C., Thienpont H. IEEE Journal of Quantum Electronics 2009, v. 44 (12), p. 1248.
6. Shen Y.R. Principles of Nonlinear Optics, Wiley, New York, 1984.
7. Kasumova R.J. Applied Optics 2001, v. 40 (28), p. 5517.
8. Kasumova R.J. Journal of Applied Spectroscopy, 2001, v. 68 (5), p. 577.
9. Kasumova R.J., Amirov Sh.Sh. Superlattices and Microstructures 2019, v. 126. p. 49.
10. Kasumova R.J., Safarova G.A., Ahmadova A.R. Open Phys. 2019, v. 126, p. 200.
11. Kasumova R.J., Safarova G.A., Ahmadova A.R. Opt. Comm. 2018, v. 427, p. 584.
12. Tagiev Z.H., Kasumova R.J. Optics & Communications 2006, v. 261, p. 258.
13. Kasumova R.J., Safarova G.A., Ahmadova A.R. Appl Opt. 2018, v. 57 (25), p. 7385.
14. Kasumova R.J., Kerimova N.V., Safarova G.A. J of Applied Spectroscopy 2021, v. 88 (1), p. 17.

SPECTRAL ACTIVITY OF THE HERBIG Ae STAR HD 31648

BN RUSTAMOV[1], KHM MIKAILOV[1], KI ALISHEVA[1,2], SO MAMMADOVA[2] and VI ALIYEVA[2]

[1]Baku State University, Baku, Azerbaijan
[2]Shamakhy Astrophysical Observatory named after N. Tusi Azerbaijan NAS, Azerbaijan
E-mail : bayram_rustam@yahoo.com

We present the results of spectral observations of the Herbig Ae star HD31648, carried out at the Cassegrain focus of the 2-m telescope of the ShAO named after N.Tusi, by using the Shamakhy Fiber Echelle Spectrograph) (ShAFES). The spectra of star HD 31648 were obtained with the spectral resolution of R = 28000, in the wavelength range of λλ3900–7500 ÅÅ. The behavior of selected spectral lines in the spectrum of the star HD31648 is described: lines of the Balmer series of hydrogen (Hα - Hδ), HeI 5876 Å, resonance sodium doublet NaI D and FeII ($\lambda\lambda$5169 Å, 5018 Å, 5169 Å).

Keywords: emission spectrum, line profiles, stellar wind, individual: HD31648
PACS : 95.55.Qf, 95.75.Fg, 97.21.a, 32.70.Fw, 33.70.Fd, 32.70.Jz, 33.70.Jg

Introduction

The formation of stars and planetary systems is one of the primary research topics in modern astrophysics. Studies of young stars with small (stars T Tauri type) and intermediate (stars Ae/Be Herbig type) masses connected with early stages of stellar evolution are among the priority areas of astrophysics.

Comparison of the observed characteristics of young stars with model calculations requires sufficiently long-term spectral observations, which make it possible to estimate the characteristic time of accretion and wind variability

According to modern astrophysical concepts, the physics of the observed particularities of young stars type Ae/Be Herbig, in general, is determined by the results of the interaction between the young star and the surrounding circumstellar medium.

The goal of this message: based on the homogeneous spectral data of the young star type Herbig Ae HD31648, to study the observed peculiarities of the star's emission in the regimes of accretion and stellar wind.

HD 31648 (MWC480) is an isolated Herbig Ae star in the Taurus-Auriga star-forming region, spectral class of the star is A2-A3e, one of the brightest (V $\sim$ $7^{m}.6$) stars of this type in the northern sky. The star HD31648 belongs to the group of photometrically quiet young stars with signs of matter outflow in the spectrum [1-2].

Observations and data reduction

Spectral observations of the star HD31648 were carried out at the Cassegrain focus of the 2-meter telescope of the Shamakhy Astrophysical Observatory named after N.Tusi, on a ShaFES fiber echelle spectrograph (Shamakhy Fiber Echelle Spectrograph) [3], by using CCD matrix STA4150A, 4096×4096 pixel (1 pix=15 mic.), cooled with liquid nitrogen. The spectra were obtained using a CCD array detector cooled with liquid nitrogen. Matrix size 4096 x 4096 pixels, 1 pix. = 15 mic. Spectral resolution R = 28000, wavelength range λλ 3800-8000 Å. During the period December 2019 - January 2020 during four nights, 2 spectra of the studied star and a whole set of calibration frames were obtained every night: dark (or bias), flat - field, ThAr, and Sky, also 2 spectra of a hot, rapidly rotating star A2 θ And, as a standard for remove telluric lines in the spectrum of HD31648. The reduction of echelle spectra was carried out according to the standard technique using the new version of the DECH 30 program developed by Galazutdinov [4]

Observation results

For the analysis the following particularities are chosen in the spectrum of the star HD3164

1. The lines of the Balmer series of hydrogen (mainly Hα and Hβ): 6562.817 Hα, 4861.332 Hβ, 4340.468 Hγ, 4101.737 Hδ, 3970.074 Hε

Emission Hα and Hβ lines in the spectrum of the star HD31648 are formed in the sufficiently extended circumstellar shell and show profiles of type P Cyg, which are direct indicators of mass ejection. The observed Hα line profile can be classified as P Cyg III, with a secondary blue emission peak, according to the classification of [5]

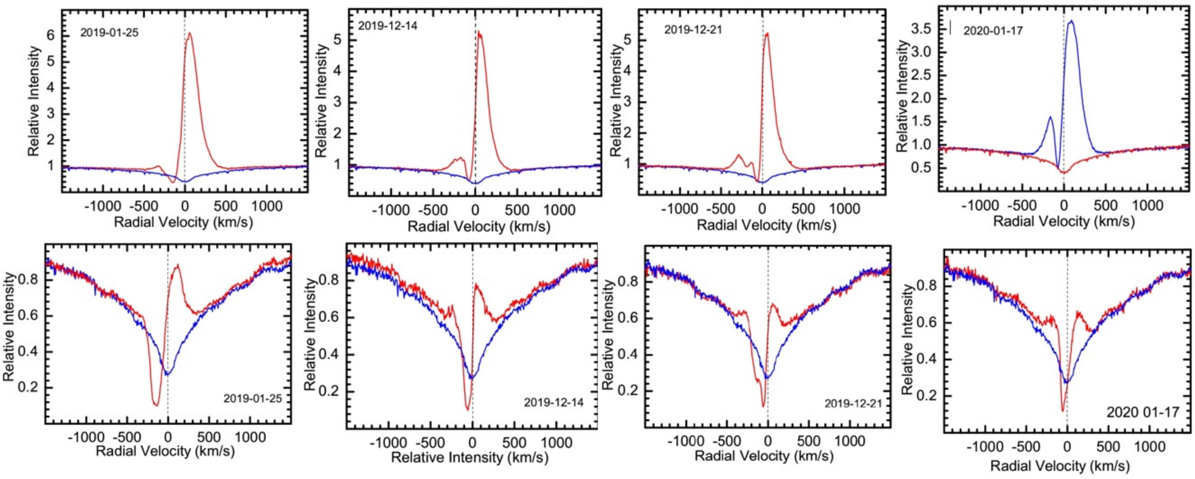

Fig. 1. Profiles of the Hα (top panel red lines) H β (bottom panel red lines) lines in the spectrum of HD 31648 and the standard star θ And (sp. A2) (blue lines)

Classic P Cyg profile was observed on January 25, 2019. A two-component profile with a ratio V/R<<1 was observed on two dates (12.14.19 and 01.17.20) besides, at the night of 01.17.20, the intensity of the blue emission component increased, while the intensity of the red emission component decreased. On 12.21.19, a secondary emission component was detected on the blue wing of the Hα line. The greatest variability is observed in the blue part of the profile. P Cyg-type structure with wide photospheric wings is observed in the central part of the Hβ line profile. The red emission component shows strong variability.

2. Resonance doublet of sodium : NaI D1 (λ 5895.923Å) and NaI D2 (λ 5889.953Å)

The sodium resonance doublet is one of the most interesting spectral peculiarities of the spectra of Ae/Be Herbig stars. Sodium atoms are completely ionized in the atmospheres of stars of spectral class A due to the low ionization energy (5.17 eV). Consequently, this line can be formed relatively in the cold peripheral part of the accretion disk. However, in some models, instead of the formation of a sodium doublet, relatively hot and dense gas is chosen along with the peripheral part of the accretion disk. Such conditions are achieved in relatively small regions of the disk or wind, adjacent to the region of formation of the Hα emission line.

The resonance doublet NaID in the spectra of HD31648 consists of two components - a narrow interstellar component (IS) and a strongly variable circumstellar (CS) component with a P Cyg structure.

According to our measurements, the ray velocities of the interstellar (IS) component on average is 13.3 km/s on both D1 and D2 NaI lines.

3. Neutral helium: HeI λ5876 Å

The helium line HeI λ5876 is formed in a hot compact layer, in the closest part of the accretion disk to the star, at a very high gas temperature (~17,000 K). This region is simultaneously the formation place of high-velocity disk wind. Consequently, the study of this line in young stars, observed in both emission and absorption, makes it possible to analyze the stellar emission both in the accretion regime and in the matter outflow regime.

The helium line HeI λ5876 adjacent to the NaID line consists of emission and absorption components. In our spectra, in one case (2019-21-12) both components are noticeably observed.

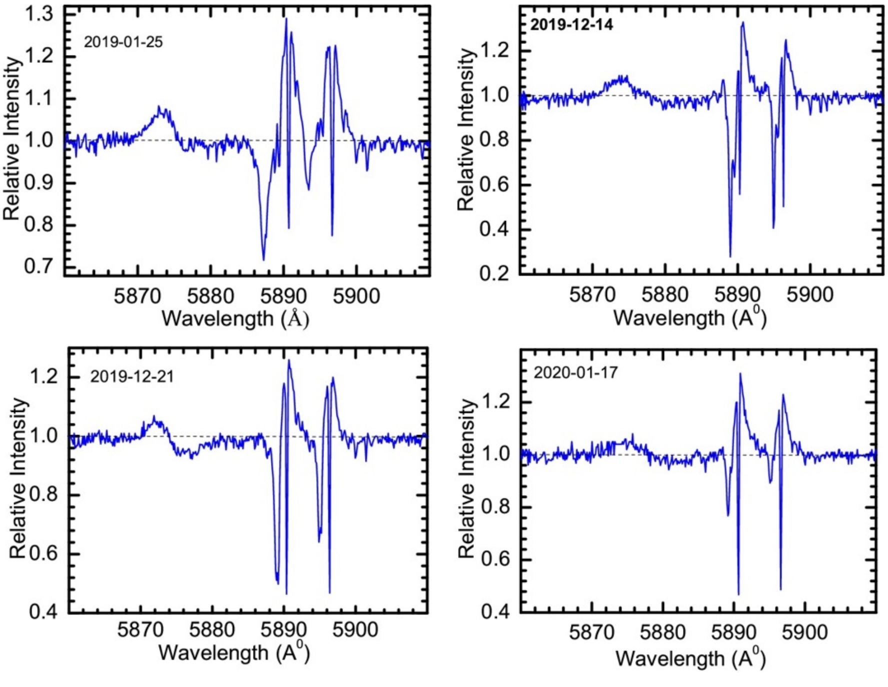

Fig. 2. Line profiles of neutral helium HeI λ5876 Å + resonance doublet D1,2 sodium in the spectrum of HD 31648.

4. Lines of ionized iron FeII 42 (λλ 4923.921 Å, 5018.434 Å, 5169.03 Å)

The FeII42 lines are one of the most noticeable peculiarities in the spectrum of HD31648, with signs of intense mass loss in the form of stellar wind.

Discussion

As it is known, the results of the interaction of a star with its circumstellar matter show itself in the form of an outflow (stellar wind) or star accretion of matter (accretion). It should be noted that in terms of observational astrophysics, spectral signs of stellar wind and star accretion of matter are shown in the so-called P Cyg and inverse P Cyg profiles, respectively, in certain diagnostic lines.

Figures 1-4 shows the profiles of selected lines for analysis in the spectrum of the star HD31648.

As can be seen from these figures, the hydrogen lines Hα and Hβ show an emission profile of the type P Cyg, but Hγ and Hδ are observed in absorption (Fig. 1).

A weak emission component was simultaneously observed in the blue side of absorption P Cyg in the line profiles Hβ, except for the date 01/25/2019 (Fig. 1), moreover the intensity of this component in the spectra obtained on December 21, 2019, and January 17, 2020. are close to the intensity of the red emission component P Cyg absorption.

On the night of 21.12.2019. a weak absorption circumstellar component appeared on the blue absorption wing, synchronously with the appearance of a secondary emission component on the blue wing of the Hα line (Fig. 1)

The variability in the intensities of the blue and red emission components in the P Cyg absorption, in the profile Hβ (on 01.17.20), accords with similar changes in the Hα line.

As can be seen from Fig. 2, the line HeI 5876Å in the spectrum of the studied star is present in the emission, shifted towards the blue side of the spectrum, and only in one spectrum (21.12.2019) is present a profile of the inverse P Cyg type with sufficiently strong absorption shifted toward the red side of the spectrum (Fig. 4)

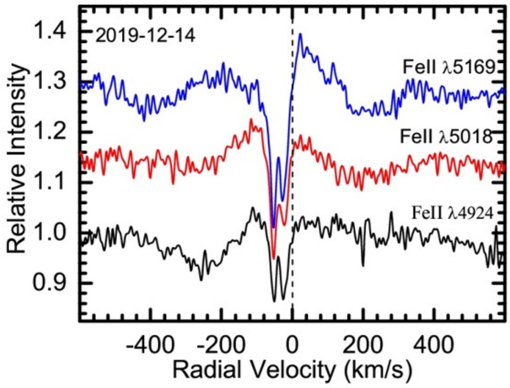

Fig. 3. Line profiles of ionized iron FeII 42 ($\lambda\lambda$ 4923.921 Å, 5018.434 Å, 5169.03 Å) in spectrum of star HD 31648

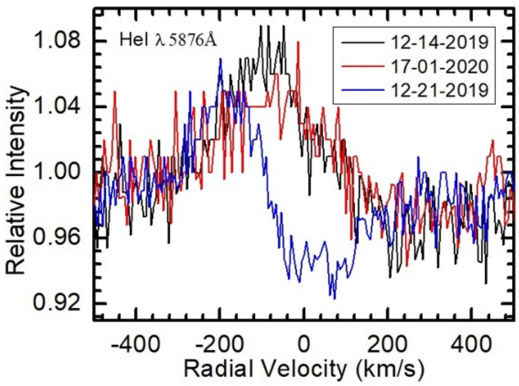

Fig. 4. Line profiles of HeI λ5876 A^0 in spectrum of star HD 31648

As noted above, a secondary emission component appeared in the same spectrum on the blue wing of the Hα line, also a weak absorption circumstellar component was detected on the blue wing of the P Cyg absorption of the Hβ line.

The circumstellar (CS) component of the sodium resonance doublet line (NaD) shows strong variability and, as a whole, correlates with changes in the Hα emission line, which indicates the proximity of the formation regions of these lines (Fiq. 2).

In spectrum, obtained at 21.12.2019, the NaID line also reacts to the above-noted variability occurred synchronously in the Hα, Hβ, and HeI lines; in this spectrum, at the level of the profile depth of the circumstellar component (CS) of the NaD lines, an absorption component was detected (Fig. 2).

A weak absorption circumstellar component noticeably stands out in the red part of the CS absorption on the dates 01.25.2019, 12.21.2019, and 01.17.2020 (Fig. 2)

One of the characteristic spectral peculiarities of young stars is the presence of a metal line shifted to the blue side of absorption (profile type P Cyg).

According to modern astrophysical visions, these lines are formed in an expanding gas envelope, and they are called "shell" lines. The line once ionized iron Fe42 (λλ 4923.921 Å, 5018.434 Å, 5169.03 Å), along with the NaID line, is a good criterion for diagnosing a stellar wind in an expanding envelope.

As can be seen from Fig. 2 in the spectrum obtained on the date of 12.14.2019. with the appearance of the absorption component in the CS absorption of the NaID lines, the bifurcation of the absorption component occurs synchronously in all three Fe42 lines (λλ 4923. 921 Å, 5018.434 Å, 5169.03 Å) (Fig. 3).

In the spectra of young stars, we often observe signs of matter outflow and accretion simultaneously. According to modern model calculations, this phenomenon occurs as a result of the interaction of the accretion disk with the stellar magnetosphere, part of the matter penetrates the magnetosphere and falls on the star, and part is thrown out.

According to modern views, the matter outflow from the surroundings of a star can also occur as a result of a magneto-centrifugal disk wind, which occurs when a partially ionized gas in the atmosphere of an accretion disk interacts with the disk's magnetic field.

The above-mentioned observed data obtained as a result of the analysis of the spectral activity of the star Herbig Ae HD31648, based on the highly dispersive spectral material, allow us to conclude that the shape of the profiles of selected spectral lines obtained by us in four spectra, generally, are repeated in published in the literature similar profiles. [6-8]

For the first time, the spectral peculiarities of the same spectrogram are studied by us simultaneously

Conclusions

1. During the period of our spectral observations, the profiles of the selected lines (Hα и Hβ, NaID1,2) show a profile of the type P Cyg, which indicates the dominant role of the stellar wind (matter outflow) at the formation of these lines.

2. On the night of January 25, 2019. the Hα line is observed in the form of a classical profile of the type P Cyg (the blue emission component is very weak). With an increase in the intensity of the blue emission component, the profile becomes of the type P Cyg III, and at the same time, the intensity of the red emission component decreases.

3. On the night of December 21, 2019, a secondary emission component was detected on the blue wing of the Hα line; at the same time, a weak absorption circumstellar component

appeared on the blue wing of the P Cyg absorption of the Hβ line, also an absorption component was detected at the level of the profile depth of the circumstellar component (CS) of the NaI D line. In the same spectrum, the HeI 5876Å line shows a profile of the inverse type P Cyg with a sufficiently strong absorption towards the red side of the spectrum. Apparently, on this nigh mass ejection from the surface of the star occurred, quite powerful and covering the whole region of the formation of these lines.

4. The variability picture of the NaI D lines is quite complicated, on the one hand, some variability elements accord with similar changes in the Hα and Hβ lines, on the other hand, the variability of the neutral sodium doublet line correlates with changes in the "shell" lines of once ionized iron - FeII 42 (λλ 4923.921 Å, 5018.434 Å, 5169.03 Å).

The behavior of the NaI D variability is related to the regions of line formation.

References

1. Augereau J.C., Lagrange A. M., Mouillet D., and Menard F., Astron. Astrophys. 2001, v. 365, p. 78. DOI: 10.1051/0004-6361:20000328
2. Montesinos B., Eiroa C., Meri´n B., and Mora A., Astor. Astrophys. 2009, v. 495, p. 901. https://doi.org/10.1051/0004-6361:200810623
3. Mikailov Kh. M., Musaev F.A., Alekberov I.A., Rustamov B.N., Khalilov O.V., Kinem. and Physics of Celes. Bodies, 2020, v. 36, p. 22. DOI: 10.3103/S0884591320010043
4. http://www.gazinur.com/ DECH -software.html).
5. Reipurth B., Pedrosa A., and Lago M. T. V. T., Astron. Astrophys. Suppl. Ser. 1996, v. 120, p. 229. DOI https://doi.org/10.1051/aas:1996286
6. Kozlova O.V.Astrophys.vol.49, №1,2006, UDC:524.3-56.
7. Beskrovnaya N. G. and Pogodin M. A. A&A 414, 2004, p. 955. DOI: 10.1051/0004-6361:20031670
8. Mendigutıa, Brittain S., Eiroa C., Meeus G., Montesino B., Mora A., Muzerolle J., Oudmaijer R. D., and Rigliaco E. IAEA, v.776 (1), 12 p. DOI:10.1088/0004-637X/776/1/44

THE THERMOELECTRIC POWER OF SUPERCONDUCTING $Bi_2Sr_2Ca_{0.8}Zn_{0.2}Cu_2O_{8+y}$

SS RAGIMOV[1,2], GI AGAYEVA[2] and AE BABAYEVA[2]

[1]Institute for Physical Problems of Baku State University, Baku, Azerbaijan
[2]Institute of Physics of Azerbaijan National Academy of Sciences, Baku, Azerbaijan
E-mail: sadiyar.raqimov@bsu.edu.az, sadiyar@mail.ru

It was investigated the temperature dependence of the specific resistivity and thermoelectric power of polycrystalline sample $Bi_2Sr_2Ca_{0,8}Zn_{0,2}Cu_2O_{8+y}$ with a partial replacement of Ca by the Zn element of the Bi-2:2:1:2 system in the 75-300K temperature interval. The obtained experimental results on the thermal power were analyzed on the framework of the Xin's two band model. It was estimated the band gap E_g=0,0595 eV of the semiconductor type Bi-O layers.

Keywords: thermal power, specific resistivity, superconductivity, two band model
PACS: 74.25.F-, 74.25.fg, 81.05.-t

Introduction

The study of transport properties is important for understanding the mechanism of superconductivity and the nature of charge carriers in high-temperature superconductors (HTSC). Studies of the temperature dependences of the electrical resistivity and thermoelectric power (S) of superconducting materials provide additional information on the conduction mechanism and the nature of charge carriers. It also provides information about the scattering mechanism, band widths and band gaps governing the transport properties of the materials [1-7].

In Bi-based high temperature superconductors there are a weak bond between Bi–O layers [6,8]. The main content elements may be replaced by other ones to improve the superconducting properties. The substitution of one element by other can reduce to significant changes in the carrier concentration or oxygen content. On the other hand the sign and the slope of the S-T plot are of value in understanding the nature of the charge carriers. The structural properties in this case do not change significantly. But a change in the concentration of charge carriers affects the superconducting properties [5-7].

In the present work we analyzed the temperature dependence of specific resistivity and the thermoelectric power of polycrystalline sample $Bi_2Sr_2Ca_{0,8}Zn_{0,2}Cu_2O_{8+y}$ with a partial replacement of Ca by the Zn element.

Results and discussion

The investigated $Bi_2Sr_2Ca_{0,8}Zn_{0,2}Cu_2O_{8+y}$ was prepared by the solid-state ceramic technique method. Sample was prepared from stoichiometric amounts of high-purity Bi2O3, $CaCO_3$, $SrCO_3$, ZnO and CuO powders. The solid state reaction of the mixed and pressed powders was performed at 1115 K in air for 30h applying intermediate grindings. Cooling was carried out with a rate of 1.50 C/min.

The phase purity of the obtained sample was investigated by X-ray analyses. The XRD analysis was performed using a Brucker-D8 advance diffractometer at room temperature in the $50 \leq 2\theta \leq 800$ range. The obtained X-ray diffractogram of $Bi_2Sr_2Ca_{0.8}Zn_{0.2}Cu_2O_{8+y}$ is shown in Fig. 1. $Bi_2Sr_2Ca_{0,8}Zn_{0,2}Cu_2O_{8+y}$ consists of two phases and on the X-ray data are observed the additional peaks. The lattice parameter of the main phase corresponds to the orthorhombic Pnnn group with lattice parameters a=5,429, b=5,431, c=30,840 Ǻ. The other phase is the tetragonal I4/mmm group with lattice parameters a=3.8097 and c=24.607 Ǻ, respectively.

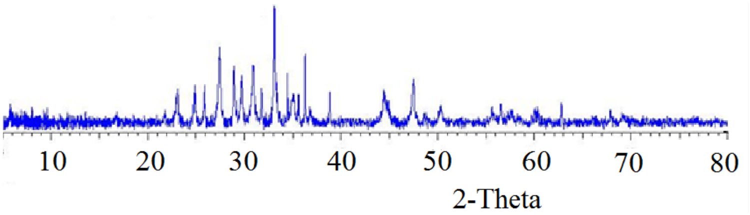

Fig. 1. The X-ray diffractogram of $Bi_2Sr_2Ca_{0,4}Zn_{0,6}Cu_2O_{8+y}$

The unit cell parameters of the $Bi_2Sr_2Ca_{0,4}Zn_{0,6}Cu_2O_{8+y}$ is differed from $Bi_2Sr_2CaCu_2O_{8+y}$ one [7]. The reason for this change is the inclusion of zinc ions in the intermediate regions of the unit cell. The zinc atoms cannot completely take the place of the element calcium. The reason of this is the fact that the ionic radii of these elements (Ca-1.04Å and Zn-0.83Å) are different. In this case the crystal structure is distorted and, consequently, the size of the unit cell is changed. As a result, additional pressure arises, and the crystal structure is deformed, and the lattice parameters change [7].

The specific resistivity and thermoelectric power measurements were carried out in the temperature range 75–320 K by the four-probe method. Sample for measurement were made in the form of a rectangular bar with dimensions of 8x3x1,2 mm^3. The obtained experimental results are shown in Fig. 2 and Fig. 3. The transition to the superconducting state occurs in a relatively narrow temperature interval between 77 and 82K. The superconducting critical transition temperature is 79,3K. The temperature variation of the electrical resistivity of $Bi_2Sr_2Ca_{0,4}Zn_{0,6}Cu_2O_{8+y}$, have the semiconductor type decreasing proportionally with the temperature (-1,1μΩ.cm/K) in the normal state. The normal state electrical resistivity (at 300K) is 0,38 mOhm/cm. This value is comparable with that found in other Bi-based HTSC [6, 9].

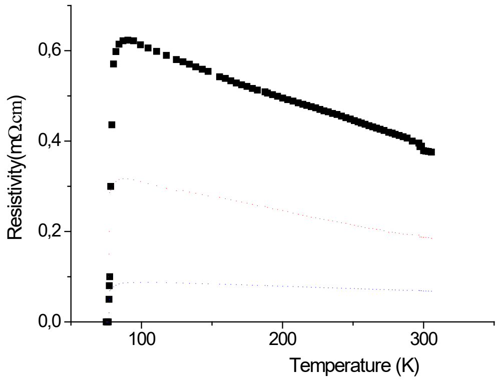

Fig. 2. The temperature dependence of the specific resistivity of $Bi_2Sr_2Ca_{0,4}Zn_{0,6}Cu_2O_{8+y}$

The temperature dependence of thermal power of $Bi_2Sr_2Ca_{0,4}Zn_{0,6}Cu_2O_{8+y}$ pass through a maximum before the superconducting phase transition and decrease linearly with increasing temperature. At temperatures above the maximum, the thermoelectric power has a negative slope, with d*S*/d*T*= -0,021V/K^2 value. The thermal power sign is positive, which is indicated that, the positive carriers are dominant. This behavior indicates to fact that, the electrons are also involved in conductivity.

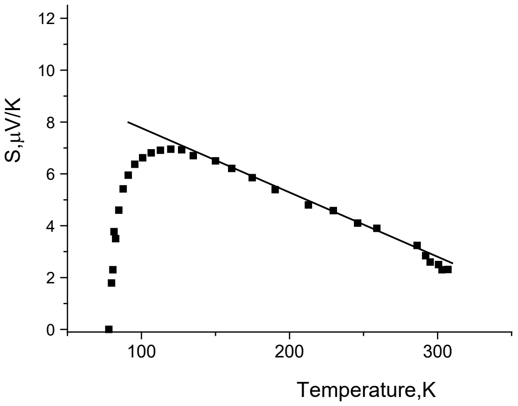

Fig. 3. The temperature dependence of the thermoelectric power of $Bi_2Sr_2Ca_{0.8}Zn_{0.2}Cu_2O_{8+y}$

In copper oxide HTSC system, the effects of their strong Coulomb interaction may play a quite important role. Therefore, the analysis of the obtained experimental results by using the standard band theory which is very useful for semiconductors is difficult. To explain the thermal power results of the HTSC systems have been proposed several models so as one band (phenomenological narrow band model [3]) and two-band (two band model with a linear *T*-term [4] and Xin's two-band model [2]) models.

In the Bi-based HTSC system the Bi-O and Cu-O layers are responsible for the conductivity. According to [10] an electron-type conduction is dominant in Bi-0 layers, while Cu-0 planes are known to have a hole type conduction. Reduction in the valence state of Bi^{3+} to $Bi^{3-\square}$ gives rise to an electronic conduction in Bi-0 planes, while the oxidation of Cu^{2+} to $Cu^{2+\square}$□gives rise to the hole conduction in Cu-0 planes [10].

The concentration of holes per copper atom and the band gap of the semiconductor type Bi-O layers are determined. The hole concentration, p, per each copper atom in HTSC materials can be calculated by using the relation [6],

$$\frac{\mathrm{T}_c}{\mathrm{T}_c^{max}} = 1 - 82{,}6(p - 0.16)^2 \tag{1}$$

According to (1) was calculated the hole concentration per copper atom p=0,1979 for $Bi_2Sr_2Ca_{0.8}Zn_{0.2}Cu_2O_{8+y}$.

The obtained experimental results on the thermal power were analyzed on the framework of the Xin's two band model [2].

Xin *et al.* developed a two-band model to analyze the thermoelectric data, where one zone is formed by Cu-O and the other by Tl-O planes [2]. The Cu-O plane contributes to the metallic conductivity of holes. In Bi-based HTSC case, the conduction electrons in the Bi-O planes have a semiconductor character. According to [10], the thermoelectric power is expressed by

$$S = -g\pi^2 \left[\frac{dln\sigma^+(E)}{dlnE}\right] T + \left[\frac{E_c}{e} + \frac{k}{e}\frac{dln\tau(E)}{dlnE} T\right] e^{-E_a/kT} \tag{2}$$

Taking into account the linear and exponential parts, (2) can be represented by

$$S = \mathrm{AT} + (\mathrm{B}\lambda + \mathrm{CT})\exp(\lambda/T) \tag{3}$$

where A, B and C are constants for a particular material, T is the temperature, $\lambda=E_c/k_B$, $E_c=E_g/2$ is the energy gap between the bottom of the conduction band and the middle of the band gap, k_B is the Boltzmann constant. The calculated values of thermal power according to Xin's two band model are shown in figure 3 by a straight line.

The obtained value of λ was used to calculate the band gap of the semiconductor type Bi-O layers. The parameter λ, which is included in the exponent depends on the band gap between the Bi-O band and the conduction band. By using the relations $\lambda=E_c/k_B$ and $E_c=E_g/2$, the energy gap value was estimated. The values of fitting parameters as well as the calculated values of E_g=0,0595 eV were A=0.0798μV/K^2, B=-0,137μV/K^2, C=-0,056μV/K^2, respectively.

Conclusion

The temperature dependences of the thermoelectric power of $Bi_2Sr_2Ca_{0.8}Zn_{0.2}Cu_2O_{8+y}$ was analyzed within the Xin's two-band model. The hole concentration per copper atom p=0,1979 and the energy gap Eg=0,0595 eV of the semiconductor-like band structure of Bi-O layers are determined. It was shown that, the partial replacement of the calcium element with zinc in $Bi_2Sr_2Ca_{0.8}Zn_{0.2}Cu_2O_{8+y}$ does not change the structure of Bi-O layers, and, therefore, does not lead to a change in the electronic band structure of $Bi_2Sr_2CaCu_2O_{8+y}$.

References

1. Chandra Sekhar M., Suryanarayana S.V., Physica C 2004, v. 415, p. 209. DOI:10.1016/j.physc.2004.08.015
2. Xin Y., Wong K. W., Fan C. X., Sheng Z. Z., and Chan F. T., Phys. Rev. B, 1993, v. 48, p. 557. DOI:https://doi.org/10.1103/PhysRevB.48.557
3. Kazmin S.A., Kaidanov V.I., Leising G. Technical Physics 1988, v. 30, p. 2955.
4. Forro L., Raki M., Henry J. Y., Ayache C., Single Crystal, Solid State Commun. 1989, v. 69, p. 1097. https://doi.org/10.1016/0038-1098(89)90493-6
5. Ragimov S.S., Askerzade I.N. Technical Physics 2010, v. 55, p. 1538. https://doi.org/10.1134/S1063784210100245
6. Ozkurt B., Ekicibil A., Ali Aksan M., Chzelik B., Eyyuphan Yakinci M., Kiymach K. J. of Low Temperature Physics 2007, v. 147, p. 31. DOI: 10.1007/s10909-006-9296-3
7. Ragimov S.S., Askerzade I.N., Agayeva G.I., J. Supercond. Nov. Magn. 2019, v. 32, p. 3033. https://doi.org/10.1007/s10948-019-5010-y
8. Pogorelov Yu.G, Santos M.C., Loktev V.M. J. of Low Temperature Physics 2011, v. 37, p. 803. DOI:10.1063/1.3651472
9. Abbasi H., Taghipour J., Sedghi H., J. Alloys and Compounds 2010, v. 494, p. 305. https://doi.org/10.1016/j.jallcom.2010.01.018
10. Awana V.P.S., Moorthy V.N., Narlikar A.V. Phys. Rev. B 1994, v. 49, p. 6385. DOI:https://doi.org/10.1103/PhysRevB.49.6385

DISPERSION OF THE INCOHERENT NEUTRON WAVES WHEN PASSING THROUGH THE MATTER

SG ABDULVAHABOVA and TO BAYRAMOVA

Baku State University, Baku, Azerbaijan
E-mail: Sacidaabdulvahabova@bsu.edu.az, Tunzalabayramova@bsu.edu.az

On the basis of the density inhomogeneity of the crystal, we have studied the distribution of incoherent neutron wave. Fluctuations in the density of the matter cause scattering neutron wave. The starting point of the calculation was the well-known formulas of the diffraction theory and the theory of multiple scattering. These formulas have been obtained under the assumption that the imaginary part of the optical potential is a local operator. The imaginary part of this potential models inelastic processes and determines the amplification of an incoherent wave in the input channel. The resulting formulas are applied to the calculation of the dispersion properties of the incoherent neutron wave. According to the results, the frequency of the scattered nucleon wave decreases with increasing density fluctuations. The results show, that the effective cross section for scattering from all nuclei of matter is not the additive sum of the effective cross section of the scattering from one nucleus. This is due to the interference of neutron waves.

Keywords: scattering, cross section, dispersion, fluctuation density
PACS: 11.55.Fv, 03.75.Be, 03.75.-b

Introduction

Reflection, refraction, diffraction, and interference are similar for light and for neutrons wave. When neutrons interact with matter, two basic kinds of interaction can be distinguished, which are normally designated as elastic and inelastic. We refer to elastic interactions when the collision leads to essentially zero energy transfer and the neutrons are only deflected in the field of the nuclei. As neutrons possess wave properties, phase relationship exists between incident and scattered beams, and interference may occur between the scattered neutrons. In a crystalline substance atoms are arranged in an orderly manner in space. Neutron waves add up the point of observation in accordance with the laws of interference if the phase difference between the scattered waves is constant (coherent scattering), we can observe the pattern of alternating in the space diffraction minima and maxima. If the order in the arrangement of atoms is broken, scattering will not be coherent.

Incoherent neutron waves

To determine the reflection factor of neutrons in the medium, we must use the wave formulation of the problem. We must therefore determine from the Schrodinger equation for given potential U the Ψ function for the neutrons in the medium.

In the theory of incoherent neutron scattering by crystals, it is shown [1, 2] by analogy with the diffraction of γ-rays that the structural factor F_τ for the unit cell of a crystal is written as the following expression:

$$F_\tau = \sum_l b_l e^{2\pi i(\tau\cdot\rho_l)b_i} e^{-W_l} , \tag{1}$$

where τ is the inverse lattice vector corresponding to the system of reflecting planes ($h\kappa l$); b_l is the amplitude of the nuclear coherent scattering.

An expression for the scattering amplitude from a single crystal plane is

$$N_c d_{hkl} \frac{\lambda}{\sin\theta} F_{hkl} = 2N_c d_{hkl}^2 F_{hkl}, \tag{2}$$

where N_c is the number of unit cells per unit volume and d is the distance between the planes ($h\kappa l$).

The asymptotic solution of the wave equation describing the parallel beam and the S-wave scattered by the center at the origin has the form

$$\Psi = e^{ikz} - b\frac{a}{r}e^{ikr}, \tag{3}$$

where b is the coupling coefficient

$$b = \frac{a_{coupling}}{a_{free}}, \tag{4}$$

and a – scattering length.

The effective cross section of the scattering of thermal neutrons by a free nucleus with zero spin away from the resonances is usually expressed in terms of the scattering amplitude b, corresponding to the radius of the impenetrable sphere R, on which the scattering occurs:

$$\sigma = 4\pi R^2 = 4\pi b^2. \tag{5}$$

If the nucleus has a spin equal to J, then taking into account the two possible mutual orientations of the nucleus spin and the neutron spin complicates the expression for the coherent scattering cross section:

$$\sigma_c = 4\pi\left(\frac{J+1}{2J+1}b_+^2 + \frac{J}{2J+1}b_-^2\right), \tag{6}$$

and incoherent scattering cross section

$$\sigma_{inc} = 4\pi\frac{J(J+1)}{2J+1}(b_+ + b_-)^2, \tag{7}$$

where b_+, and b_- is the scattering amplitude when the total spin I of the neutron and nucleus is equal to $J+1/2$ and $J-1/2$, respectively. The presence of two possible states of the "neutron-nucleus" system makes it necessary to consider the coherence and incoherence of scattered waves in the interaction of a neutron even with an isolated nucleus, if the latter has a non-zero spin. The coefficients for b_+ and b_- in equation (6) have the meaning of weight functions for two possible states of the system. The total scattering cross section σ for a nonzero spin nucleus is equal to the sum of the coherent σ_c and incoherent σ_{inc} *cross* sections.

Now suppose that the plate substance contains of N localized impurity - scatters and these centres scatters spherically symmetric wave with the scattering length a_l

$$a_l = \frac{1}{kctg\delta_l} = \begin{cases} (\delta_l - \pi)/k & \text{for} \quad |\delta_l - \pi| << 1, \\ \delta_l / k & \text{for} \quad |\delta_l| << 1. \end{cases} \tag{8}$$

where δ_l scattering phase.

Refractive indices for neutron is close to unity and difficult to measure its. If the plate has a thickness *T* and refractive index *n* the neutron wave undergoes a phase shift and exits in the form of

$$\psi_k(z>T)=e^{ikz}-2\pi a_l NT\frac{e^{ikz}}{k^2}, \tag{9}$$

here *k* momentum of neutron after scattering.

The movement of neutrons in matter is fully described by frequency for each wave vector. The resultant field of the scattered neutrons is a superposition of waves scattered by nuclei at all times prior to this moment t

$$\Psi(z>T)=a^2\sum_i\frac{1}{T_i^2}+\sum_{i\neq j}\frac{\exp[i(z_i-z_j+n(T_i-T_j))]}{T_iT_j}. \tag{10}$$

The function of thickness

$$T(s)=\int_{-\infty}^{+\infty}\rho(r)dz, \tag{11}$$

and the normalization condition has the form

$$\int T(s)d^2s=A. \tag{12}$$

The amplitude in terms of the transmitted momentum is follows

$$f(\mathbf{q})=\frac{ik}{2\pi}\int\exp(i\mathbf{qb})\sum_{k,k'}\langle\Psi_k|\Gamma(\mathbf{b})|\Psi_{k'}\rangle d\mathbf{b}, \tag{13}$$

$$\Gamma(\mathbf{b})=1-\prod_{j=1}^{A}[1-\gamma_j(\mathbf{b}-\mathbf{s_j})], \tag{14}$$

here **q** is the transfer momentum, k is the value of the wave vector of the nucleon, **b** is the impact-parameter vector, $\Psi(\mathbf{r}_1,\mathbf{r_2},...,\mathbf{r}_A)$ is the ground state wave function of the nuclei, $\Gamma(\mathbf{b})$ is the total nucleon–nuclei interaction profile function, $\gamma_j(\mathbf{b})$ is the profile function for the nucleon-nucleon interaction, brackets $\langle||\rangle$ mean interactions over the nucleon coordinates [1].

For incoherent scattering of the neutrons we obtain [3]:

$$F_c(q)=\frac{ik}{2\pi}\int d^2be^{iqb}\left[1-\exp\left\{-\frac{2\pi}{ik}f(0)T(b)\right\}\right]. \tag{15}$$

Then, for the *z>T* the wave can be expressed as [4]

$$\psi_k(z>T)=e^{ikz}-2\pi a_l NT(n-1)\frac{e^{ikz}}{k^2}. \tag{16}$$

If (1) submit in the form

$$\psi_k\left(z > T\right) \approx e^{ikz}\left[1 + ik(n-1)T\right], \tag{17}$$

we obtain

$$n - 1 = -2\pi TN\frac{1}{k^2}. \tag{18}$$

Optical theorem relates the refractive index of substance with the scattering cross section of individual atoms and nuclei of which consist the material.

If the refractive index contains an imaginary part, it is necessary to divided this index into two parts: real and imaginary:

$$\mathrm{Re}(n-1) = \frac{2\pi N}{k^2}\mathrm{Re}\, f_\kappa(0); \tag{19}$$

$$\mathrm{Im}\, n = \frac{2\pi N}{k^2}\mathrm{Im}\, f_\kappa(0). \tag{20}$$

Consider the effect of the density inhomogeneity $\delta\eta$ of the crystal on the distribution of incoherent neutron wave. Inhomogeneity can be caused by dynamic density fluctuations, and be statistical in nature. Fluctuations in the density of the target material cause scattering neutron wave.

The imaginary part of the amplitude related to inelastic scattering and determines the weakening of the incoherent wave in the entrance channel.

Optical theorem relates the refractive index of substance with the scattering cross section of individual atomics nuclei of the material. According to the optical theorem

$$\mathrm{Im}\, f(0) = -k(\sigma_{abs} + \sigma_{inel})/4\pi, \tag{21}$$

where referring to [5]

$$\sigma_{abs.} = NV\langle(\eta)\rangle, \tag{22}$$

and

$$\sigma_{inel.} = N\sigma_{el}V < \eta >, \tag{23}$$

where σ_{abs} cross section of absorption and σ_{inel} cross section of inelastic scattering.

We now focus attention on the dispersion of the neutron waves. For any waves

$$k_z^2 = k^2 \cos\theta^2 = k^2(1 - \sin^2\theta), \tag{24}$$

where θ is the angle of incidence, and

$$k_{1z}^2 = k^2 n^2 \cos(\theta_1) = k^2\left(n^2 - \sin^2\theta_1\right). \tag{25}$$

From the refraction law we obtain

$$\sin^2\theta_1 = 1/n^2 \sin^2\theta. \tag{26}$$

Comparing equations (25) and (26), we get

$$k_z^2 - k_{1z}^2 = k^2(1-n^2)\ . \tag{27}$$

We have here a direct analogy with light for wavelengths corresponding to x rays and ultraviolet rays, since the same dispersion law is also valid for light. After calculation we get

$$\omega^2 = \omega_0 - 4\pi^2 N^2 \left\langle \left(\frac{\delta\eta}{\eta} \right)^2 \right\rangle, \tag{28}$$

where

$$\omega_p^2 = 4\pi N e^2 m\,, \tag{29}$$

is the so called plasma frequency.

Conclusion

The starting point of the calculation was the well-known formulas of the diffraction theory and the theory of multiple scattering. An optical model has been proposed in order to take into account scattering on in homogeneities of nuclear matter.

The study shows that the frequency of a coherently scattered nucleon wave decreases with increasing density fluctuations. The expression for dispersion allows us to determine the fluctuation in the density of nuclear matter, thereby helping to study the structure of nuclei. In the approximation of a thin target the solution of the equation for the total scattering amplitude is identical to the expression obtained in the usual eikonal approximation and differs significantly, at least functionally, from the solution for the case of a thick target. The results show, that the effective cross section for scattering from all nuclei of matter is not the additive sum of the effective cross section of the scattering from one nucleus. This is due to the interference of neutron waves.

References

1. Sitenko A.G. PEPA 1973, v. 4 (2), p. 546.
2. Gurevich A.I., Lomonosov V.V. JETP 1996, v. 82 (3), p. 493.
3. Abdulvahabova S.G., Masti D. Russian Journal of Physics 2008, v. 11, p.235.
4. Abdulvahabova S.G., Barkhalova N.Sh., Bayramova T.O. Journal of Radiation Research 2015, v. 2, p. 53.
5. Abdulvahabova S.G., Barkhalova N.Sh., Bayramova T.O. Journal of Low Dimensional Systems 2018, v. 2 (2), p. 4.

ELECTRIC QUADRUPOLE TRANSITIONS IN NEUTRON CLUSTER TRANSFER REACTIONS

SG ABDULVAHABOVA[1] and IG AFANDIYEVA[2]

[1]Departement of Matter Structure, Faculty of Physics, Baku State University, Baku, Azerbaijan
[2]Department of Physics, Faculty of Energy, Azerbaijan State University of Oil and Industry, Baku, Azerbaijan
E-mail: sacidaabdulvahabova@bsu.edu.az afandiyeva.irada@asoiu.edu.az

In this article in the frameworks of clusters model, the electric quadrupole transitions in (p,t) reactions are discussed. Reactions were considered in which transitions occur from the ground state of an even target nucleus to the ground state of an even residual nucleus, and the spins of the initial and final states are equal to zero. In this case, the most important residual interaction is the pair interaction. These motions enhance the electric quadruple matrix elements and give the events a unique signature, which can be used for identification. The study shows a strong population in (p,t) reactions of the 0^+ excited states in the rare-earth regions can be associated with the density distribution of single - particle levels and the alignment of the corresponding quadrupole moments in the vicinity of the Fermi surface of these nuclei. So the corresponding transfer matrix element is diagonal in the spin states of the nucleus. In the neutron clusters transfer reactions, the low-lying 0+ levels will be more strongly excited in nuclei in which the single-particle quadrupole transitions near the Fermi surface have the same sign. Violation of E2-additivity occurs for strongly interacting protons and neutron clusters. In the framework of the weak coupling limit it is possible to describe the empirical quadrupole moment for a proton-neutron cluster state.

Keywords: neutron cluster, electric quadrupole transitions, direct nuclear reactions
PACS: 25.45.De, 24.50.+g, 21.60.Gx

Introduction

A cluster model was developed on the basis of the idea that nuclei sometimes behave like molecules consisting of nucleon fragments [1,2]. In the cluster model, the structure of the nucleus is represented as a set of configurations of nucleons and clusters consisting of several particles. The radial wave functions of two neutrons cover each other in the peripheral region of the nucleus. This leads to the a "cross-linking" of the wave functions of nucleons of target *A* nucleus and nucleons of *B* final nucleus.

The cluster model allows us to reduce the expression for the wave function of a multinucleon nucleus to an expression for a single-particle wave function of its component clusters. The binding energy of a cluster is relatively small, and this fact allows us to develop a theory that treats the states of the continuum as accurately as the bound states.

The results of experiments on (t, p) and (p, t) reactions indicate that the captured or stripped off neutrons in the nucleus are correlated as cluster. In these reactions some levels are highly excited. The behaviour of the electric quadruple transition gives us information about the structure of these levels. The information obtainable from (t, p) and (p, t) reactions is different from that obtained from single-nucleon transfer reactions; from the latter only the single particle character of the levels is obtained [3]. The sets of data obtained from the single nucleon transfer reactions have already furnish quantitative information about nuclear structure. But data from two nucleon and one nucleon transfer reactions are mutually complementary.

In this article, in the model of clusters electric quadrupole transitions considering pair correlation in the processes of neutron cluster transfers are discussed.

Matrix element of electric quadruple transitions

The study of quadrupole interactions in nuclei is used for characterizing different nuclear states and to obtain information about structural, electric and magnetic properties. Now we illustrate the use above constructed approach for evaluating matrix elements of E2 transition. When the nucleus is deformed it acquires an electric –multiple moments and emits electric radiation. The matrix element of the E2 transitions has following view: the matrix element of the transition from state *i* to state *f* can be written as follows:

$$W_{i \to f} = \int \Psi_f V \Psi_i d\xi_i d\xi_f \quad . \tag{1}$$

We will choose the potential *V* in the following form:

$$V = V_{av} + V_{pair} + V_Q \, . \tag{2}$$

In (2), V_{av} is the Saxon - Woods potential, describes the average field, V_{pair} is the residual pair and V_Q long-range residual quadrupole-quadrupole interaction.

We will consider even nuclei in which pairing correlation is important. The pairing correlation is increases the electric quadruple matrix elements and can be used for identification of the type of the motions.

Matrix element for E2 transition is:

$$M = \frac{\left\langle \Psi_f \left| \sum_{m=1}^{A} r_j^2 Y_{20}(\theta, \varphi) \right| \Psi_i \right\rangle}{\sqrt{N_i N_j}} , \tag{3}$$

where

$$\Psi_i = \Psi_{00} = \Psi_{00}(\xi) f(\vec{r}_p) \chi_{1/2, m_p} , \tag{4}$$

$$\Psi_f = \Psi_{20} = \left\{ \exp\left[-\frac{1}{2} \sum_{i=1}^{A} \sum_{j=1}^{2} \frac{1}{2} (u_{ij}^2 + v_{ij}^2) - \frac{1}{2} \sum_{l=1}^{A} R_l^2 \right] \right\} F_t(\vec{r}_t) \chi_{1/2, m_t} , \tag{5}$$

N_i and N_j the normalization integrals, Jacobi variables describe the motion of neutron cluster inside the nucleus:

$$u_l = r_{l1} - r_{l2} \, ; \, v_l = r_{l1} + r_{l2} \, , \tag{6}$$

χ - spin function; $\mathbf{r}_{ji}$ is the radius vector of the *j*-th nucleon in the *l*-th nucleon cluster;

$$R_l = \frac{1}{2} \sum_{j=1}^{2} r_{jl} \, , \tag{7}$$

and *x* = *b*/*a* parameter of isolation, $F_t(r_t)$ distorted function of triton.

We will discuss proton-nucleus collisions without wave function overlap. This is consistent with the fact that impact parameters *b* larger than the sum of the nuclear radii, *R*, i.e. *b* > 2*R*. Triton can be produced in these collisions through an interaction of the fields of the proton and neutron cluster. If the transfers momentum are small enough (q<kc/R), the fields of incident proton interacted coherently to all neutrons cluster on the surface of the nucleus. The

restrictions on the momentum transfer do not prevent the production of systems in high-energy collisions.

Scattering may be accompanied by transitions between different states of the *L* and *J*, compatible the conservation the total angular momentum. However, the orbital angular momentum and spin are not good quantum numbers and the partial wave corresponding to a certain *L* and S , may cause scattered wave with $L' \neq L, S' \neq S$. If we take into accounts that the total angular momentum and parity is conserved, the amplitude of the scattered waves is a matrix, the elements of which depend on the following quantum numbers: *J*, *L* and S. For quadrupole transitions $\Delta J = J_f - J_i = 2$.

We will neglect the internal interaction of the nucleons in the clusters and effects of the Pauli principle between the nucleons in the clusters are taken into account by introducing short range repulsion between the clusters.

The wave function of the triton must be chosen so that the whole wave function may be antisymmetric with respect to exchange of two neutrons

$$\chi_{1/2,m_t}(t) = \sum < 1/2 m_p S_1 M_{S_1} \; | 1/2 m_t > \chi_{1/2 m_p}(p) \chi_{S_1 M_{S_1}}(n,n') \delta_{S_1 0}, \tag{8}$$

from which we get

$$\left\langle \chi_{1/2m_p}(p)\chi_{SM_S}(n,n') \,|\, P_1V_1 + P_3V_3 \,|\, \chi_{1/2m_t}(t) \right\rangle = \left\langle 1/2m_p SM_S \; |1/2m_t \right\rangle \sqrt{2S+1}(-)^S \left[\frac{1}{4}V_1 + \frac{3-2S(S+1)}{4}V_3 \right], \tag{9}$$

Thus, we get

$$M = \sum \left\langle JMI_iM_i \,|\, I_fM_f \right\rangle \left\langle SM_SLM_L \,|\, JM \right\rangle (-1)^S \left(\frac{A+2}{A} \right)^{(N-1+L/2)} \sqrt{2S+1}(-)^S \left[\frac{1}{4}V_1 + \frac{3-2S(S+1)}{4}V_3 \right], \tag{10}$$
$$x\sqrt{S(\alpha_f I_f; SLJ; \alpha_i I_i)} \int \varphi^+(k_{p,} r_p) \Psi^*(r) \varphi^+(k_t, r_p) dR dr dr'$$

where

$$S(\alpha_f I_f; SNLJ; \alpha_i I_i) = \sum | C(\alpha_f I_f; SNLJ; \alpha_i I \;) |^2 \tag{11}$$

and spectroscopy amplitude $C(\alpha \, I_i; SNLJ; \alpha_f I_f)$ defined as

$$C(\alpha \, I_i; SNLJ; \alpha_f I_f) = \sum (-1)^l \left(\frac{A+2}{A} \right)^{(N-1+L/2} \left\langle \frac{1}{2} l_n(j_n); J \,|\, \frac{1}{2}\frac{1}{2}(S) l_n l(L); J \right\rangle \left\langle n_n l_n n_{n'} l_{n'}; L \,|\, NLnL \right\rangle \tag{12}$$

where *(n_nl_nj_n)* and *(n_{n'}l_n,j_{n'})* are the quantum numbers of the two transferred neutrons, and *J* is the transferred total angular momentum with *Z* component *M.* The resultant orbital angular momentum *L* is composed of the orbital angular momentum of their center of the gravity *L M_z* and that of their relative motion *lm_l*.

The strong population in (p,t) reactions of the excited states in the in rare-earth regions can be associated with the density distribution of single - particle levels and the alignment of the corresponding quadrupole moments in the vicinity of the Fermi surface of these nuclei [4].

In the framework of the weak coupling limit it is possible to describe the empirical quadrupole moment for a proton-neutron cluster state. For this case quadrupole moment is a linear combination of the respective proton and neutron cluster quadrupole moments. If the experimental quadrupole moment of a triton state does not agree with the theoretically value, this could be due to strong interactions between proton and neutron cluster. In this case, the wave function of the triton cannot be divided into wave's functions of composite particles.

Conclusion

The article was limited by the fact that the internal states of the incident proton and emitted triton and any intermediate state neutron cluster are fully *S*-states. So the corresponding transfer matrix element is diagonal in the spin states of the nucleus.

In the neutron cluster transfer reactions, the low-lying 0+ levels will be more strongly excited in nuclei in which the single-particle quadrupole transitions near the Fermi surface have the same sign [5] and our results also confirm this fact.

The calculated matrix element of the electric quadrupole transition is very sensitive to the cutoff radius of the radius of the initial nucleus due to internal contributions. We cannot get good results without just cutting off the nuclear radius. Some of the parameters used have not yet been established due to the lack of experimental data. But it is known for sure that the reaction is insensitive to the choice of the optical potential of the triton.

The theory of two-nucleon transfer still has some disadvantages compared to the case of the reaction theory of one-nucleon transfer. It can be concluded that reactions (p, t) and (t, p) can be used to use only quantitative information about the structure of the nucleus.

References

1. Oertzen W., Freer M., and Kanada-Enyo Y. Phys. Rep. 2006, v. 432 (2), p. 43.
2. Neudatchin V. G., Struzhko B. G., and Lebedev V. M., Phys. Elem. Partic. 2005, v. 36 (4), p. 889.
3. Abdulvahabova S.G., Barkhalova N.Sh., Bayramova T.O. Journal of Radiation Research 2016, v. 2 (1), p. 106.
4. Kulp W. D. Search for Intrinsic Collective Excitations in 152Sm. arXiv: 0805.1912v1 [nucl-ex] 2008.
5. John L Wood Do we understand excited 0+ states in nuclei? Journal of Physics: Conference Series, 2012, v. 403, p. 012011. DOI:10.1088/1742-6596/403/1/012011

STRUCTURAL ANALYSIS OF VAL-TRP DIPEPTIDE

SG RAHIMZADE and GA AKVERDIEVA

Baku State University, Baku, Azerbaijan
E-mail: sararahimzada@bsu.edu.az gulnaraakverdieva@bsu.edu.az

The present study of Val-Trp dipeptide has been performed using molecular mechanics framework, followed by AM1 and PM3 quantum chemical methods. The calculation results showed that folded and extended conformations are realized for this molecule. The geometry, energy parameters, dipole moment, HOMO and LUMO energies and other electronic parameters were calculated for stable structures of title molecule. The differences in the electronic structure between two characteristic conformations of dipeptide were revealed. The redistribution of charges as a result of folding of the peptide chain leads to a decrease in the dipole moment.

Keywords: molecular mechanics, quantum chemistry methods AM1 and PM3, valine, tryptophan
PACS: 36.20.Ey, 36.20.Fz, 36.20.Hb

Val-Trp dipeptide is frequently prescribed for a range of diseases including hypertension, proteinuric chronic kidney disease, and heart failure [1,2]. Despite the interest in the biological role of Val-Trp dipeptide, there is no the investigations of its conformational and electronic properties so far, which can appear an important basis for the study of the structure-functional interactions.

The aim of this work is to reveal the structural particularities of Val-Trp dipeptide by molecular mechanics and quantum chemical methods. The conformational profiles of Val-Trp dipeptide were investigated within molecular mechanics framework using version of ECEPP (Empirical Conformational Energy Program for Peptides) [3,4]. The molecule was calculated in zwitterionic form in relation to water environment. The quantum chemical calculations of this molecule were conducted by AM1 and PM3 methods, parameterized for calculating the electronic structures of biopolymers using the demonstration version of software package HyperChem 8.03 [5] (www.hyper.com).

The calculation results showed that conformations of two shapes of backbone, folded and extended, are realized for this molecule, and the stability of dipeptide is found to be very sensitive to the positions of the side chains of the aminoacid residues. The optimal conformations of folded ($E_{rel.}$=0.0 kcal/mol) and extended ($E_{rel.}$=1.79 kcal/mol) backbone shapes are illustrated in Figure 1. The geometry parameters and stabilizing interaction energies in the mentioned preferable conformations of the molecule have been determined. The dihedral angles of these structures are given in Table 1. It was established that the distances between protonated nitrogen atom and neighboring oxygen atom of the C-terminal carboxyl group are 4.56 Å and 6.15 Å, the distances from CG1 atom of side chain of Val to CZ2 atom of Trp side chain are 3.90 Å and 7.17Å, the distances from CG1 atom of side chain of Val to atom NE1 of Trp side chain are 4.19 Å and 7.14 Å, the distances from atom CG2 of side chain of Val to CZ2 atom side chain of Trp are 5.41 Å and 7.38 Å, the distances from atom CG2 of side chain of Val to NE1 atom of side chain of Trp are 6.37 Å and 7.47 Å in the optimal folded and extended structures, respectively.

The above data demonstrates that the mentioned distances in the optimal folded structure are shorter than those in the optimal extended structure and, thus, favours efficient interactions. This molecule is stabilized also by formation of the hydrogen bonds. It was found that the folded conformation is stabilized by formation of two hydrogen bonds with length 2.8 Å (E = -0.16 kcal/mol) between the hydrogen related by the peptide bond with the nitrogen atom of the main chain of Trp residue and two oxygen atoms of the C-terminal carboxyl group, and the extended conformation is stabilized by formation of two hydrogen bonds with length 2.9 Å and 2.3 Å (E = -0.11 and E= -0.66 kcal/mol) between the terminal amine cation and the oxygen related by the peptide bond with the carbon of the main chain of Val residue.

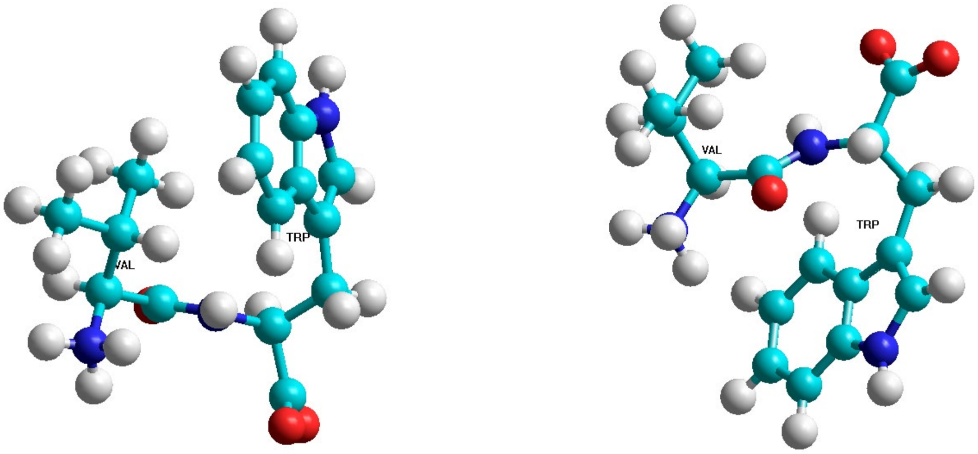

(a) **(b)**

Fig. 1. The optimal folded (a) and extended (b) structures of Val-Trp

Table 1. The geometrical parameters (in degrees) for optimal folded and extended structures of Val-Trp dipeptide

Conformation	**Angles**	
	Val	**Trp**
Folded	φ= -42.3, ψ= -64.9 ω= 178.8, χ_1=177.5 χ_2= 61.6, χ_3= -61.4	φ= -99.6, ψ= 133.9 χ_1= -56.4, χ_2= -89.8
Extended	φ= -74.9, ψ= 148.8 ω= 180.0, χ_1= 65.2 χ_2= 176.3, χ_3= 179.2	φ= -138.1, ψ= 161.7 χ_1= -56.4, χ_2= -102.3

Since each particular conformation is characterized by its own electronic distribution, it was interested to study the electronic structures of the optimal conformations of two shapes of backbone and, thus, to try to reveal qualitative and quantitative estimates of their differences. The calculated by AM1 and PM3 electronic parameters of title molecule are listed in Table 2. The calculations were performed in the valence electron approximation in single point.

As seen from Table 2, the isolated atomic energy are not different for both structures. The total, binding energies and heat of formation of the mentioned conformations are different for investigated structures only on 1.551 kcal/mol by AM1 method and on 0.761 kcal/mol by PM3. However, for the folded and extended structures the electronic energy differ appreciably, on 1322.400 and 1295.270 kcal/mol by AM1 and PM3 methods, respectively, but the core-core interaction energy on 1320.849 and 1295.504 kcal/mol by AM1 and PM3

Table 2. The electronic parameters of the optimal folded and extended structures of Val-Trp

Electronic parameters	AM1		PM3	
	Folded structure	**Extended structure**	**Folded structure**	**Extended structure**
Total energy, kcal/mol	-90291.997	-90293.548	-82640.172	-82640.933
Binding energy, kcal/mol	-4322.987	-4324.538	-4346.209	-4346.970
Isolated atomic energy, kcal/mol	-85969.010	-85969.010	-78293.963	-78293.963
Electronic energy, kcal/mol	-676957.875	-678280.275	-664413.516	-665708.781
Core-Core interaction energy, kcal/mol	586665.878	587986.728	581773.344	583067.848
Heat of formation, kcal/mol	23.072	21.521	-0.150	-0.911
Dipole moment, debyes (D)	20.025	23.478	20.315	23.872
HOMO (eV)	-7.393	-7.427	-7.359	-7.305
LUMO (eV)	-1.351	-1.223	-1.902	-1.723
Energy gap (eV)	6.042	6.204	5.457	5.582

methods, respectively. As seen from represented results of AM1 and PM3 methods both structures of dipeptide has large energy gap (ΔE), that indicate this dipeptide is a hard molecule. The dipole moment of the folded structure is lower than that of the extended structure on 3.453 and 3.557 D owing to the approach of the charged terminal groups of the molecule, calculated by AM1 and PM3 methods, respectively. The conformational differences cause also the electron redistribution, and consequently, affect the electron population, the orbital energies and, as result, the effective charges on the atoms. These parameters proved to differ noticeably for the two structures. The calculated by AM1 and PM3 methods atomic charges in the optimal folded and extended structures of Val-Trp dipeptide are represented in Table 3. It was revealed that changes are in the charges of the atoms of both main and side chains for considered structures.

As seen from the calculation results by AM1 method, for both structures three H atoms of α-amino group, C atom of carbonyl group of Val, H atom of amid group of Trp residue, C atom of the C-terminal carboxyl group, HD1 and HE1 atoms of indole ring of Trp have a large positive charge, but O atom of the carbonyl group of the main chain and CG2 atom of the side chain of Val residue, N atom of amide group of backbone of Trp residue, NE1,CG, CZ2 and CZ3 atoms of the indole ring of Trp residue, two O atoms of the C-terminal carboxyl group of this molecule have a large negative charge. As seen from the calculation results by PM3 method, for both structures N atoms of α-amino group, HA atom of Val, C atom of carbonyl group of Val residue, N atom of amid group of backbone of Trp residue, C atom of the C-terminal carboxyl group, HD1, NE1 atoms of the indole ring of Trp have a large positive charge, but CA atom of Val, O atom of backbone carbonyl group of Val residue, CG1 and CG2 of the side chain of Val residue, CA atom of backbone of Trp residue, CG, CD1, CD2, CE2, CZ2 and CZ3 atoms of the indole ring of Trp residues, two O atoms of the C-terminal carboxyl group of this molecule

Table 3. The atomic charges in the optimal folded and extended structures of Val-Trp dipeptide

Name of atom	**AM1 method**		**PM3 method**	
	Folded structure	**Extended structure**	**Folded structure**	**Extended structure**
N (NH$_3^+$)	-0.029763	-0.022671	0.845589	0.850231
1H (NH$_3^+$)	0.269157	0.258049	0.039333	0.025447
2H (NH$_3^+$)	0.250201	0.264195	0.022385	0.041562
3H (NH$_3^+$)	0.236971	0.234882	0.007660	0.001419
CA Val	-0.144631	-0.142443	-0.334165	-0.329204
HA Val	0.160404	0.145731	0.140521	0.126384
C Val	0.262219	0.277535	0.158636	0.166587
O Val	-0.323877	-0.398871	-0.361529	-0.450869
CB Val	-0.136105	-0.130591	-0.108323	-0.086197
HB Val	0.117456	0.085730	0.098442	0.061641
CG1 Val	-0.204882	-0.227691	-0.123852	-0.145050
1HG1 Val	0.107551	0.108831	0.072977	0.075831
2HG1 Val	0.118034	0.045001	0.083459	0.016729
3HG1 Val	0.082793	0.131380	0.054757	0.104728
CG2 Val	-0.225710	-0.217873	-0.127164	-0.134952
1HG2 Val	0.117089	0.104193	0.082094	0.069621
2HG2 Val	0.089203	0.139686	0.058931	0.103301
3HG2 Val	0.044208	0.084355	0.013907	0.054094
N Trp	-0.304708	-0.280719	0.132287	0.184772
H Trp	0.213869	0.248282	0.069364	0.102647
CA Trp	-0.057683	-0.062426	-0.171284	-0.184798
HA Trp	0.126068	0.123179	0.110864	0.108217
C (COO$^-$)	0.322014	0.328194	0.407883	0.414636
O (COO$^-$)	-0.513190	-0.566354	-0.557256	-0.620574
OXT (COO$^-$)	-0.577657	-0.518485	-0.635498	-0.563399
CB Trp	-0.096941	-0.096486	-0.022875	-0.021953
1HB Trp	0.111093	0.106511	0.080997	0.074160
2HB Trp	0.114588	0.118795	0.082609	0.088815
CG Trp	-0.131388	-0.117089	-0.127514	-0.110401
CD1 Trp	-0.086605	-0.079793	-0.238168	-0.228692
HD1 Trp	0.183826	0.186361	0.156597	0.158127
CD2 Trp	-0.113282	-0.111683	-0.127309	-0.126591
NE1 Trp	-0.217317	-0.214473	0.308993	0.313483
HE1 Trp	0.247304	0.247582	0.070352	0.070231
CE2 Trp	0.039477	0.038030	-0.142262	-0.143769
CE3 Trp	-0.090442	-0.086085	-0.053795	-0.056683
HE3 Trp	0.131142	0.143209	0.108275	0.116371
CZ2 Trp	-0.174383	-0.181616	-0.137755	-0.142810
HZ2 Trp	0.136274	0.137427	0.113131	0.114505
CZ3 Trp	-0.190934	-0.224104	-0.169288	-0.202133
HZ3 Trp	0.117350	0.117970	0.095906	0.098000
CH2 Trp	-0.103785	-0.119345	-0.075936	-0.091581
HH2 Trp	0.124990	0.123690	0.098025	0.098117

have a large negative charge. The identified sites can be donors or acceptors for possible interactions with active residues of specific receptor. Despite insignificant differences in the values of partial charges calculated by two methods, the results obtained by both AM1 and PM3 methods point out that the noticeable differences between the folded and extended favorable structures are in the charges of HA atom and O atom of carbonyl gr oup of backbone of Val residue, of HB, CG1, 2HG1, 3HG1, CG2, 1HG2, 2HG2, 3HG2 atoms of the aliphatic side chain of Val residue, in the charges of N and H atoms of amide qroup of backbone of Trp residue, of CZ3 and CH2 atoms of the indole ring of Trp residue. Thus, the redistribution of charges as a result of folding of the peptide chain is observed both for the atoms of the backbone and side chains of valine and tryptophan residues, that leads to the slight displacement of the positive charge and decrease of the dipole moment of the molecule.

Thus, the calculations identified the different features of the electronic structure of two characteristic favorable conformations of Val-Trp dipeptide. It can be concluded that the both used quantum chemical methods are sensitive to the changes in the charge distribution on atoms and as result to the changes in the dipole moments, depending on the conformational rearrangements of the peptide chain of this molecule.

References

1. Rudolph S, Lunow D, Kaiser S, Henle T. Food Chem. 2017, v. 224, p. 19. doi: 10.1016/j.foodchem.2016.12.039.
2. Lunow D, Kaiser S, Rückriemen J, Pohl C, Henle T. Food Chem. 2015, v. 166, p. 596. doi: 10.1016/j.foodchem.2014.06.059.
3. Godjayev N.M., Maksumov I.S., Ismailova L.I. Russian J of Struc. Chem. 1983, v. 24, p. 147 (In Russ.)
4. Akverdieva G.A., Godjayev N.M. J. Modern Technology & Engineering 2017, v. 2, p. 140. http://jomardpublishing.com/UploadFiles/Files/journals/JTME/V2N2/HakverdiyevaG.pdf
5. Allinger N.L.,Yuh Y., QCPE 395, Quantum chemistry program exchange, Indiana Univ., Indiana, 1982.

ON TUNNELING IN MULTILAYER STRUCTURES

ShH ZEYNALOVA

Azerbaijan Nathional Aviation Academy, Baku, Azerbaijan
E-mail: shehla_372@mail.ru

The questions of the analysis of the tunneling phenomenon in semiconductor multilayer structures are considered, schemes of electron tunneling through the energy barrier and the current-voltage characteristics of the resonant tunneling diode are presented. Based on the analysis of existing techniques for studying the tunneling effect, the expediency of using a two-barrier quantum structure for the development of multilayer photo electronic devices with improved optical properties is shown.

Keywords: tunneling, semiconductor, multilayer structures, nanostructure, quantum-dimensional layers, resonant tunnelling
PACS: 03.65.Xp, 68.65.Ac, 42.55.Px

Introduction

Tunneling is one of the many effects or phenomena occurring in semiconductor multilayer structures. Quantum particles, including electrons, are able to penetrate the energy barrier, even in cases where their energy is below this barrier, which is their unique property, which is widely used in the creation of various semiconductor devices with a multilayer structure, and the process of such a transfer of particles is called exactly tunneling.

A feature of this effect is the transfer of charge from one layer to another through the p-n junction or dielectric layer, with the appearance of a sufficiently large current, and the maintenance of this process during the time of exposure to the applied voltage (usually reverse), depending on the size (area and thickness) of the junction and each the adjacent layer, as well as other factors affecting the duration of the phenomenon.

Statement of the problem

In classical electronics, it is accepted that a particle with an energy E less than the potential energy U of the barrier is reflected from this barrier. However, with a sufficiently thin layer of a semiconductor or dielectric placed between the layers of the heterostructure, due to result of wave processes, a particle passes through this barrier, spending a certain amount of energy. The charge transfer scheme is shown in Fig. 1a, and in Fig. 1b, the wave character of the process of the transition of an electron through the barrier is shown.

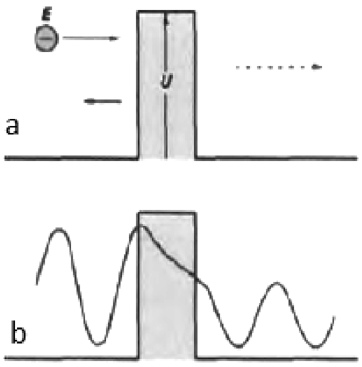

Fig. 1. Tunneling of an electron with energy E through a potential barrier of height U, U> E

Thus, the particle loses part of its energy, which depends on the geometric dimensions of the barrier, the difference between the energy of the falling down electron and the height of the barrier.

Moreover, the further application of this phenomenon in the development of new semiconductor devices is associated with a comprehensive study of tunneling using simulation.

Solution of the problem

Currently, there are a number of models describing tunneling [1-3]. In [2], photo-stimulated tunneling through a three-barrier asymmetric structure with a hyperfine dielectric is considered. On the basis of a simple model, the boundary conditions on the envelope wave functions are obtained in the case of contact of materials with significantly different nature of the electronic spectrum.

The study of electron tunneling through thin potential barriers and the analysis of the interaction of these electrons with the energy levels of size quantization in potential wells separating the barriers, which ensures the speed of MIS devices, are discussed in [3]. In order to provide clarity, estimation of the electron wavelength for metal and semiconductor executed. The passage of an electron over a symmetrical quantum well is shown in Fig. 2 and the form of quantum well a uniform electric field is shown in Fig. 3.

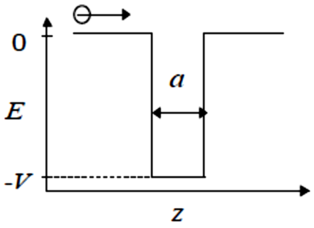

Fig. 2. Passage of an electron over a quantum well

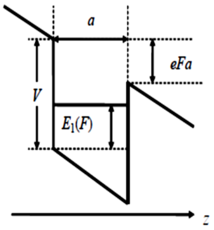

Fig. 3. The form of symmetrical quantum well in a uniform electric field.

A polycrystalline structure with a high silicon content, determines also the contribution of barrier conductivity (tunneling) to the total conductivity and possible negative TCR values, as is shown in Fig. 4 [5].

At high-temperature annealing in an oxidizing atmosphere, oxygen penetrates through the gold layer to nickel, which leads to the formation of nickel oxide. Such an oxide layer will exhibit dielectric properties, which prevents the formation of an ohmic contact based on a single nickel layer. When a gold film is added, gold atoms also penetrate into the oxide layer and are distributed in it, which makes it possible to ensure sufficient conductivity of the composition due to the tunneling effects [6].

In Fig. 5 are presented the operating scheme and current-voltage characteristic of the resonant tunnel diode, where: a - the potential difference is equal to zero; b - resonant voltage on the device; c - current-voltage characteristic [1].

The resonance level in a quantum well of the given heterostructure is shown in Fig. 6 and in Fig. 7 is shown the current flow diagram in a symmetric resonant tunneling diode with such structure, under the voltage [4].

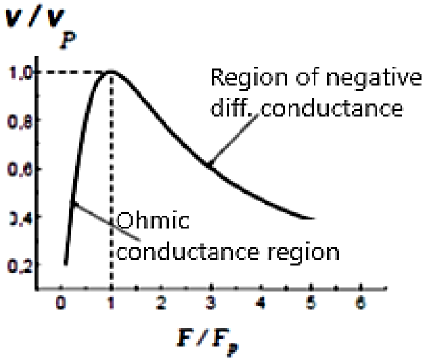

Fig. 4. Dependence of the drift speed on the electric field strength during vertical transfer

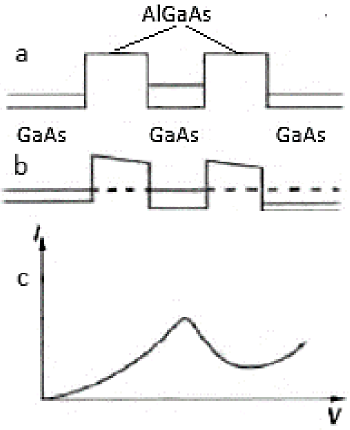

Fig 5. The operating scheme and current-voltage characteristic

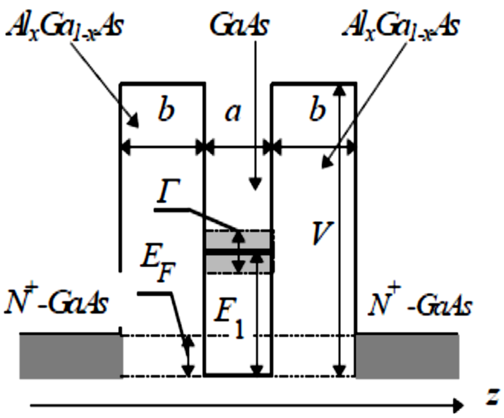

Fig. 6. Diagram of a resonant tunneling diode based on a GaAs/Al$_x$Ga$_{1-x}$As heterostructure with one resonance level in a quantum well

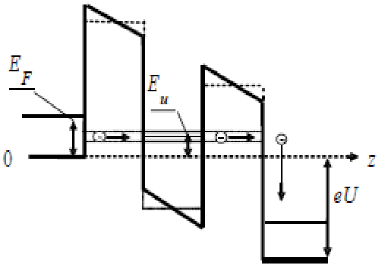

Fig. 7. The current flow diagram in a symmetric resonant tunneling diode

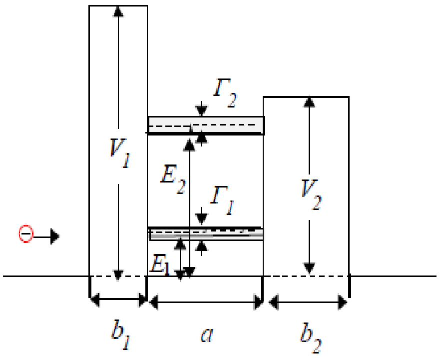

Fig. 8. Potential relief of an asymmetrical double barrier quantum structure with two resonant energy levels E_1 and E_2 in a quantum well

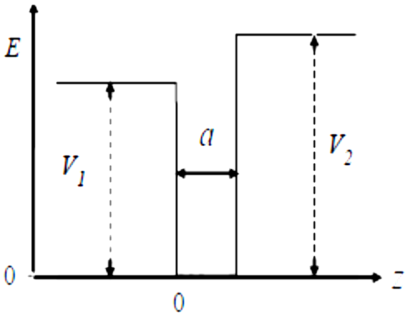

Fig. 9. Profile of asymmetrical quantum well

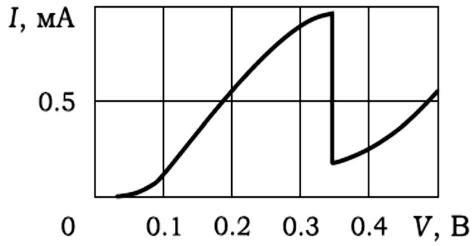

Fig. 10. Resonant tunneling diode based on a double-barrier quantum structure

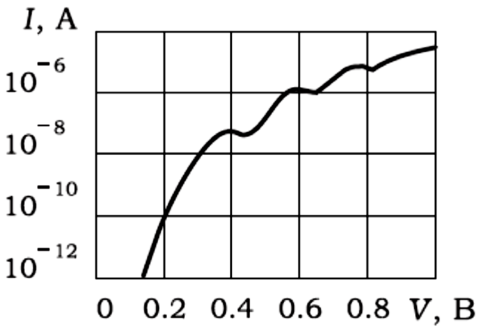

Fig. 11. Resonant tunneling diode based on a double-barrier quantum structure with parabolic quantum well

Potential relief of an asymmetrical double barrier quantum structure with two resonant energy levels E_1 and E_2 in a quantum well is shown in Fig. 8, and profile for the such structure in Fig. 9. The resonator is a device in the form of a transparent plate with semitransparent edges, which can work as an optical filter, passing electromagnetic waves through itself only with certain frequencies [4].

A double barrier with a quantum well is the main structural element of modern resonant tunneling semiconductor devices. For efficient tunneling through each of the barriers, the thicknesses of the potential barriers and the quantum well are small enough, and the quantized discrete energy levels in the well promote the movement of an electron across the well [7]. In this case, on the current-voltage characteristic there are sections with negative differential conductivity (Fig. 10), The voltage value between adjacent current bursts on the characteristic is equal to a constant value, which is determined by the distance between the energy levels in the quantum well (Fig. 11).

Thus, a double-barrier quantum structure can be considered as a unit cell of a wide class of more complex multilayer hetero-structures. The electrical, optical, and other physical properties of such structures are determined by the quantization of the energy spectrum of electrons and their tunneling between neighboring cells [8]. The analysis results also make it possible to form quantum structures with fundamentally new characteristics and with different parameters of semiconductor layers. This is facilitated by the constructive simplicity of the double-barrier quantum structure, which contains a minimum number of ultrathin epitaxial layers, which provides the quasi-ballistic flight of electrons, the coherence of electron waves, and the efficiency of resonant tunneling.

Conclusions

Thus, the operation of modern high-speed devices is based on the effect of electron tunneling across quantum-dimensional layers, with a sufficiently small thickness, when the quantum-mechanical (wave) properties of an electron are manifested.

If, in the early works, the features of the formation of a space charge in the inversion layer near the semiconductor surface were considered, then in the works considered, tunneling in nanometer-scale systems in resonant and near-resonance levels, where the quantum-mechanical nature of quasiparticles is manifested, was studied. In this case, to describe the effect of carrier tunneling transfer matrix method used.

Therefore, one of the important directions in the study of multilayer, especially nanostructures, is the simulation of this process under various conditions, taking into account the thickness of the layers, both from a semiconductor and a dielectric.

References

1. Kovtun G.P., Verevkin A.A. Nanomaterials: Technologies and Materials Science: A Review. - Kharkov: NSC KIPT, 2010, 73 p.
2. Vdovin EE, Khanin Yu.N. JETP Letters 2018, v. 108 (9), p. 674.
3. Chugrov I.A., Demidov E.S., Ershov A.V. Bulletin of the Nizhny Novgorod University. N.I. Lobachevsky, 2011, v. 3 (1), p. 44.
4. Borisenko S.I. Physics of semiconductor nanostructures: textbook / S.I. Borisenko. - Tomsk: Publishing house of the Tomsk Polytechnic University, 2010, 115 p.
5. Gurin S.A. Research and development of thin-film heterogeneous structures of sensitive elements of pressure sensors with extreme operating conditions. Diss.c.t.s. Penza, 2016, 157 p.
6. Tarasov S.A. Physical and technological foundations for the creation of light-emitting and photodetecting solid-state devices with specified spectral and energy characteristics. Diss. Doctor of Technical Sciences St. Petersburg, 2016, 326 p.
7. Usanov D.A., Skripal A.V. Physical foundations of nanoelectronics. Study guide for students of the Faculty of Nano- and Biomedical Technologies. Saratov, 2013, 128 p.
8. Vorobiev L.E., Ivchenko E.L., Firsov D.A., Shalygin V.A. Optical properties of nanostructures: Textbook. Posobie, Ed. E.L. Ivchenko and L.E. Vorobyov. SPb.: Naukv, 2001, 188 p.

OBSERVATIONAL CONSTRAIN ON PRIMORDIAL BLACKHOLES

SOHRAB RAHVAR

Department of Physics, Sharif University of Technology, P.O.Box 11365-9161, Tehran, Iran
E-mail: rahvar@sharif.edu

In this paper I review the formation of Primordial Black Hole (PBH) formation and observational consequences of the PBHs from the point of view of gravitational wave data and their interaction with the earth. We show that heavy black holes (more than 80 solar mass) can be considered as the source of gravitational waves. On the other hand we are obtained the likelihood of collision of small mass black holes (in the order of the lunar mass) with the earth and considered the consequences of this collision. We show that even assuming that hundred percent of dark matter is made of PBHs, the rate at the consequence of this collision with the earth is negligible.

Keywords: black hole, gravitational wave, dark matter, collision, Earth
PACS: 95.35.+d, 04.70.-s, 04.80.Nn

Introduction

Recent observations of gravitational wave data indicates that gravitational wave is sourced by the merging of the binary black hole systems where their masses are somehow in the astrophysical ranges and for a few of them their masses are much larger than what we expect from the astrophysical predictions for the mass of blackholes [1]. A possible candidate for the existence of heavy blackholes with the masses in the range of 60-100 solar mass is the Primordial Black Holes (PBHs) which have been formed in very early universe. Figure (1) represent the mass of progenitor of blackholes in the gravitational wave data and GW170729 is a candidate with 80 solar mass blackholes for the progenitors. This event cannot be interpreted with the formation of astrophysical blackholes. We aim to interpret it as a PBH candidate [2].

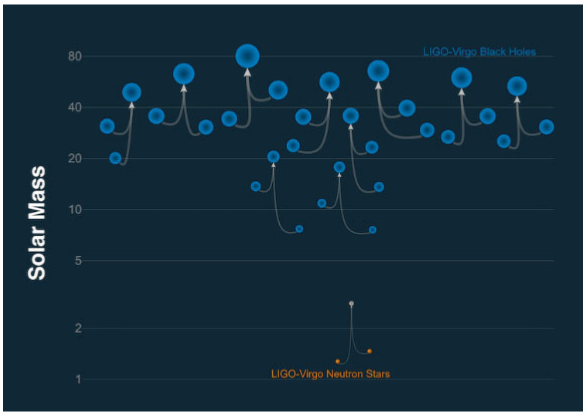

Fig. 1. The mass of Massive of binary blackholes from analysis of the gravitational wave events as a result of merging of massive blackholes.

Results and discussion

Let us assume all the dark matter of universe is made of PBHs with a Dirac-Delta mass function in the order of 80 solar mass. For a halo with the mass of M filled with the blackholes with the mass of m_{pbh}, we can define an impact parameter for blackhole collisions where the energy of gravitational wave change the sign of the total kinetic energy of the blackholes (i.e $E_1 + E_2 < 0$). In this case we will have a bound binary system. The rate of this collision for a halo with the mass of M is given by [3]

$$R(M) = \frac{1}{2}\int \left(\frac{\rho}{m_{pbh}}\right)^2 < \sigma v > dV \tag{1}$$

where $\sigma = \pi \left(\frac{85\pi}{3}\right)^2 R_S^2 \left(\frac{v}{c}\right)^{\frac{18}{7}}$ is the cross section of effective scattering of blackholes and v is the relative velocities of the interacting blackholes. We integrate the rate of binary blackhole formation over all the dark halos. Assuming Press -Schechter mass function for the halos, we obtain the rate in a comoving frame [4], then along our past light-cone we obtain the rate in terms of redshift per solid angle as shown in Figure (2). Here we assume that $100\ \%$ of dark matter is made of PBHs. Since the PBHs along the cosmological line of sight can magnify the signal of the gravitational wave we also take into account the gravitational lensing due to the compact object [5]. This effect will have a small effect in enhancing the signal of gravitational waves as the wavelength of the gravitational waves and the Schwarzschild radius of the lenses are in the same order and result would be scattering the gravitational wave encountering with the lenses.

We simulate gravitational wave source and measure the strain of the wave at the position of earth. The LIGO detectors measures the noisy signals of GWs, hence we add the background noise of detectors to the simulated signals and follow the standard method of detection of the gravitational waves. We define the detection efficiency of gravitational wave detection by dividing the ratio of the detected events to the overall simulated events within a given redshift bin (i.e. $\epsilon(z) = N_{obs}(z, z+\delta z)/N_{sim}(z, z+\delta z)$). The result of detection efficiency is plotted in Figure (2) with solid lines.

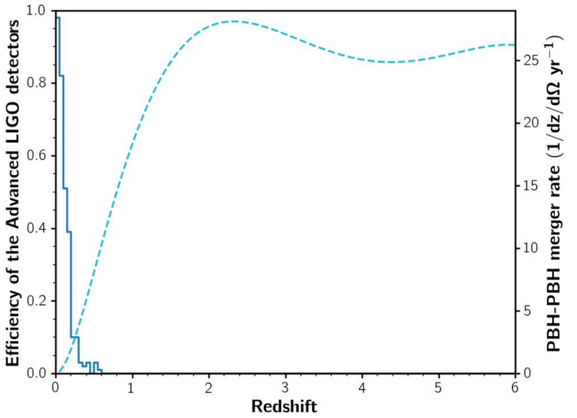

Fig. 2. The rate of binary blackhole formation as a function of redshift shown in dashed curve.

Multiplying the detection efficiency to the theoretical distribution of events in terms of redshift provide us the expected number of GW events in terms of the redshift where integrating over the redshift results in the total number of events that we expect to detect per year.

The comparison of the observed GW events (seven events from 117 days observation by O2) [6,7] with the expected number of events assuming 100% of dark matter is made of PBHs (0.5 event for 117 days) reveals that $N_{obs} \gg N_{expected}$. However, 0.5 event is comparable with one observed massive blackhole. We can conclude that dark matter can be made of heavy PBHs if the rest of GW events are generated by the astrophysical blackhole. Hence the observation of GW event doesn't rule out that massive PBHs (i.e. $\sim 100\ M_{\odot}$) composed all the dark matter of the Universe.

The other possibility that is not excluded by the other observations is very low mass PBHs, in the order of lunar mass that is composed the halo of large scale structures. In this case we can assume that Milky way halo and the dark disk is made of these small mass blackholes. In this case as earth is orbiting around the center of Milky Way, the primordial blackholes can collide with the earth [9]. Let us assume a blackhole with the relative velocity of v is approaching toward the earth. Under the gravity of earth the path of blackhole can bend and collide with the earth. Using the conservation of energy and angular momentum the impact parameter obtain as $b = R_e \left(1 + \frac{2GM_e}{Re\, v^2}\right)^{1/2}$. So the cross section for the collision would be $\sigma = \pi b^2$. Since the Galactic halo is isothermal and have maxwell distribution for the particles of the dark halo as well as the dark disk, we can calculate the rate of collision taking into account the distribution of the velocities of the PBHs. The overall results would be $\frac{dN}{dt} = 10^{-8} f \left(\frac{M_{pbh}}{10^{23}\, gr}\right)^{-1}\ Gyr^{-1}$.

Since the blackhole evaporate by the Hawking radiation, all the blackholes with the initial mass of $10^{14} gr$ is already evaporated. Here we adapt a narrow window for the mass of PBHs in the order of $10^{15} gr$ which is not ruled out by the other observations. Then assuming 100% of halo is made of smaller black holes, we expect to have almost 4 collision of blackholes during the lifetime of the earth. One of the important issue on the collision of a PBH with earth is that either it can be trapped inside the earth or just collide and cross the interior of the earth. In order to answer this question, we take the two time scales of the transit time of the blackholes through the earth and the dissipative time scale. The transit time scale is given by $t_T = \frac{R_e}{v}$ and the dissipative time scale is given by $t_D = \frac{v}{\frac{dv}{dt}}$. Our calculation indicates both for the dynamical friction and accretion of matter on the blackhole t_D is much larger than the transit time scale which guarantees that no PBH traps inside the earth.

Conclusion

Concluding this study, the analysis of the GW leave a room for the PBHs as the candidate for the heavy blackholes as the source of gravitational waves. Further data of gravitational waves can put more constrain on this hypothesis. On the other hand, the small mass PBHs as the candidate for the dark matter is very difficult to be detected and earth could be a natural detectors for this range mass of PBHs. We show that the collision of the PBHs with earth, considering hundred percent of dark matter made of PBHs results in 4 collision during the lifetime of the earth and fortunately PBHs doesn’t trap inside the earth. Identifying the trace of the PBH collision with the earth is very difficult and should be distinguished with the other geological features. So the low mass PBHs cannot be ruled out just by the collisions with the earth.

Reference

1. Abbott B. et al. (LIGO Scientific, Virgo), Phys. Rev. X 2019, v. 9, p. 031040.
2. Khalouei E., Ghodsi H., Rahvar S and Abedi J. Phys. Rev. D 2021, v. 103, p. 084001
3. Bird S., et al. Phys. Rev. Lett. 2016, v. 116, p. 201301.
4. Press W. H. and Schechter P. Astrophys. J. 1974, v. 187, p. 425.
5. Naderi T., Mehrabi A. and Rahvar S., Phys. Rev. D 2018, v. 97, p. 103507.
6. Abbott B. et al. (LIGO Scientific, Virgo), Phys. Rev. X 2016, v. 6, p. 041015.
7. Abbott B. et al. Physical Review Letters 2017, v. 119, p. 161101.
8. Rahvar S. Monthly Notices of the Royal Astronomical Society 20121, v. 507 (1), p. 914.

HIGH ANGULAR RESOLUTION AND TIME DELAY OF UNIQUE DOUBLE GRAVITATIONALLY LENSED QUASARS SDSS J1721+8842 FROM MAIDANAK OBSERVATORY

IM ASFANDIYAROV[1], ShA EHGAMBERDIEV[1,2]

[1]Ulugh Beg Astronomical Institute of the Uzbekistan Academy of Sciences, Astronomicheskaya 33, 100052 Tashkent, Uzbekistan
[2]Department of Astronomy and Astrophysics, Physics Faculty, National University of Uzbekistan, 4 University str., Tashkent 100174, Uzbekistan
E-mail: ildar@astrin.uz

In this paper we presents the results of the detection of active variability and optical oscillations of the intrinsic light curves and of gravitationally lensed quasars SDSS J1721+8842, for the period 2018-2020 based on observations from the Maidanak observatory.

Keywords: detection, active variability, optical oscillations, light curves, quasars
PACS: 95.10.-a, 95.45.+I, 95.90.+v

We presents the results of the detection of active variability and optical oscillations of the intrinsic light curves and of gravitationally lensed quasars SDSS J1721+8842, for the period 2018-2020 based on observations from the Maidanak observatory (Fig.1). Based on the best observations from the AZT-22 telescope with a quality of seeing=0.6-0.7”, followed by digital processing of MCS deconvolution [1], high angular resolution images with a value of FWHM=0.26” of individual lensed point components, their light curves and lensing elliptical galaxy were obtained [2]. Precision astrometry of individual lensed components was obtained, which made it possible to estimate the measurement accuracy of ±0.015”. The intrinsic active optical variability of the components of lensed quasars that characterize nonstationary processes and oscillations resulting from variable energy release in active nuclei and accretion disks around super massive black holes is determined. The sequence of variables of the lensed components A-C-B-D of SDSS J1721+8842 with a time delay is determined: AC=-8.5±1.7 days, AB=-10.3±1.7 days, and AD=-18.7±2.8 days.

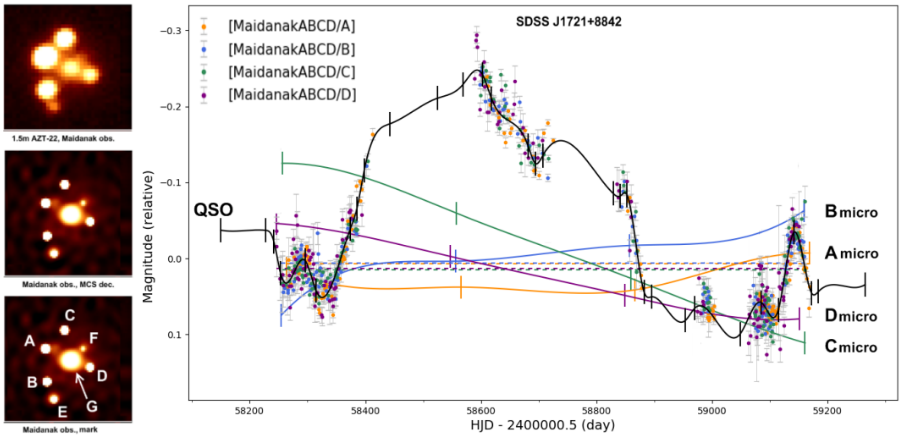

Fig. 1. Results of MCS deconvolution of SDSS J1721+8842 from Maidanak observatory and intrinsic light curve(QSO) of lensed quasars and extrinsic microlensing(A-C micro) for the 2018-2020y.

At present studies of gravitationally-lensed quasars (GLQs) with the detection of active optical variability are of increasing astrophysical interest due to the increasing accuracy of measurements of the Hubble constant, H0. Successive increases in the accuracy of H0 measurements by various methods have revealed a 4.0 σ 6.1 σ difference (Fig. 2) within the standard Λ-CDM model of the Universe between H0 measurements for the early Universe from the Plank space mission based on cosmic microwave background radiation (CMB) fluctuations, and a number of H0 measurements for the late Universe by local methods of stars like cepheids, supernovas, gravitational lensing GLQ, etc. [3]. Thus, further studies may serve both to reveal unaccounted or new physical phenomena and their possible systematic influence in one or both directions of H0 measurements for the early and late Universe, and to revise the whole standard Λ-CDM model and, possibly, to discover new physics of cosmology.

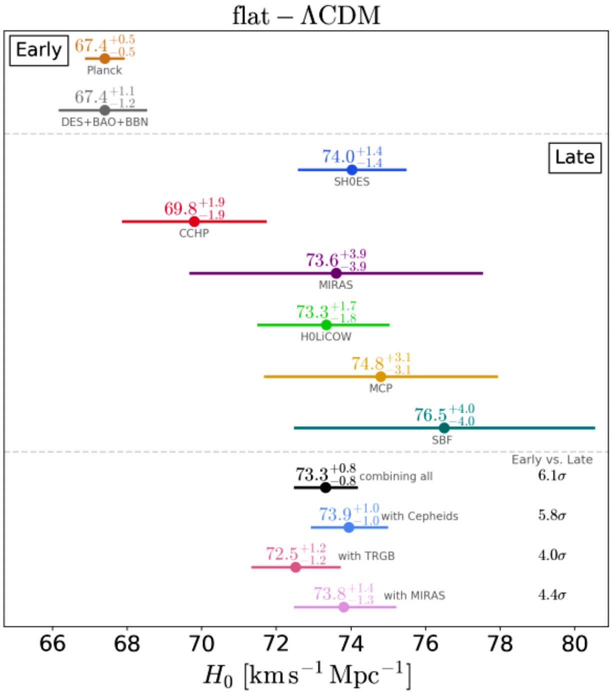

Fig. 2. The difference in measurements of the Hubble constant H0 for the early and late Universe.

The researches in various independent directions of H0 measurements, including those based on gravitational lensing and GLQs, allowing to measure H0 directly, in contrast to other local methods of measurements, relying on intermediate calibrations, has increased substantially at the present time. The ability to obtain high angular resolution of GLQs is necessary to separate the lensed components and measure the times delay between them with high accuracy that need for measurement of H0.

By high angular resolution is meant the possibility to significantly increase the angular resolution of the digital GLQ images for a given observatory, given telescope and camera, exceeding the possible actual observable limit. This is possible by applying modern digital processing methods based on the principle of inverse mathematical convolution called deconvolution, in particular the MCS [1] and FIREDEC [4] methods with a detailed consideration of the instrumental profile of point sources for individual stars, noise filtering and separation into point components and galaxy background.

For example, on images with the quality seeing~0.6-0.7" observed at the Maidanak observatory with 1.5 m AZT-22 telescope, by MCS deconvolution it is possible to "restore" the image blurred by the atmosphere to the value FWHM=0.26" and to generally identify the lasing galaxy[5,6].

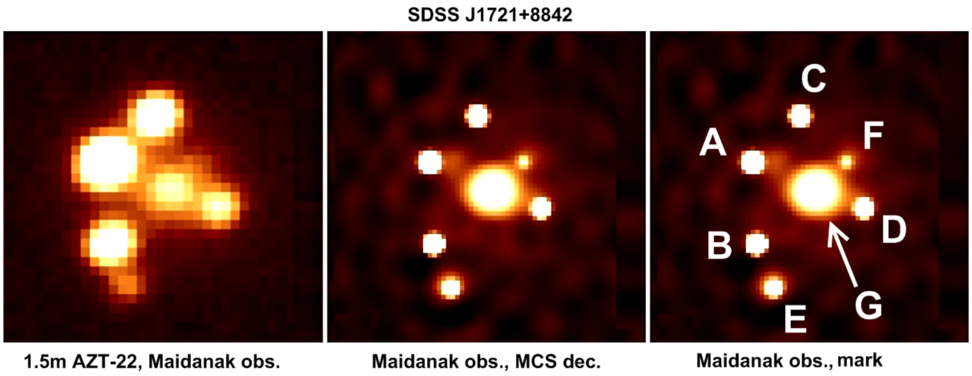

Fig. 3. The results of the best GLQ observations SDSS J1721+8842from the Maidanak Observatory (left), digital image processing by MCS deconvolution (center), identification of lensed ABCD components and lensed G galaxies (right).

Observations of the studied GLQ SDSS J1721+8842 at the Maidanak observatory were carried out in the period 2018-2020 on the AZT-22 telescope with the SNUCAM 4Kx4K camera in the R filter. A light curve of the for the observation period from May 25, 2018, to November 15, 2020, including the general variability of all 6 lensed components of the GLQ, was obtained from the data processing in the IRAF by differential aperture photometry (Fig.4).

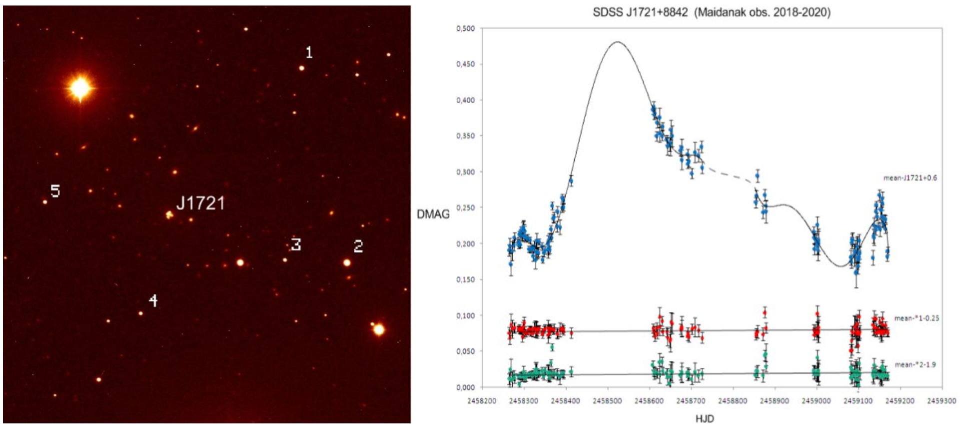

Fig. 4. Observation field and general light curve of SDSS J1721+8842 for 2018-2020, approximated by polynomials and straight lines of the two constant referent stars.

Differential aperture photometry, which characterizes the general light curve, was performed with aperture measurements of 30 pixels that ~8" included all lensed components and galaxy. Photometry was performed relative to the average value (mean) of the magnitudes of 5 selected referent stars and also with calculation of the RMS errors of measurements. The light curves for 2018-2019 and 2020 are separately approximated by polynomials of degree 6 (separated by dashed lines in Fig.4), which show a characteristic total active optical variability with an amplitude of about 0.3 magnitudes and oscillations characterizing the variable energy release in the acretic disk around super massive black holes of the lensed quasar.

This intrinsically relatively fast optical variability with a characteristic time of about 10-30 days, compared to the expected slow external variability of the order of months due to microlensing on moving stars and their clusters in the lensing galaxy, will allow us to calculate times delay with a higher accuracy from the combined observational results in the future.

Measurement of the time delay requires separation and photometry of the individual lensed components. Based on the results of MCS deconvolution of all observational data, the light curves of the 4 lensed components of the SDSS J1721+8842 GLQ are obtained(Fig.5). For all components of the GLC SDSS J1721+8842, the general internal active optical variability of the quasar and the influence of the small external microlensing variability are revealed.

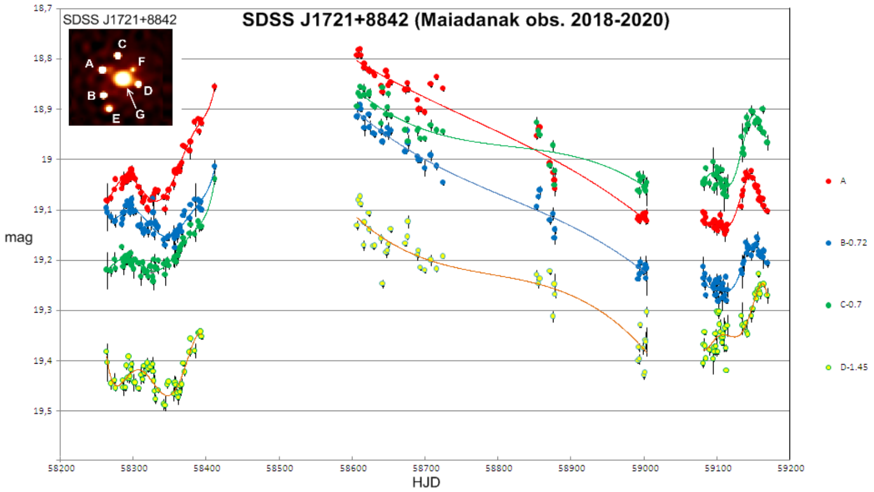

Fig. 5. Light curves of the individual lensed components of the SDSS J1721+8842 based on MCS deconvolution and identification of microlensing effects.

The analysis of light curves of SDSS J1721+8842 was carried out using the technique of approximation by splines specially developed software in PyCS. Thus, the brightness changes of the components of the lensed quasar SDSS J1721+8842 in the sequence A-C-B-D were determined with time delays: AC=-8.5±1.7 days, AB=-10.3±1.7 days and AD=-18.7±2.8 days.

Reference

1. Magain P., Courbin F., & Sohy S. ApJ 1998, v. 494, p. 472.
2. Asfandiyarov I.M., Ehgamberdiev Sh.A., Millon M., Courbin F. Uzbek Journal of Physics 2020, v.22 (6), p.325.
3. Licia Verde, Treu Tommaso, Riess Adam G. Nature Astronomy 2019, v. 3, p. 891.
4. Cantale N. et al. A&A 2016, v. 589, p. A81. https://doi.org/10.1051/0004-6361/20142400
5. Asfandiyarov M., Egamberdiev Sh. A., Burkhonov O. A., Courbin F., Millon M. Doklady Akademii Nauk 2019, v.6, p. 37.
6. Asfandiyarov M., Egamberdiev Sh. A. Doklady Akademii Nauk 2020, v. 5, p. 14.

MAGNETOHYDRODYNAMIC SEISMOLOGY OF THE CORONA OF THE SUN BY KINK OSCILLATIONS

VM NAKARIAKOV[1,2]

[1]Physics Department, University of Warwick, United Kingdom; ORCID: 0000-0001-6423-8286
[2]Special Astrophysical Observatory of RAS, St. Petersburg, Russia
E-mail: V.Nakariakov@warwick.ac.uk

Processes operating in the outer part of the atmosphere of the Sun, the fully-ionised and magnetically-dominated plasma of the solar corona, remain one of the major puzzles of the Solar System. The solar physics research community is well supported by a number of ground-based and spaceborne observational facilities providing us with a wealth of high-precision data throughout the electromagnetic wave spectrum, from radio to gamma-rays. However, several key parameters of the solar corona, in particular, the magnetic field, are not open to direct observations. The method of magnetohydrodynamic (MHD) seismology, based on the estimation of plasma parameters by MHD waves, provides us with a paradigm-changing diagnostic tool for probing the plasma in the corona. Modern MHD seismology utilises confidently detected kink, sausage and slow MHD modes of various plasma structures to reveal key parameters of the corona, and processes operating there. In the paper, we present the current state-of-the-art in MHD seismology with the use of kink oscillations, based upon high-precision EUV observations and elaborated theory of MHD modes of a plasma cylinder. Kink oscillations allow for estimating the absolute value of the magnetic field, density stratification scale height, and also density contrast and transverse profile.

Keywords: corona of the Sun, MHD waves, coronal loops, plasma waves, turbulence
PACS: 96.60.Pb, 96.50.Tf

Introduction

The corona of the Sun is the outermost part of the solar atmosphere. The corona consists of an almost fully-ionized almost hydrogen plasma characterised by a very high temperature, typically exceeding one million K. The electron concentration varies from 10^{8} cm^{-3} in coronal holes to 10^{11-12} cm^{-3} in so-called active regions. The plasma is penetrated by a magnetic field which is generated by dynamo processes in the solar interior, and emerges through the solar surface. Regions of the corona in which the magnetic field is seen to bend and return to the solar surface are called the “closed” corona, while the regions in which the field goes outward to fill up the solar system and reach the interstellar medium is known as the “open” corona. In the steady regime, the closed corona occupies the volume up to a half of the solar radius (~ $7\text{x}10^{10}$ cm). Typical values of the magnetic field are estimated from a few G to several tens of G, while direct measurements are absent. From the plasma physics point of view, despite the huge temperatures, the corona is a “cold” plasma environment, as the plasma parameter β is typically much low than unity, i.e., magnetic forces dominate over thermal pressure forces.

The corona is seen to be highly non-uniform, see Figure 1, and consists of myriads of dense structures stretched along the magnetic field. In other words, some magnetic flux tubes are filled in with a denser plasma. Those flux tubes are surrounded by a more rarefied plasma penetrated by the magnetic field too. Most spectacular examples of such plasma structures are coronal loops, clearly seen in the figure. Typical minor radii of the loops are about 10^{8} cm. Regions of the corona in which the loops are hottest and densest can host most powerful phenomena in the solar system, such as flares and coronal mass ejections (CMEs), and are called active regions. Often, coronal active regions are situated over sunspots, pores and other photospheric concentrations of the magnetic field.

The interest in the solar corona is both practical and fundamental. From the practical point, the corona is the birthplace of space weather, determining the physical conditions in the near-Earth's space which affect various technologies such as navigation and communication systems, electric supply lines, pipelines, satellites, and many others. Forecasting of extreme events, for example, flares and coronal mass ejections (CMEs) requires comprehensive understanding of physical conditions in solar coronal active regions, and processes operating in them. For astrophysics, the corona is the only stellar coronae open to high-resolution observations, which is invaluable for stellar physics, in particular, for the study of basic processes of plasma astrophysics, such as magnetic reconnection, charged particle acceleration and turbulence, and also for the determination of habitable zones of exoplanets. Moreover, the corona is served as a natural plasma laboratory. Indeed, the vast variety of combinations of plasma parameters allows for the study of physical processes important for numerous applications, for example, for controlled thermonuclear fusion efforts. In addition, the corona offers several specific unanswered yet questions: what does compensate huge radiative and thermo-conductive losses of the coronal plasma, i.e., heats the corona; which mechanism determines rapid releases of the magnetic energy in flares and CMEs, and how is the solar wind accelerated up to 1000 km s^{-1}.

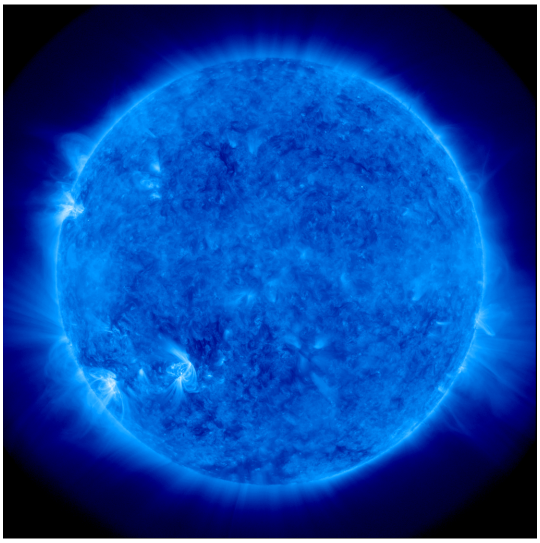

Fig. 1. The corona of the Sun observed in the EUV band, in the 171Å channel of the Atmospheric Imaging Assembly on the Solar Dynamics Observatory spacecraft. The colour palette is artificial.

The corona is intensively monitored and explored with a fleet of spacecraft, with EUV and soft X-ray imaging telescopes and spectrometers, and energetic particle detectors, and a number of ground-based optical coronagraphs and radio telescopes and interferometers. The choice of the observational facilities is dictated by the extreme conditions in the corona. In the EUV band, which is most used in the coronal study, the main information is obtained from the photons produced by atomic transitions in multiply ionised minor ions. For example, the popular 171 Å bandpass is sensitive to the Fe IX and Fe X ionization states of iron, at a characteristic temperature of about 10^6 K. A major limitation of coronal observations is the intrinsic difficulty with the measurement of the magnetic field, the physical parameter which determines the energetics and structure of the corona. In particular, the EUV and soft X-ray bands, this difficulty relates to the inherent thermal broadening of the emission lines, significantly exceeding the line splitting by the Zeeman effect. There are interesting perspectives for the estimation of the magnetic field by the electron cyclotron frequency in the radio band, but, unfortunately, the spatial resolution of the radio observation is intrinsically rather poor. Likewise, several other key parameters of the coronal plasma, such as transport coefficients and the scale of fine structuring, are not open to direct observations. A promising indirect method allowing for obtaining this crucial information is *magnetohydrodynamic (MHD) seismology*.

MHD modes of a plasma cylinder

Theoretical modelling of MHD waves in the corona is based on the consideration of MHD perturbations of a plasma cylinder, i.e., a 1D non-uniformity of the plasma parameters across the axis of a cylinder stretched along the magnetic field [1, 2]. The main feature of this model is the existence of magnetoacoustic waves guided by the cylinder. Locally the waves are oblique, i.e., their local wave vector has an angle with respect to the axis of the cylinder, while globally the wave energy is transferred along the cylinder. The structure of the perturbations inside and outside the cylinder is determined by the radial profiles of the equilibrium parameters, in particular, of the Alfvén and sound speeds. Another important parameter of the wave perturbations (or modes) is the integer azimuthal number m. Modes with $m=0$ are called sausage, with $m=\pm 1$ are kink, and with $|m|>1$ are ballooning of fluting. Properties of modes with different azimuthal symmetries are very different [2]. In the low-β plasma of the corona, phase speeds of MHD modes of a cylinder appear in two bands. The fast band is restricted by the Alfvén speeds inside and outside the cylinder, C_{Ai} and C_{Ae}, respectively, and the slow band is limited by the so-called tube (or cusp) speed, C_{T} determined by the sound and Alfvén speeds inside the cylinder, and the internal sound speed C_{si}. The cusp speed is usually slightly lower than the sound speed, and the slow band is rather narrow. In the infinite field approximation, the cusp speed approaches C_{si}. Most fast modes are leaky in the in the long-wavelength limit, when the parallel wavelength is large in comparison with the radius of the cylinder (or the minor radius of the loop modelled by the cylinder), i.e., the cylinder acts as a fast magnetoacoustic antenna. The exception is the kink mode, with the phase speed approaching in the long wavelength limit the kink speed,

$$C_{\mathrm{k}} \approx C_{A\mathrm{i}}\sqrt{\frac{2}{1+\rho_{\mathrm{ext}}/\rho_{\mathrm{int}}}}\,, \tag{1}$$

where ρ_{ext} and ρ_{int} are the equilibrium plasma densities outside and inside the cylinder, respectively. In the slow band, in the long wavelength limit, all modes approach the cusp speed.

Together with the effect of guided wave propagation, the field-aligned structuring of the plasma introduces wave dispersion, i.e., the dependence of phase and group speeds of the waves on oscillation periods and hence wavelengths. It is connected with the presence of a characteristic spatial scale in the system, the radius of the cylinder. If the radial profile of the Alfvén speed is smooth, all fast modes except the sausage one experience linear coupling with torsional Alfvén waves [3]. These waves which are propagating alternate twistings and rotations of the cylinder, are incompressive and dispersionless. Importantly, torsional waves are not global, i.e., in contrast with fast and slow modes, they do not involve in the wave motion the whole volume of the cylinder: perturbations of each surface of the constant Alfvén speed propagate along the cylinder at this speed. Because of that, the linear coupling is not reversable, i.e., the energy of fast waves is continuously transferred to torsional waves which are very difficult to detect observationally. In particular, in the initial phase of the coupling, also called resonant absorption, the amplitude of a kink oscillations decreases according to the Gaussian dependence on time, which then becomes exponential with the damping time linearly proportional to the kink oscillation period P_{kink}, see [4]. The coefficient of the proportionality depends on the density contrast in the cylinder, and on the steepness of the radial profile of the Alfvén speed.

The approximate description of MHD modes of coronal plasma structures, such as coronal loops, in terms of the cylinder model, neglects the plasma stratification, the magnetic field bending and twisting, and the variation of the cross-sectional area of the magnetic flux tube with height. However, all these effects are known to be minor, and results of the cylinder model of coronal loop oscillations are adequate. Moreover, observations show that the loop minor radius is approximately constant along the loop, suggesting that the magnetic field is constant too. The cylinder model is the standard approach in the description of MHD oscillations of solar coronal loops.

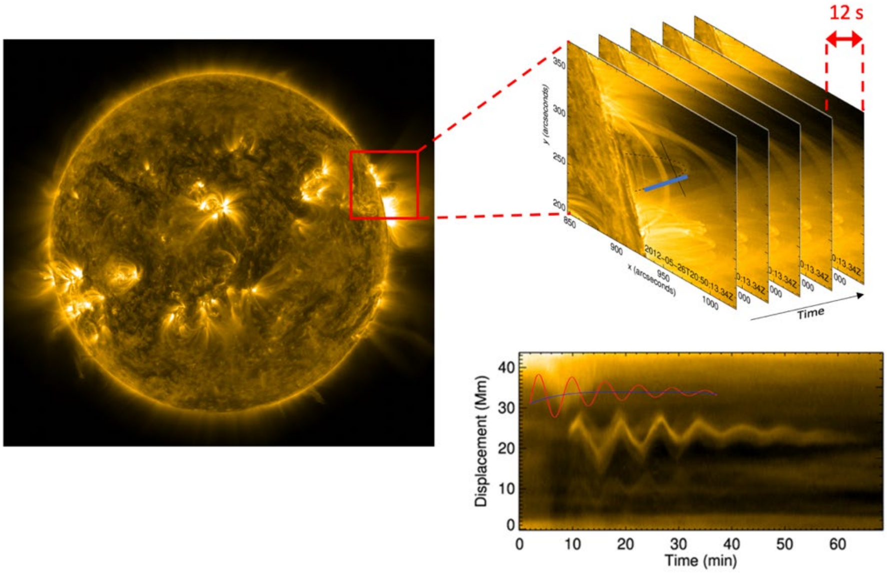

Fig. 2. Construction of a time-distance map illustrating a kink oscillation of a coronal loop, shown in the bottom right panel. The left panel shows an EUV image with the red box indicating the region-of-interest. The top right panel shows a sequence of images of the region-of-interest taken at different instants of time with the cadence of 12 s, with the blue solid line indicating the slit taken across an oscillating loop, used for the time-distance map.

Kink oscillations of coronal plasma loops

The high spatial and time resolution and sensitivity of modern EUV imagers, such as the Atmospheric Imaging Assembly (AIA) on the Solar Dynamics Observatory (SDO) [5], allows for confident detection of oscillatory transverse displacements of coronal loops, called kink oscillations. Figure 2 shows the standard time-distance technique used for the analysis of the oscillations. Usually, the oscillation is identified by eye in a digital movie of an active region of interest. Then, a slit across the oscillating loop is chosen, and the distribution of the EUV intensity along the slit is determined in a sequence of images. The intensity distribution could be considered as an elongated rectangle of one (or several) pixels wide. Such rectangles are stacked next to each other to form a map with the horizontal axis corresponding to the times when the images were consecutively taken, and the vertical axis giving the direction along the slit, i.e., the direction of the oscillation of interest. In such a time-distance map, a waveform representing the oscillatory displacements of the loop is clearly seen. This waveform could be fitted by a guessed function, such as, for example, a decaying sinusoid. The use of some approximation technique, such as the least square error method or more sophisticated technique based on Bayesian statistics, gives us parameters of the best-fitting function, such as the oscillation period, damping time, and initial amplitude and phase. By the way, the waveform shown in the bottom right panel, is rather “triangular” than a sinusoid, which indicates a possible presence of higher harmonics of the oscillation.

Kink oscillations of coronal loops are seen in two different regimes. The *large-amplitude rapidly decaying* kink oscillations are standing, usually fundamental harmonics of the loops, with the maximum displacement amplitude at the loop apex, and nodes at footpoints. The standing nature is revealed by the same phase of the oscillatory displacements at different segments of the loop. In this regime, oscillations are induced by low-coronal eruptions by the mechanical displacement of the loop from its equilibrium. Typical displacement amplitudes after the excitation range from 10^8 to 10^9 cm, with the mean value of about 3×10^8 cm [6]. Obviously, these values are subject to the line-of-sight projection effect, as the displacements are observed projected on the plane of the sky. Lengths of oscillating loops are estimated in the range $1.5\text{-}4.2\times10^{10}$ cm. Typical oscillation periods span from 1 min to 29 min, with the mean at about 6 min, and the damping times are from a few minutes to several tens of minutes. Importantly, the oscillation period shows a linear dependence on the loop length, see Fig. 3, confirming the standing wave nature of this phenomenon, i.e., that kink oscillations are natural oscillations of the loops. The observed scattering of the data should be attributed to the scattering of values of the kink speed in different loops, which ranges from 8×10^7 cm s^{-1} to 3.3×10^8 cm s^{-1}, with the mean value at 1.3×10^8 cm s^{-1}. Likewise, the damping time is seen to scale linearly with the oscillation period, which is consistent with the damping by resonant absorption. On the other hand, the quality factor determined by the ratio of the damping time to the oscillation period is found to depend on the oscillation amplitude to the minus 2/3, indicating the nonlinear nature of this effect. Occasionally, second and third parallel harmonics are detected, while their amplitudes are typically much lower than of the fundamental harmonic. The oscillation periods of higher harmonics are shorter than of the fundamental mode. The displacements are either in anti-phase in the opposite legs of the loop, in the second harmonic, or, in the third harmonic, in phase in the legs and in anti-phase with them at the apex.

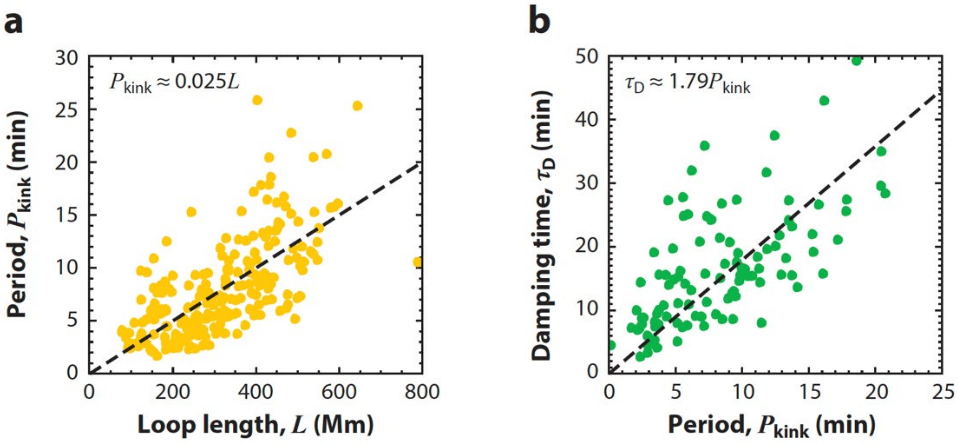

Fig. 3. Relationships between periods and damping times of decaying kink oscillations, and lengths of the oscillating loops coronal loops, (a) The oscillation period versus the loop length. (b) The exponential damping time versus the oscillation period. The dashed curves show the best-fitting linear dependences. Adapted from [6].

In quiet periods of the solar activity, i.e., in the time periods without flares or eruptions, coronal loops are seen to oscillate with much lower amplitude, from about 5×10^6 cm to 5×10^7 cm. However, the amplitude is not steady, and sometimes grow in time [7]. In this regime, kink oscillations do not experience any noticeable damping. The oscillation periods of *decayless kink oscillations* scale linearly with the estimated lengths of the loops too, and displacements are simultaneous everywhere along the loop. Thus, like in the decaying regime, the decayless oscillations are natural modes of the loops, and their parameters are determined by the parameters of the hosting loop. Sometimes, the second parallel harmonic is detected too, with the displacement in the opposite legs being in anti-phase with each other.

Coronal loop seismology with kink oscillations

Properties of waves carry information about properties of the medium they propagate through. The use of coronal MHD waves for the diagnostics of the plasma structures they are supported by is known as MHD seismology of the corona. Coronal MHD waves of all kinds are used for seismology (e.g., [8, 9]), while the most popular are kink oscillations.

In the long wavelength limit, typical for low parallel kink harmonics of loops, the ratio of the loop length L_{loop} to the oscillation period P_{kink} is about the kink speed (see Eq. (1)). The oscillation period can be determined by a time-distance map (see Figure 3), while the loop length can be estimated my measuring the apparent distance between footpoints under the assumption that the loop has a semi-circular or elliptic shape. Thus, one gets the estimation of the kink speed, which in turn depends, via the Alfvén speed, upon the absolute value of the magnetic field in the loop. The expression for the estimation of the magnetic field (see [10]) is thus

$$B_0 \approx \frac{L_{\text{loop}}}{P_{\text{kink}}} \sqrt{2\mu_0 \rho_{\text{int}} \left(1 + \frac{\rho_{ext}}{\rho_{int}}\right)}\,, \tag{2}$$

where μ_0 is the magnetic permeability of vacuum. The main shortcoming of this method is the uncertainty in the estimation of the plasma density and the density contrast inside and outside the loop. But the estimation of the Alfvén speed in an active region, which requires the knowledge of the density inside the loop only, is useful too. In addition, despite the magnetic field being almost constant along the loop, the plasma density is subject to stratification, i.e., is not constant along the loop. However, parameters of the oscillation are primarily determined by the kink speed at the segment where the oscillation amplitude is highest, justifying the applicability of Eq. (2).

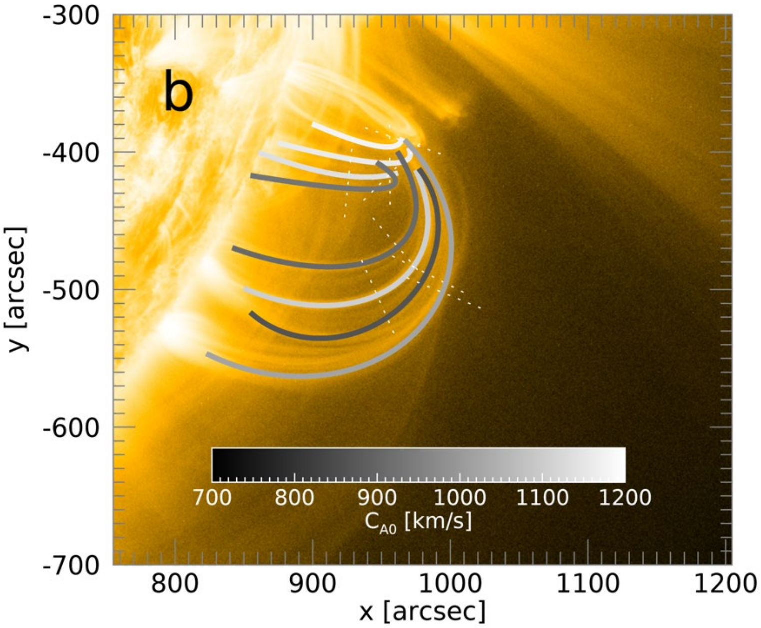

Fig. 4. Mapping the Alfvén speed in a coronal active region by decayless kink oscillations. The colour of the broad curves following the coronal loops shows the internal Alfvén speed $C_{A\mathrm{i}}$. The EUV image of obtained with SDO/AIA at 171 Å is used as the background. Artificial slits used for creating time–distance plots are marked with the straight dotted lines. Adapted from [11].

The most powerful application of this method is based on the use of decayless kink oscillations, as it allows for the determination of the active region parameters before a flare or eruption. This informal is crucial for forecasting of space weather drivers. Figure 3 shows a map of the Alfvén speeds inside loops forming an active region, determined by decayless kink oscillations.

In cases when multiple parallel harmonics are detected, the ratio of their periods could be used for estimating the density stratification. The idea of this estimation is based on the structure of the oscillation amplitude along the loop: if in the fundamental harmonic the highest amplitude is at the apex, in the second harmonic it is in the legs. Thus, different harmonics probe the kink speed, and hence the plasma density at different locations, i.e., heights. In the isothermal corona, the plasma density depends upon the height z exponentially, $\rho \propto \exp{(-z/\Lambda)}$, where Λ is the scale height. The expression

$$\Lambda \approx \frac{L_{\text{loop}}}{\pi^2}\left(1-\frac{P_{\text{kink}}^{(1)}}{2P_{\text{kink}}^{(2)}}\right)^{-1}. \tag{3}$$

gives us the estimation of the scale height by the ratio of periods of the fundamental and second harmonics, $P_{\text{kink}}^{(1)}$ and $P_{\text{kink}}^{(2)}$, respectively [12].

The damping scenario of rapidly-decaying kink oscillations provides us with useful seismological information too, especially if the waveform shows both Gaussian and exponential damping regimes. In this case, seismological inversions for the transverse density profile and contrast ratio are possible [13].

Conclusions

The corona of the Sun is a natural plasma environment consisting of a broad variety of plasma structures with various combinations of parameters. The study of physical processes operating in the corona is of interest for fundamental plasma physics and stellar astrophysics, and also for practical applications in space weather. Moreover, investigation of the coronal plasma behaviour provides us with information important for ongoing efforts in controlled fusion. But extreme conditions in the corona, especially its high temperature and almost full ionisation make it difficult to measure several key parameters of the corona, such as the magnetic field and fine structuring of the plasma.

High-precision EUV observations of oscillatory processes in the solar corona create a solid ground for the seismological diagnostics of various plasma structures. In particular, kink oscillations give us information about the absolute value of the magnetic field in the oscillating loops, density stratification scale height, and transverse profile of the plasma. A promising feature of this method is the possibility to make the diagnostics in pre-flare time intervals by the kink oscillations in the decayless regime. A shortcoming of this approach is a very low amplitude of oscillations in this regime. It is expected that advanced resolution will be achieved with the solar EUV imagers of the next generation, such as the Extreme Ultraviolet Imager on the Solar Orbiter [14].

The intensive development of MHD seismology during last two decades makes this branch of solar physics a mature research field which offers the research community even more shiny perspectives. Here we summarise several ongoing and future challenges connected with seismology by kink oscillations. One of the promising topics is revealing the nature of coronal loops, which are the main building block of coronal active regions. It remains unclear why the minor radii of loops remain almost constant, suggesting, by the conservation of the magnetic flux, the constant magnetic field. As kink oscillations are highly sensitive to the transverse structuring of the plasma, they can shed light on the internal structure of a loop. They can reveal, in particular, whether the loop is a bundle of plasma threads, or it is constructed of coaxial shells. Likewise, the presence of fine, sub-resolution surface electric currents could be revealed. Another important future research avenue is the development of methods for the seismological estimation of the free (non-potential) magnetic energy which could be released in flares and various eruptions. It is also of interest to estimate the fraction of the energy released by microflares (and nanoflares) which is converted into kink oscillations. This information would be important for estimating the flare energetics and the nanoflare scenario of coronal heating. For seismological purposes it is of interest to study a possible association of parameters of kink oscillations with the class of the hosting active region. The variation of the kink oscillation parameters with the solar cycle requires attention too. In theory, revealing the mechanism responsible for the decayless regime of the oscillations is one of the primary tasks. Likewise, the understanding of nonlinear mechanisms of the kink oscillation decay is required. Thus, the study of kink oscillations of coronal loops, and their use for plasma diagnostics is a rapidly developing and important branch of modern solar physics.

Funding

This research was funded by the Russian Foundation for Basic Research, grant number 18-29-21016.

References

1. Zajtsev, V.V., Stepanov, A.V. Geomagn. Aeron. Fiz. Solntsa 1975, v. 37, p. 3.
2. Nakariakov, V.M., Kolotkov, D.Y. Annu. Rev. Astron. Astrophys. 2020, v. 58, p. 441. DOI: 10.1146/annurev-astro-032320-042940
3. Goossens, M.L., Arregui, I., Van Doorsselaere, T. Front. Astron. Space Sci. 2019, v. 6, id. 6. DOI: 10.3389/fspas.2019.00020
4. Nakariakov, V.M., et al. Space Sci. Rev. 2021, v. 6, id. 73. DOI: 10.1007/s11214-021-00847-2
5. Lemen, J.R., et al. Solar Physics 2012, v. 275, p.17. DOI:10.1007/s11207-011-9776-8
6. Nechaeva, A., et al. Astrophys. J. Suppl. Ser. 2019, v. 241, id. 31. DOI: 10.3847/1538-4365/ab0e86
7. Wang, T., et al. Astrophys. J. Lett. 2012, v. 751, id. L27. DOI: 10.1088/2041-8205/751/2/L27
8. Liu, W., Ofman, L. Solar Phys. 2014, v. 289, p.3233. DOI: 10.1007/s11207-014-0528-4
9. De Moortel, I., Nakariakov, V. M. Phil. Trans. Royal Soc. A 2012, v. 370, p. 3193. DOI: 10.1098/rsta.2011.0640
10. Nakariakov, V. M., Ofman, L. Astron. Astrophys. 2001, v. 372, p. L53. DOI: 10.1051/0004-6361:20010607
11. Anfinogentov, S.A., Nakariakov, V.M. Astrophys. J. Lett. 2019, v. 884, id. L40. DOI: 10.3847/2041-8213/ab4792
12. Andries, J., et al. Space Sci. Rev. 2009, v. 149, p. 3. DOI: 10.1007/s11214-009-9561-2
13. Pascoe, D.J., Hood, A.W., Van Doorsselaere, T. Front. Astron. Space Sci. 2019, v. 6, id. 22. DOI: 10.3389/fspas.2019.00022
14. Rochus, P., et al. Astrophys. 2020, v. 642, id.A8. DOI: 10.1051/0004-6361/201936663

Printed: 25.01.2022
Volume 31,25 p.s.. Amount 100

Baku State University Publising House.
33, Acdemician Z. Khalilov street,
Baku, Azerbaijan
Tel: (+99412) 538 87 39 / 538 50 16
e-mail: bdumetbee@gmail.com
www.bsu.edu.az